NASA Contractor Report 3524

Configuration Design Studies and Wind Tunnel Tests of an Energy Efficient Transport With a High-Aspect-Ratio Supercritical Wing

Preston A. Henne, John A. Dahlin,
Charles C. Peavey, and Donna S. Gerren

NASA

NASA Contractor Report 3524

Configuration Design Studies and Wind Tunnel Tests of an Energy Efficient Transport With a High-Aspect-Ratio Supercritical Wing

Preston A. Henne, John A. Dahlin,
Charles C. Peavey, and Donna S. Gerren
McDonnell Douglas Corporation
Long Beach, California

FOREWORD

This document presents the results of a contract study performed for the National Aeronautics and Space Administration (NASA) by Douglas Aircraft Company, of McDonnell Douglas Corporation. This work was part of Phase II of the Energy Efficient Transport (EET) project of the Aircraft Energy Efficiency (ACEE) program.

Acknowledgements for their support and guidance are given to the NASA technical monitor for the contract, Mr. T.G.. Gainer of the Energy Efficient Transport Project Office at the Langley Research Center, and to Mr. J.R. Tulinius, the on-site NASA representative; also, to Dr. R.T. Whitcomb of Langley Research Center, for his creativity in providing industry with the versatile and practical concept that has been successfully demonstrated by tests and fuel-efficiency studies of the supercritical wing. Acknowledgement is also given to the Director and staff of the Ames Research Center, where the extensive test program was conducted.

The Douglas personnel who made significant contributions to this work were:

M. Klotzsche	ACEE Program Manager
A.B. Taylor	EET Project Manager
P.A. Henne	Task Manager, Aerodynamic Design (Report author)
J.T. Callaghan	Aerodynamic Project Engineer - EET
C.C. Peavey	Aerodynamic Design (Report author)
J.A. Dahlin	Aerodynamic Design (Report author)
D.S. Gerren	Aerodynamic Design (Report author)
D.K. Steckel	Aerodynamic Design (Retired)
D.G. MacWilkinson	Aerodynamic Design
D.L. McDowell	Aerodynamic Design
J.D. Cadwell, et.al.	Aerodynamics Wind Tunnel Model Group

CONTENTS

ILLUSTRATIONS

ILLUSTRATIONS (Cont)

ILLUSTRATIONS (Cont)

ILLUSTRATIONS (Cont)

TABLES

SUMMARY

This report presents the results of the design, fabrication, and wind-tunnel testing of models of a fuel-efficient advanced-technology aircraft derived from detailed system studies of a medium-range, narrow-body transport. The task was an extension of an earlier study which showed that the use of high-aspect-ratio supercritical wing technology can achieve significant reductions in fuel burned and direct operating cost. The results of the earlier study were used to develop a wing configuration with improved performance in terms of reduced drag creep and extended buffet boundary. Nacelles and pylons, flap linkage fairings, and tail surfaces were tested. The effect of engine nacelle placement on drag and longitudinal characteristics was examined and found to be substantial. The effect of horizontal tail span on longitudinal stability characteristics was determined, and the effect of boundary layer transition location on lift curve slope was also investigated.

INTRODUCTION

Recent research on supercritical wings has shown conclusively that there is a definite performance advantage to be obtained from the use of this technology. However, the manner in which this advantage is used and the magnitude of the gains are functions of many variables and are difficult to assess without detailed studies that evaluate the airplane realistically as an integrated system fulfilling current social, operational, and economic needs.

The Douglas Aircraft Company has for some time been studying various sizes of advanced-technology transports employing supercritical wing technology. The environment in which these studies have been made was one of rapidly rising inflation, concern over fuel prices and availability, and increasingly stringent noise regulations. It became apparent in these studies that:

(1) Due to the increased cost of producing a new aircraft, advanced technologies would be needed to design and build an aircraft which could compete with today's transports and offer an economic advantage.

(2) Concern over fuel meant that this new design would have to be more fuel-efficient and hence the new technologies most probably could not be used to improve the level of comfort or significantly increase speed.

(3) Greater aerodynamic efficiency in terms of low-speed lift/drag would be needed to supplement engine technology in meeting new noise requirements.

Preliminary systems studies had shown the benefit of applying the supercritical technology advantage to a combination of increased thickness and higher aspect ratio. In light of this and other factors previously mentioned, a detailed study of the thick, high-aspect-ratio, supercritical wing was included as part of the Douglas EET effort.

Phase I of this EET contract effort was associated with fundamental, high-speed development of efficient, high-aspect-ratio, supercritical wing geometry for the DC-X-200, a 200-plus passenger, wide body, medium-range transport[2]. Five wing configurations were tested to determine the high-speed effects of airfoil leading and trailing edge geometry and wing spanload. Baseline nacelle/pylon, flap support fairing, aileron, and tail surface components were also evaluated with selected wing configurations. The results of the initial-phase studies demonstrated that the use of high-aspect-ratio, supercritical wing technology can achieve significant reductions in fuel burned and direct operating cost.

This report summarizes the results of the second phase of the EET contract effort for the development of high-aspect-ratio, supercritical wing high-speed technology. In this second phase, the characteristics established and evaluated in Phase I activity have been utilized to develop a more optimum wing configuration. The wing development has also extended to the more timely case of the Advanced Technology Medium Range (ATMR) transport, a 170-180 passenger narrow-body configuration. In addition to the basic wing/body development, considerable attention has been directed to nacelle/pylon location effects, horizontal tail configuration effects, and influences of boundary layer transition on lift curve slope in the cruise regime. The specific objectives of the Phase II efforts were to:

(1) Build and test a more optimum wing based on the results of the Phase I tests.

(2) Design, build, and test five pylons in order to investigate the effects of longitudinal and vertical movement of the nacelle as well as an alternate spanwise position.

(3) Design, build and test two horizontal tails in order to study the effect of tail span on the pitching moment characteristics with and without nacelles and pylons.

(4) Study, in the wind tunnel, the effects of transition movement on the lift curve slope in the cruise regime.

The wing geometry configuration was developed through a combination of supercritical wing technology and advanced aircraft system studies. The supercritical wing technology included both Douglas and NASA contributions. The geometry development utilized application of existing experimental data and theoretical methods. Available experimental results included two-dimensional, high-Reynolds-number data from the NAE 5-foot wind tunnel as well as three-dimensional data from the NASA-Ames 11-foot, the Rockwell International 7-foot, and the NASA-Langley 8-foot wind tunnels. Theoretical analyses included considerable use of the Douglas versions of the two-dimensional Bauer, Garabedian, and Korn program[3] (Program H), its inverse counterpart[4], the three-dimensional Jameson program (FLO22)[5], and its inverse counterpart[6].

A model of the ATMR configuration was tested in the NASA Ames Research Center 11-foot transonic wind tunnel. High Reynolds number data, including forces, moments and wing pressure distributions, were obtained at Mach numbers of 0.3 to 0.9. The data were analyzed to study the wing performance characteristics, the effects of nacelle placement and horizontal tail span on performance, and the effect of transition movement on the lift curve slope.

SYMBOLS

All dimensional values presented in this report are given both in the International System of Units (SI)[1] and in U.S. Customary Units, the principal measurements and calculations having been made using the latter system. Longitudinal and lateral aerodynamic characteristics are referenced to the aircraft stability axes. Force and moment data are nondimensionalized by trapezoidal wing area and are presented in coefficient form.

Symbols and coefficients used in this report are defined as follows:

AR	wing aspect ratio, based on adjusted wing area (trapezoidal reference area, exposed glove area, plus area of exposed trailing-edge extensions)
B_{3A}	model fuselage
C_D	aircraft drag coefficient
C_L	aircraft lift coefficient
$C_{L_{max}}$	aircraft maximum lift coefficient
C_m	aircraft pitching moment coefficient
$C_{m_{ac}}$	aircraft pitching moment coefficient about wing aerodynamic center
$C_{m_{\bar{c}/4}}$	aircraft pitching moment coefficient about 25% of mean aerodynamic chord
C_p	pressure coefficient
$C_{p_{TE}}$	wing trailing edge pressure coefficient
CG	center of gravity
FRP	fuselage reference plane
H_{1C}, etc.	model horizontal tail
HRP	horizontal tail reference plane
L_H	horizontal tail length
L_V	vertical tail length

L.E.	leading edge
M	Mach number
M_{DIV}	drag divergence Mach number
MAC	mean aerodynamic chord
N/M/F	modification to Jameson FLO-22 program to include Nash-MacDonald turbulent boundary layer and approximate fuselage effects
N_{1C}	model nacelle
P_{1C},etc.	model pylon
Re	Reynolds number
$Re_{\bar{c}}$	Reynolds number based on mean aerodynamic chord
S	wing reference area (planform area)
S_H	horizontal reference area (planform area)
S_V	vertical tail reference area (planform area)
S_W	wing reference area (planform area)
T_1, etc.	boundary-layer transition configuration
T.E.	trailing edge
V_H	vertical tail volume
V_{1C}	model vertical tail
W_1	defined wing geometry
W_{1A}	model wing constructed for testing of defined geometry
W_3-W_8	defined wing geometries tested in Phase I
WRP	wing reference plane
X_{1A}	model wing-fuselage fillet
b	wing span
$b_{F_{1A}}$	model flap linkage fairing
b_H	horizontal tail span

c	airfoil chord or local wing chord
$\bar{c}$	length of mean aerodynamic chord
c_ℓ	section lift coefficient
i_H	horizontal stabilizer incidence angle, positive for trailing edge down
i_W	wing sectional twist angle
t/c	thickness-to-chord ratio
Γ	dihedral angle
ΔC_{D_C}	compressibility drag increment
Λ	sweep angle
$\Lambda_{c/4}$	sweep angle of quarter-chord
α	angle of attack
α_F	fuselage angle of attack, positive for nose-up
λ	wing taper ratio (trapezoidal)
η	fractional distance along wing semispan

CONFIGURATION DEFINITION

The rapidly increasing cost of fuel and the impact of airline deregulation in airline route networks have combined to identify requirements for an advanced technology medium-range transport (ATMR). In addition, the increasing age of the Boeing 727 airline fleet and the fuel consumption levels of this aircraft offer a significant replacement market for a fuel efficient aircraft with a passenger capacity between 170 and 180. Douglas in-house system studies of the ATMR included design goals of lower fuel consumption, greater economy, and reduced noise. When compared to a typical 727 in domestic service, the ATMR's fuel burned per seat is nearly 50 percent less.

Performance requirements, including a 2,600 nautical mile design mission, 130 knot approach speed, 35,000 foot initial cruise altitude and 7,000 foot takeoff field length requirements, resulted in the selection of a maximum takeoff gross weight of 203,500 pounds, an engine thrust of 32,000 pounds, and a reference wing area of 1,600 square feet. A three-view of the ATMR configuration is shown in Figure 1.

PASSENGER: 178 MIXED CLASS [96/86 cm (38/34 IN.)]

CARGO: 15 CONTAINERS (OPTIONAL) PLUS
           6.43 m^3 (227 FT^3) BULK = 39.56 m^3 (1397 FT^3)

45.23 m
(148.4 FT)

40.05 m
(131.4 FT)

13.5 m
(44.3 FT)
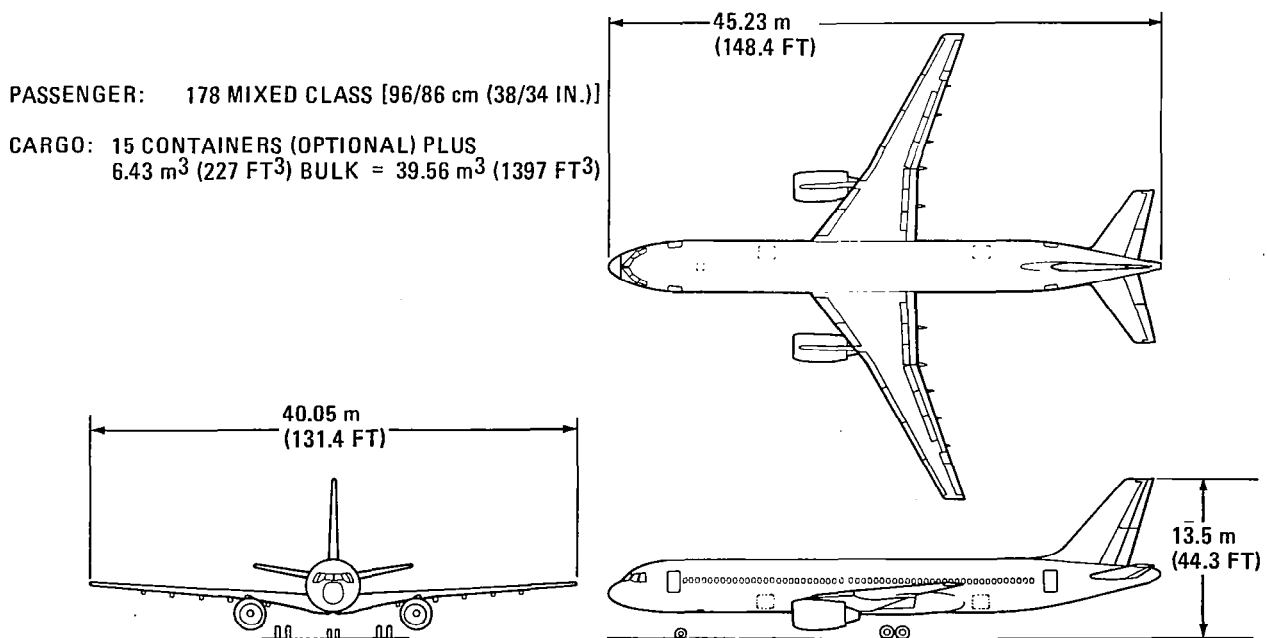
FIGURE 1. ATMR-11 — GENERAL ARRANGEMENT

One of the principal advanced aerodynamic technologies incorporated in this design is a high-aspect-ratio supercritical wing. The development of the high-speed wing geometry included heavy reliance on two-dimensional and three-dimensional test data and transonic computational flow methods[3-6]. The test data were used to determine broad design criteria, while the computational methods were applied to accomplish the many detailed designs analyzed before the final wing selection. The Phase I testing[2] provided an excellent starting point for this wing development.

The wing aspect ratio was re-evaluated in the ATMR system studies and the results of the analysis are presented in Figure 2. The variation of the fuel burned with adjusted aspect ratio (includes exposed yehudi and glove areas) indicates that minimum fuel burned is obtained between 10.0 and 10.5. The selected ATMR value is 10.0; the corresponding reference aspect ratio (trapezoidal) is 11.1.
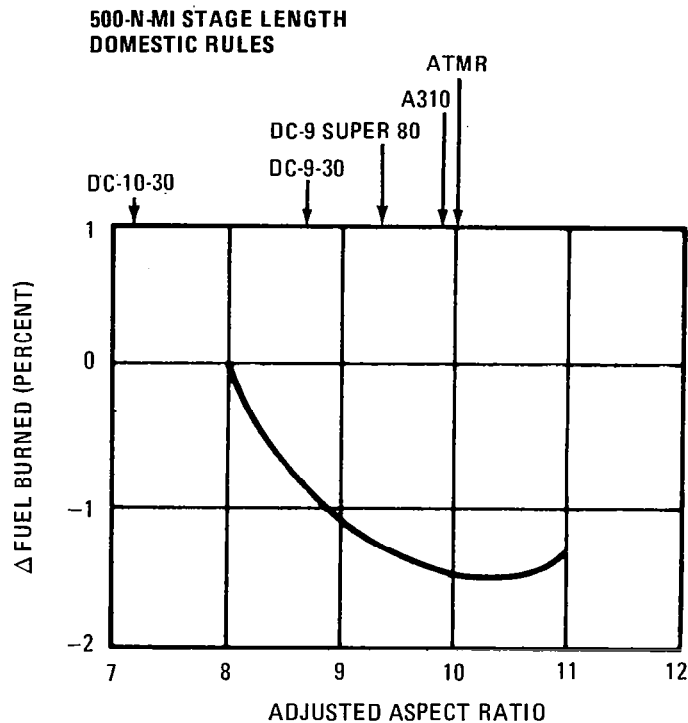
FIGURE 2. EFFECT OF ASPECT RATIO ON FUEL BURNED

The ATMR nominal design Mach number was 0.8 and the design C_L was 0.55. Based upon the Phase I test results shown in Figure 3, the previous wing configurations had a drag divergence Mach number in excess of 0.8.
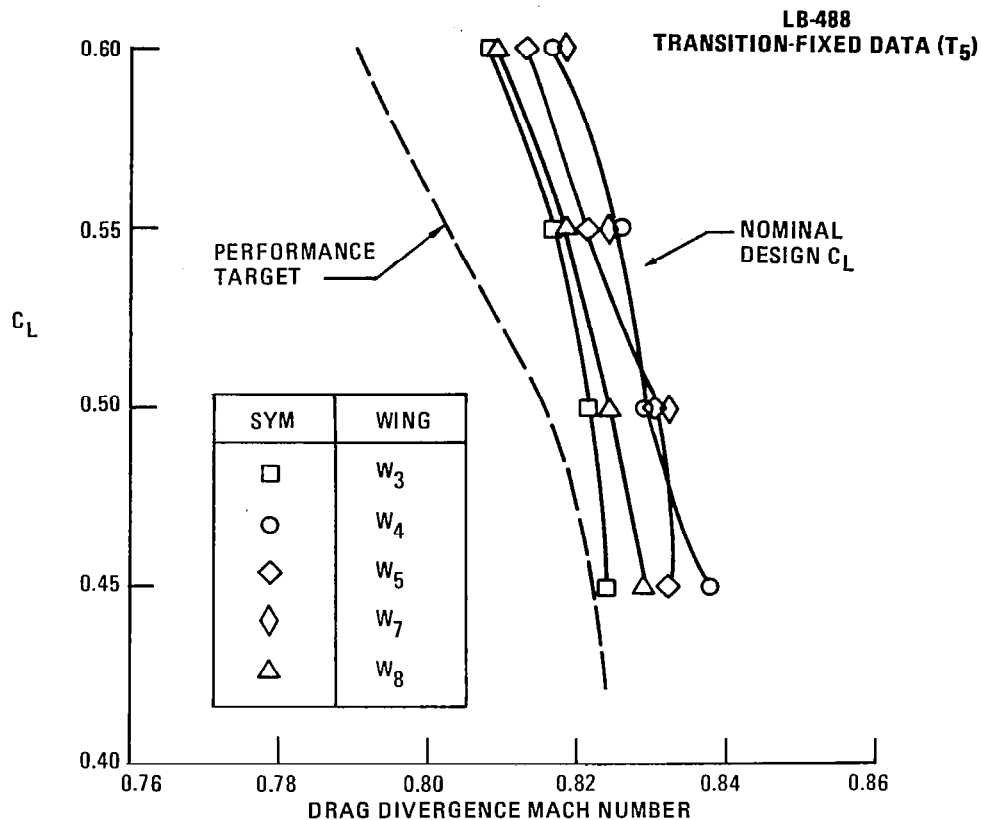
FIGURE 3. COMPARISON OF MEASURED AND PERFORMANCE-TARGET DRAG DIVERGENCE MACH NUMBER CHARACTERISTICS — EET PHASE·I RESULTS[2]

This capability was achieved with the wide-body, DC-X-200 fuselage[2] which was derived from the DC-10 aircraft cross section. It should be noted that the ATMR fuselage design was a new design and had a much smaller diameter; its length-to-diameter ratio was in excess of 10.3, compared to about 7.0 for the DC-X-200. The fuselage fineness ratio has a strong effect on the wing design, and the more slender ATMR configuration represents a significant improvement as shown in Figure 4. The local induced Mach number in the wing region due to the fuselage alone is shown for both the wide-body and the narrow-body configurations. The average difference across the span is approximately 0.01 in Mach number. The excess Mach number capability demonstrated in Phase I, in conjunction with the significant favorable effect of a narrower fuselage, allowed a wing sweep reduction from $28.9°$ to $26.0°$. The sweep reduction was made while maintaining the same wing average thickness-to-chord ratio and is illustrated in Figure 5.
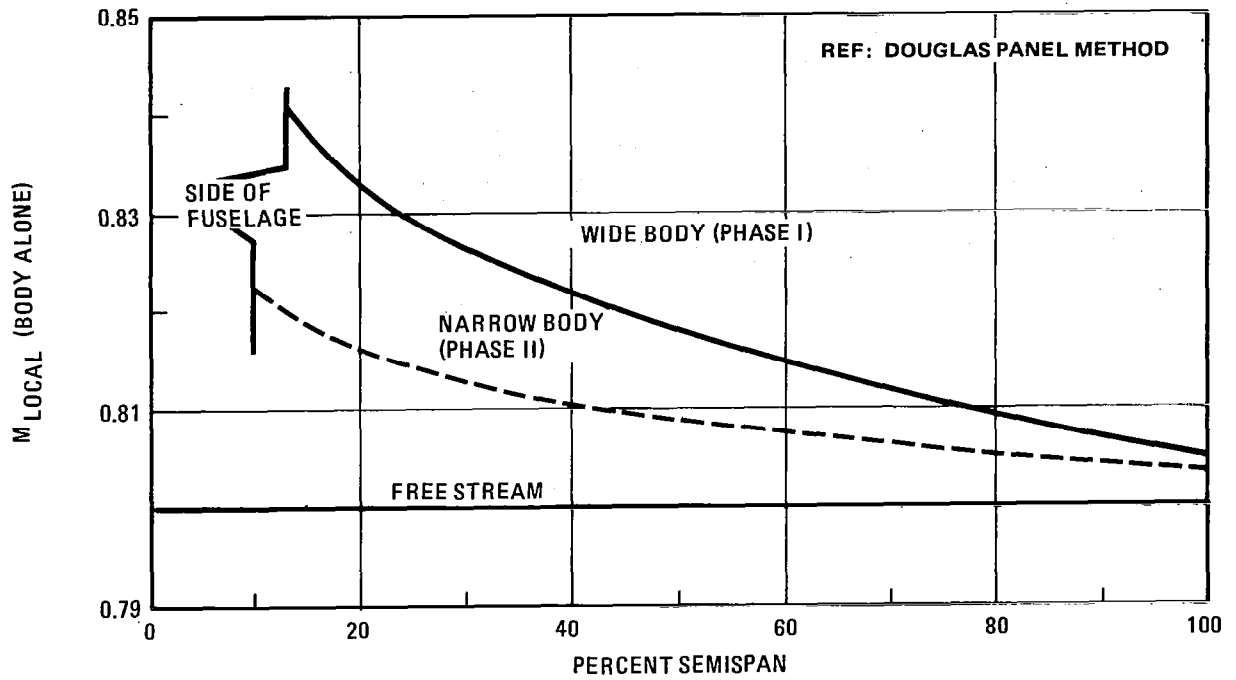
FIGURE 4. EFFECT OF BODY CONFIGURATION ON SPANWISE VARIATION OF MACH NUMBER
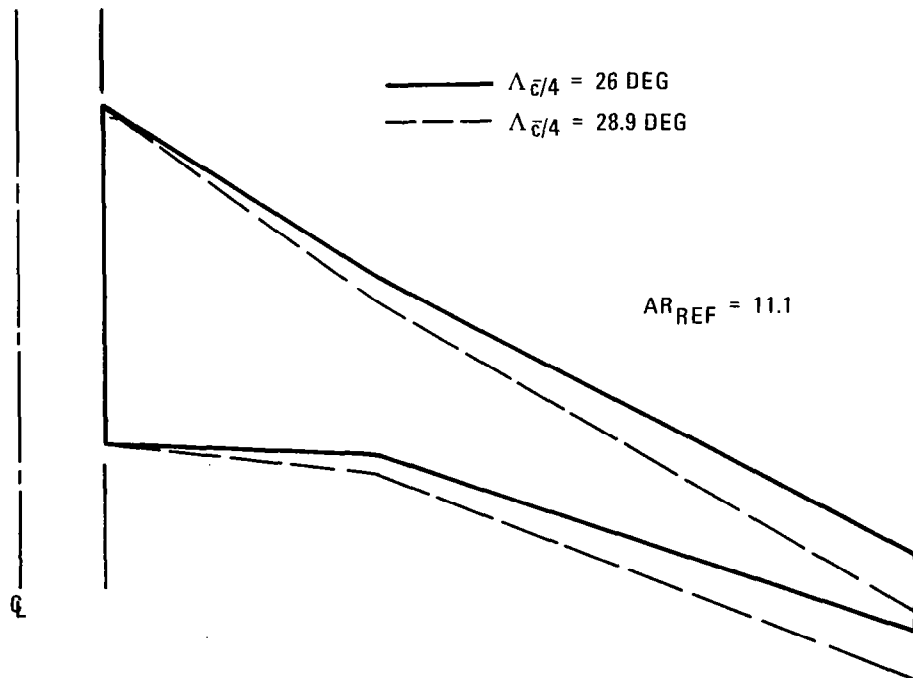
FIGURE 5. ATMR WING PLANFORMS

14

The selection from the systems studies of the general characteristics of aspect ratio, sweep, and thickness provided a basis for detailed wing design and development. In terms of high-speed drag, buffet, and pitching moment characteristics, the W_8 wing from Phase I[2] had the best overall aerodynamic characteristics. The airfoil sections from the W_8 wing were used as a starting point in the new wing development.

In a systematic study using the Douglas direct and inverse 2-D and 3-D methods, the wing planform and airfoil section contours were further developed. Modifications were developed for reduced drag creep prior to drag divergence, increased buffet lift coefficient, and increased low speed $C_{L_{max}}$. Airfoil modifications to the leading edge radius and aft loading were considered while holding the maximum thickness-to-chord ratio constant. Modest changes in the leading-edge glove planform were also evaluated.

The inboard panel airfoil sections were changed considerably in the leading edge region. The Phase I testing included wake profile measurements which indicated that high suction peaks and strong shocks on the inboard panel caused a significant amount of premature drag creep. The Douglas Inverse 3-D Method was utilized to redefine the inboard surface pressure distribution development. This development is illustrated in Figure 6. A substantial reduction in the suction peak was accomplished while observing a constraint on airfoil maximum thickness-to-chord ratio.

Improvements in the outboard panel airfoil sections were also made. The leading-edge radius and aft camber of the W_8 airfoils were increased to improve the high speed buffet C_L capability as well as the low speed $C_{L_{max}}$ of the outer panel.

The final wing configuration, designated LB-506 W_1, had an average exposed maximum thickness-to-chord ratio of 0.123. The spanwise distribution of maximum thickness-to-chord ratio is shown in Figure 7. The spanwise distribution of airfoil maximum-length-line twist is shown in Figure 8. (A maximum-length-line chord is defined as connecting the midpoint of an airfoil trailing edge and the point at the leading edge that is farthest from that midpoint.) This wing configuration had better calculated performance

in the high-speed cruise and buffet regimes as well as the low-speed, high-lift regime. The calculated reduction in drag creep relative to W_8 was 0.0006 at both 0.75 and 0.8 Mach number. The calculated increase in buffet lift coefficient at 0.8 Mach number was 0.04, while the calculated improvement in low-speed $C_{L_{max}}$ was approximately 0.03.
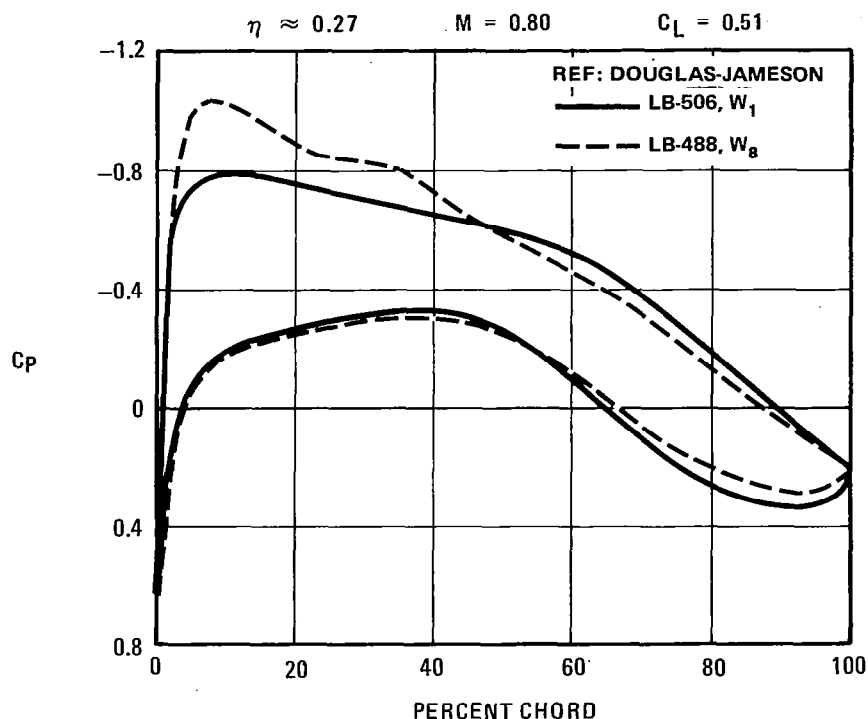
FIGURE 6. COMPARISON OF CALCULATED WING SECTIONAL PRESSURE DISTRIBUTIONS
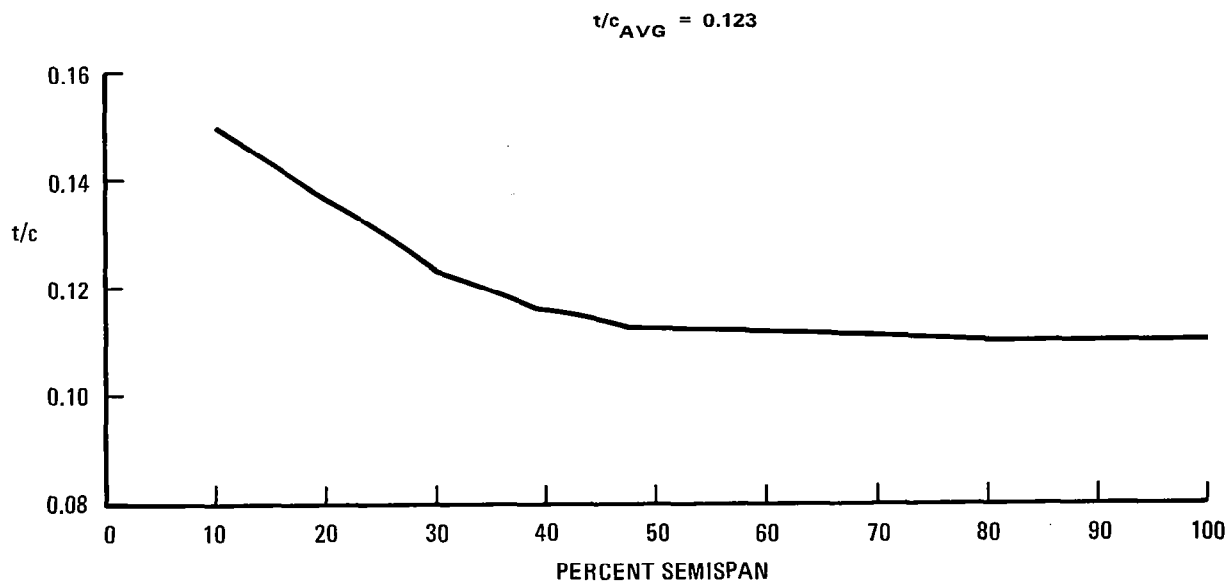
FIGURE 7. WING W_1 SPANWISE THICKNESS DISTRIBUTION

η	i_W(DEG)	AIRFOIL
0.09755	3.02	079
0.200	2.66	080
0.300	1.76	081
0.390	1.36	082
0.475	0.98	083
0.800	−0.93	087
1.000	−3.22	087
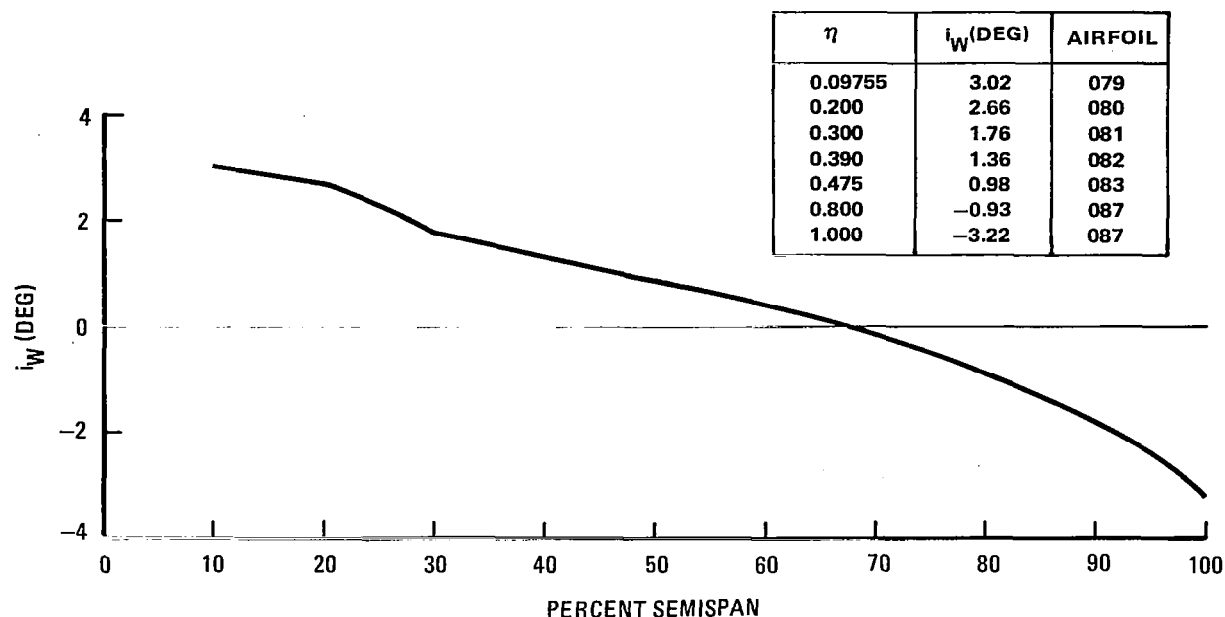
FIGURE 8. WING W_1 SPANWISE GEOMETRIC TWIST DISTRIBUTION FOR DESIGN 1-g LOAD

Calculated isobars on the W_1 wing geometry at 0.8 Mach number are presented in Figures 9 and 10 for C_L's of 0.55 and 0.8 respectively. The 0.55 C_L design point shows highly swept inboard isobars along with the formation of a distinct shock on the outer panel. The 0.8 C_L condition corresponds approximately to the calculated buffet onset point. At this condition the existence of a strong shock along most of the wing is apparent.

M = 0.80
$Re_{\bar{c}}$ = 5.95 MILLION
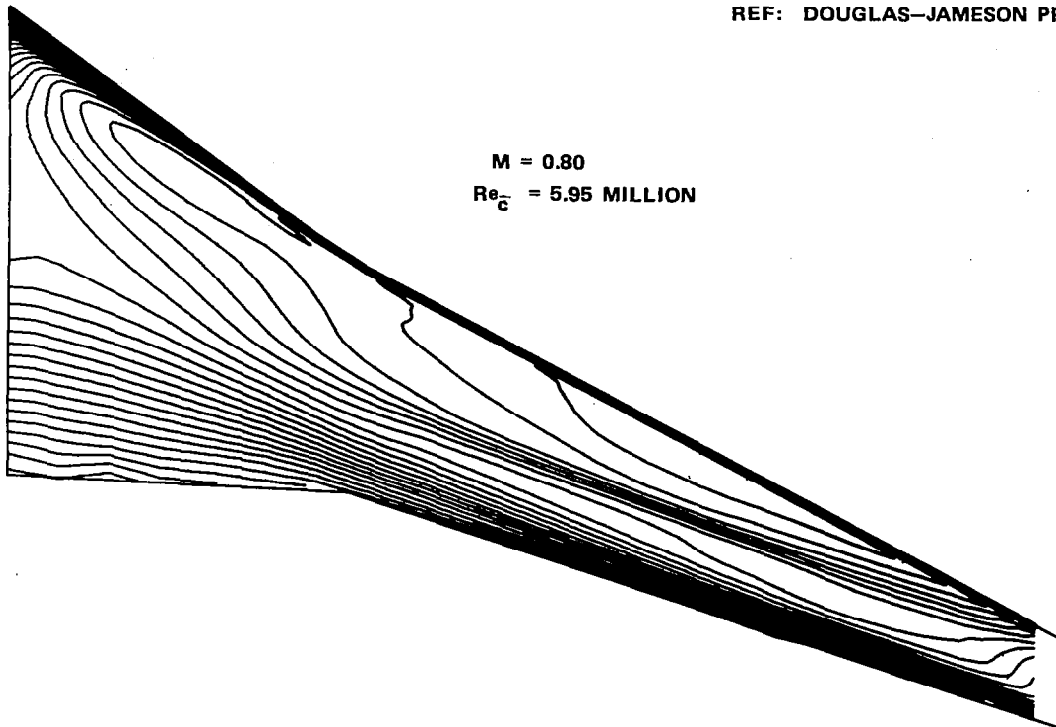
FIGURE 9. WING W_1 CALCULATED UPPER SURFACE ISOBARS, C_L = 0.55

M = 0.80
$Re_{\bar{c}}$ = 5.95 MILLION
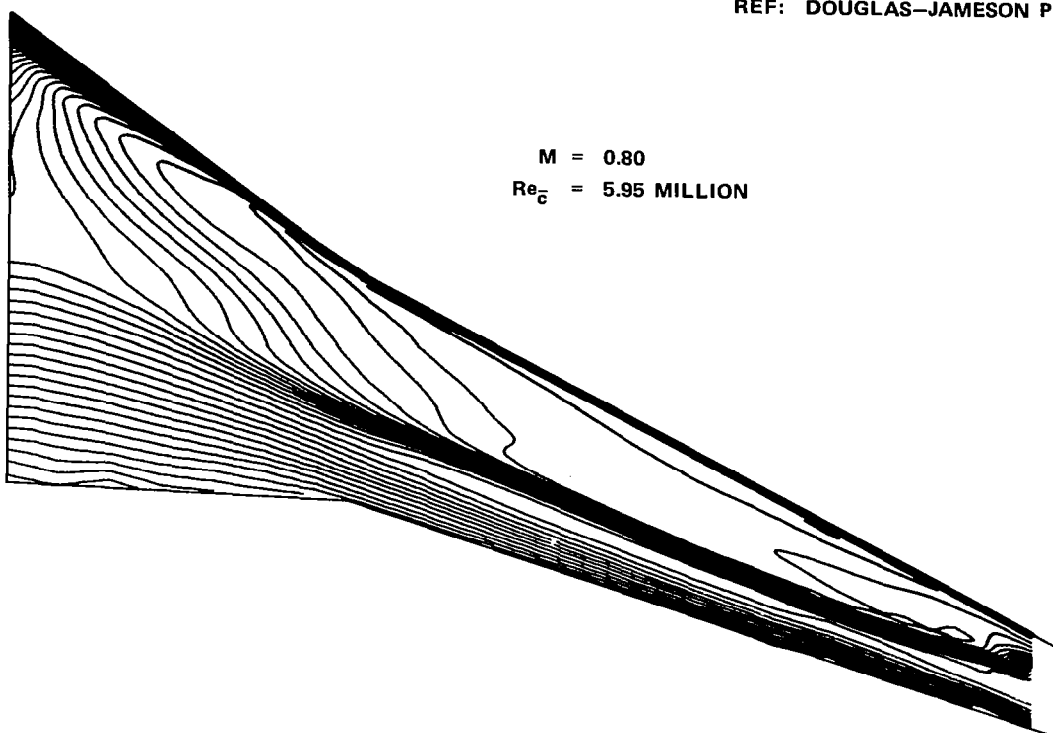
FIGURE 10. WING W_1 CALCULATED UPPER SURFACE ISOBARS, C_L = 0.8

TEST PLAN AND MODEL DESCRIPTION

A high-speed wind tunnel test program, consisting of two tunnel entries, has been completed. The goal of the first test was to obtain high Reynolds number, high-speed data on wing W_1 as part of the wing development process. Force and moment data as well as flow visualization photographs to aid in boundary layer transition analysis were obtained. Wing pressure distributions were also obtained to aid in analysis of the drag data. This test was designated LB-506A and was completed in May, 1980.

After the first test was successfully completed, the second test was initiated to address other areas of the configuration. The large size of the nacelles relative to the wing chord of the high-aspect-ratio super-critical wing made the nacelle/pylon integration an area for concern. A nacelle placement study was included in the second test to determine the influence of the nacelle location on performance and on stability and control. Two horizontal tails of different planform area and aspect ratio were also designed to evaluate their effect on longitudinal stability characteristics. This test was designated LB-506B and was completed in April, 1981.

The tests were conducted in the NASA Ames Research Center 11-foot transonic wind tunnel. By virtue of its size and pressurization, this tunnel is capable of Reynolds numbers from 3.5 million per foot to 8.0 million per foot at Mach numbers from 0.3 to 0.9.

The model tested was a sting-mounted, 5.59-percent scale model of the ATMR aircraft. The components constructed for the tests included the fuselage, wing, wing-body fillet, vertical stabilizer, two alternate horizontal tails, a nacelle with five alternate pylons, and a set of flap linkage fairings for the wing. The model is shown in three-view in Figure 11, and installed on its sting mount in the tunnel in Figure 12. Figure 11 shows the inboard nacelle location.

MODEL SCALE = 0.0559
PYLON P_{5A} SHOWN

NOTES:
ALL DIMENSIONS ARE IN
CENTIMETERS (INCHES)
MODEL SCALE, UNLESS
OTHERWISE SPECIFIED

TRAPEZOIDAL AREAS:

S_W = 0.4645m^2 (5.000 FT^2)

S_H = 0.1144m^2 (1.231 FT^2)

S_V = 0.0865m^2 (0.931 FT^2)

2^0

44.277 (17.432)

Y_{MAC} = 46.007 (18.113)

$\stackrel{\text{C}}{\text{L}}$ 68.481 (26.961)

L_h = 124.412 (48.981)

$X_{\overline{C}/4}$ = 136.875 (53.888)

L_v = 100.952 (39.745)

227.06 (89.395)

24.079 (9.480) DIA

FRP

37.203 (14.647)

13.485 (5.309)

248.69 (97.911)

X = 0

X 13.553 (5.336)
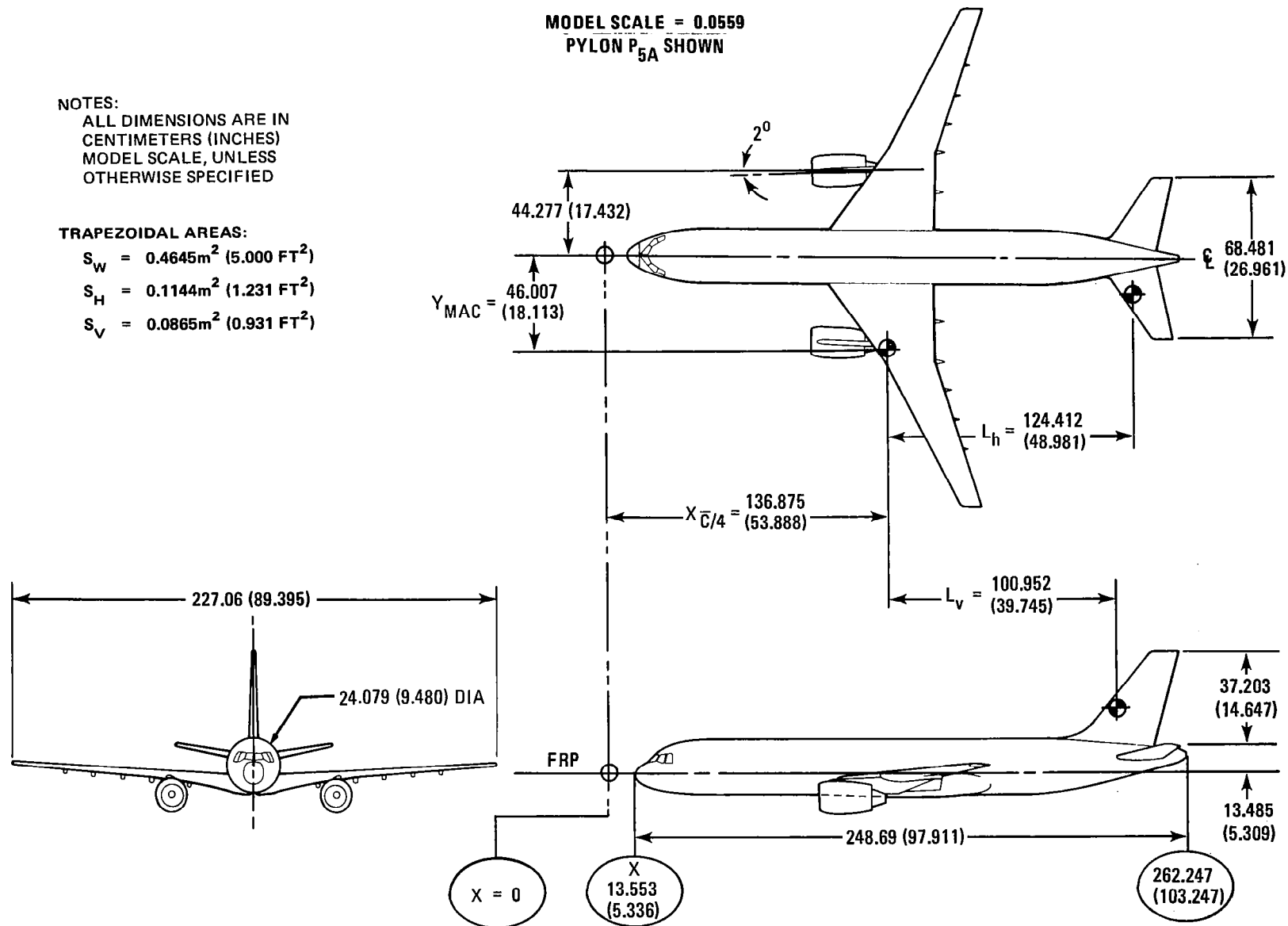
262.247 (103.247)

FIGURE 11. MODEL THREE-VIEW

FIGURE 12. MODEL INSTALLED ON STING IN ÁMES 11-FOOT TRANSONIC WIND TUNNEL

The model's large size and its long support sting would have led to such large loads on the support system that the drive could have been over- loaded. To prevent this, a device referred to as a load compensator was installed during high-angle-of-attack testing. This consisted of a cable attached to the sting, exerting a constant downward force to relieve part of the load on the support system drive.

Boundary layer transition location was controlled during most of the tests by glass beads applied to the various surfaces. The application pat- terns of these transition strips, or trips, are designated as T_x. The model hardware notation and transition patterns are all identified in Table 1. Dimensions given in this table are full scale, based on a model scale of 5.59 percent.

The B_{3A} fuselage represented the narrow-body ATMR fuselage. The removable nose housed a dynamics damper, scanivalve assemblies (for collec- ting surface pressure measurements), and electrolytic alignment bubbles. The centerbody housed the ARC Task MKII 4-inch internal strain gage balance, and the body shell incorporated spirit levels for referencing the model on the pitch and roll axes. The aft fuselage had provisions for mounting ver- tical and horizontal tail surfaces. The horizontal tails were mounted on a rotatable trunnion which extended through the aft fuselage, for varying tail incidence. The aft lower fuselage was modified by a hole to permit entry of the support sting. The sting cavity was instrumented with 20 static pressure orifices (or taps), which were used to correct the balance data for the effect of the opening.

Wing W_{1A} was the model designation for wing W_1 in the clean, cruise wing line diagram is shown in Figure 13. The wing was constructed with

TABLE 1

CONFIGURATION NOTATION

B_{3A} Model ATMR/EET fuselage. Full scale dimensions: Length = 68.96 m (1751 in.); constant section diameter = 6.68 m (169.6 in.). The aft lower fuselage is modified to permit entry of the support sting.

$^bF_{1B}$ Set of 8 flap mechanism fairings for wing W_{1A}, which are minimum enclosures for the linkage motion system. This set is used with pylons P_{1C}, P_{2A}, P_{3A} and P_{4A}, which incorporate an integral flap linkage fairing into their aft ends, forming the second fairing of five on each side.

$^bF_{2A}$ Set of 10 flap linkage fairings for wing W_{1A}. This set is used with pylon P_{5A}, which does not incorporate an integral fairing, and includes a pair of fairings which substitute for those integral fairings.

H_{1C} Variable incidence horizontal tail, aspect ratio = 4.10. Full scale dimensions: S_H = 36.046 m^2 (388.0 sq ft); b_H = 12.064 m (474.98 in.). Slab-type.

H_{2A} Variable incidence horizontal tail, aspect ratio = 6.0. Full scale dimensions: S_H = 39.762 m^2 (428.0 sq ft); b_H = 15.446 m (608.11 in.).

N_{1C} Set of two flow-through nacelles for the Pratt and Whitney JT10D engine. Maximum diameter = 2.464 m (97.00 in.), full scale.

P_{1C} Pylons for mounting N_{1C} on the wing. Nacelle fan exit location: X = 22.264 m (876.55 in.), Z = -2.7018 m (-106.37 in.), Y = 28.971 m (311.844 in.), full scale. Includes #2 flap linkage fairing.

TABLE 1

CONFIGURATION NOTATION (CONTINUED)

P_{1C_F}	Pylon P_{1C} with wood fairing installed for testing without nacelles.
P_{2A}	Pylons for mounting N_{1C} on the wing. Nacelle fan exit location: X = 22.882 m (900.86 in.), Z = -2.7018 m (-106.37 in.), Y = 28.971 m (311.844 in.), full scale. Includes #2 flap linkage fairing.
P_{3A}	Pylons for mounting N_{1C} on the wing. Nacelle fan exit location: X = 23.2939 m (917.084 in.), Z = -2.7018 m (-106.37 in.), Y = 28.971 m (311.844 in.), full scale. Includes #2 flap linkage fairing.
P_{4A}	Pylons for mounting N_{1C} on the wing. Nacelle fan exit location: X = 22.8621 m (900.084 in.), Z = 2.4980 m (-98.345 in.), Y = 28.971 m (311.844 in.), full scale. Includes #2 flap linkage fairing.
P_{5A}	Pylons for mounting N_{1C} at the inboard location on the wing (33.19% semispan). Nacelle fan exit location: X = 21.8081 m (858.587 in.), Z = -2.5740 m (-101.342 in.), Y = 24.655 m (265.387 in.), full scale.
1C	Vertical tail. Full scale dimensions: S_V = 27.69 m^2 (298 sq ft), b_V = 6.6556 m (262.03 in.). AR = 1.6.

TABLE 1

CONFIGURATION NOTATION (CONTINUED)

W_{1A} Model ATMR/EET wing. Full scale trapezoidal dimensions: $S = 148.64 \, m^2$ (1600 sq ft), $b = 40.6198 \, m$ (133.267 ft), $AR = 11.10$, $= 0.275$, $MAC = 4.0538 \, m$ (159.600 in.), $= 5.00^0$, $c/4 = 26.00^0$. The model is rigged with dihedral and twist modified to account for aeroelastic deflections, such that it represents the airplane wing under a 1-g loading at the test conditions of $M = 0.8$, $Re = 8$ million per foot, and $C_L = 0.55$. The wing is instrumented with 7 complete rows and one partial row of pressure taps.

X_{1A} Wing-fuselage fillet for B_{3A} and W_{1A}.

T_x Boundary-layer transition strip, consisting of glass beads, applied to various surfaces. Subscript denotes specific pattern applied to the wing. Patterns on fuselage, nacelles and pylons, and flap linkage fairings are the same for all runs during which they were installed, and are as follows:

Fuselage (B_{3A})	3.2 mm (1/8 in.) wide band of 0.058 mm (0.0023 in.) diameter beads, 32 mm (1.25 in.) aft of nose.
Flap linkage fairings (b_{F1A})	3.2 mm (1/8 in.) wide band of 0.058 mm (0.0023 mm) diameter beads around each fairing, 8 mm (0.3 in.) aft of leading edge.
Pylons (P_{1C}, P_{2A}, P_{3A}, P_{4A}, P_{5A})	3.2 mm (1.8 in.) wide band of 0.058 mm (0.0023 in.) diameter beads, 2.5 mm (0.1 in.) aft of leading edge.

25

TABLE 1

CONFIGURATION NOTATION (CONTINUED)

Nacelles (N_{1C})	fan cowl: 3.2 mm (1/8 in.) wide band of 0.058 mm (0.0023 in.) diameter beads, 5 mm (0.2 in.) aft of leading edge on inside and outside surfaces.
	core cowl: 3.2 mm (1/8 in.) wide band of 0.058 mm (0.0023 in.) diameter beads, 8 mm (0.3 in.) aft of leading edge on inside and outside surfaces.
	internal support pylon: 3.2 mm (1/8 in.) wide band of 0.058 mm (0.0023 in.) diameter beads, 8 mm (0.3 in.) aft of leading edge on both surfaces.
T_1	Free transition on wing (no transition strip).
T_2	3.2 mm (1/8 in.) wide band of 0.081 mm (0.00320 in.) diameter beads on wing upper surface, from 13 mm (0.5 in.) aft of L.E. at side of body to 96 mm (3.8 in.) at planform break, to 41 mm (1.6 in.) at 80% semispan to 13 mm (0.5 in.) at tip. Lower surface transition-free.
T_4	3.2 mm (1.8 in.) wide band of 0.069 mm (0.0027 in.) diameter beads on wing upper surface, at a constant 8 mm (0.3 in.) aft of L.E. from side of body to tip. Lower surface transition-free.

TABLE 1

CONFIGURATION NOTATION (CONTINUED)

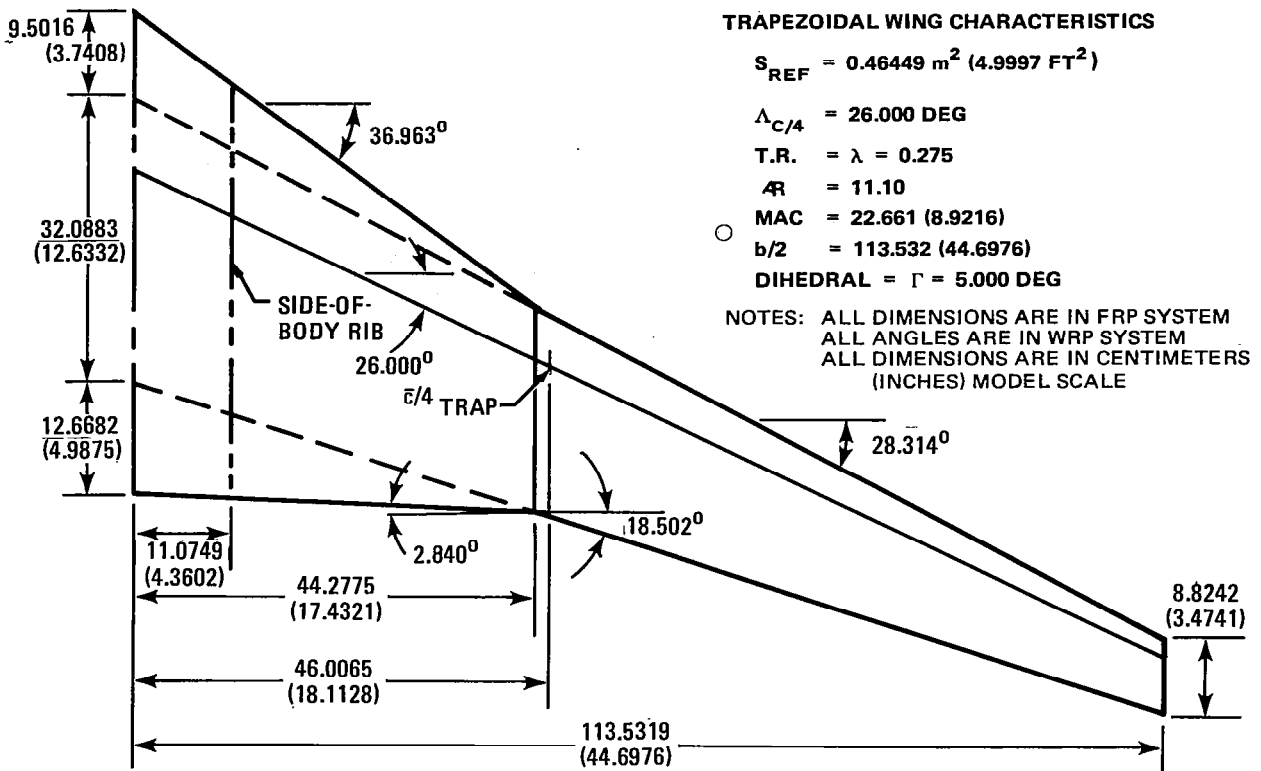|	
T_5	3.2 mm (1/8 in.) wide band of 0.081 mm (0.0032 in.) diameter beads on wing upper surface, 13 mm (0.50 in.) aft of L.E. at side of body, to 75 mm (2.95 in.) at planform break (39% semispan), to 27 mm (1.06 in.) at 80% semispan, to 9 mm (0.35 in.) at tip. Lower surface transition-free.
T_6	3.2 mm (1/8 in.) wide band of 0.081 mm (0.0032 in.) diameter beads on wing upper surface, 13 mm (0.50 in.) aft of L.E. at side of body, to 23 mm (0.91 in.) at planform break, to 27 mm (1.06 in.) at 80% semispan, to 9 mm (0.35 in.) at tip. Lower surface transition-free.
T_7	Wing upper surface transition pattern same as T_6. On wing lower surface, 3.2 mm (1/8 in.) wide band of 0.081 mm (0.0032 in.) diameter beads, from 13 mm (0.50 in.) aft of L.E. at side of body, to 74 mm (2.90 in.) at planform break to 34 mm (1.33 in.) at 80% semispan, to 9 mm (0.35 in.) at tip.

TRAPEZOIDAL WING CHARACTERISTICS
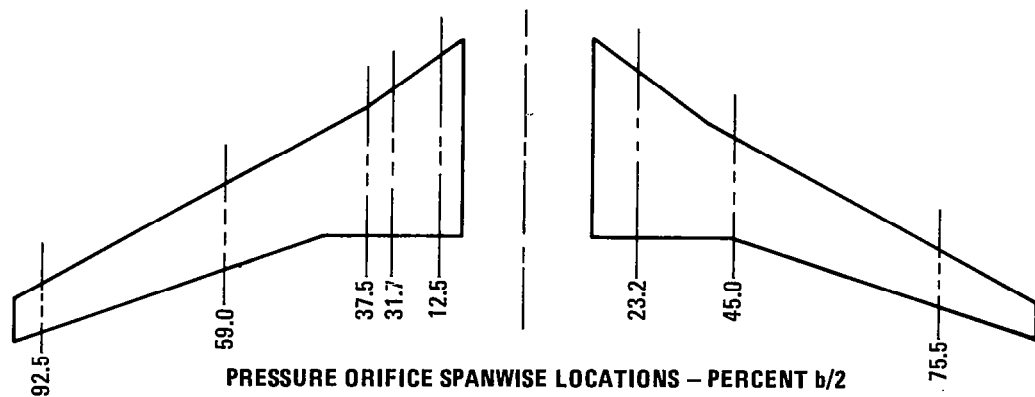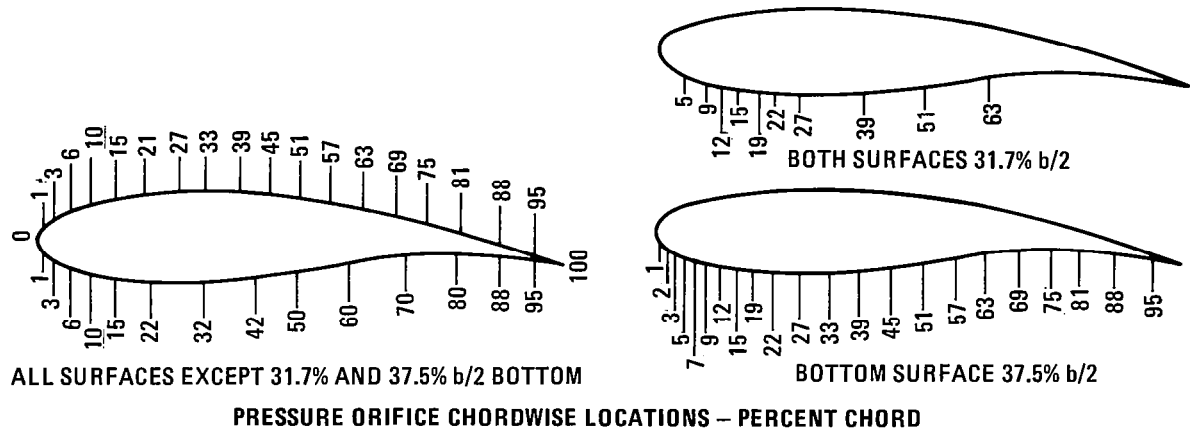
S_{REF} = 0.46449 m^2 (4.9997 FT^2)

$\Lambda_{c/4}$ = 26.000 DEG

T.R. = λ = 0.275

AR = 11.10

MAC = 22.661 (8.9216)

b/2 = 113.532 (44.6976)

DIHEDRAL = Γ = 5.000 DEG

NOTES: ALL DIMENSIONS ARE IN FRP SYSTEM
ALL ANGLES ARE IN WRP SYSTEM
ALL DIMENSIONS ARE IN CENTIMETERS
(INCHES) MODEL SCALE

9.5016
(3.7408)

36.963°

32.0883
(12.6332)

SIDE-OF-
BODY RIB

26.000°

c̄/4 TRAP

28.314°

12.6682
(4.9875)

2.840°

18.502°

11.0749
(4.3602)

44.2775
(17.4321)

8.8242
(3.4741)

46.0065
(18.1128)

113.5319
(44.6976)

FIGURE 13. WING W_{1A} LINE DIAGRAM

BOTH SURFACES 31.7% b/2

ALL SURFACES EXCEPT 31.7% AND 37.5% b/2 BOTTOM

BOTTOM SURFACE 37.5% b/2

PRESSURE ORIFICE CHORDWISE LOCATIONS – PERCENT CHORD

PRESSURE ORIFICE SPANWISE LOCATIONS – PERCENT b/2

FIGURE 14. WING PRESSURE ORIFICE LOCATIONS

28

A pair of flow-through nacelles, designated N_{1C}, represented the Pratt and Whitney JT10D engine configuration and consisted of a fan cowl and a core cowl. Five pylons were constructed to support the nacelles in five different locations relative to the wing. The baseline pylon, P_{1C}, was tested in LB-506A. All five were tested in LB-506B to examine the nacelle placement effects. The five nacelle/pylon assemblies are illustrated in Figures 15 and 16. Pylons P_{2A} and P_{3A} moved the nacelle aft from the baseline position with no vertical movement. Pylon P_{4A} moved the nacelle upward, at the same longitudinal location as P_{2A}.

Pylons P_{1C}, P_{2A}, P_{3A} and P_{4A} all featured an integral flap linkage fairing. Pylon P_{5A} was located inboard at 33.19% semispan instead of 39%, which no longer corresponded to a flap support station; so it did not incorporate a flap linkage fairing. All five pylons canted the nacelle inboard 2^O and pitched it up 2^O relative to the FRP. None of the pylons was cambered.
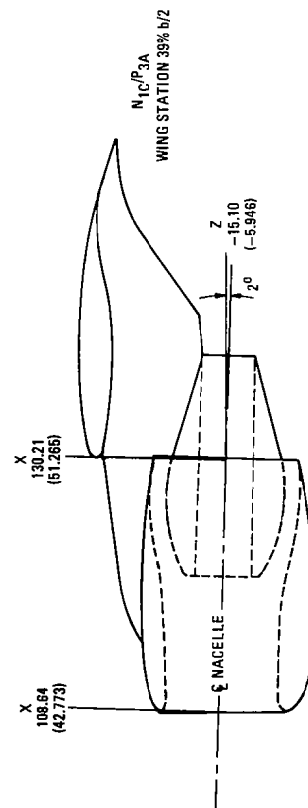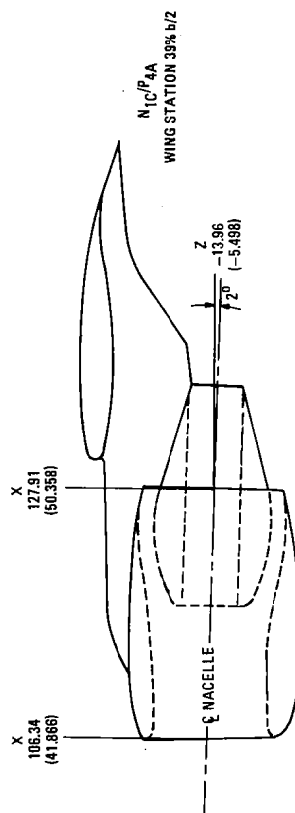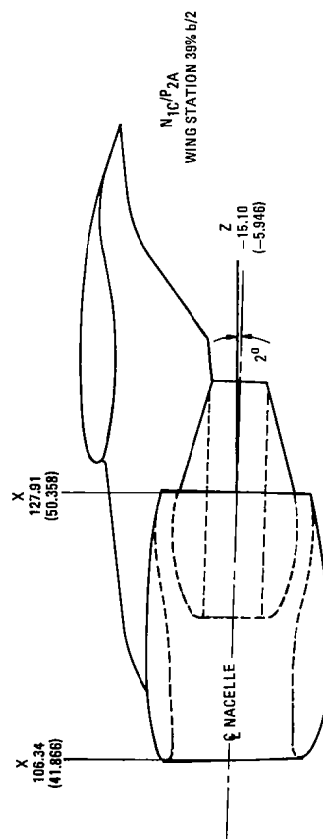
A set of eight flap linkage fairings, b_{F1B}, was tested with pylons P_{1C} to P_{4A}. For pylon P_{5A}, without the integral flap linkage fairing, a fifth fairing was added to each wing at the 39% semispan station, and the set of ten fairings was then designated B_{F2A}.

Two horizontal tails and one vertical tail were tested. Line drawings for the horizontal tails are presented in Figures 17 and 18, and the vertical is shown in Figure 19. Horizontal tail H_{1C} was the baseline tail, tested in LB-506A. It had an aspect ratio of 4.10 and a planform area of 0.1144 m^2 (1.2312 square feet). For LB-506B, horizontal H_{2A} was larger and had a much higher aspect ratio, 0.1196 m^2 (1.2869 square feet) and 6.0, respectively. Filler blocks were made which could replace the empennage, providing a smooth surface on the aft fuselage for tail-off testing.

The model dimensional data are summarized in Table 2.
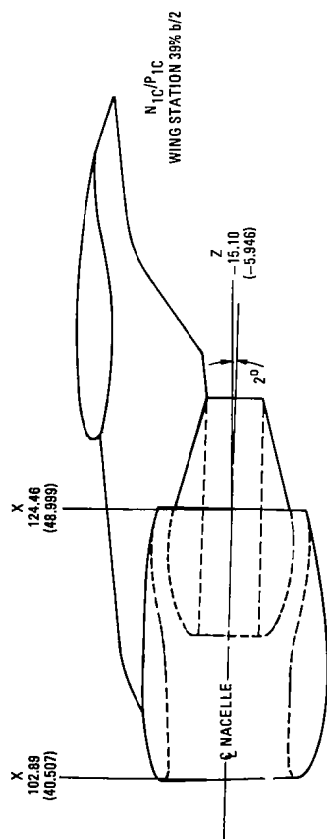
WING LEADING EDGE COORDINATES
AT 39% b/2: X = 130.21 (51.265)
Z = −4.311(−1.697)

N_{1C}/P_{1C}
WING STATION 39% b/2

N_{1C}/P_{2A}
WING STATION 39% b/2

N_{1C}/P_{3A}
WING STATION 39% b/2

N_{1C}/P_{4A}
WING STATION 39% b/2

X
124.46
(48.999)

X
102.89
(40.507)

Z
−15.10
(−5.946)

2°

NACELLE

X
127.91
(50.358)

X
106.34
(41.866)

Z
−15.10
(−5.946)

2°

NACELLE

X
130.21
(51.265)

X
108.64
(42.773)

Z
−15.10
(−5.946)

2°

NACELLE

X
127.91
(50.358)

X
106.34
(41.866)

Z
−13.96
(−5.498)

2°

NACELLE

NOTE: ALL DIMENSIONS ARE IN FRP SYSTEM
ALL DIMENSIONS ARE IN CENTIMETERS
(INCHES) MODEL SCALE

FIGURE 15.   NACELLE/PYLON ASSEMBLIES, PYLONS P_{1C}, P_{2A}, P_{3A}, AND P_{4A}

30

X
100.34
(39.503)

X
121.91
(47.995)

N_{1C}/P_{5A}
WING STATION 33.19% b/2

WING LEADING EDGE
COORDINATES:
X = 125.349 (49.350)
Z = −4.981 (−1.961)

¢ NACELLE

Z
−14.39
(−5.665)

2°

NOTE: ALL DIMENSIONS ARE IN FRP SYSTEM
        ALL DIMENSIONS ARE IN CENTIMETERS
        (INCHES) MODEL SCALE
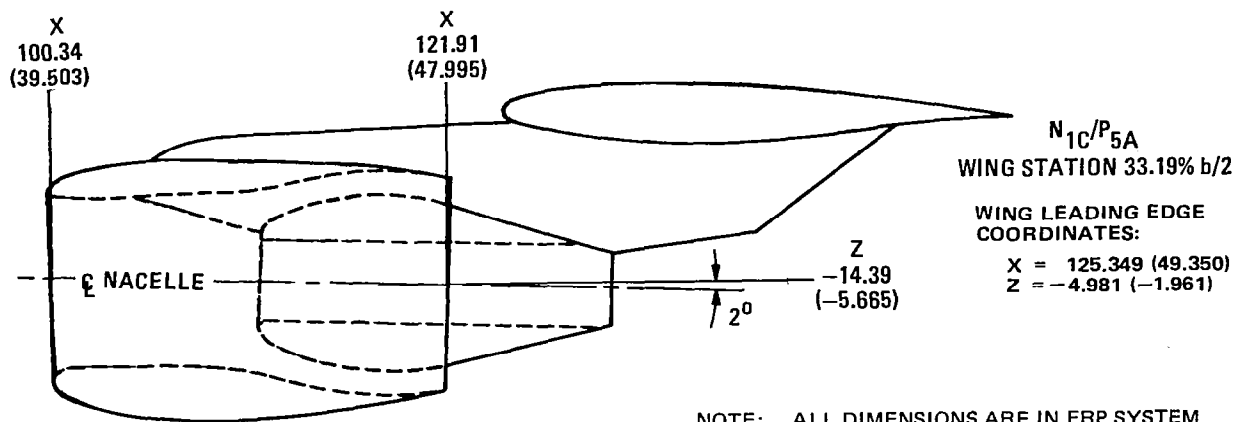
FIGURE 16.   NACELLE/PYLON ASSEMBLY N_{1C}/P_{5A}

S_H = 0.1126 m² (1.2125 FT²)

AR = 4.10

λ = .350

SWEEP $C_{H/4}$ = 30°

Γ_H = 10.0°

Y_H
0.0

HORIZONTAL
STABILIZER
ORIGIN
X = 229.022 (90.166)

Y_H
14.372
(5.6584)

+Y_H

30°

MAC_{H4}
X_H = 14.484 (5.7024)

24.745
(9.7420)

PIVOT AXIS 65.42% $\bar{c}_{ROOT}$
X = 245.21 (96.539)
Z = 6.759 (2.661)

Y_H
34.2402
(13.4804)

SIDE OF
FUSELAGE

8.661
(3.4097)

MAC_H = 17.993 (7.0839)

+X_H
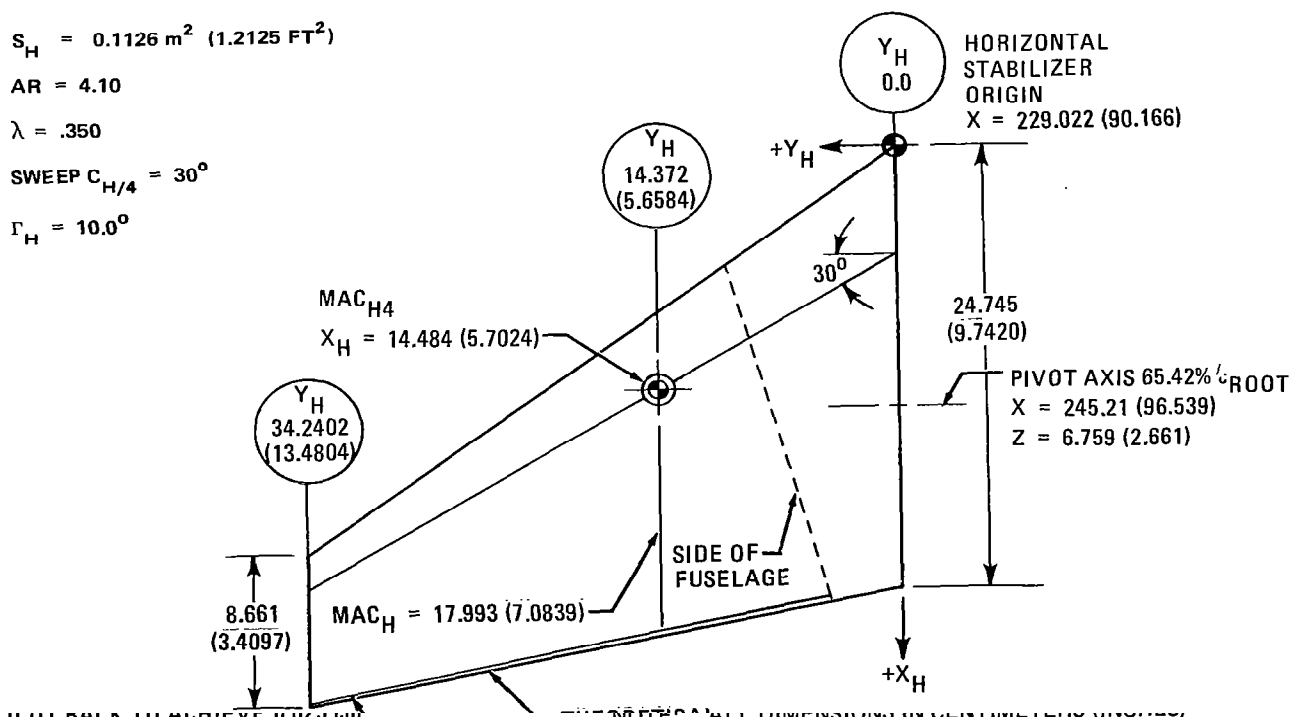
S_H = 0.1242 m^2 (1.3374 FT^2)
AR = 6.0
λ = 0.35
SWEEP C$_{H/4}$ = 30 DEG
Γ_H = 10.00 DEG

HORIZONTAL STABILIZER ORIGIN
X = 231.26 (91.048)

Y_H 0.0

Y_H 18.400 (7.244)

30°

21.318 (8.393)

PIVOT AXIS
65.42% c$_{ROOT}$
X = 245.21 (96.539)
Z = 6.759 (2.661)

MAC$_{H/4}$
X_H = 15.954 (6.281)

SIDE OF FUSELAGE

+X_H

Y_H (17.259)

NOTE: ALL DIMENSIONS IN CENTIMETERS (INCHES)
MODEL SCALE UNLESS OTHERWISE SPECIFIED

MAC$_H$ = 15.375 (6.053)

THEORETICAL TRAILING EDGE

7.462 (2.938)

MODEL ACTUAL TRAILING EDGE
[CUT BACK TO ACHIEVE 0.025 cm
(0.010 INCH) THICK TRAILING EDGE]

FIGURE 18. HORIZONTAL STABILIZER H$_{2A}$ DIAGRAM

S_V = 0.0865m^2 (0.9312 FT^2)
AR = 1.600
λ = 0.35
SWEEP C$_{V/4}$ = 35°

NOTE: ALL DIMENSIONS IN CENTIMETERS (INCHES)
MODEL SCALE UNLESS OTHERWISE STATED

12.057 (4.7469)

X_F 217.998 (85.8258)

MAC$_{V/4}$
X_V = 19.829 (7.8067)
Z_V + 15.617 (6.1483)
MAC$_V$ = 25.050 (9.8620)

37.204 (14.6474)

+Z_V

ACTUAL MODEL TRAILING EDGE
[CUT BACK TO BE 0.025cm
(0.010 IN.) THICK]

THEORETICAL TRAILING EDGE

35°

+X_V

VERT. STAB. ORIGIN

34.4485 (13.5624)

FUSELAGE INTERSECTION
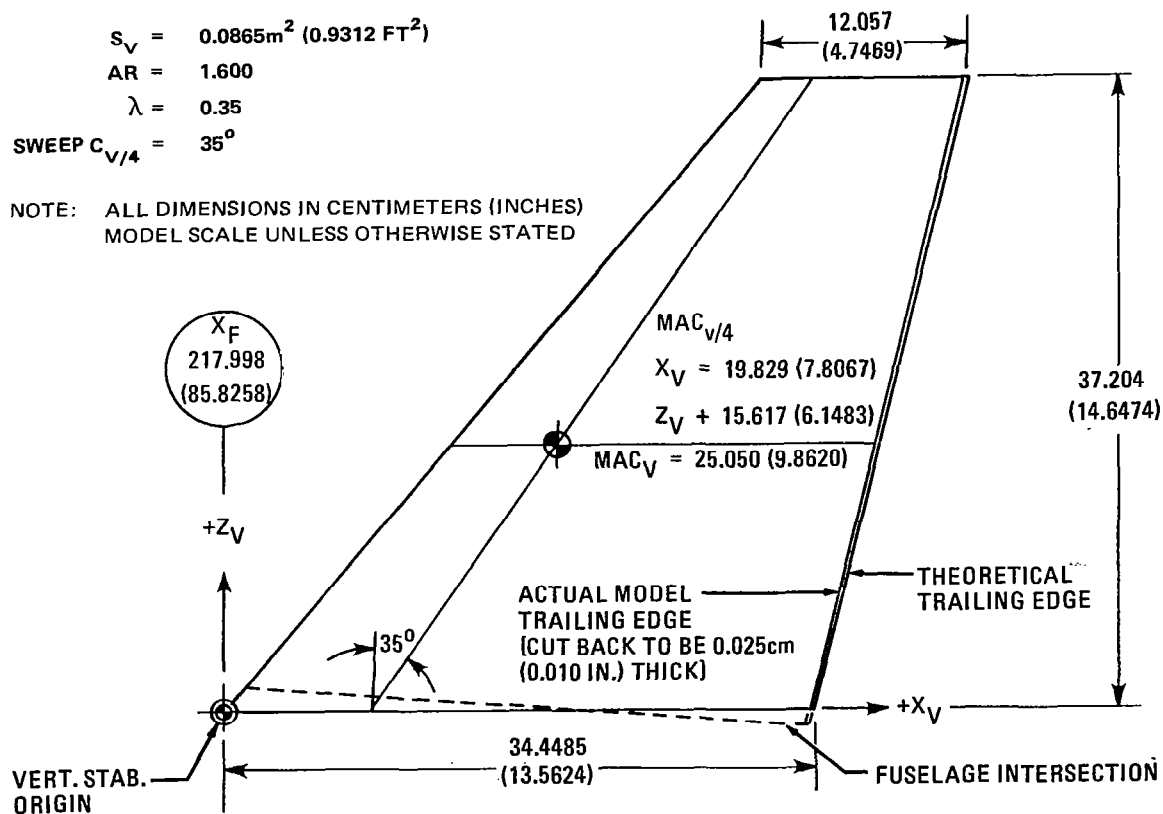
FIGURE 19. VERTICAL STABILIZER V$_{1C}$ DIAGRAM

32

TABLE 2

DIMENSIONAL DATA

Component	Unit	Model Scale Dimension
Fuselage (B_{3A})		
Length	cm (in.)	248.694 (97.911)
Diameter-constant section	cm (in.)	24.079 (9.480)
Wing - all dimensions projected onto FRP		
Area (trapezoidal)	m^2 (sq ft)	0.46449 (4.9997)
Span	cm (in.)	227.064 (89.3953)
Trapezoidal root chord	cm (in.)	32.0883 (12.6332)
Total root chord	cm (in.)	54.2582 (21.3615)
Tip chord	cm (in.)	8.8242 (3.4741)
Mean aerodynamic chord (MAC)	cm (in.)	22.661 (8.9216)
Spanwise location of MAC	cm (in.)	46.0065 (18.1128)
Fuselage station of 25% MAC	cm (in.)	136.875 (53.8876)
Aspect ratio		11.10
Taper ratio		0.275
Sweepback of quarter-chord line	deg.	26.00
Dihedral angle	deg.	5.00
Vertical stabilizer (V_{1C})		
Gross area	m^2 (sq ft)	0.0865 (0.9312)
Span	cm (in.)	37.204 (14.647)
Theoretical root chord	cm (in.)	34.448 (13.562)
Theoretical tip chord	cm (in.)	12.057 (4.747)
Mean aerodynamic chord	cm (in.)	25.049 (9.862)
Tail length	cm (in.)	100.952 (39.745)
Fuselage station of 25% MAC_V	cm (in.)	237.825 (93.632)
Aspect ratio		1.6
Taper ratio		0.35
Sweepback of quarter-chord line	deg.	35.00

TABLE 2

DIMENSIONAL DATA (CONTINUED)

Component	Unit	Model Scale Dimension	
		H_{1C}	H_{2A}
Horizontal Stabilizer			
Planform area	m²(sq ft)	0.11264(1.2125)	0.12425(1.3374)
Span	cm (in.)	68.481(26.961)	84.696(33.345)
Root chord (theoretical)	cm (in.)	24.745(9.742)	21.318(8.393)
Tip chord (theoretical)	cm (in.)	8.661(3.410)	7.462(2.938)
Mean aerodynamic chord (MAC)	cm (in.)	17.993(7.084)	15.375(6.053)
Tail length	cm (in.)	106.632(41.981)	110.343(43.442)
Fuselage station of 25% MAC_H	cm (in.)	243.505(95.868)	247.216(97.329)
Aspect ratio		4.10	6.0
Taper ratio		0.35	0.35
Sweepback of quarter-chord line	deg.	30.00	30.00
Dihedral angle (HRP)	deg.	10.00	10.00
Fuselage station of axis of rotation for incidence	cm (in.)	245.209(96.539)	
Distance above FRP	cm (in.)	6.759(2.661)	

TABLE 2

DIMENSIONAL DATA (CONTINUED)

Component	Unit	Model Scale Dimension				
Nacelles and Pylons		P_{1C}/N_{1C}	P_{2A}/N_{1C}	P_{3A}/N_{1C}	P_{4A}/N_{1C}	P_{5A}/N_{1C}
Spanwise location	% b/2	39.00	39.00	39.00	39.00	33.19
Distance below wing L.E. of fan exit centerline, in fuselage system (percent local wing chord)	%c	46.0	46.0	46.0	41.0	34.0
Distance ahead of wing L.E. of fan exit centerline, in fuselage system (percent local wing chord)	%c	25.0	10.0	0.0	10.0	12.45
Toe-in angle	deg.	2.00	2.00	2.00	2.00	2.00
Cant angle (nose-up)	deg.	2.00	2.00	2.00	2.00	2.00
Flap Linkage Fairings ($b_{F_{2A}}$)		No. 1	No. 2	No. 3	No. 4	No. 5
Spanwise location of intersection of centerline with wing T.E.	% b/2	24.57	39.00	49.71	64.66	78.49
Cant Angle (nose-inboard)	deg.	0.00	0.00	3.10	7.43	11.43
Nacelle maximum diameter	cm(in.)	13.772(5.422)				

DATA ANALYSIS

The wind tunnel test data were analyzed to determine the basic aerodynamic performance characteristics, to establish the effects of design variables on aerodynamic characteristics, and to assess the validity of the design methods in predicting the characteristics. In the sections that follow, each of the significant aerodynamic characteristics is discussed in terms of the design variables studied and the test results.

Basic Data

Basic force data for the configurations tested are presented graphically in the Appendix. Drag polars, lift curves, and pitching moment curves are shown for each configuration. Both transition-fixed and transition-free data are shown where appropriate. Transition-free data are generally used to evaluate buffet boundary and stability characteristics, since Douglas experience has shown that for characteristics at lift coefficients above cruise, transition-free data correlate better with flight test results. Transition-fixed data are used for drag-rise characteristics. Table 3 summarizes the configurations tested and the Appendix figure numbers of the plotted corresponding force and moment data.

Wing/Body Drag Characteristics

In Figure 20 the drag rise characteristics for the basic wing/body are presented for a range of lift coefficients. These curves are taken directly from the test data and contain no corrections for Reynolds number or for tunnel blockage or lift interference. The data were obtained at the maximum Reynolds number available, which was constant above 0.7M but decreased at lower Mach numbers.

TABLE 3

SUMMARY OF PLOTTED FORCE AND MOMENT DATA

Configuration	Wing Transition	Load Compensator	Remarks	Figures
$B_{3A}W_{1A}X_{1A} + T_1$	Free	Off		A-1 to A-3
$B_{3A}W_{1A}X_{1A} + T_1$	Free	On		A-4
$B_{3A}W_{1A}X_{1A} + T_2$	Fixed	On		A-5 to A-8
$B_{3A}W_{1A}X_{1A} + T_2$	Fixed	Off		A-9 to A-11
$B_{3A}W_{1A}X_{1A}P_{1CF} + T_2$	Fixed	On		A-12
$B_{3A}W_{1A}X_{1A}P_{1C}N_{1C} + T_2$	Fixed	Off		A-13 to A-15
$B_{3A}W_{1A}X_{1A}P_{1C}N_{1C}b_{F_{1A}} + T_2$	Fixed	Off		A-16, A-17
$B_{3A}W_{1A}X_{1A}P_{1C}N_{1C}b_{F_{1A}} + T_4$	Fixed	Off		A-18
$B_{3A}W_{1A}X_{1A}P_{1C}N_{1C}b_{F_{1A}} + T_1$	Free	On		A-19, A-20
$B_{3A}W_{1A}X_{1A}P_{1C}N_{1C}b_{F_{1A}} + T_1$	Free	On	low Re	A-21, A-22
$B_{3A}W_{1A}X_{1A}P_{1C}N_{1C}b_{F_{1A}}H_{1C}V_{1C} + T_1$	Free	On		A-23, A-24
$B_{3A}W_{1A}X_{1A}P_{1C}N_{1C}b_{F_{1A}}H_{1C}V_{1C} + T_1$	Free	On	low Re	A-25, A-26
$B_{3A}W_{1A}X_{1A}P_{1C}N_{1C}b_{F_{1A}}H_{1C}V_{1C} + T_2$	Fixed	Off	vary i_H	A-27, A-28
$B_{3A}W_{1A}X_{1A} + T_2$	Fixed	Off	Repeat LB-506A	A-29 to A-31
$B_{3A}W_{1A}X_{1A} + T_5$	Fixed	Off		A-32 to A-34
$B_{3A}W_{1A}X_{1A}P_{1C}N_{1C} + T_5$	Fixed	Off		A-35 to A-37
$B_{3A}W_{1A}X_{1A}P_{1C}N_{1C}b_{F_{1A}} + T_5$	Fixed	Off		A-38 to A-40

38

TABLE 3

SUMMARY OF PLOTTED FORCE AND MOMENT DATA (CONTINUED)

Configuration	Wing Transition	Load Compensator	Remarks	Figures
$B_{3A}W_{1A}X_{1A}P_{2A}N_{1C} + T_5$	Fixed	Off		A-41 to A-43
$B_{3A}W_{1A}X_{1A}P_{3A}N_{1C} + T_5$	Fixed	Off		A-44 to A-46
$B_{3A}W_{1A}X_{1A}P_{4A}N_{1C} + T_5$	Fixed	Off		A-47 to A-49
$B_{3A}W_{1A}X_{1A}P_{5A}N_{1C} + T_5$	Fixed	Off		A-50 to A-52
$B_{3A}W_{1A}X_{1A}P_{5A}N_{1C}{}^bF_{2A} + T_5$	Fixed	Off		A-53 to A-55
$B_{3A}W_{1A}X_{1A}(H_{1C}V_{1C}) + T_1$	Free	On	vary i_H	A-56 to A-64
$B_{3A}W_{1A}X_{1A}P_{1C}N_{1C}{}^bF_{1A}(H_{1C}V_{1C}) + T_1$	Free	On	vary i_H	A-65 to A-71
$B_{3A}W_{1A}X_{1A}(H_{2A}V_{1C}) + T_1$	Free	On	vary i_H	A-72 to A-78
$B_{3A}W_{1A}X_{1A}(H_{2A}V_{1C}) + T_1$	Free	On	vary Re	A-79, A-80
$B_{3A}W_{1A}X_{1A}P_{1C}N_{1C}{}^bF_{1A}(H_{2A}V_{1C}) + T_1$	Free	On	vary i_H	A-81 to A-87
$B_{3A}W_{1A}X_{1A}P_{5A}N_{1C}{}^bF_{2A}(H_{2A}V_{1C}) + T_1$	Free	On	vary i_H	A-88 to A-94
$B_{3A}W_{1A}X_{1A}P_{5A}N_{1C}{}^bF_{2A}(H_{2A}V_{1C}) + T_1$	Free	On	vary Re	A-95, A-96
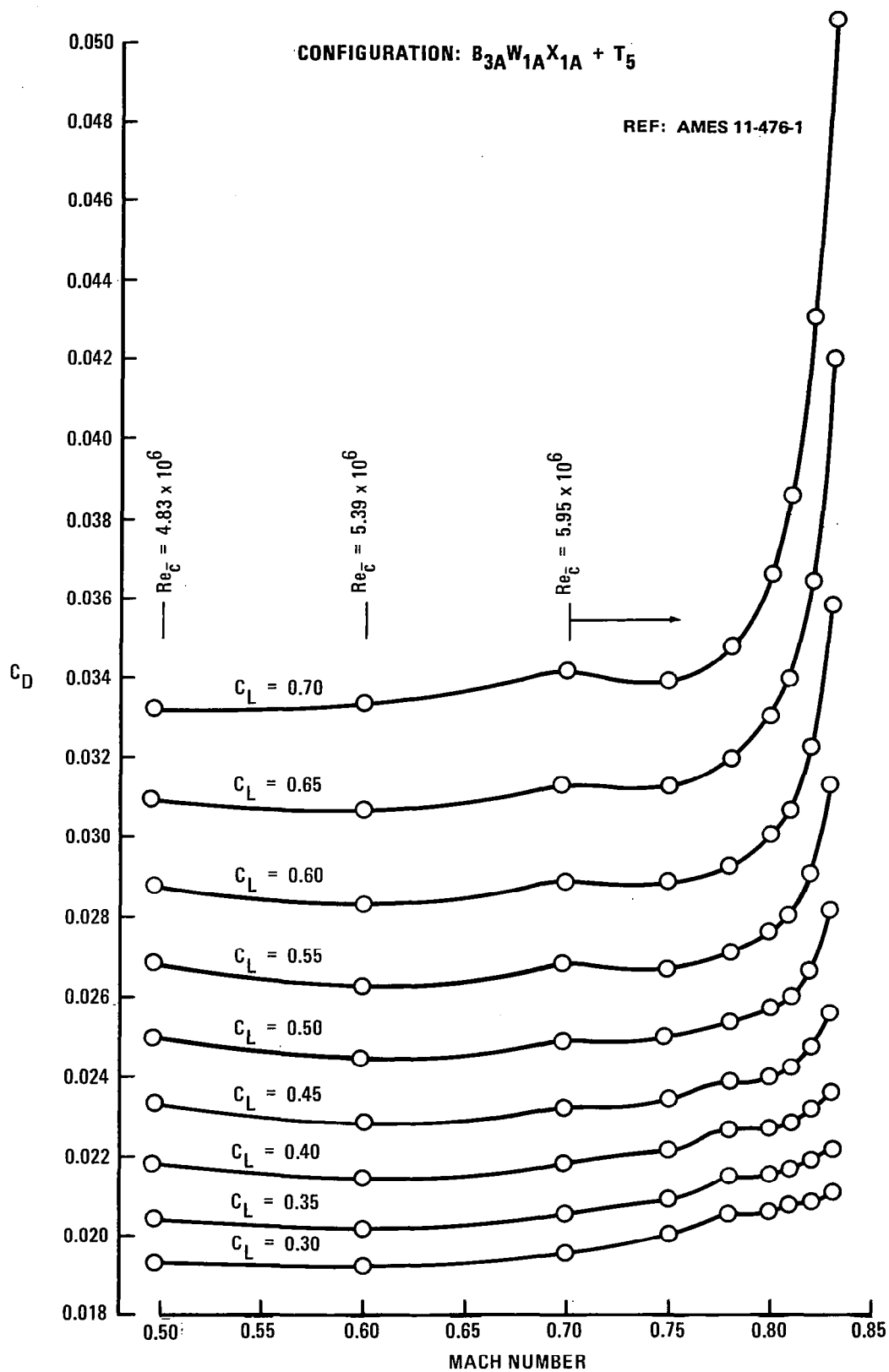
FIGURE 20. WING/BODY DRAG-RISE CHARACTERISTICS, TRANSITION T_5

40

Transition pattern T_5 was used for determination of cruise compressibility drag characteristics. The T_5 location was fixed at a position on the chord to theoretically match high-Reynolds-number, compressibility drag characteristics at the cruise Mach number and C_L. This transition location was selected based upon 3-D flow calculations at both wind tunnel model and flight Reynolds numbers and upon wind tunnel model flow visualization results.

The transition strip pattern for T_5 is presented in Figure 21. Also shown in Figure 21 is an alternate transition position T_2 which is further aft along the airfoil chord. A comparison of the compressibility drag characteristics for the two transition patterns is presented in Figure 22. This comparison illustrates the sensitivity of the drag measurements to transition position. In the cruise Mach number regime, the difference in compressibility drag increment is approximately five to six drag counts.

η	X/C, UPPER SURFACE	
	T_2	T_5
0.125	0.030	0.029
0.390	0.420	0.325
0.800	0.300	0.200
1.000	0.140	0.100

LOWER SURFACE TRANSITION-FREE
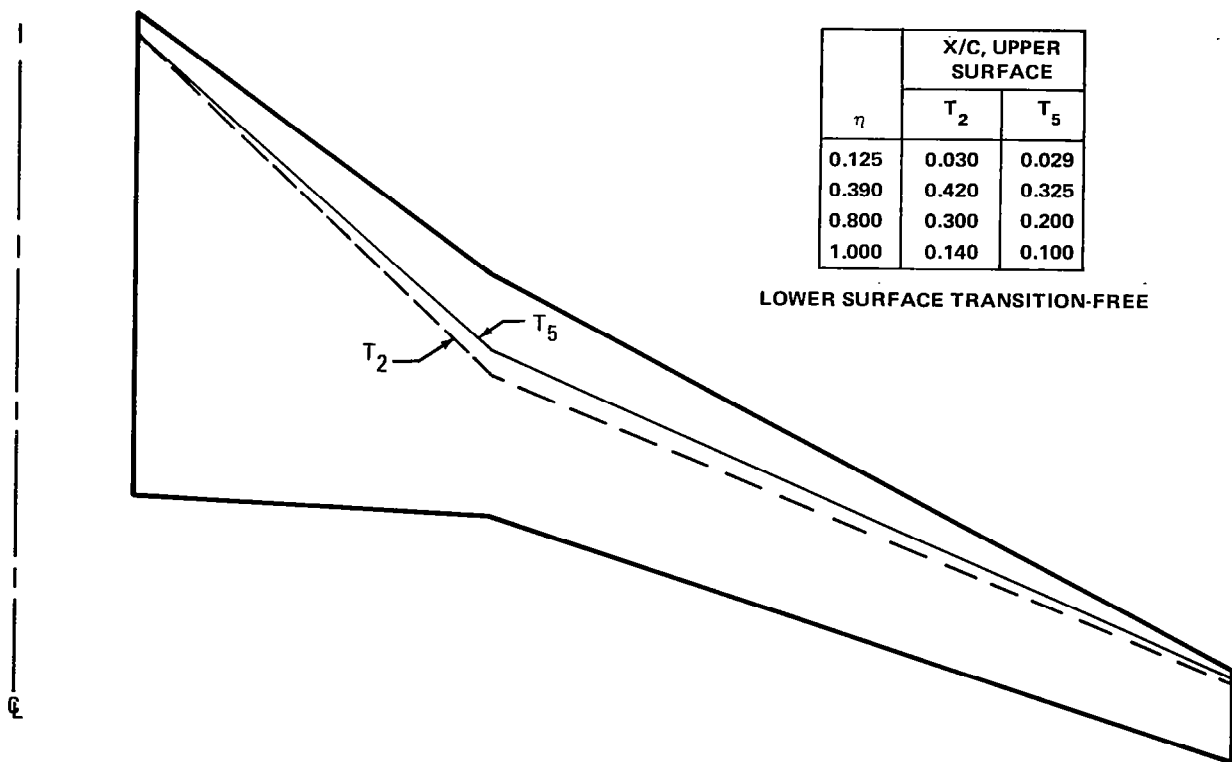
FIGURE 21. PLANFORM VIEW OF TRANSITION STRIP PATTERNS T_2 AND T_5
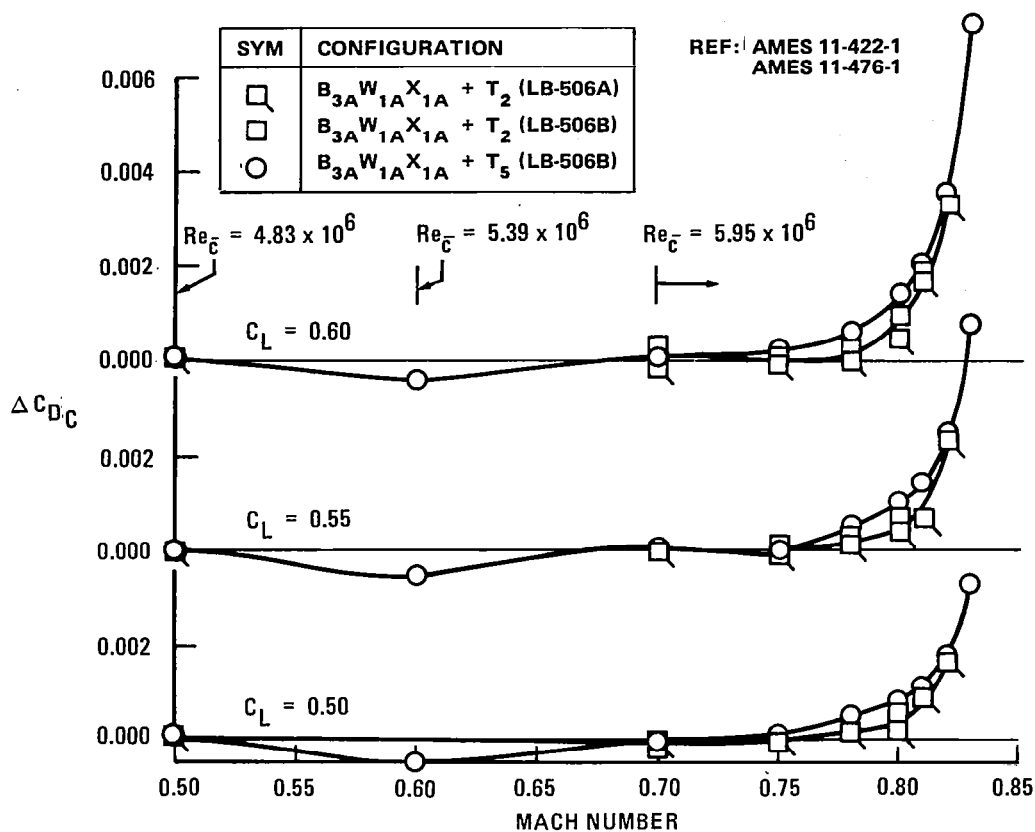
FIGURE 22. EFFECT OF TRANSITION LOCATION ON WING/BODY DRAG-RISE CHARACTERISTICS

The drag divergence Mach number is defined by the point along the drag rise at which $dC_D/dM = 0.05$. The basic wing/body drag divergence Mach number boundaries for both the T_2 and T_5 transition patterns are presented in Figure 23. The different transition patterns have a small effect on drag divergence Mach number. At the nominal design C_L of 0.55 the T_5 drag divergence Mach number is higher by approximately 0.003. The compressibility drag rise results in Figure 22 indicate this improvement is the result of an increased drag creep level with transition T_5. With the T_5 transition position the nominal design Mach number of 0.8 was exceeded by nearly 0.01.

In Figure 24 the T_2 transition compressibility characteristics for the W_1 wing/body are compared to the measured results[2] from the Phase I W_8 wing/body with a similar transition position. The premature drag creep associated with the W_8 wing has been substantially reduced with the W_1 wing design. As discussed in the configuration definition section, the premature drag creep was largely reduced by modifying the inboard airfoils.

42
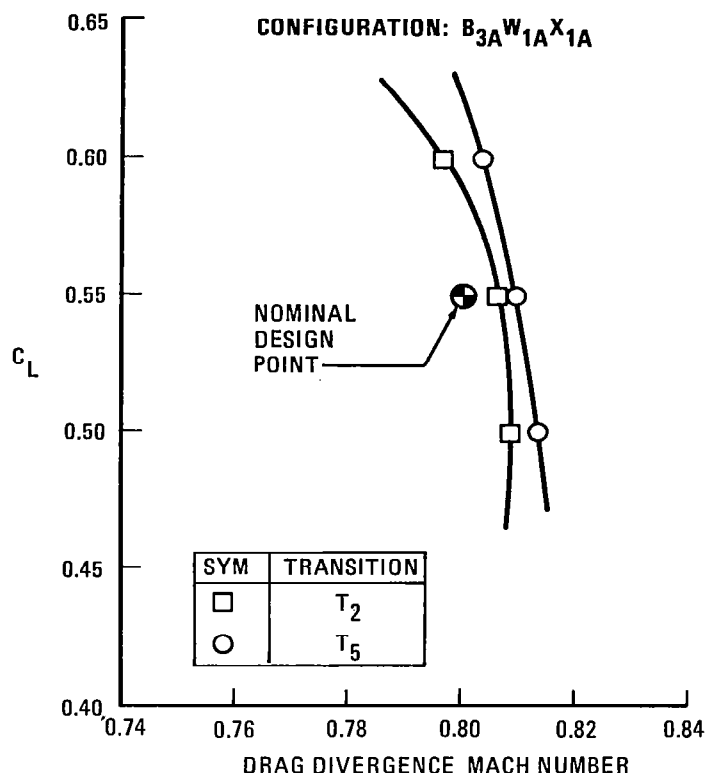
FIGURE 23. EFFECT OF TRANSITION LOCATION ON WING/BODY DRAG DIVERGENCE MACH NUMBER
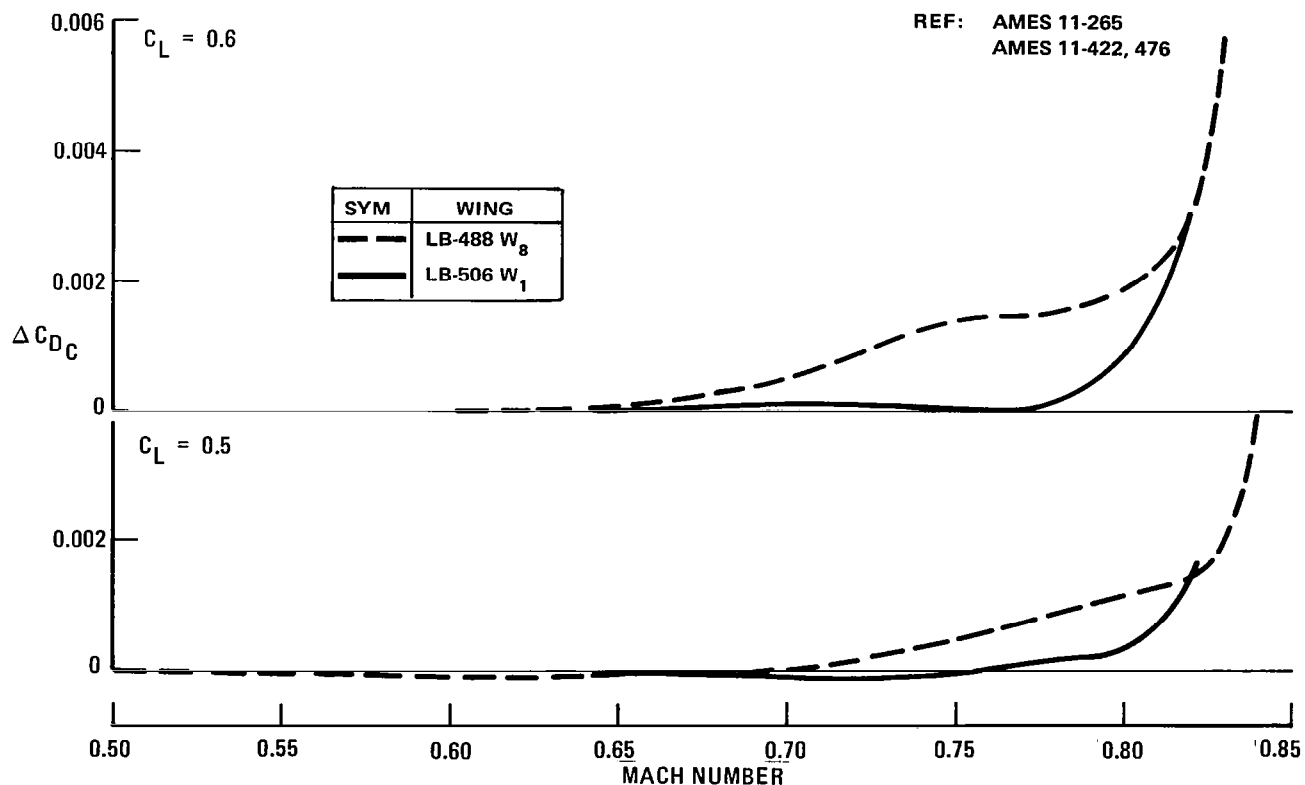
FIGURE 24. COMPARISON OF COMPRESSIBILITY DRAG-RISE CHARACTERISTICS
OF PHASE I W_8 AND PHASE II W_1

The measured inboard pressure distributions from the Phase I wing W_8 and the current W_1 wing are compared in Figure 25. A substantial reduction in the upper surface velocities and corresponding shock strengths has been obtained.
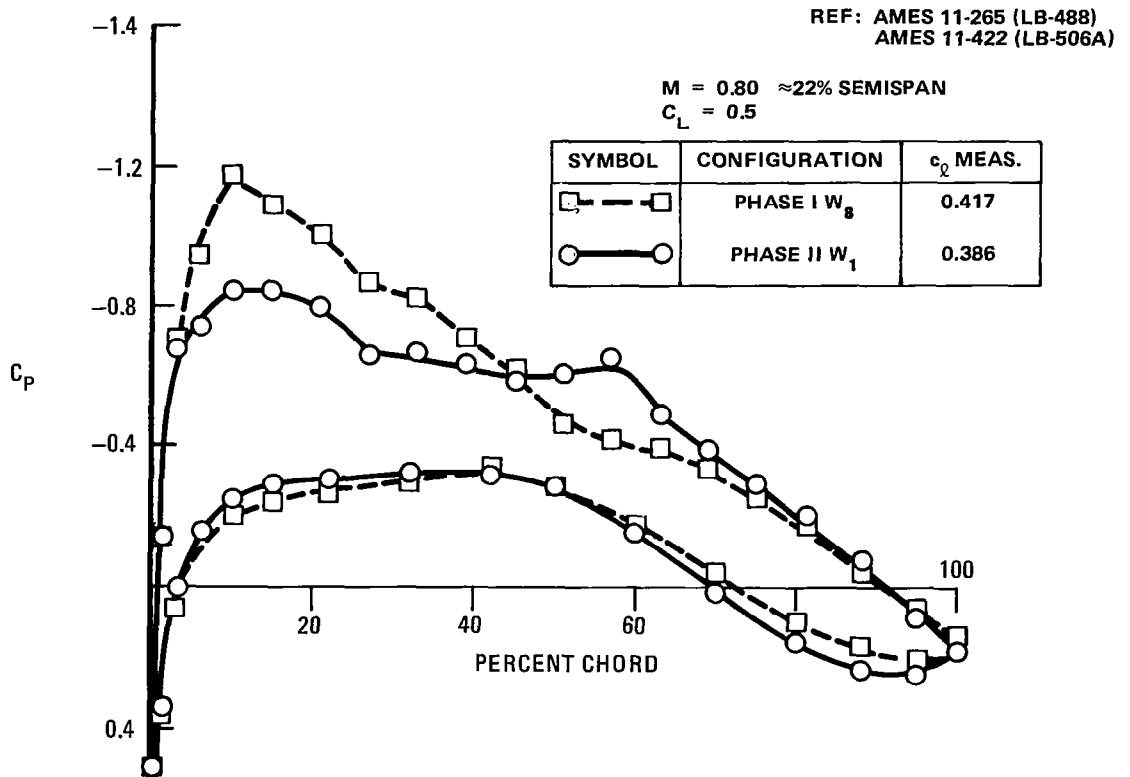
FIGURE 25. MEASURED INBOARD CHORDWISE PRESSURE DISTRIBUTIONS FOR PHASE I W_8 AND PHASE II W_1

Nacelle/Pylon Drag Characteristics

As described in the Test Plan and Model Description section, five different nacelle positions were tested. These positions were obtained with five different symmetrical pylons. The nacelle configuration was the same for all the testing. The five pylons were selected to assess the effect of longitudinal, vertical, and spanwise nacelle position on configuration drag characteristics.

The baseline pylon, P_{1C}, located the nacelle at the planform break station of 39% semispan. The P_{1C} fan exit position was 25% of the local wing chord ahead of the wing leading edge at the pylon span station. The P_{1C} fan exit was centered at 46% of the local wing chord below the wing leading edge. Pylons P_{2A} and P_{3A} maintained these same spanwise and vertical nacelle positions but moved the nacelle progressively closer to the wing leading edge. The P_{2A} pylon located the fan exit at 10% of the local wing chord ahead of the wing leading edge. With P_{3A}, the fan exit was aligned with the wing leading edge.

Figure 26 presents the nacelle/pylon drag increment at 0.8 Mach number. Included in the figure is a parasite drag estimate of the isolated nacelle and pylon. This was obtained by calculating the wetted-area skin friction drag and applying the appropriate form factor for each component of the nacelle/pylon assembly. (The form drag accounted for 32 percent of the parasite drag estimate.) Near the design lift coefficient of 0.55 the P_{1C} pylon configuration has a drag increment very close to the calculated parasite drag level. This indicates very little interference drag due to the nacelle and pylon, despite the presence of a shock on the wing lower surface near the pylon. However, this shock is localized and weak at the higher lift coefficients. It is also possible that the nacelles and pylons affect the wing spanwise lift distribution such that the wing induced drag is decreased, similar to the Phase I configuration[2]. At low lift coefficients a substantial interference penalty is shown. This interference can be attributed to the supersonic velocity regions and strong shocks on the wing lower surface near the wing/pylon intersection. As the nacelle is moved closer to the wing leading edge, using pylons P_{2A} and P_{3A}, interference drag penalties are shown even for the design lift coefficient range.

45
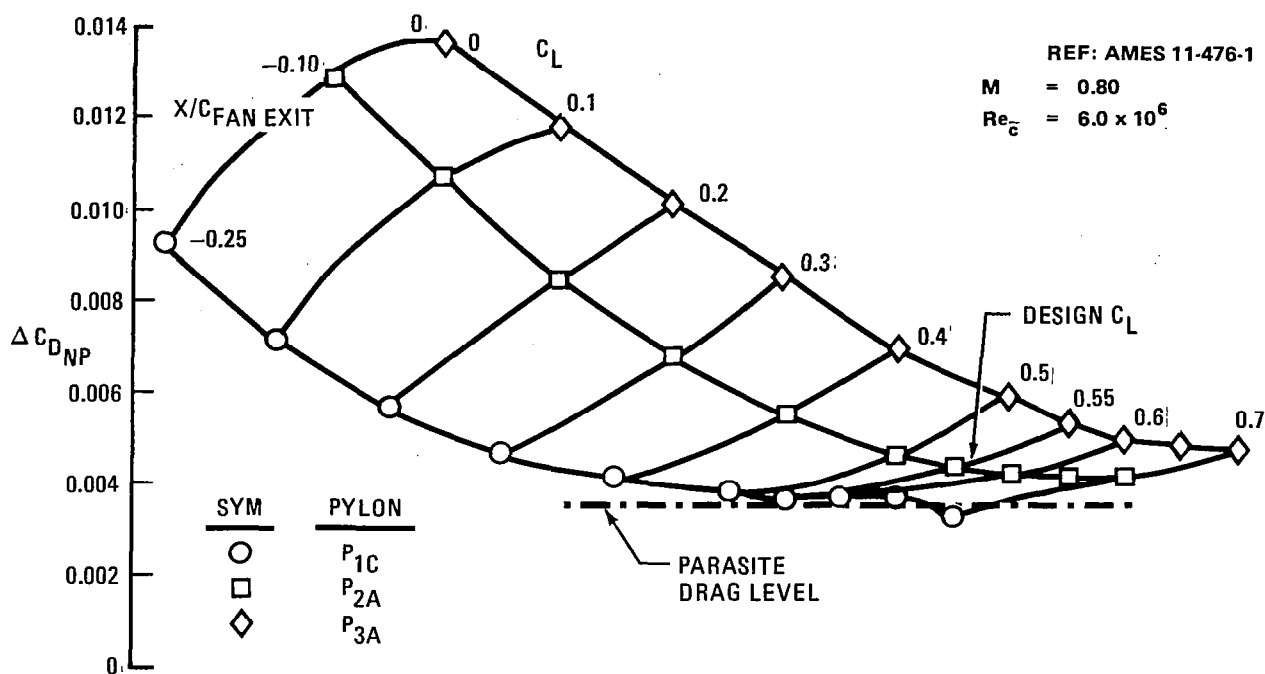
FIGURE 26. EFFECT OF NACELLE LONGITUDINAL POSITION ON NACELLE/PYLON
INCREMENTAL DRAG

For the furthest-aft location, P_{3A}, the penalty at 0.55 lift coefficient is in excess of fifteen drag counts.

The effect of the nacelle longitudinal position on the local wing pressure distribution at 37.5 percent semispan is shown in Figure 27. This station is just inboard of the pylon. The differences in total lift coefficient as well as section lift coefficient are also indicated in the figure. The pylon introduces a significant suction peak on the wing lower surface and suppresses the wing upper surface velocities. The P_{1C} lower wing surface suction peak is supersonic and terminates in a shock wave, as indicated by the pressure rise at approximately fifteen percent chord. The measured pressure distributions for P_{2A} and P_{3A} indicate a progressive increase in the size of the lower surface supersonic region. It must be noted that the P_{1C}, P_{2A}, and P_{3A} pylons included integral flap linkage fairings. The change in the lower surface pressure distributions aft of the mid-chord region is associated with the fairing configuration effects on the local pressure distribution.

46

SYM	α	c_{ℓ}	C_L	CONFIG	FAN EXIT – X/C
O	0.980	0.645	0.605	CLEAN WING	–
——	0.970	0.547	0.551	PYLON P_{1C}	–0.25
------	0.900	0.521	0.525	PYLON P_{2A}	–0.10
–·–·–	0.880	0.495	0.510	PYLON P_{3A}	0.00

M = 0.80

$Re_{\bar{c}}$ = 5.95 x 10^6

η = 0.375
(INBOARD OF PYLON)
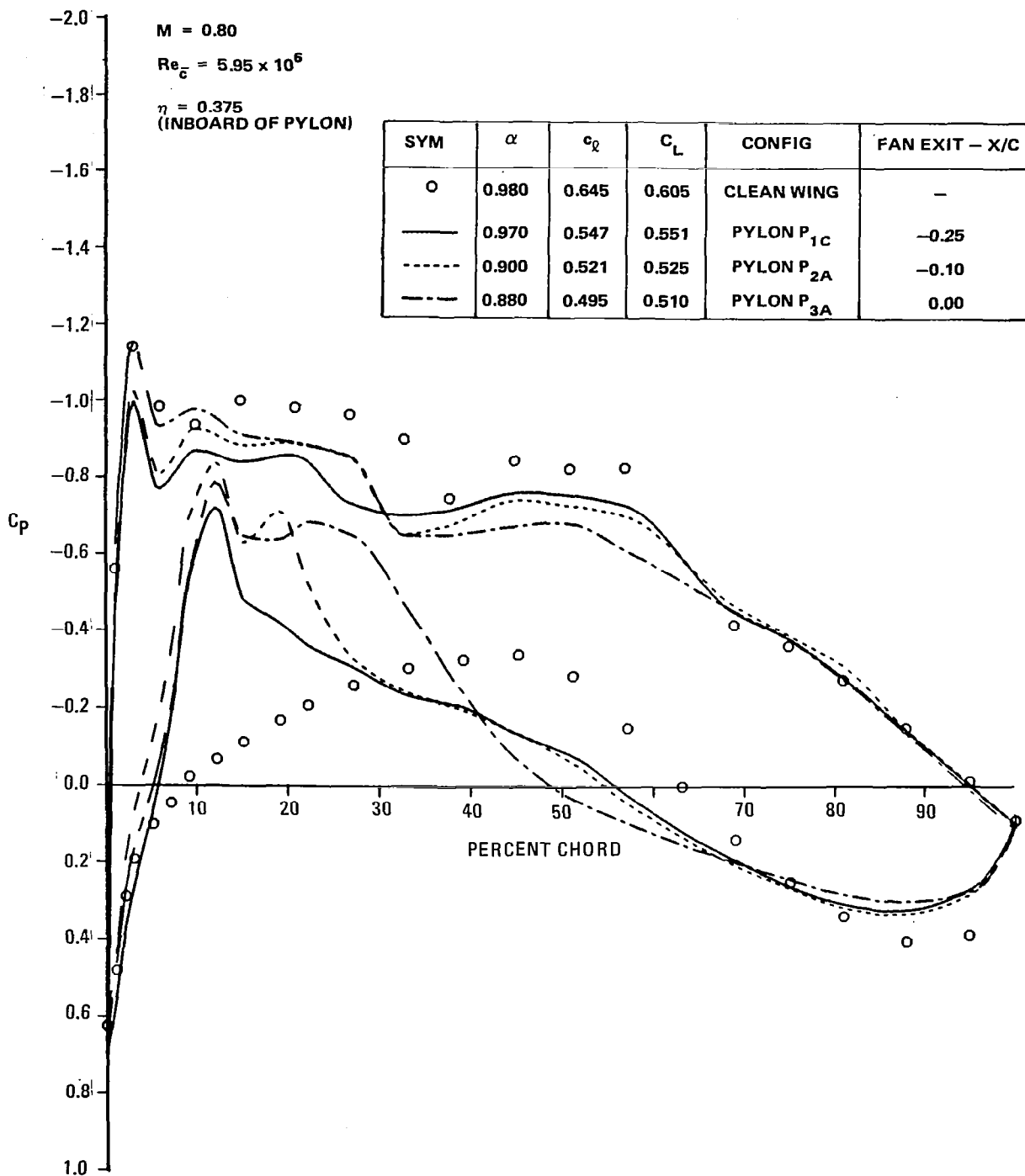
FIGURE 27. EFFECT OF NACELLE LONGITUDINAL POSITION ON WING CHORDWISE PRESSURE DISTRIBUTION

The effect of the nacelle longitudinal position on the compressibility drag characteristics is indicated in Figure 28. The drag rise measurements indicated in Figure 28 were obtained with the complete set of flap hinge fairings installed. As indicated, the aft movement of the nacelle leads to a progressive deterioration of the drag divergence characteristics. The interference effect is the largest at the lower lift coefficients, as would be expected with a lower surface interference problem.

The nacelle vertical position was changed by using pylon P_{4A}. The position of the fan exit centerline was changed from 46.0 with pylons P_{1C}, P_{2A} and P_{3A}, to 41.0 percent chord below the wing leading edge with P_{4A}. The fan exit was located at the same longitudinal station with P_{4A} as with P_{2A}, at 10 percent chord ahead of the wing leading edge. The nacelle/pylon drag increments at 0.8 Mach number for both the P_{2A} and P_{4A} nacelle positions are shown in Figure 29. As indicated, the vertical position change resulted in only small differences in the nacelle/pylon drag increment, with pylon P_{2A} giving one to two counts higher drag in the cruise C_L range.

The nacelle spanwise position was changed by using pylon P_{5A}. P_{5A} located the nacelle 9.408 cm (3.704 in.) below the wing leading edge, which was higher than P_{1C}, P_{2A}, and P_{3A} because of configuration design constraints. The effect of the spanwise position on the nacelle/pylon drag increment is illustrated in Figure 30. The symbols are the measured drag increment for the inboard position. Two lines are shown for the comparable outboard position. The solid line is an interpolation of the P_{1C}, P_{2A}, and P_{3A} data matching the P_{5A} non-dimensional fan exit position (x/c = 0.1245) ahead of the wing leading edge. The dashed line is an interpolation of the same data matching the P_{5A} actual distance (x = 2.300 cm or 3.270 in.) between the exit and the wing leading edge. The two are different because of the wing chord variation spanwise. In the cruise C_L range the difference is on the order of two drag counts.

48
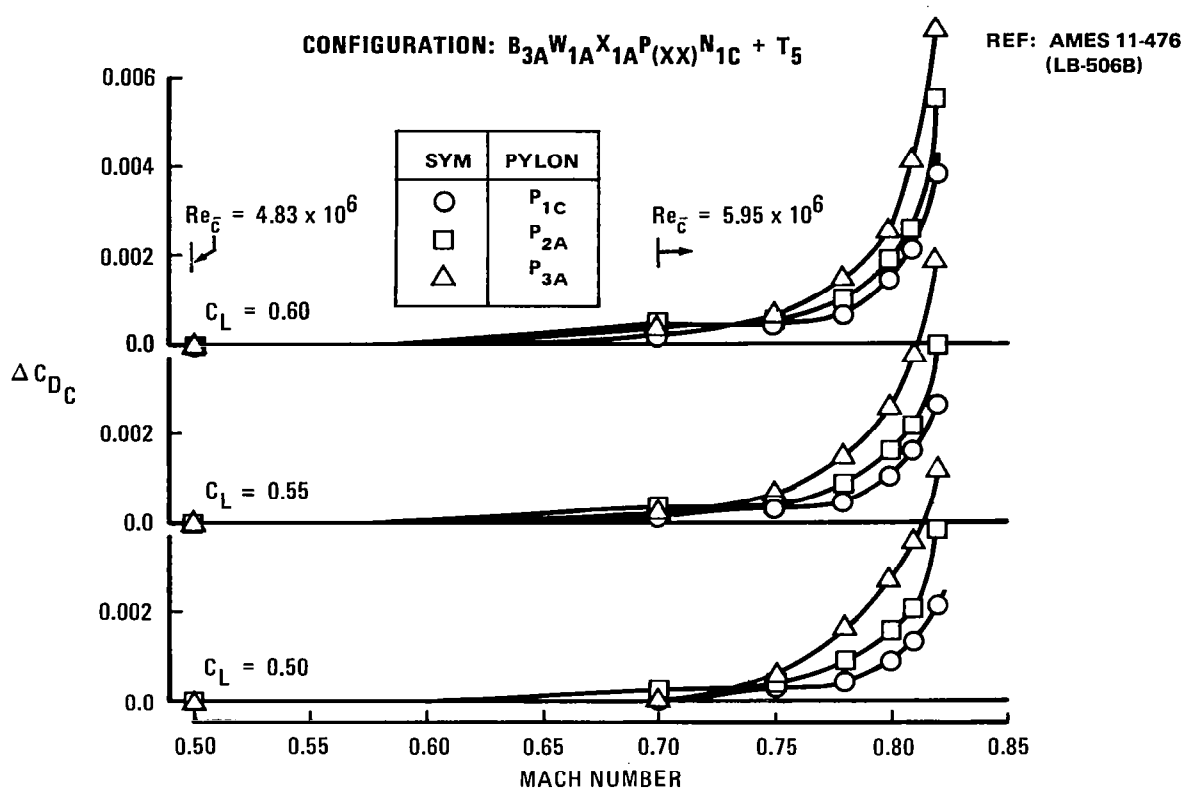
FIGURE 28. EFFECT OF NACELLE LONGITUDINAL POSITION ON COMPRESSIBILITY DRAG-RISE
CHARACTERISTICS
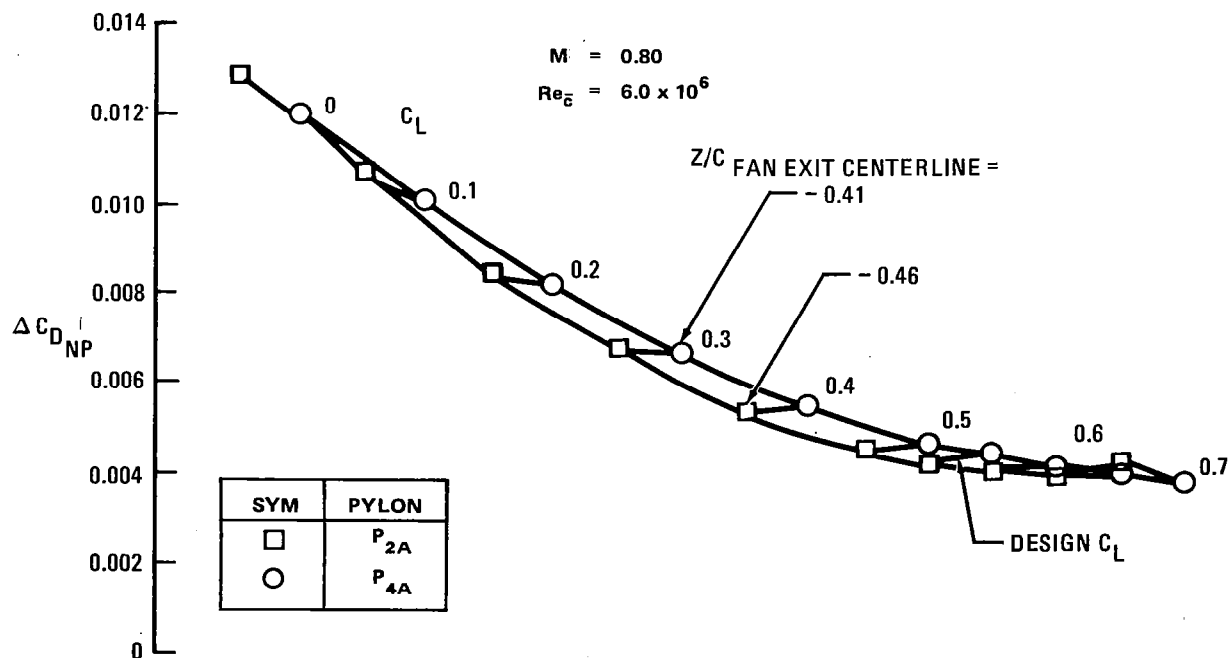
FIGURE 29. EFFECT OF NACELLE VERTICAL POSITION ON NACELLE/PYLON INCREMENTAL DRAG

$M = 0.80$

$Re_{\bar{c}} = 6.0 \times 10^6$

$\Delta C_{D_{NP}}$

DESIGN C_L

C_L

SYM	η	PYLON	
O	0.332	P_{5A}	
——	0.390	$P_{1C}P_{2A}P_{3A}$	MATCHING P_{5A} X/C FAN EXIT
– – –	0.390	$P_{1C}P_{2A}P_{3A}$	MATCHING P_{5A} X FAN EXIT
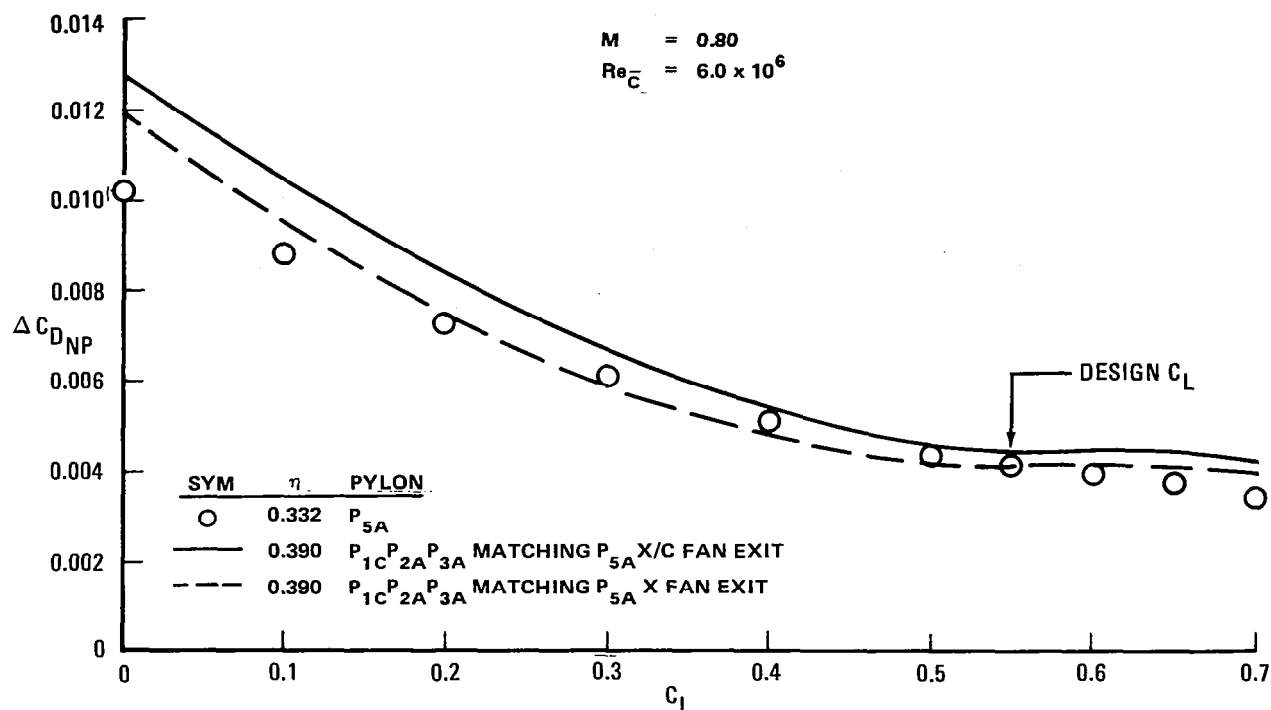
FIGURE 30. EFFECT OF NACELLE SPANWISE POSITION ON NACELLE/PYLON INCREMENTAL DRAG

Flap Linkage Fairing Drag Characteristics

Measurements were made of the effect of adding four flap linkage fairings to the lower surface of each wing panel. These four are in addition to the integral fairing included in the pylon trailing edge. The flap linkage fairing drag increment at both 0.5 and 0.8 Mach number is illustrated in Figure 31. At 0.5 Mach number the measured increment is approximately twice the interference-free parasite drag estimate. This factor of two is not uncommon for such fairings. The 0.8 Mach number drag data show a slightly larger penalty in the cruise regime. These results suggest modest improvements of two to three drag counts could be obtained through configuration development of the flap linkage fairings.

Tail-Off Configuration Drag Divergence Characteristics

The compressibility drag characteristics of the tail-off configuration are shown in Figure 32. The dashed line is the data uncorrected for the reduced Reynolds number at 0.5 Mach number. The solid line includes a correction to give the compressibility drag increment at a constant Reynolds
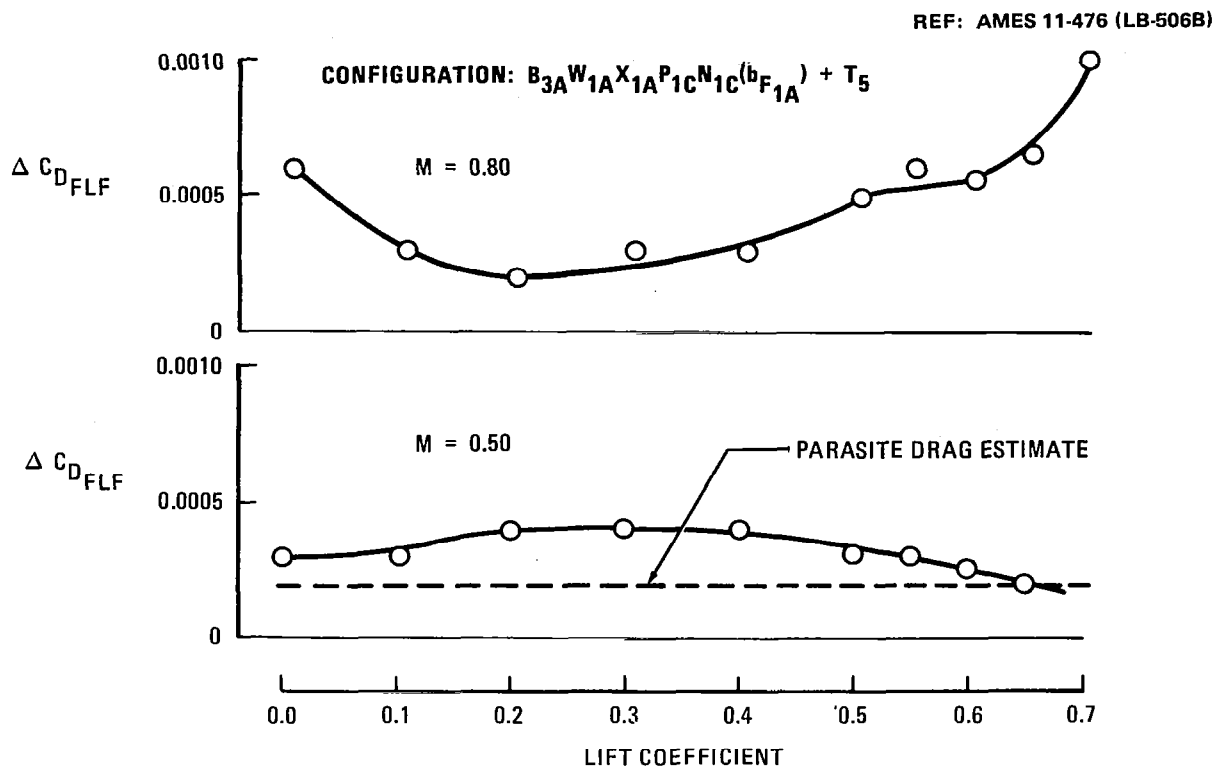
FIGURE 31. FLAP LINKAGE FAIRING INCREMENTAL DRAG WITH NACELLES AND PYLONS INSTALLED
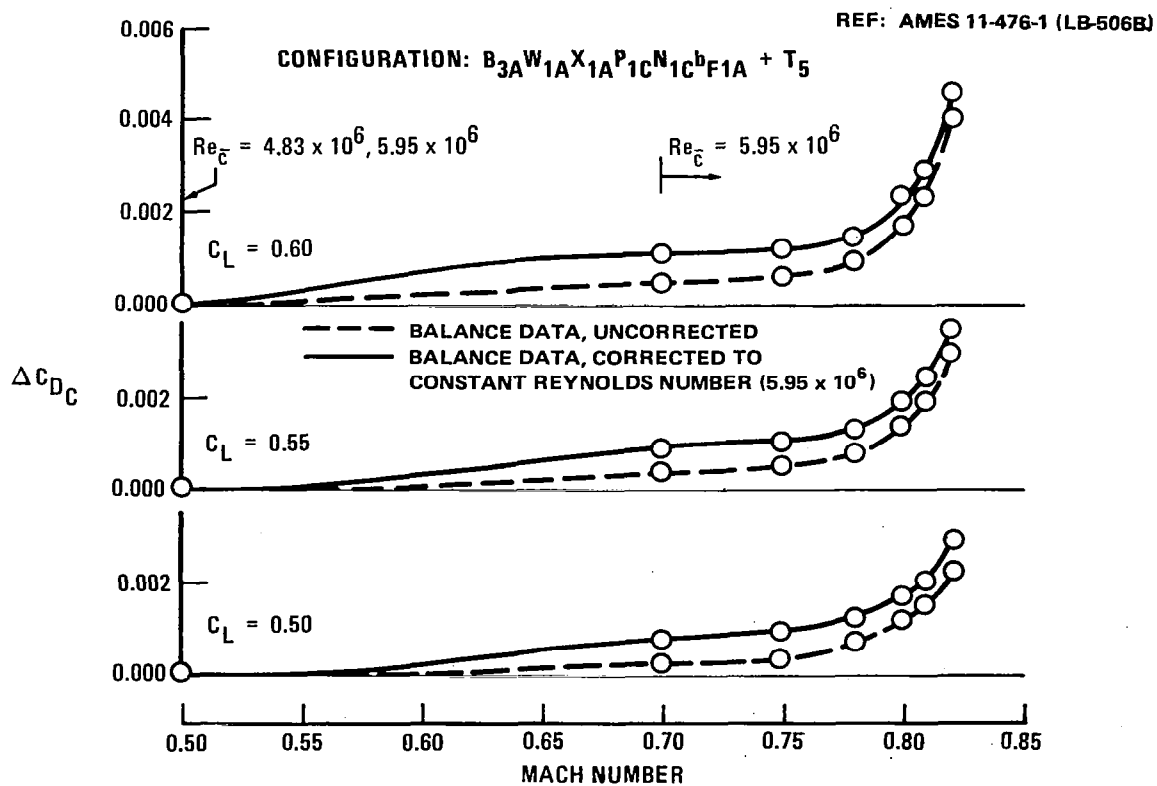
FIGURE 32. TAIL-OFF COMPRESSIBILITY DRAG-RISE CHARACTERISTICS

number. The correction lowers the total drag at 0.5 Mach number. This effectively increases the compressibility drag as shown. At the 0.55 design C_L and 0.8 design Mach number the tail-off configuration compressibility drag increment is approximately nineteen drag counts.

The compressibility drag increment in the 0.65 - 0.75 Mach number range may be slightly high because of the low Reynolds number of the wind tunnel tests. The wind tunnel and theoretical results indicated that, in this Mach number range, weak shocks were developed on the wing upper surface near the leading edge. These shocks were likely to cause a premature boundary layer transition well ahead of the boundary layer trip, which could have caused an excess drag level through two means: first, the amount of turbulent run to the trailing edge would have been increased, leading to higher skin friction drag. Second, the premature transition would have increased the boundary layer thickness and reduced the wing aft camber, so that the lift that was lost would have to be regained by increasing the angle of attack. The increased angle of attack would have caused stronger shocks on the upper surface and an attendant wave drag increase. Theoretical calculations suggest that, at the tunnel Reynolds numbers, the drag level in the Mach number range from 0.65 to 0.75 could be artificially high by several drag counts.

The drag divergence Mach number for the tail-off configuration is illustrated in Figure 33. Also shown, as a dashed line, is the basic wing/body drag divergence boundary. The additional components account for a reduction of approximately 0.005 in drag divergence Mach number.

Tail-Off Configuration High-Speed Buffet Characteristics

Previous buffet boundary correlations of flight data and wind tunnel test data obtained in the NASA Ames 11-foot wind tunnel have shown that transition-free wind tunnel data agree well with the flight data, while transition-fixed data tend to be conservative. At high Mach numbers, the degree of conservatism depends upon the transition strip position. To get closer agreement with the flight data, the transition has to be located fairly far aft along the wing chord, for if it is fixed too far forward, the
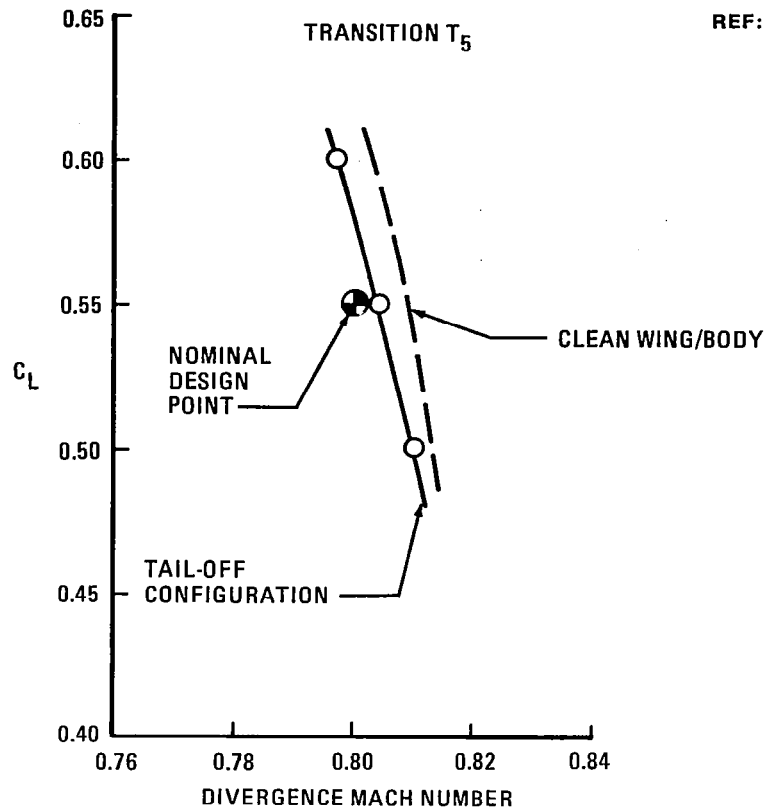
FIGURE 33. TAIL-OFF DRAG DIVERGENCE CHARACTERISTICS

boundary layer along the aft part of the wing will be over-thickened and start to separate at a low lift coefficient. However, if transition is fixed aft along the wing chord, the transition-fixed and transition-free buffet boundaries tend to approach each other. (At low Mach numbers, transition will occur near the leading edge whether transition is fixed or not.)

Several different criteria are used to determine buffet boundary. Three of the most common criteria are lift curve break, trailing edge pressure divergence, and lift coefficient versus Mach number break. The first two apply to both low and high speed parts of the boundary, while the third can be used only for the high speed portion. Each of these criteria tend to be somewhat subjective; different individuals analyzing the same measurements can often define different buffet boundaries. Consequently, it is prudent to compare the derived buffet levels using multiple criteria to add confidence in the results.

Figure 34 is a composite plot of transition-free lift curves for the complete tail-off configuration. Included on the plot are tick marks indicating lift-curve-break buffet onset. In Figure 35 the lift coefficient at constant angle of attack is presented versus Mach number for the same data. The peak C_L indication of buffet onset is identified in the figure. Figures 36, 37, and 38 illustrate the variation of trailing edge pressure with lift coefficient at different span stations for 0.781, 0.802, and 0.822 Mach numbers, respectively. Included in the figures is an arrow at the most critical span station. The arrow indicates the divergence of the trailing edge pressure from its previous trend by -0.04 in pressure coefficient. This point at the most critical station gives an indication of buffet onset.

The corresponding buffet lift coefficient boundary from each of the three criteria are presented in Figure 39. In the cruise Mach number regime, the lift curve break and trailing-edge pressure divergence criteria are in reasonable agreement. However, the peak C_L criteria seems inconsistent with the other two. At 0.8 Mach number this criteria gives an optimistic buffet lift coefficient by over 0.1 in C_L, while at 0.83 Mach number this criteria gives a pessimistic buffet lift coefficient by about the same amount. At 0.7 Mach number and below, the trailing-edge pressure divergence criteria gives a higher buffet boundary than the lift curve break criteria. This variation indicates that the boundary layer in the trailing edge region at approximately 0.9 lift coefficient has gotten quite thick (lift loss) but has not separated (pressure divergence).

Pitching Moment Characteristics

The tail-off transition-free pitching moment characteristics at 0.8 Mach number are presented in Figure 40. Results are shown for the nacelles/pylons/flap linkage fairings on and off. In the cruise C_L range, the addition of the nacelle/pylon/flap linkage fairings had a destabilizing effect, as would be expected. The corresponding tail-on characteristics utilizing the baseline horizontal tail, H_{1C}, are shown in Figure 41. Again, the nacelle/pylon/flap linkage fairings had a destabilizing effect in the cruise C_L range. At high lift coefficients (above 0.9), a high-speed pitch-up was evident. This undesirable effect was weakened by the nacelle/pylon/flap linkage fairing effect.

CONFIGURATION: $B_{3A}W_{1A}X_{1A}P_{1C}N_{1C}{}^{b}F_{1A} + T_1$
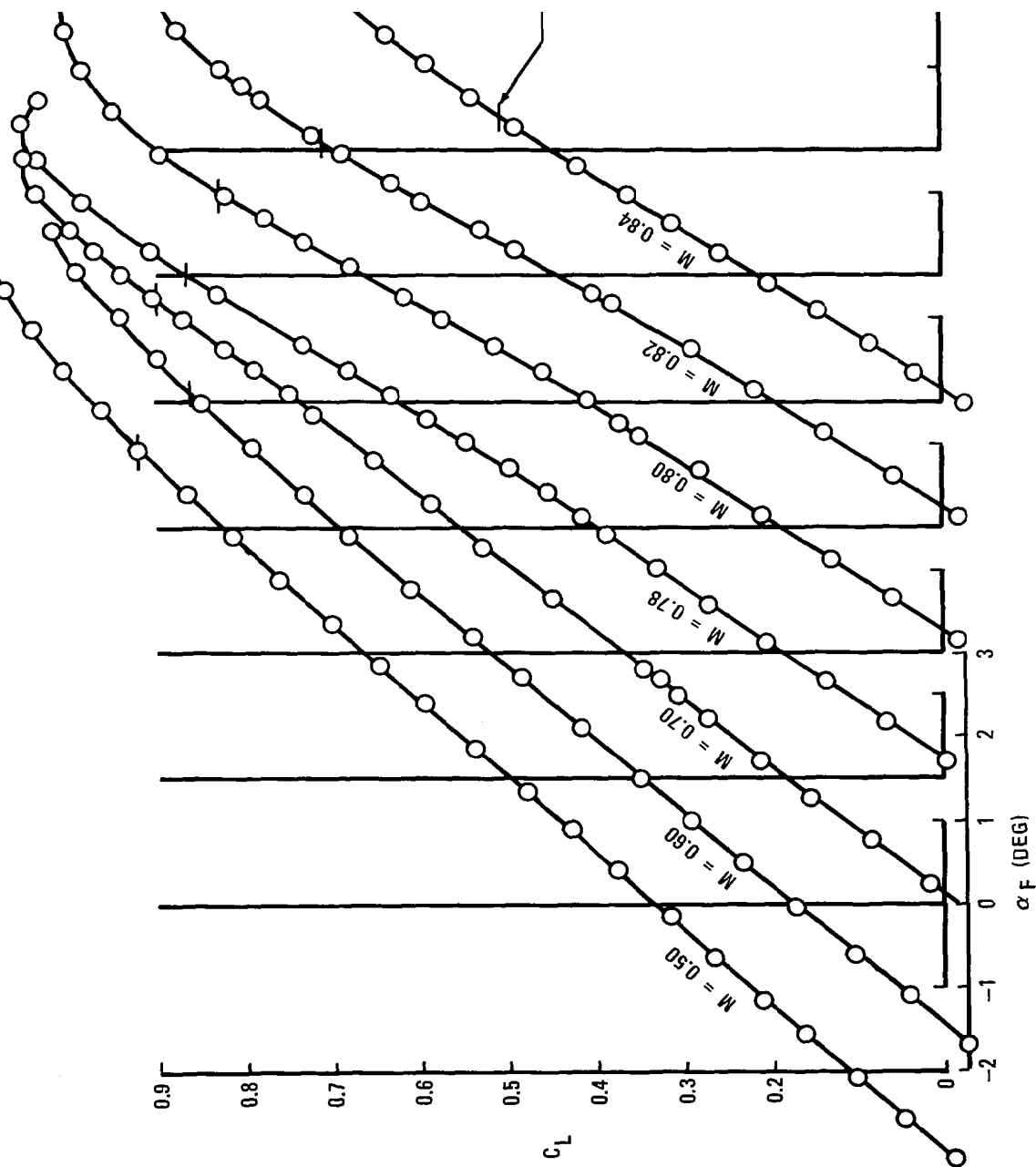
FIGURE 34. TAIL-OFF LIFT CHARACTERISTICS, TRANSITION-FREE

55
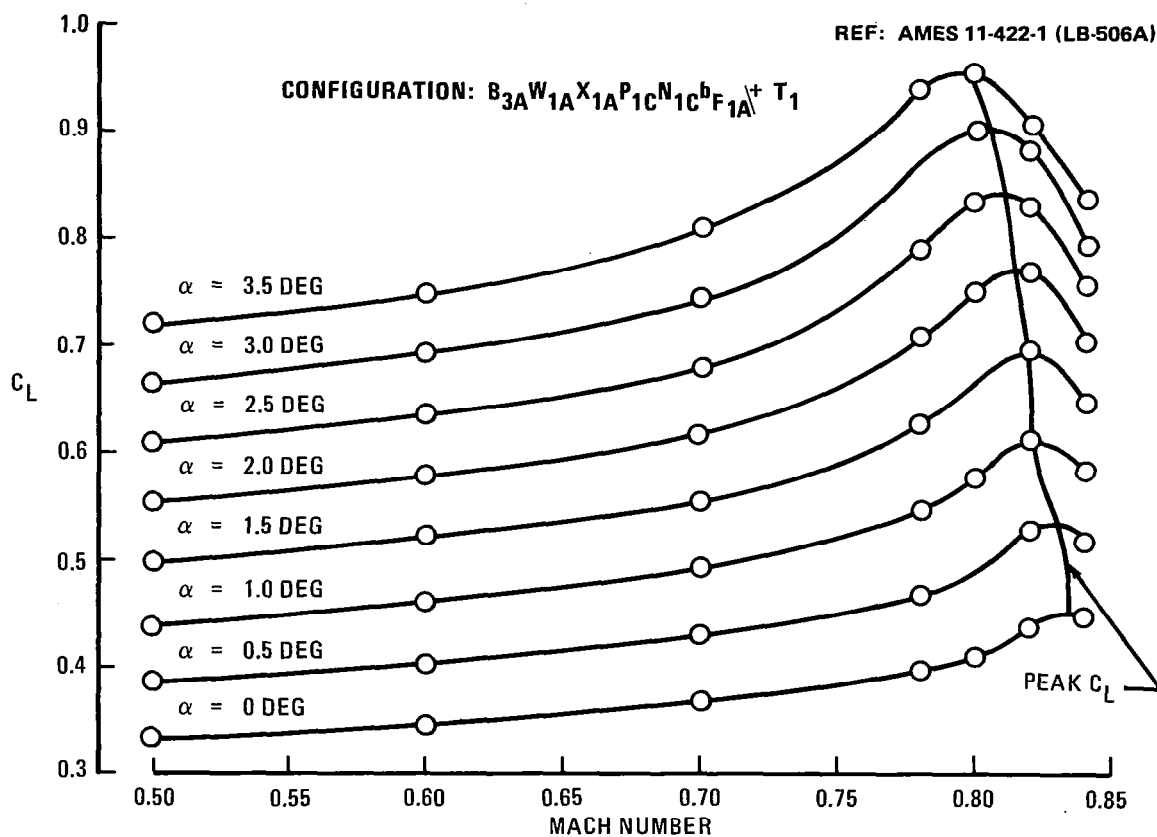
FIGURE 35. CONSTANT ANGLE-OF-ATTACK LIFT CHARACTERISTICS

CONFIGURATION: $B_{3A} W_{1A} X_{1A} N_{1C} P_{1C} {}^{b}F_{1A} + T_1$

M = 0.781
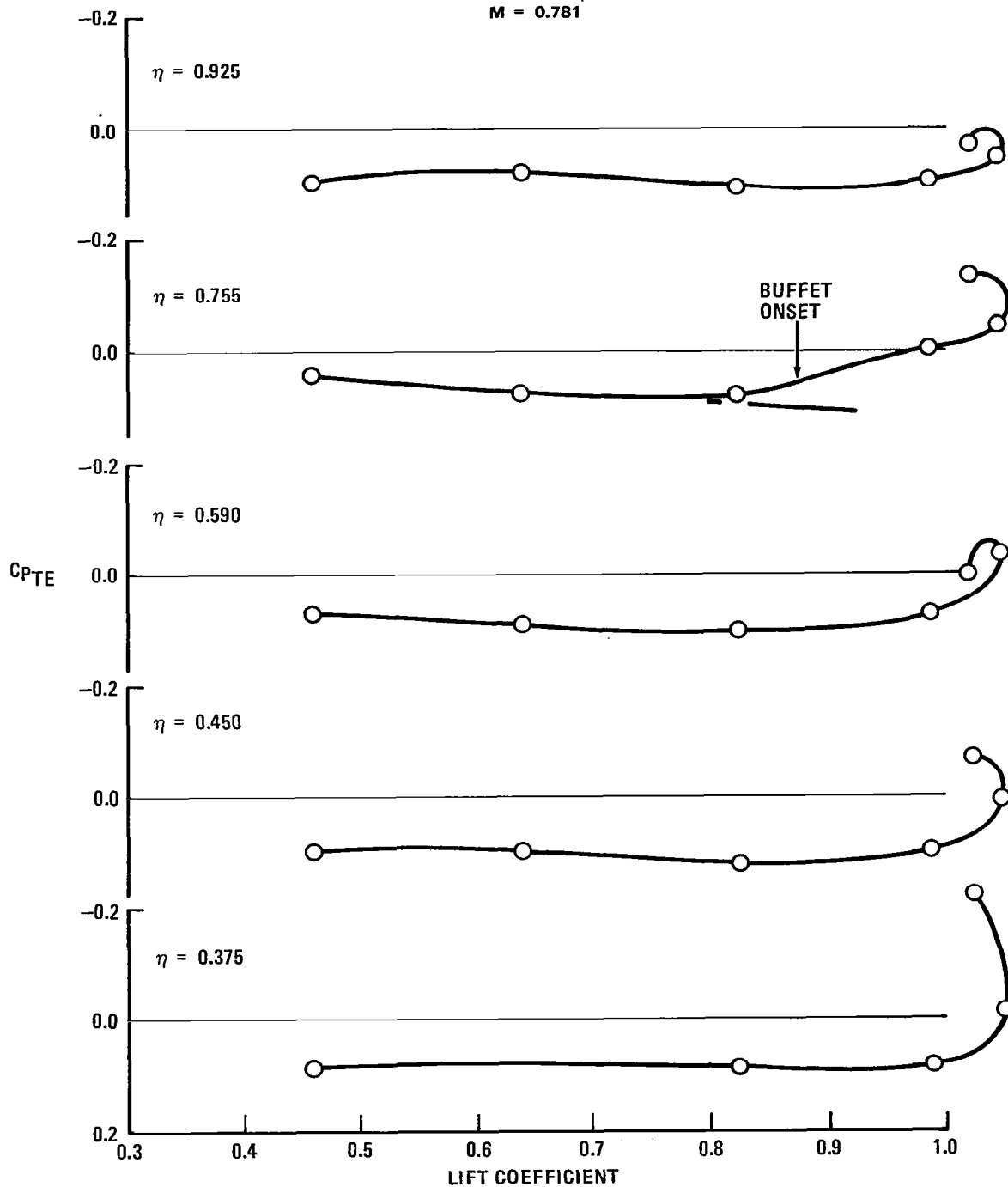
FIGURE 36. TRAILING-EDGE PRESSURE CHARACTERISTICS, M = 0.781

CONFIGURATION: B_{3A} W_{1A} X_{1A} N_{1C} P_{1C} $^bF_{1A}$ + T_1
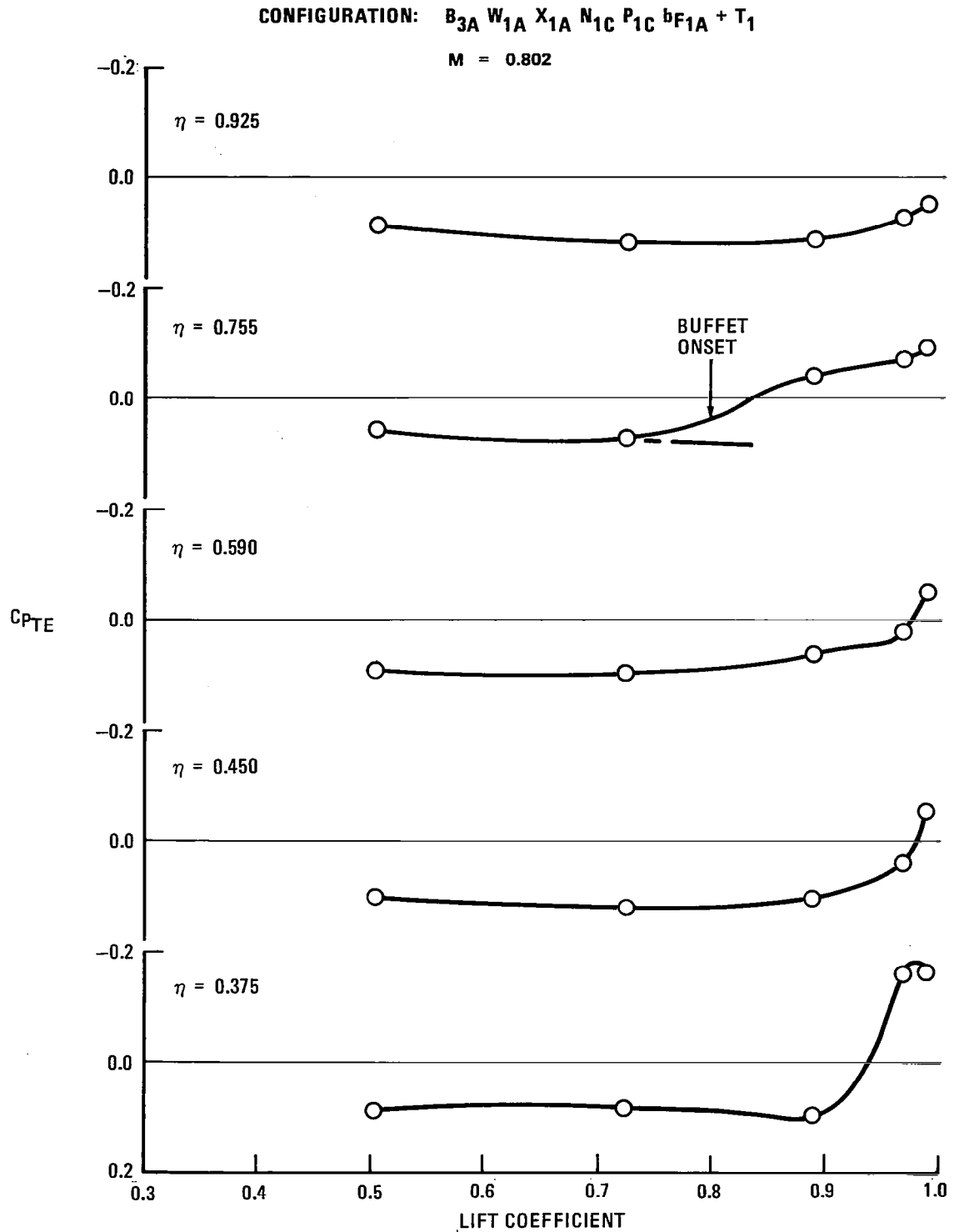
$M = 0.802$

FIGURE 37. TRAILING-EDGE PRESSURE CHARACTERISTICS M = 0.802

58
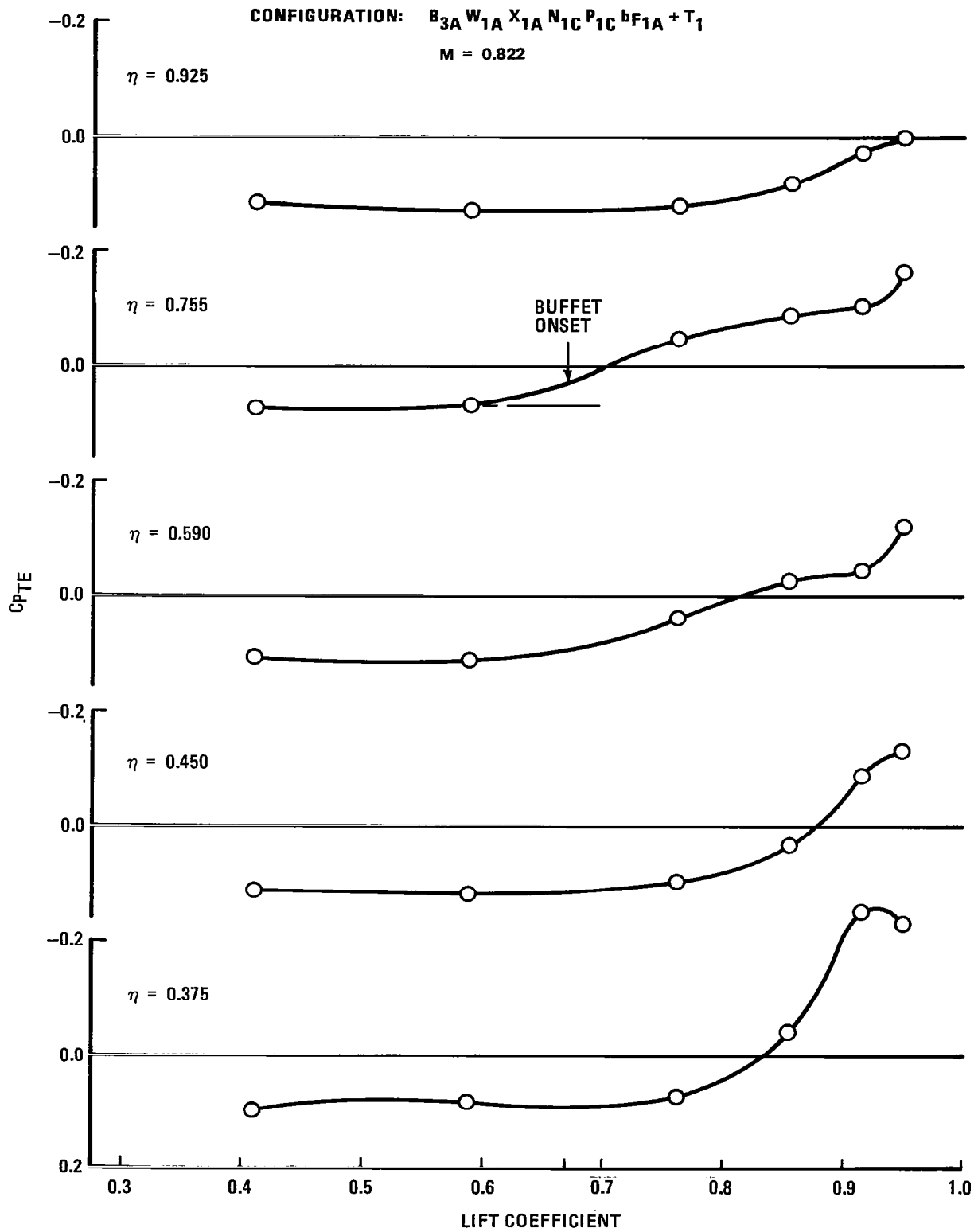
FIGURE 38. TRAILING-EDGE PRESSURE CHARACTERISTICS, M = 0.822

59

CONFIGURATION: $B_{3A}W_{1A}X_{1A}P_{1C}N_{1C}{}^{b}F_{1A} + T_1$

*NOTE: NO T.E. PRESSURE DIVERGENCE
REACHED BELOW C_L = 1.0

MACH NUMBER
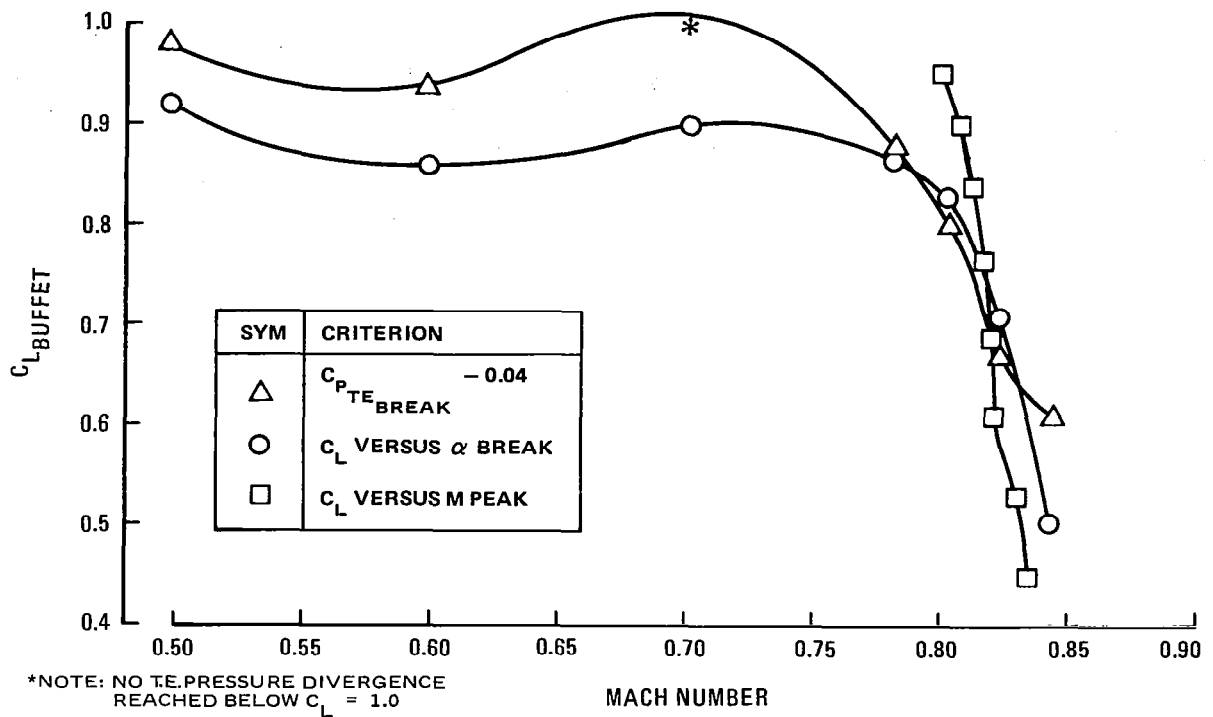
FIGURE 39. TAIL-OFF HIGH-SPEED BUFFET BOUNDARY BY VARIOUS CRITERIA
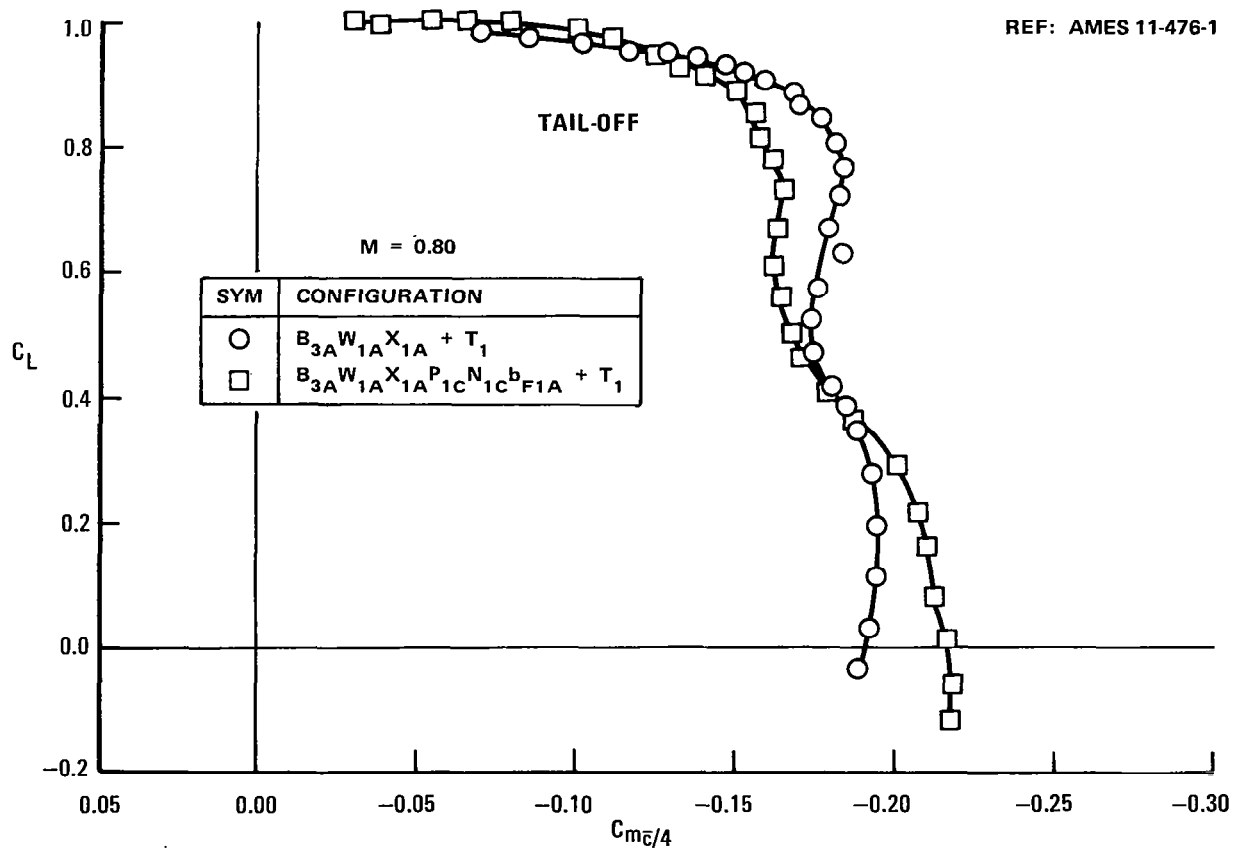
FIGURE 40. EFFECT OF NACELLES, PYLONS, AND FLAP LINKAGE FAIRINGS ON PITCHING
MOMENT CHARACTERISTICS (TAIL-OFF)

60
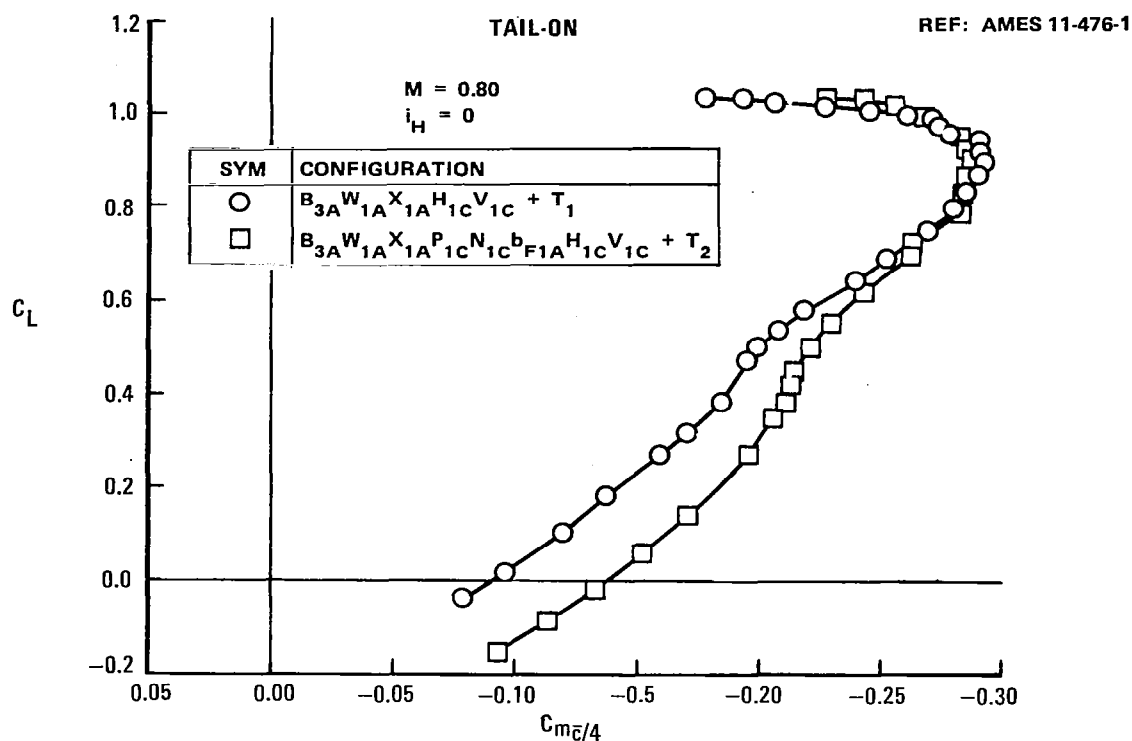
FIGURE 41. EFFECT OF NACELLES, PYLONS AND FLAP LINKAGE FAIRINGS ON PITCHING MOMENT CHARACTERISTICS (TAIL-ON)

The pitch-up tendency observed for this configuration prompted a more thorough examination of the high-speed pitch characteristics during the second tunnel entry. In the second entry, the effects of the horizontal tail configuration, nacelle/pylon position, and Reynolds number on high-speed pitch characteristics were all evaluated.

In Figure 42 the planforms of the baseline horizontal tail, H_{1C}, and the alternate horizontal tail, H_{2A}, are shown. The baseline horizontal tail had an aspect ratio of 4.1, while the alternate had an aspect ratio of 6.0. The horizontal to wing span ratios were 0.297 and 0.380 for H_{1C} and H_{2A}, respectively. The effect of this variation in horizontal tail configuration is illustrated in Figure 43. The data in Figure 43 are presented as pitching moment coefficient versus angle of attack. The results indicate a significant reduction in the high-speed pitch-up tendency with the H_{2A} tail. The angle of attack range for pitch-up has been reduced from approximately two degrees to approximately one degree.

CONFIGURATION	AR_H	V_H	b_H/b
H_{1C}	4.1	1.159	0.297
H_{2A}	6.0	1.207	0.380
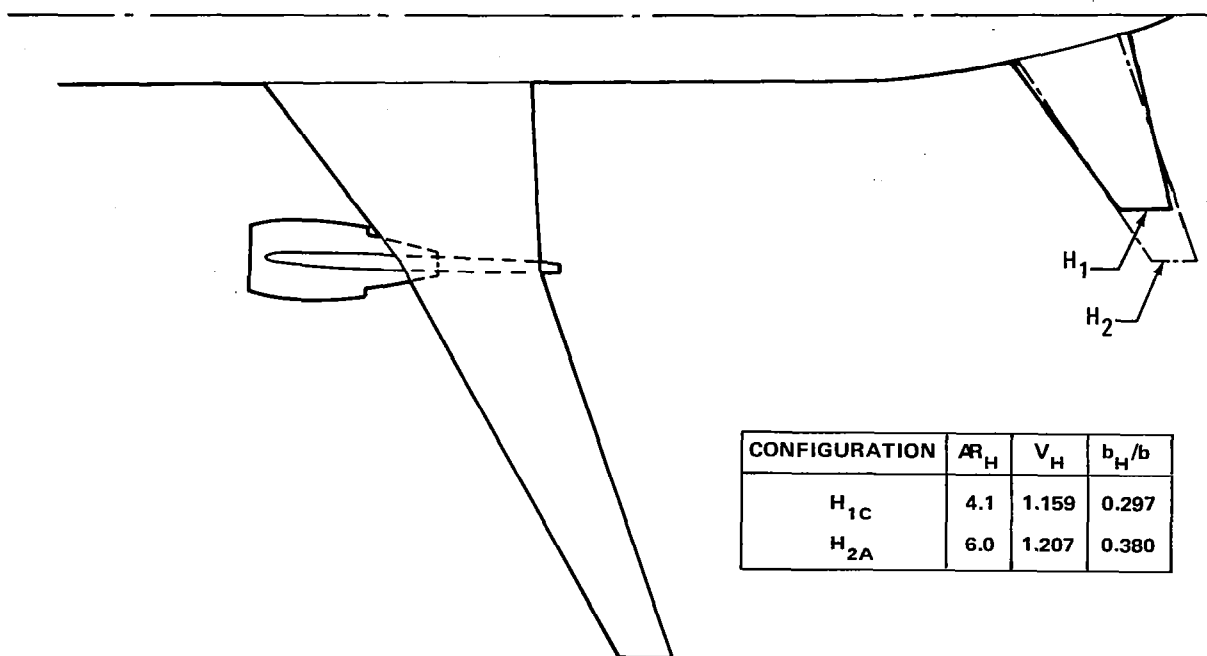
FIGURE 42. TAIL CONFIGURATIONS TESTED TO DETERMINE EFFECTS OF HORIZONTAL TAIL CONFIGURATION ON NONLINEAR CHARACTERISTICS

TRANSITION FREE

i_H = −3 DEGREES

P_{1C} PYLON

SYM	HORIZONTAL	AR_H	b_H/b
□	H_{1C}	4.1	0.297
O	H_{2A}	6.0	0.380
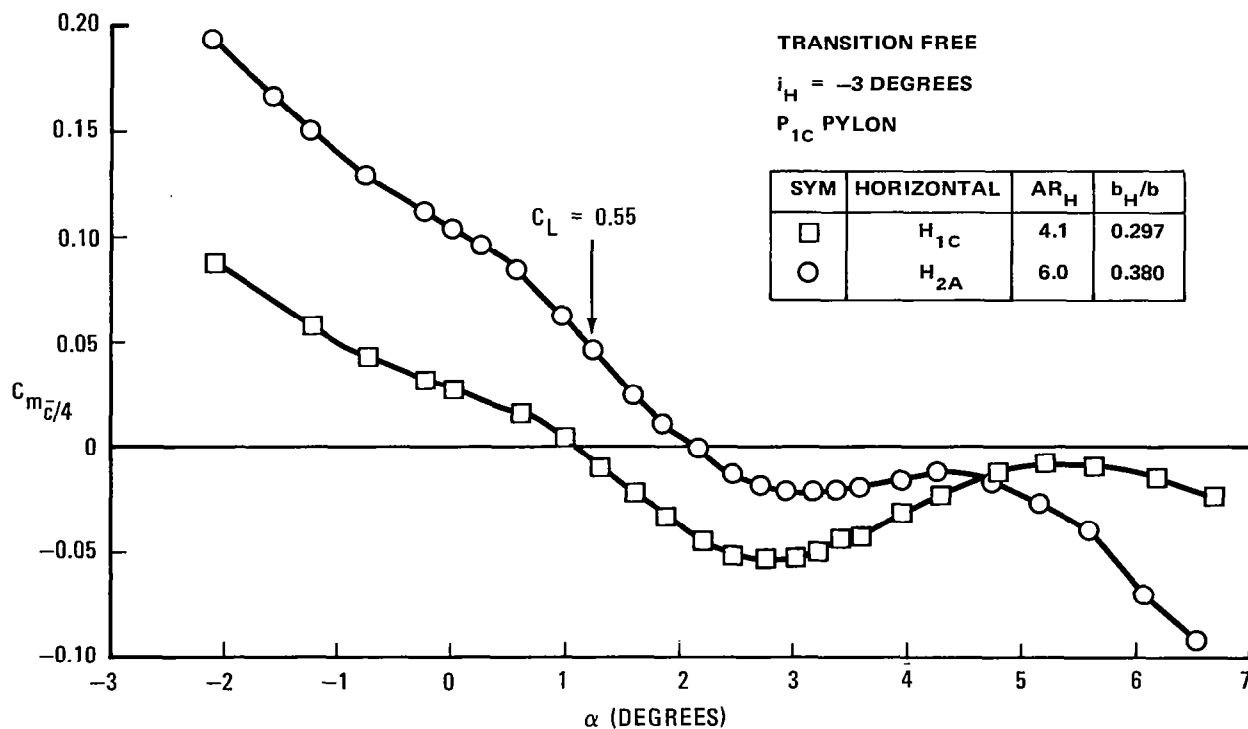
FIGURE 43. EFFECT OF HORIZONTAL TAIL CONFIGURATION ON CRUISE PITCHING MOMENT CHARACTERISTICS

62

The effect of nacelle/pylon spanwise position is indicated in Figure 44. The P_{1C} pylon located the nacelle at 39 percent semispan, while the P_{5A} pylon located the nacelle at approximately 33 percent semispan. The results show a significant degradation of the pitch characteristics with the inboard nacelle location, even with the H_{2A} tail.

The effect of Reynolds number on the high-speed pitch characteristics is illustrated in Figure 45. These data show a large Reynolds number effect on the pitch-up tendency. As the Reynolds number was reduced by one-half, the pitch-up became much more severe. These results emphasize the requirement for high Reynolds number testing, and allow the speculation that with increased Reynolds number beyond that tested, the configuration pitch characteristics might be further improved.

Nonlinear Lift Curve Characteristics

Nonlinear lift-curve characteristics, particularly apparent with advanced wing configurations, are a cause for concern in the design of the wing structure for dynamic gust loads. For lack of better three-dimensional transonic dynamics design rationale, the maximum local lift-curve slope is conventionally extrapolated for dynamic gust load analyses. The extrapolation is made for an angle-of-attack change due to a dynamic gust, and yields the wing gust load. This extrapolation is illustrated graphically in Figure 46. The combination of high-aspect-ratio wing and advanced airfoils gives a high local lift-curve slope and a correspondingly high gust load. In the absence of data to the contrary, the high gust loads lead to structural weight penalties.

Previous comparisons of transition-fixed and transition-free wind tunnel test data indicated that boundary layer transition movement with angle of attack had an effect on lift curve shape. Based on these observations, and the significance of the lift curve slope to wing structural weight, a systematic study of the effect of boundary layer transition fixing on the lift curve was conducted.
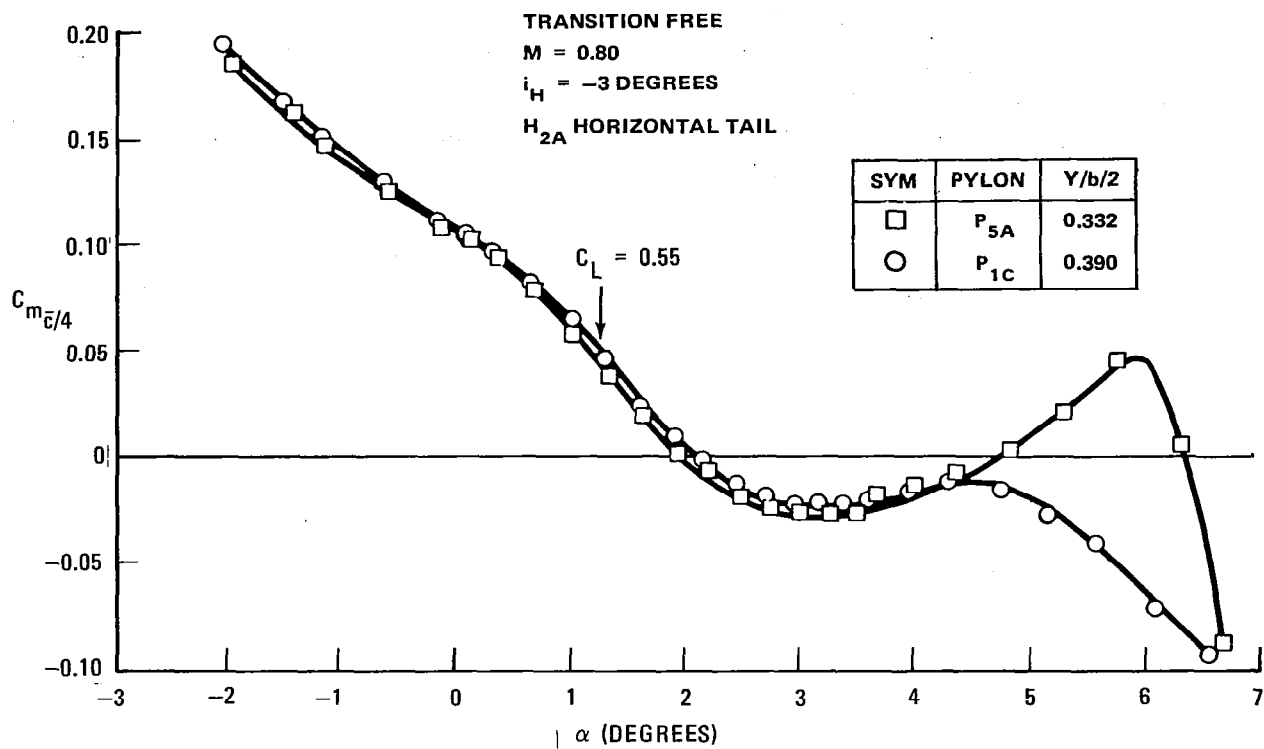
FIGURE 44. EFFECT OF NACELLE SPANWISE LOCATION ON TAIL-ON PITCHING MOMENT CHARACTERISTICS
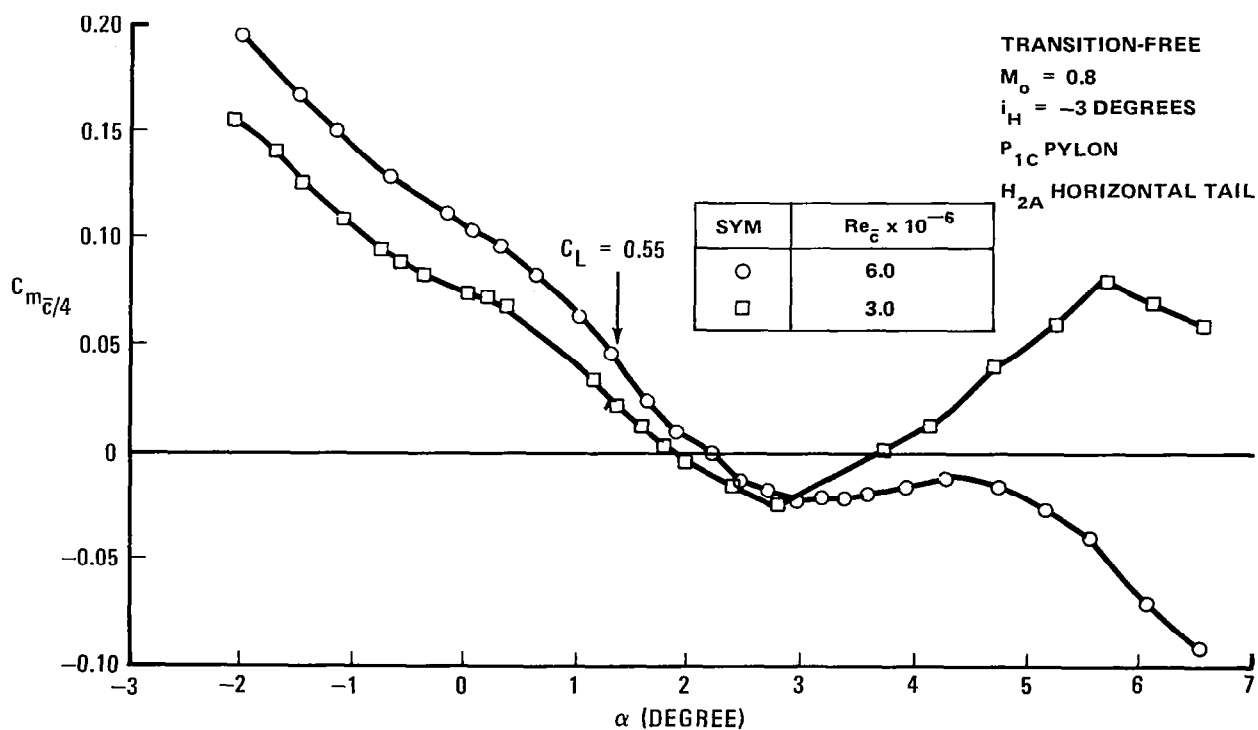
FIGURE 45. EFFECT OF REYNOLDS NUMBER ON CRUISE PITCHING MOMENT CHARACTERISTICS
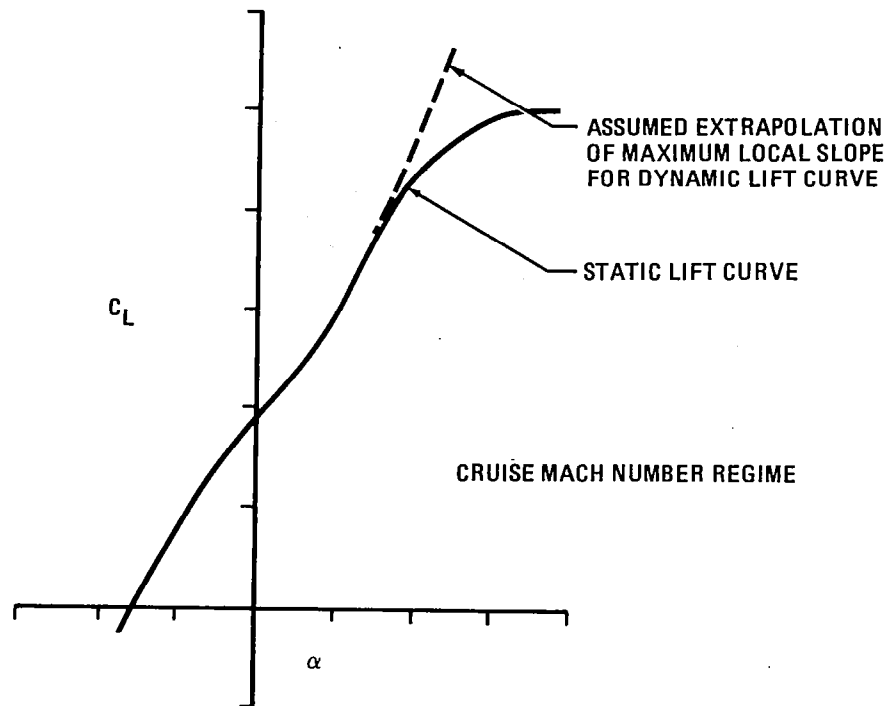
FIGURE 46. INTERACTION OF NONLINEAR STATIC LIFT CURVE AND DYNAMIC LIFT ANALYSIS

Four different boundary layer transition configurations were tested and analyzed to determine the effect of transition on the maximum local lift-curve slope. A composite plot of lift curves from all four transition patterns at 0.8 Mach number is shown in Figure 47. The T_1 configuration was transition-free. The T_5 configuration had transition fixed aft on the upper surface only. The T_6 configuration had transition fixed forward on the upper surface only. The T_7 configuration had the T_6 upper surface trip plus a lower surface trip. The trip patterns are illustrated on the planform sketch inset to the figure. The lift curve nonlinearity is particularly evident in the transition free (T_1) data. The transition-free lift curve has the highest local slope of nearly 0.18. All three transition-fixed results have a maximum local slope essentially 0.01 less than the transition-free data. Some lift-curve nonlinearity remains in all the transition-fixed data.
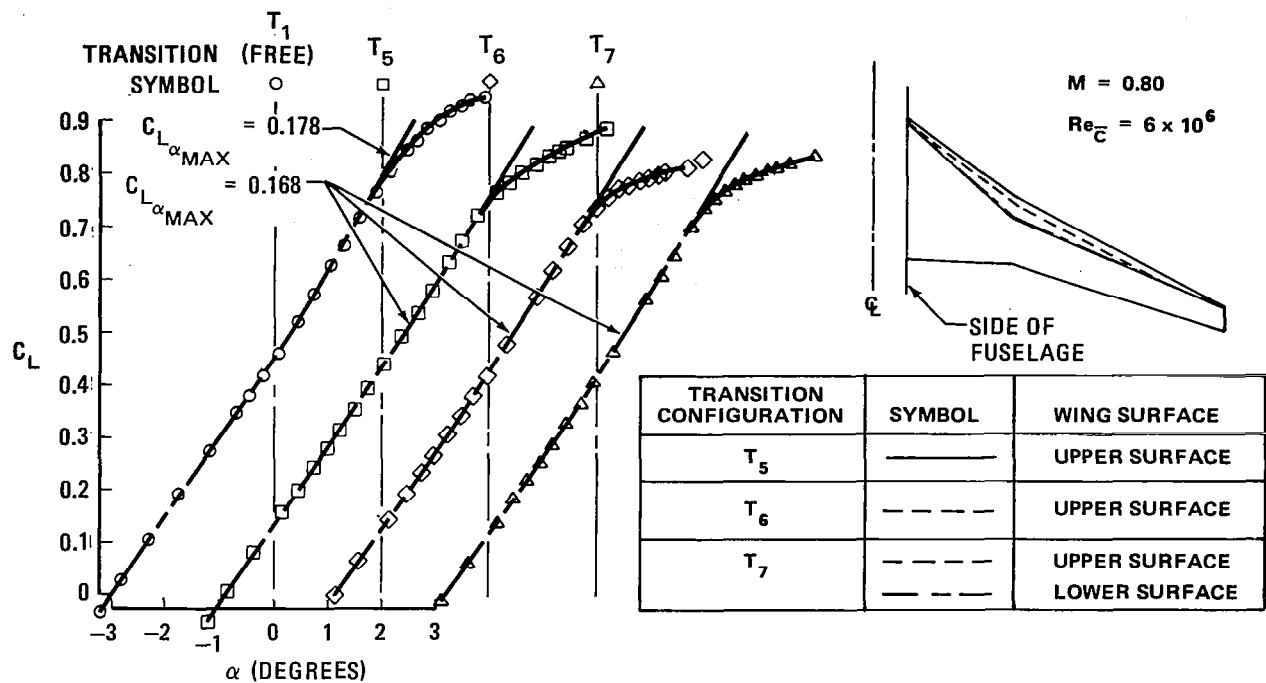
FIGURE 47. EFFECT OF BOUNDARY LAYER TRANSITION LOCATION ON MAXIMUM LOCAL LIFT CURVE SLOPE

Full scale Reynolds number characteristics would be more likely to resemble the transition-fixed lift curve data, because full scale transition, occurring naturally near the leading edge, does not move with angle of attack changes. This modest reduction in lift curve slope leads to lower gust loads and an attendant reduction in wing weight.

COMPARISON OF DATA WITH ESTIMATES

Wing surface pressure distributions calculated by the Douglas-Jameson program are compared to test data in Figures 48-55, for Mach numbers of 0.50, 0.75, 0.80, 0.82 and 0.84. Figures 50-53 compare results at M=0.80 for four lift coefficients. The subsonic (M=0.5) comparison is very good. As the Mach number was increased, the calculated pressures agreed quite well with the test data, although there were some discrepancies in the upper surface pressures, particularly at the 23 to 45 percent semispan stations. These discrepancies may be the result of approximate fuselage modelling or lack of spanwise mesh resolution in the planform break area.

The Douglas-Jameson program was also used to assess the drag and buffet characteristics of wing W_1. The calculated drag divergence and buffet boundaries are compared to the results derived from the test data in Figure 56. The drag divergence Mach number calculated in the cruise C_L range (circles) is in excellent agreement with the test data (squares). The buffet boundary was calculated utilizing a semi-empirical method which correlates shock location and strength with buffet onset. The comparison with transition-free test data analyzed with the lift-curve-break method is very good. The buffet C_L's at the cruise Mach number of 0.8 are within 0.03 of each other. The comparison is even better at the off-design Mach numbers.

Wing pitching moments calculated by the Douglas-Jameson program and wing pitching moments obtained from the test data by integration of the wing pressures have been analyzed. Comparisons of the calculated and experimental results at M=0.5 and M=0.8 are presented in Figure 57. The calculations fall within 0.01 in pitching moment coefficient of the test data over the entire range of lift coefficients evaluated, and at both Mach numbers the slopes of the curves accurately match the test data.
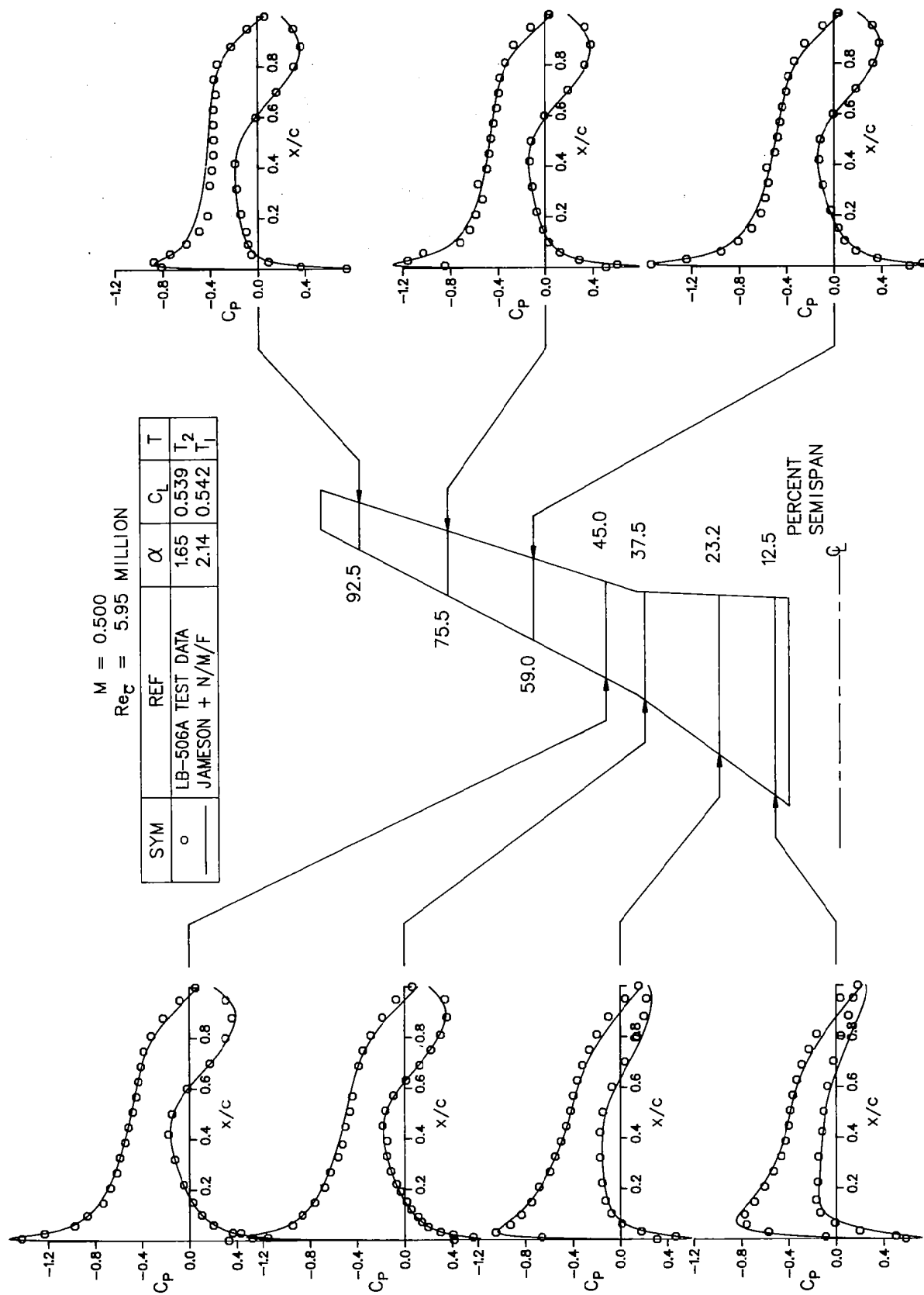
FIGURE 48. COMPARISON OF CALCULATED AND EXPERIMENTAL CHORDWISE PRESSURE DISTRIBUTIONS
M = 0.50, C_L = 0.54

M = 0.500
$Re_{\overline{c}}$ = 5.95 MILLION

SYM	REF	α	C_L	T
o	LB-506A TEST DATA	1.65	0.539	T_2
—	JAMESON + N/M/F	2.14	0.542	T_1

92.5
75.5
59.0
45.0
37.5
23.2
12.5

PERCENT SEMISPAN

68

SYM	REF	α	C_L	T
$\Box$	LB-506A TEST DATA	0.97	0.546	T_2
——	JAMESON + N/M/F	1.28	0.545	T_J

M = 0.750
$Re_{\bar{c}}$ = 5.95 MILLION
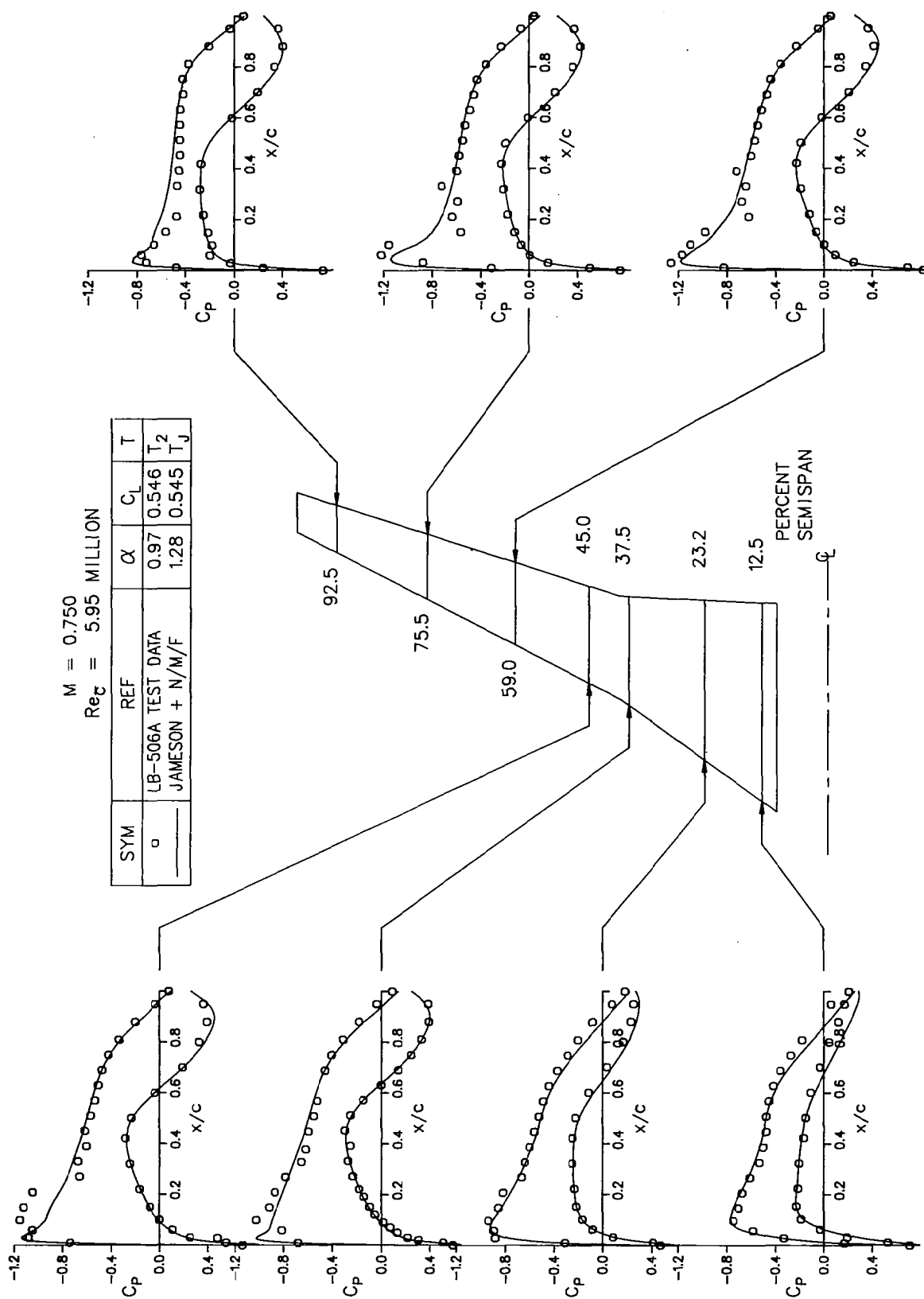
FIGURE 49. COMPARISON OF CALCULATED AND EXPERIMENTAL CHORDWISE PRESSURE DISTRIBUTIONS
M = 0.75, C_L = 0.55

69
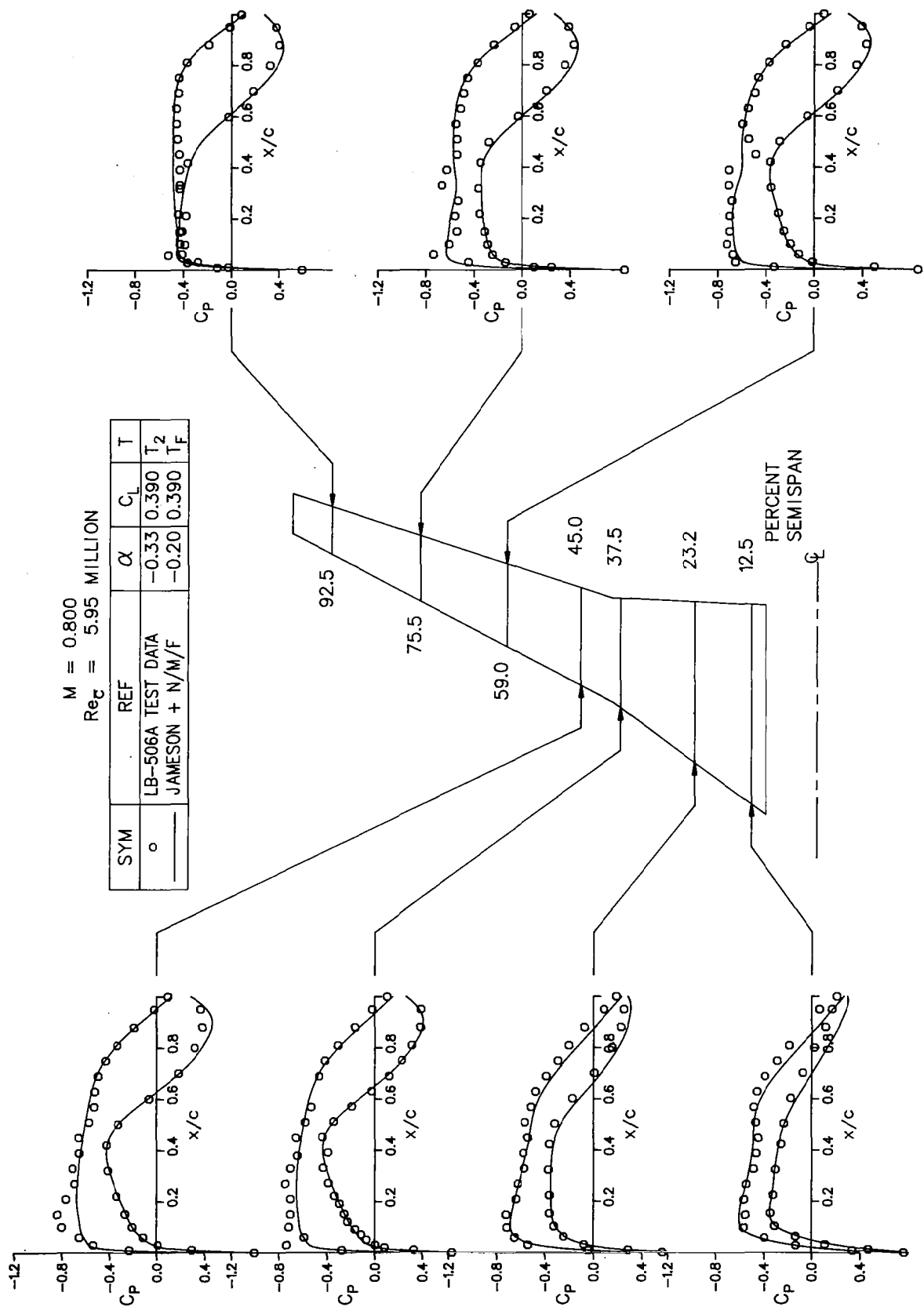
M = 0.800
$Re_{\bar{c}}$ = 5.95 MILLION

SYM	REF	α	C_L	T
o	LB-506A TEST DATA	-0.33	0.390	T_2
—	JAMESON + N/M/F	-0.20	0.390	T_F

92.5

75.5

59.0

45.0

37.5

23.2

12.5

PERCENT
SEMISPAN

C_P

x/c

FIGURE 50. COMPARISON OF CALCULATED AND EXPERIMENTAL CHORDWISE PRESSURE DISTRIBUTIONS
M = 0.80, C_L = 0.39

70

M = 0.800
$Re_{\overline{c}}$ = 5.95 MILLION

SYM	REF	α	C_L	T
o	LB-506A TEST DATA	0.65	0.550	T_2
—	JAMESON + N/M/F	0.92	0.549	T_D

92.5
75.5
59.0
45.0
37.5
23.2
12.5

PERCENT
SEMISPAN
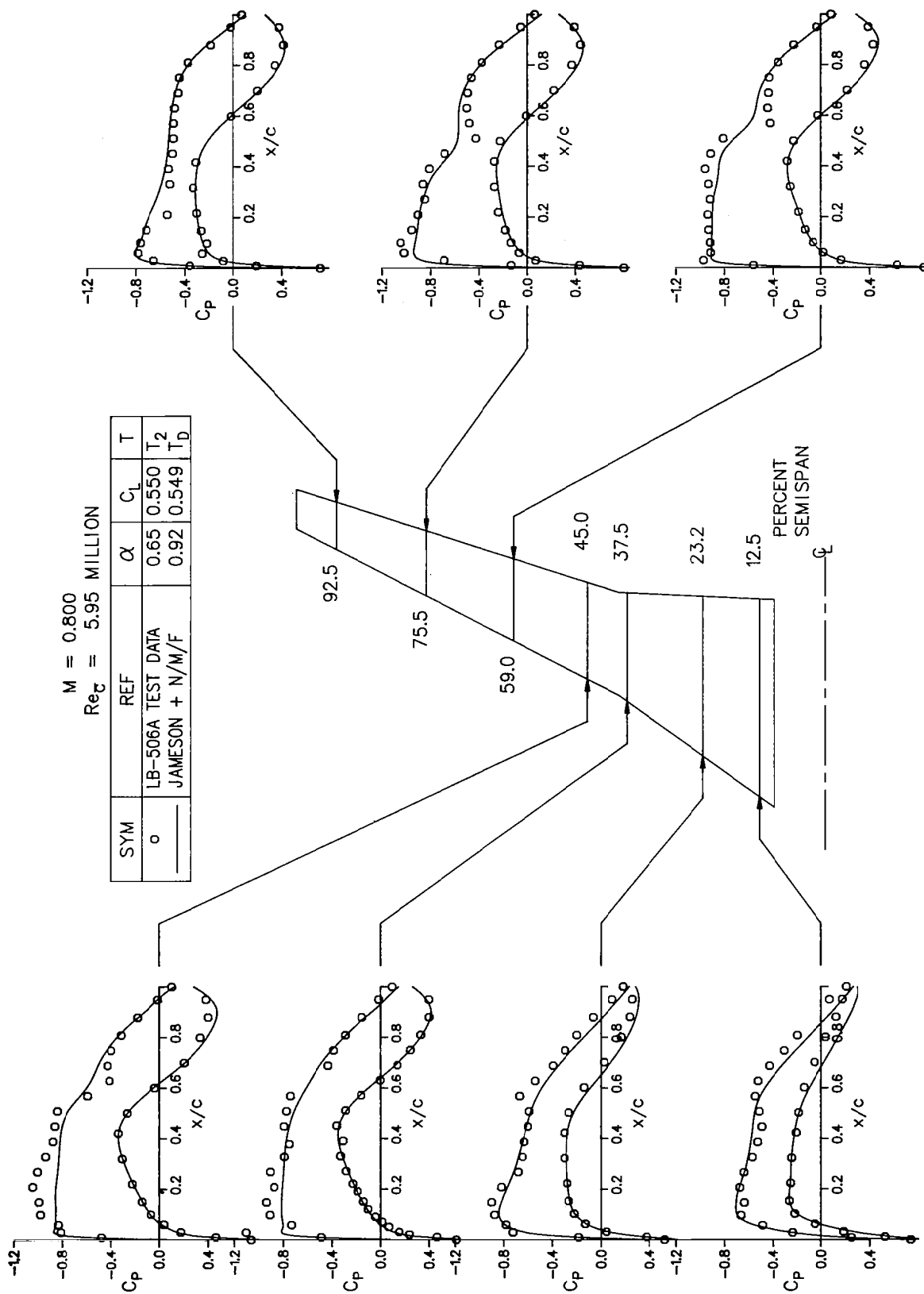
FIGURE 51. COMPARISON OF CALCULATED AND EXPERIMENTAL CHORDWISE PRESSURE DISTRIBUTIONS
M = 0.80, C_L = 0.55
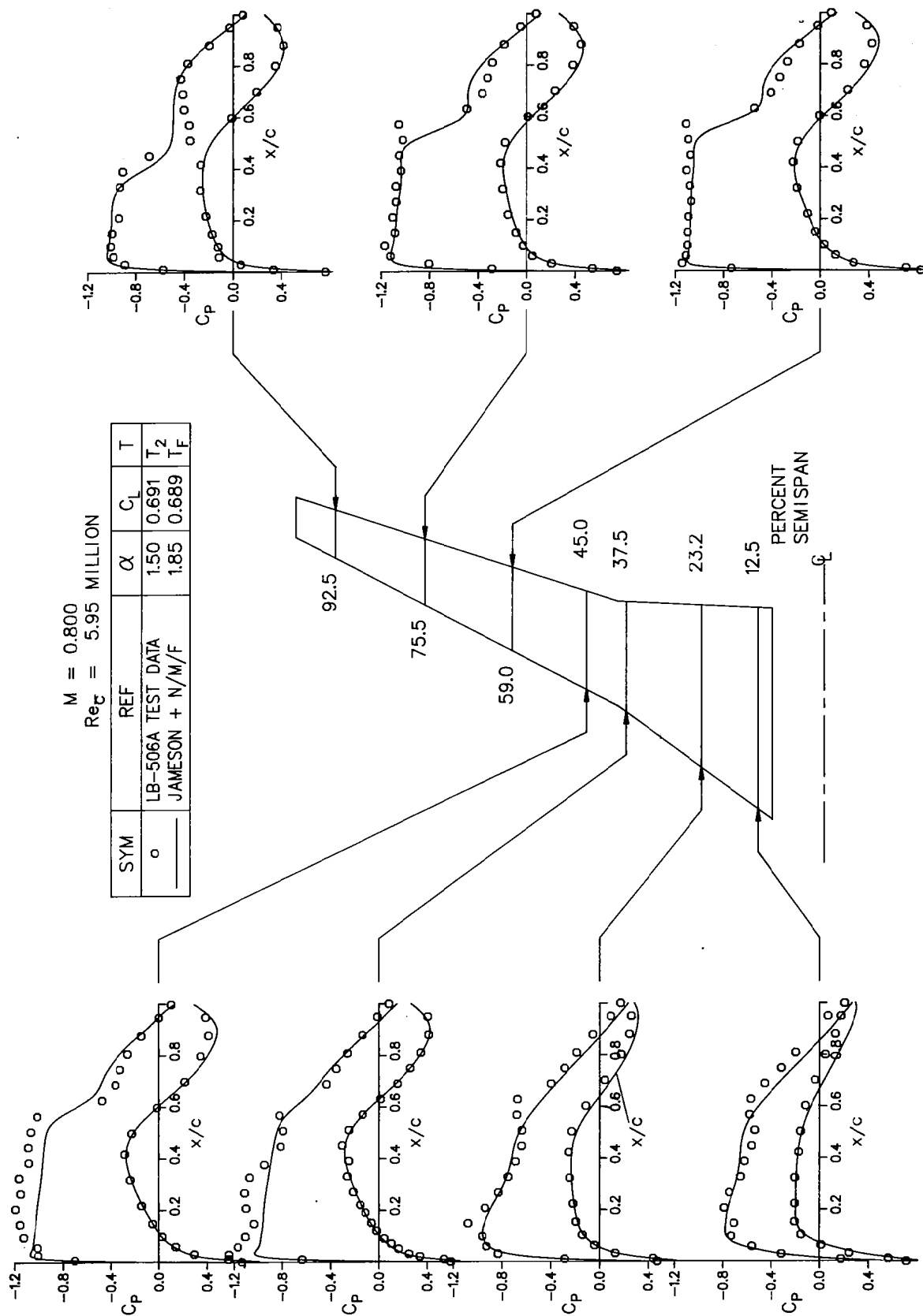
FIGURE 52. COMPARISON OF CALCULATED AND EXPERIMENTAL CHORDWISE PRESSURE DISTRIBUTIONS

M = 0.80, C_L = 0.69

M = 0.800
Re_c = 5.95 MILLION

SYM	REF	α	C_L	T
o	LB-506A TEST DATA	1.50	0.691	T_2
——	JAMESON + N/M/F	1.85	0.689	T_F

72
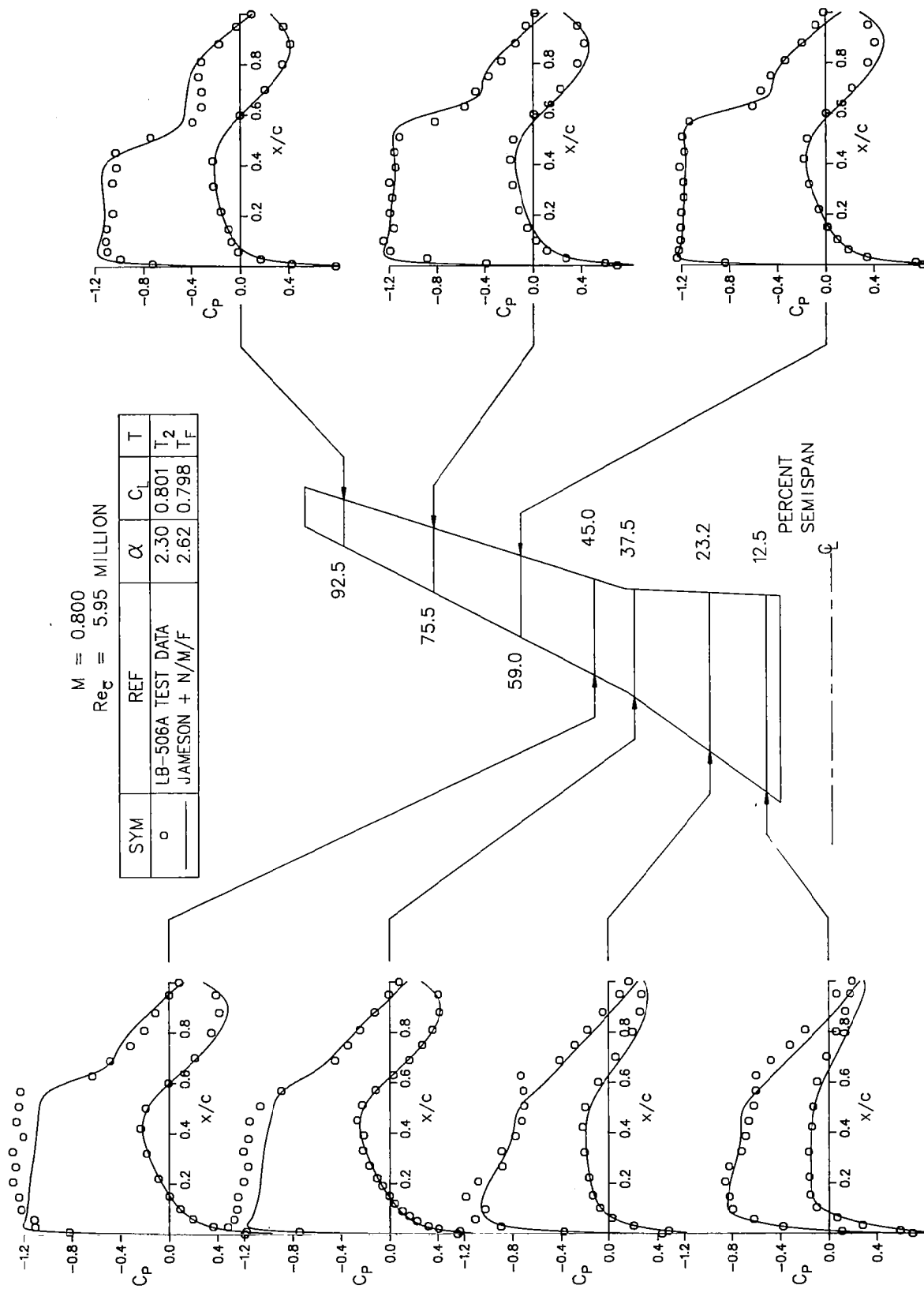
FIGURE 53. COMPARISON OF CALCULATED AND EXPERIMENTAL CHORDWISE PRESSURE DISTRIBUTIONS
M = 0.80, C_L = 0.80

M = 0.800
Re_c = 5.95 MILLION

SYM	REF	α	C_L	T
o	LB−506A TEST DATA	2.30	0.801	T_2
	JAMESON + N/M/F	2.62	0.798	T_F
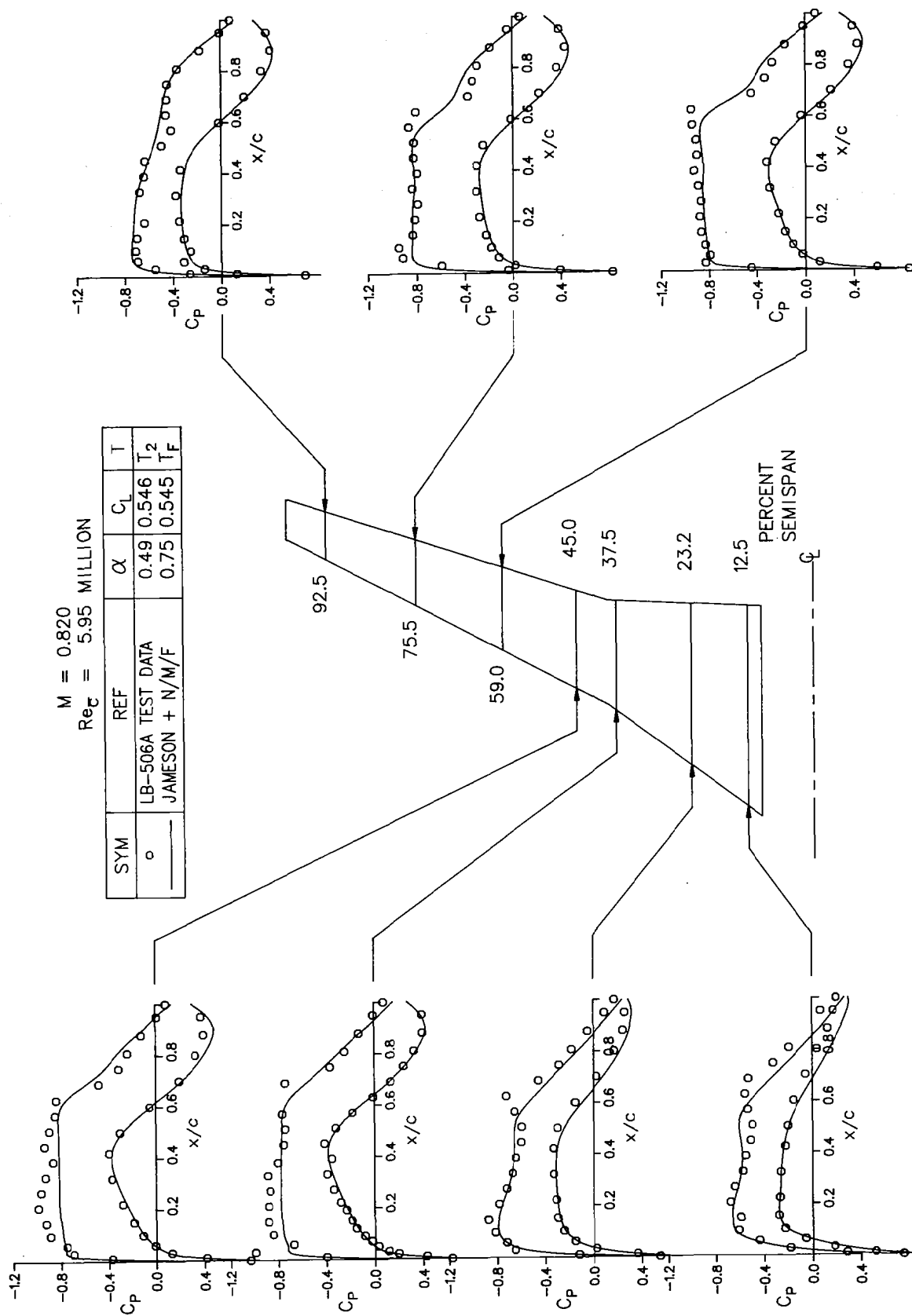
FIGURE 54. COMPARISON OF CALCULATED AND EXPERIMENTAL CHORDWISE PRESSURE DISTRIBUTIONS
M = 0.82, C_L = 0.55

M = 0.820
$Re_{\bar{c}}$ = 5.95 MILLION

SYM	REF	α	C_L	T
o	LB-506A TEST DATA	0.49	0.546	T_2
—	JAMESON + N/M/F	0.75	0.545	T_F
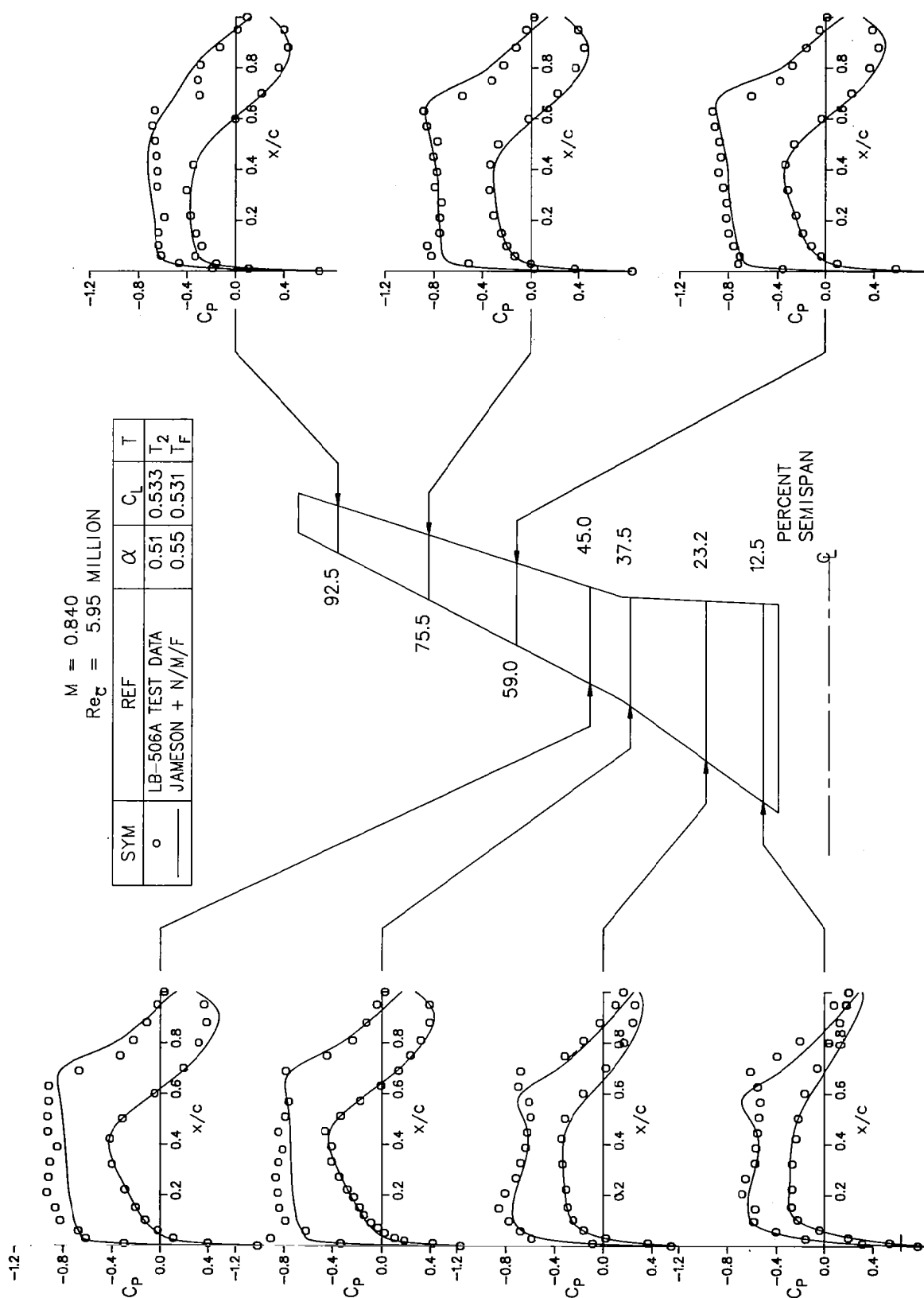
FIGURE 55. COMPARISON OF CALCULATED AND EXPERIMENTAL CHORDWISE PRESSURE DISTRIBUTIONS
M = 0.84, C_L = 0.53

M = 0.840
Re_c = 5.95 MILLION

SYM	REF	α	C_L	T
o	LB-506A TEST DATA	0.51	0.533	T_2
	JAMESON + N/M/F	0.55	0.531	T_F

75

C_L

SYM	SOURCE
O	CALCULATED (JAMESON)
☐	LB-506 TEST DATA
	(C_{L_α} BREAK METHOD FOR BUFFET)

BUFFET BOUNDARY
(TRANSITION-FREE)

DRAG
DIVERGENCE
(TRANSITION-FIXED)

MACH NUMBER
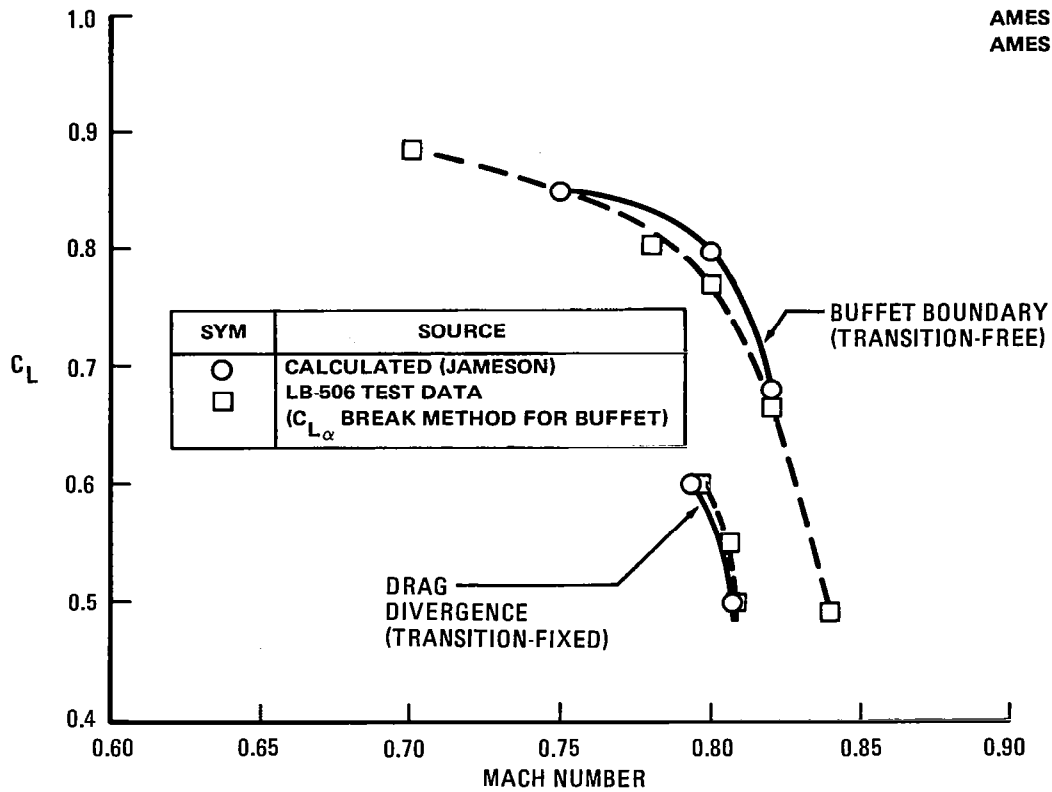
FIGURE 56. COMPARISON OF CALCULATED AND EXPERIMENTAL HIGH-SPEED BUFFET AND DRAG DIVERGENCE BOUNDARIES

TRANSITION FIXED (T_2)

SYM	REFERENCE
O	LB-506A INTEGRATED PRESSURE DATA
——	DOUGLAS-JAMESON PROGRAM

$C_{L_{WING/BODY}}$

M = 0.50

M = 0.80
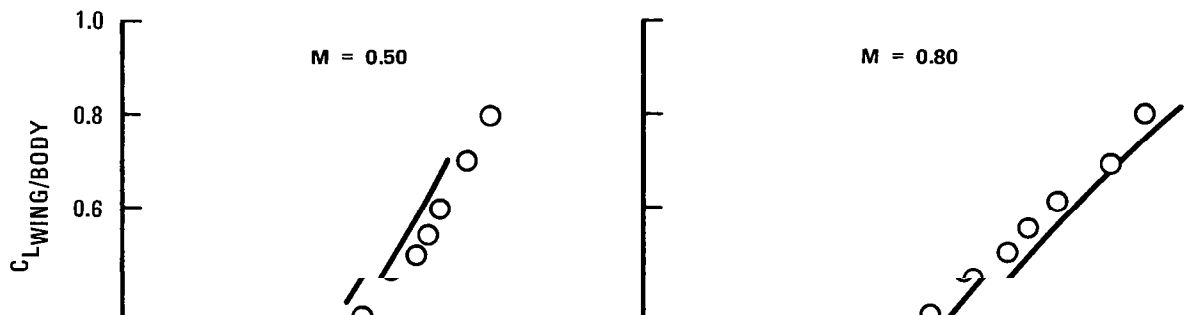
The complete, clean wing/body model configuration on its sting mount was panelled for the Douglas-Neumann panel method. The wing included a frozen boundary layer displacement thickness. The panel representation is shown in Figure 58. An alternate panelling was generated to represent the "free-air," sting-off configuration. Both geometries were analyzed at zero Mach number (no compressibility effects). The contribution to the configuration pitching moment due to the fuselage is compared to test data in Figure 59. The solid line represents the sting-on results and the dashed line the sting-off results. The difference between them is the calculated effect of the sting on pitching moment, since it was found that the sting had negligible effect on the wing's moment contribution. The sting-on results show excellent agreement with the test data.

The effect of the nacelles on the pitching moment was evaluated by panelling the wing alone, with and without the nacelles and baseline pylons. The calculated and measured results are compared in Figure 60. The agreement with the measured data is very good, considering the lack of viscous and compressibility effects in this analysis.
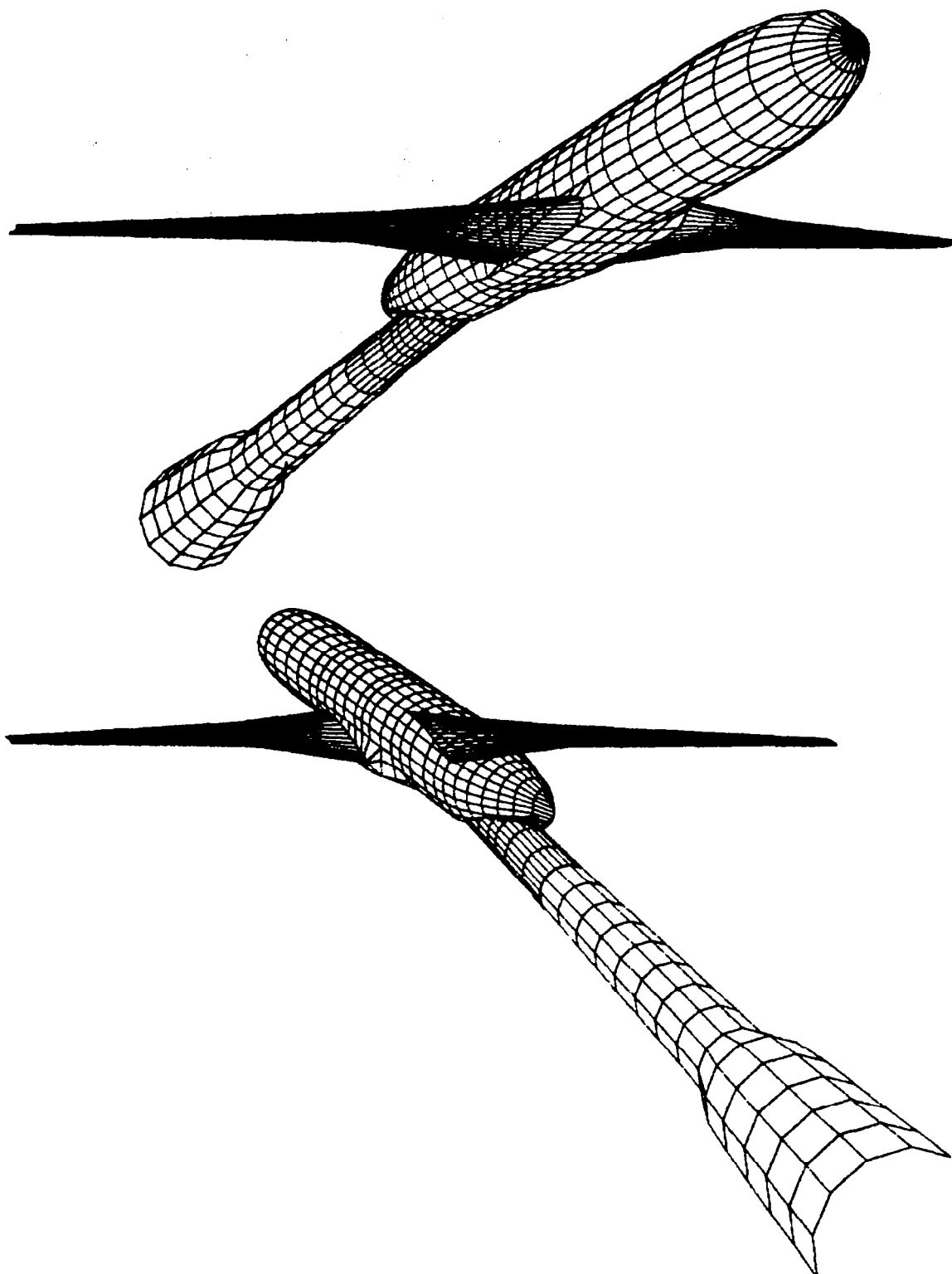
FIGURE 58. PANEL REPRESENTATION OF STING-MOUNTED WIND TUNNEL MODEL

78
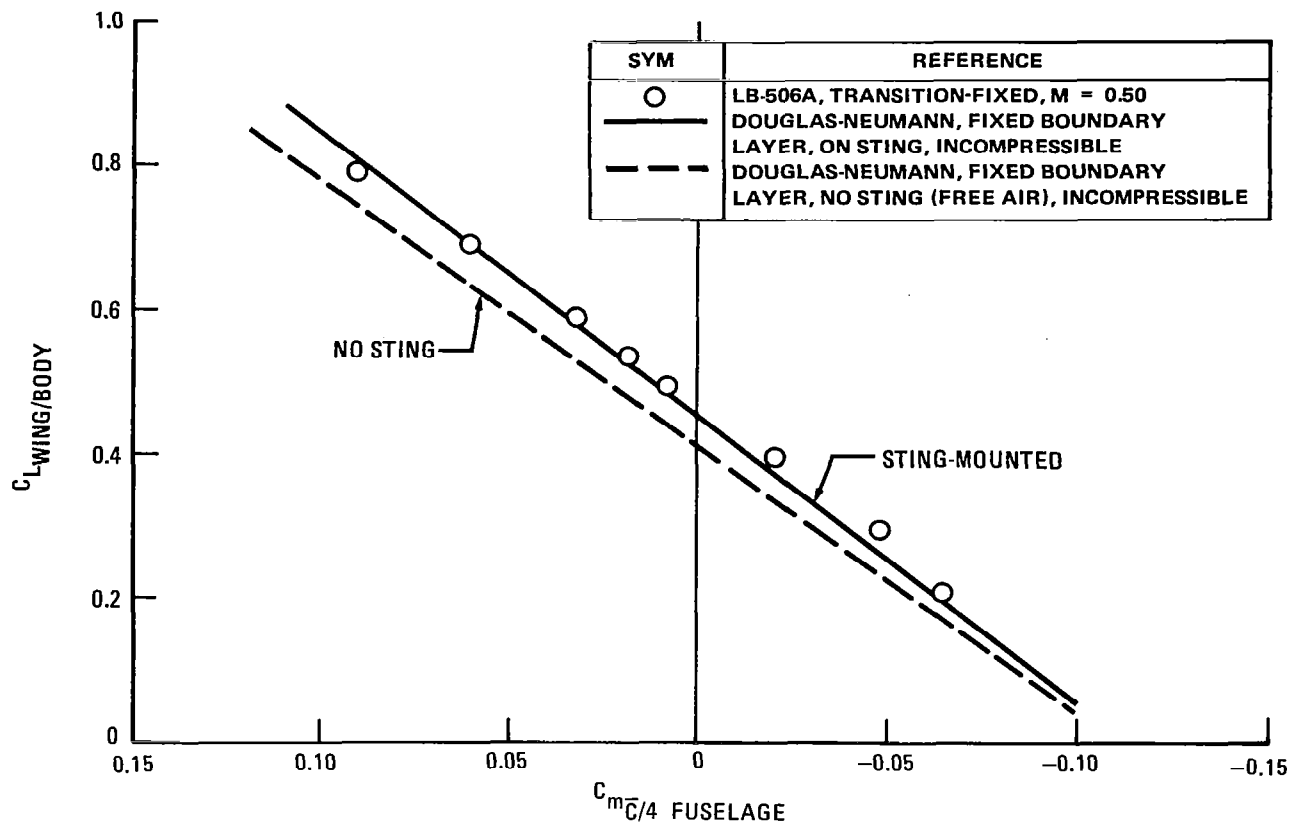
FIGURE 59. COMPARISON OF CALCULATED AND EXPERIMENTAL FUSELAGE CONTRIBUTION
TO WING/BODY PITCHING MOMENT
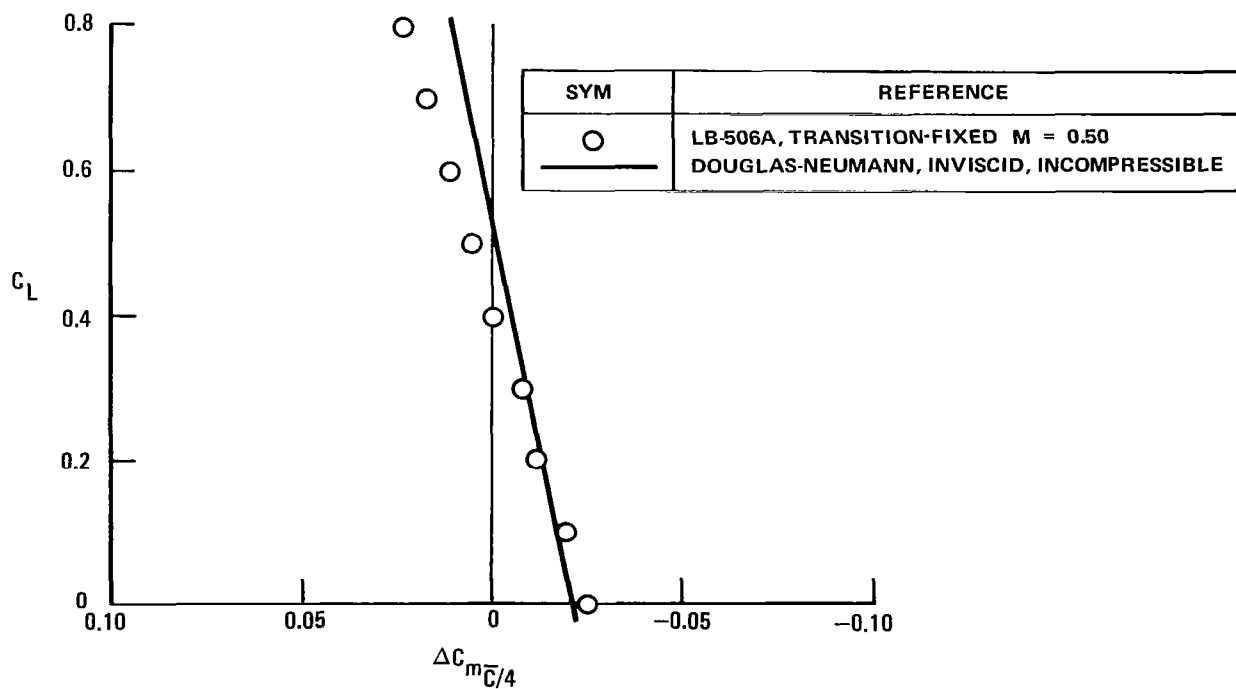
FIGURE 60. COMPARISON OF CALCULATED AND EXPERIMENTAL PITCHING MOMENT INCREMENTS
DUE TO NACELLES AND PYLONS, P_{1C}/N_{1C}

CONCLUSIONS AND RECOMMENDATIONS

Conclusions

Design studies and wind tunnel tests of a high-aspect-ratio, supercritical wing suitable for a fuel-efficient, medium-range, narrow-body transport have been completed. The wing gross characteristics such as aspect ratio, sweep, and average thickness were derived from comprehensive systems studies. The wing-aerodynamic design was developed to achieve cruise drag, buffet boundary, and off-design performance goals. This aerodynamic development was accomplished through application of previous wind tunnel test results and advanced computational procedures. The following conclusions are drawn from the analysis of the test data:

(1) The high-speed drag characteristics of the high-aspect-ratio, super-critical wing design were as good as, or slightly better than predicted. In particular, the drag divergence Mach number was slightly higher than the design Mach number and the level of premature drag creep was substantially reduced when compared to previous Douglas designs.

(2) The effect of nacelle position on nacelle/pylon drag increment was investigated. The longitudinal position was found to have the largest impact on the drag increment. The baseline nacelle position (fan exit 25 percent chord ahead of the wing leading edge) had a drag increment very close to the calculated parasite drag of the isolated nacelle and pylon at the design Mach number (0.80) and lift coefficient (0.55). Substantial interference penalties were measured for nacelle positions further aft than the baseline position. In the cruise condition these penalties were as large as fifteen drag counts or approximately five percent of aircraft drag. The nacelle vertical and spanwise position changes caused only small drag effects.

(3) The effect of flap linkage fairings was found to be typical of previous configurations. The measured drag increments suggest that small reductions of the installation drag might be achieved with careful configuration development.

(4) The complete configuration buffet boundary characteristics were quite good. At the design Mach number of 0.8 the indicated buffet C_L was in excess of 0.8. This level of C_L provides a comfortable 1.45-g margin to buffet from the 0.55 design C_L.

(5) The basic configuration tail-on high-speed pitch characteristics exhibited an undesirable pitch-up at post-buffet lift coefficients. The effects of the horizontal tail configuration, the spanwise nacelle position, and the test Reynolds number on the pitch-up tendency were all evaluated. All three variations had a significant effect on the high-speed pitch-up. The largest effect was found to be due to Reynolds number. As Reynolds number was increased a considerable improvement in the pitch-up was obtained.

(6) Lift curve nonlinearity can have an impact on wing structural weight. The effect of boundary layer transition on the maximum lift curve nonlinearity was evaluated using different boundary layer transition strip configurations. Fixing transition provided a significant reduction in the maximum local lift curve slope when compared to transition-free. However, the location of the trip was found to have little effect on the lift curve slope. Only part of the lift curve nonlinearity is associated with transition movement. Part of the nonlinearity remained in the transition-fixed results.

Recommendations

Three areas worthy of further investigation have been identified during the course of this Phase II effort. These areas are the development of acceptable high-speed pitch characteristics, the reduction of nacelle/pylon interference for configurations with the nacelle close to the wing, and the development of a more fundamental understanding of dynamic lift effects in 3-D transonic flows. Each of these areas can have a significant influence on the application of high-aspect-ratio supercritical wing technology to a fuel-efficient transport design.

REFERENCES

1. Mechtly, E.A.: The International System of Units - Physical Constants and Conversion Factors. NASA SP-7012, 1973.

2. Steckel, D.K.; Dahlin, J.A.; and Henne, P.A.: Results of Design Studies and Wind Tunnel Tests of High-Aspect-Ratio Supercritical Wings for an Energy Efficient Transport. NASA CR-159332, 1980.

3. Bauer, F.; Garabedian, P.R.; and Korn, D.G.: Supercritical Wing Sections. Springer-Verlag, New York, 1972.

4. Tranen, T.L.: A Rapid Computer-Aided Transonic Airfoil Design Method. AIAA Paper No. 74-501, 1974.

5. Jameson, A.; and Caughey, D.A.: Numerical Calculation of the Transonic Flow Past a Swept Wing. NASA CR-153297, 1977.

6. Henne, P.A.: An Inverse Transonic Wing Design Method. AIAA Paper No. 80-0330, 1980.

APPENDIX

PLOTTED FORCE AND MOMENT DATA
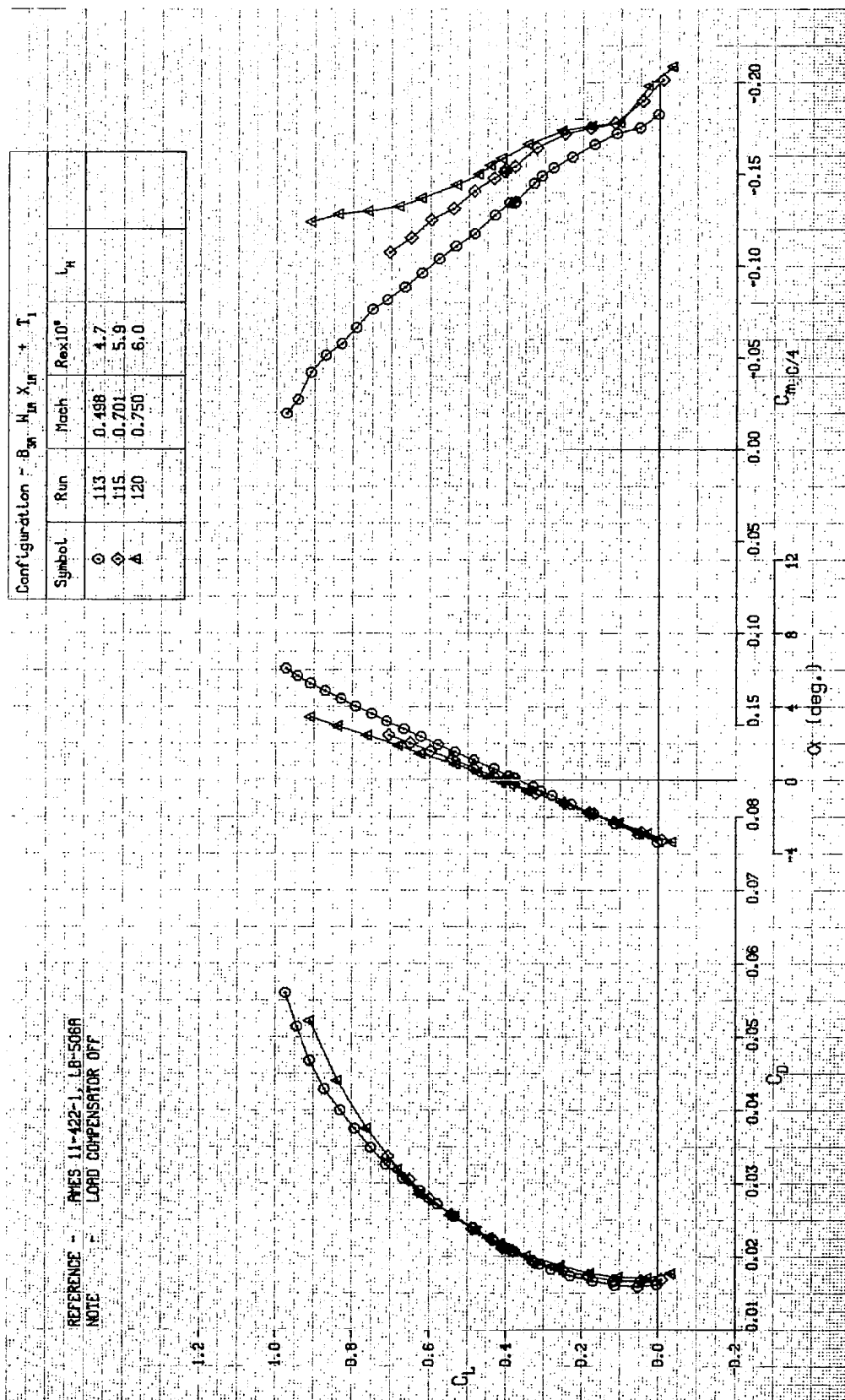
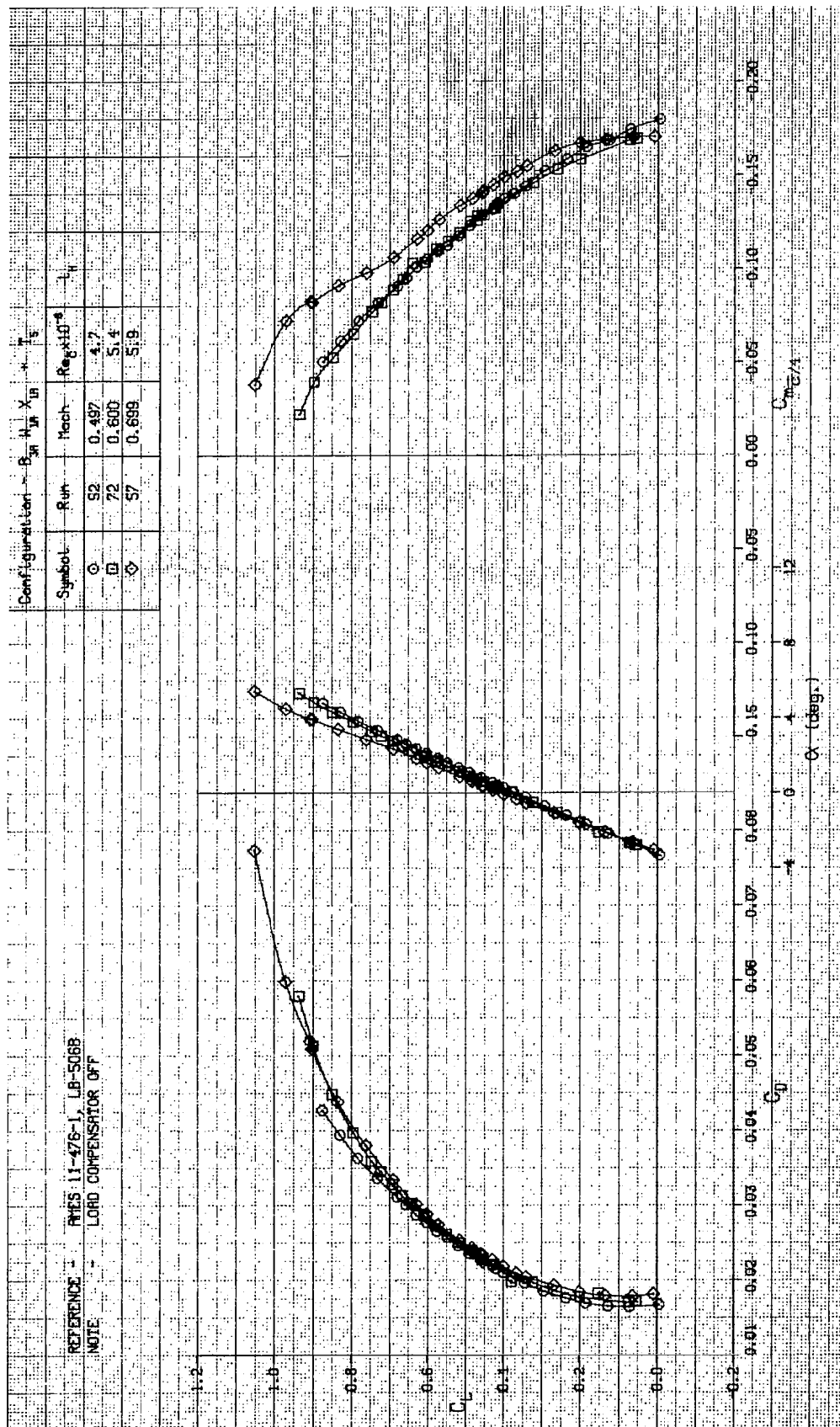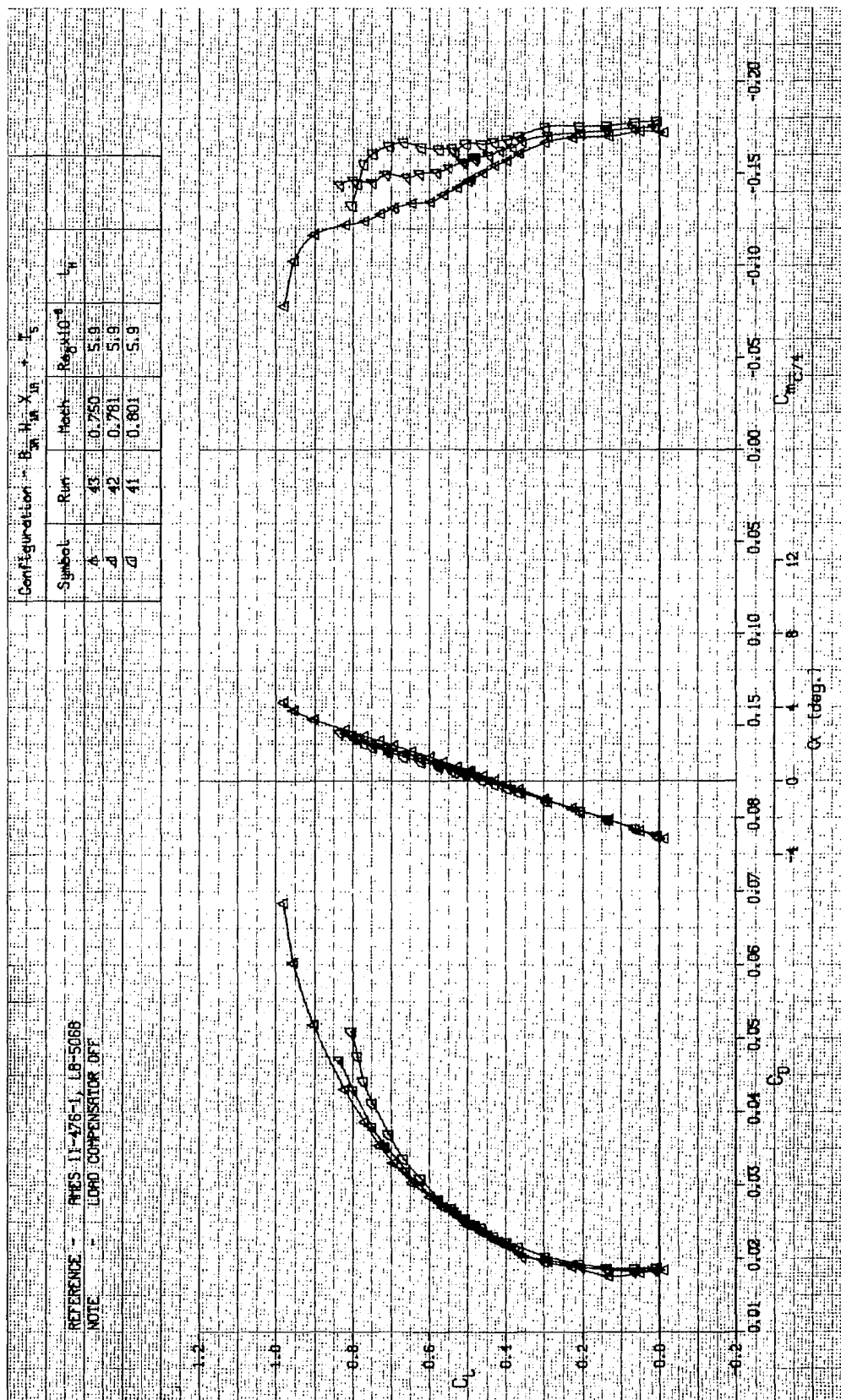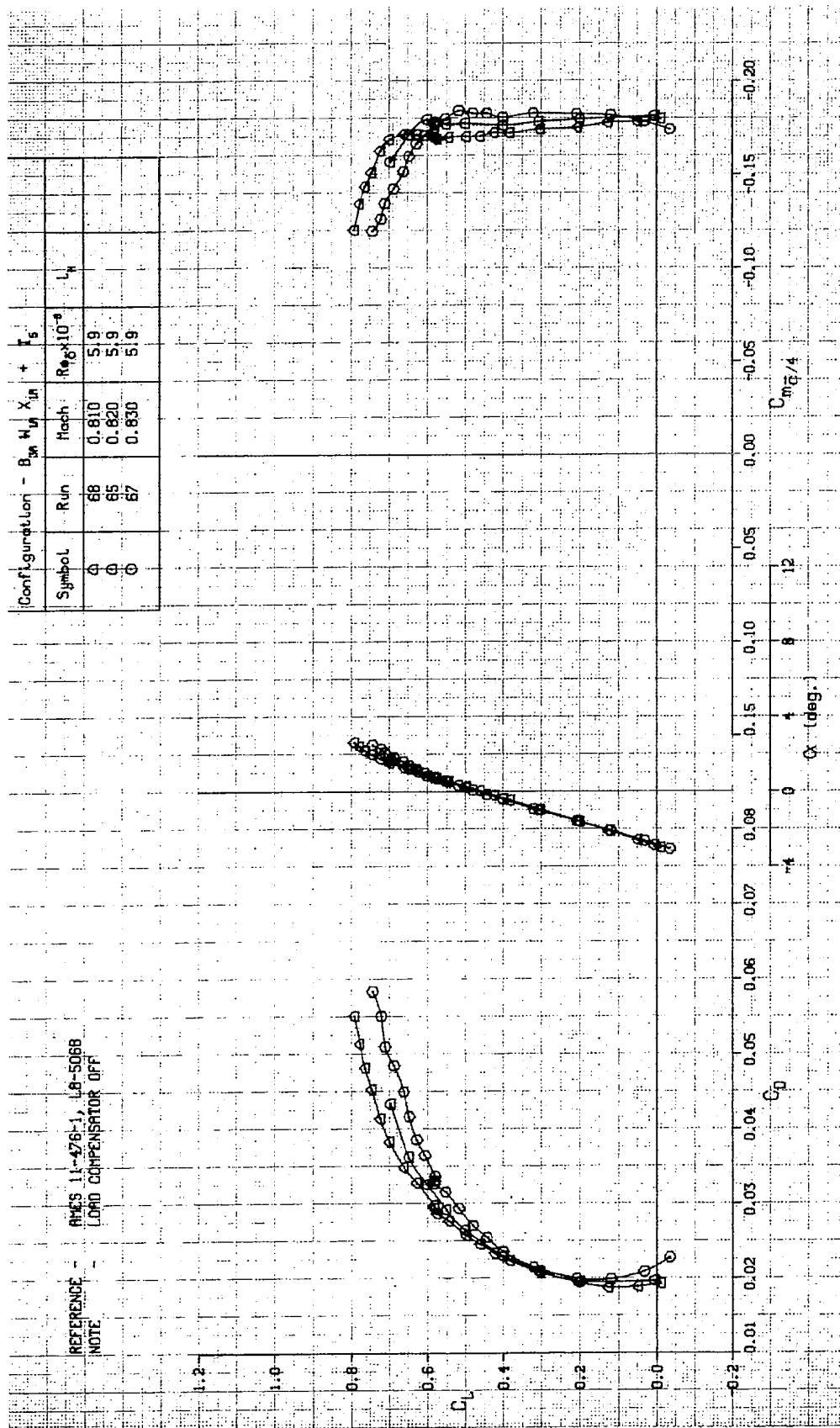FIGURE A-1.   LIFT, DRAG, AND PITCHING MOMENT CHARACTERISTICS OF WING W_1, TRANSITION FREE

A-1
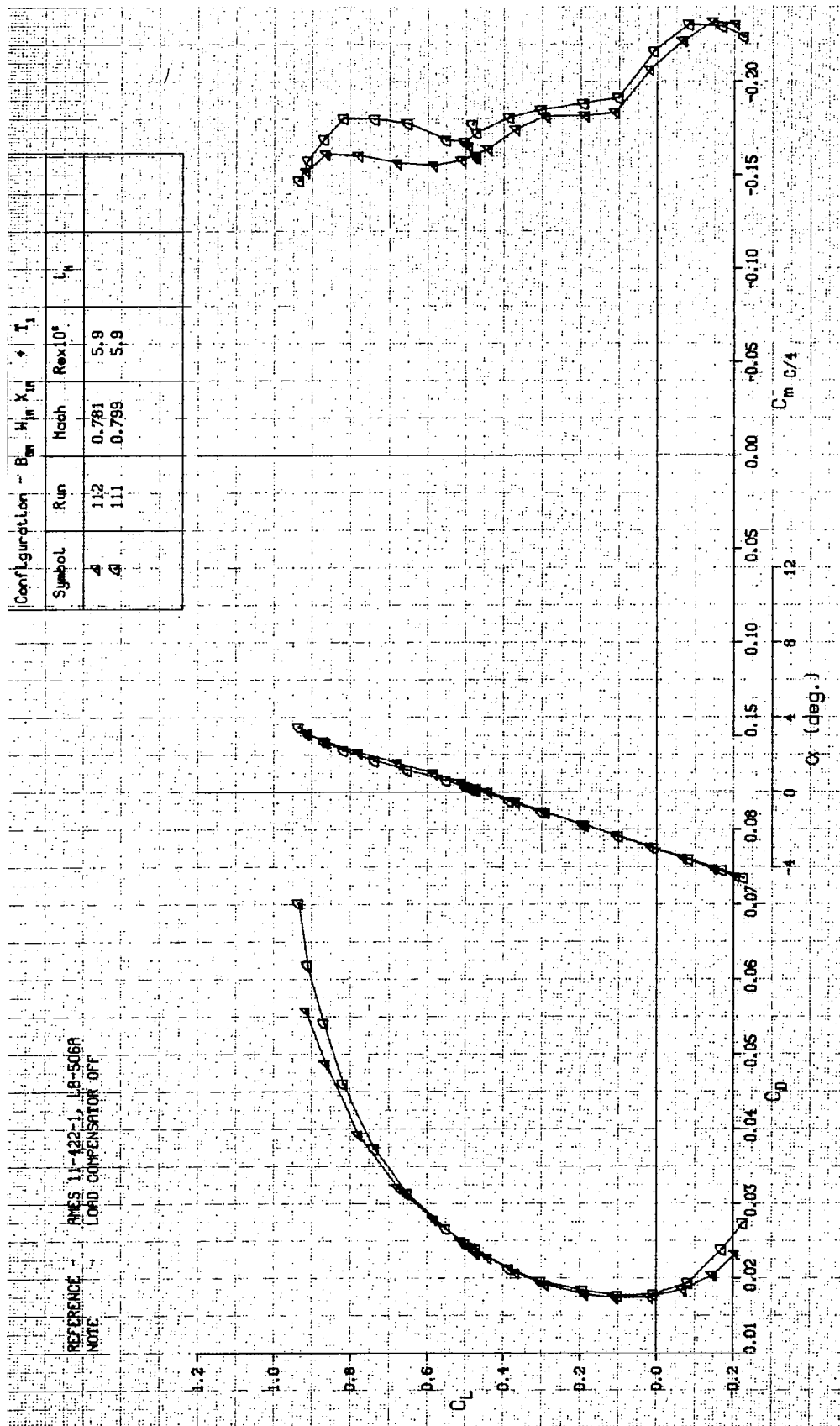
FIGURE A-2. LIFT, DRAG, AND PITCHING MOMENT CHARACTERISTICS OF WING W_1, TRANSITION FREE
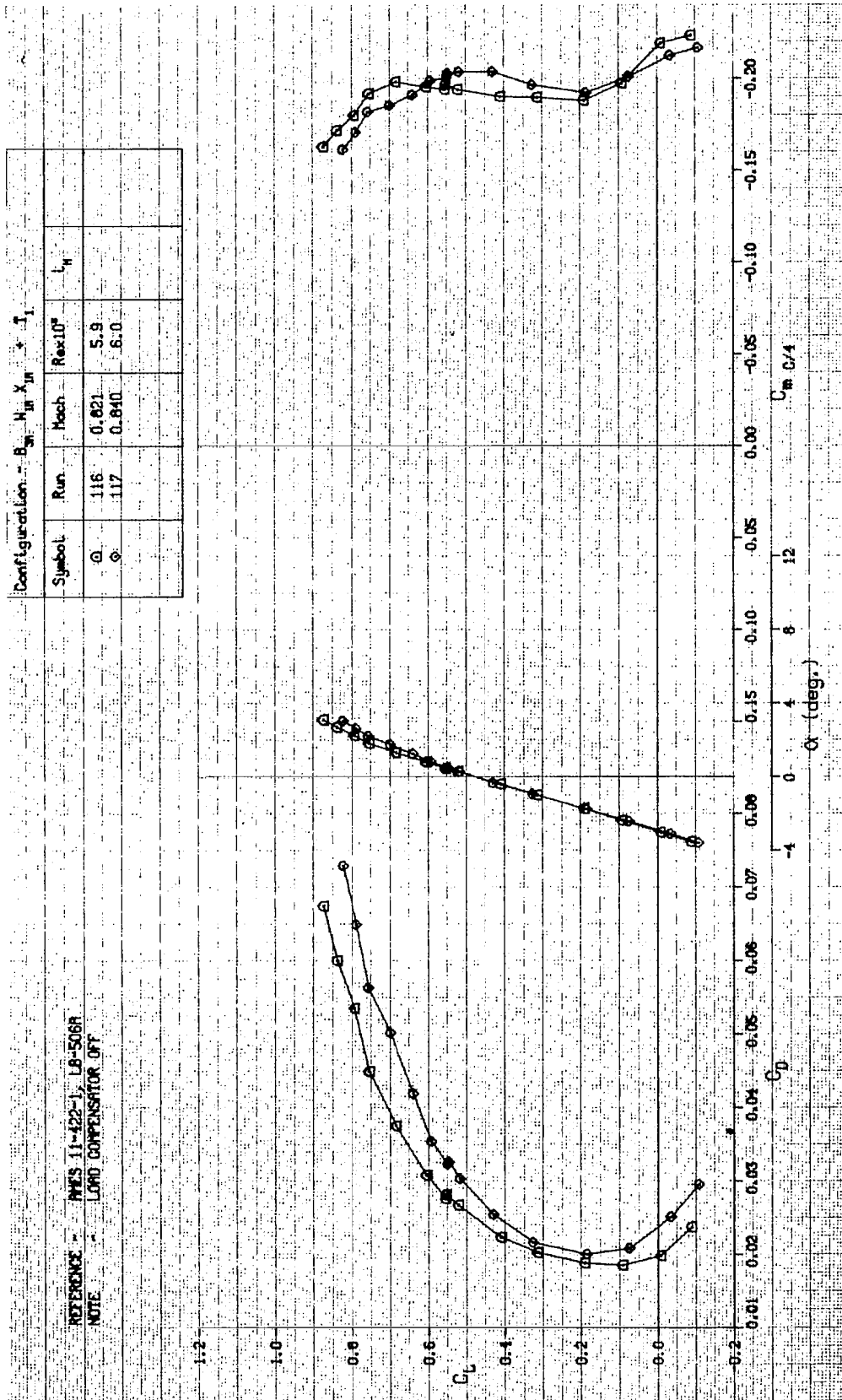
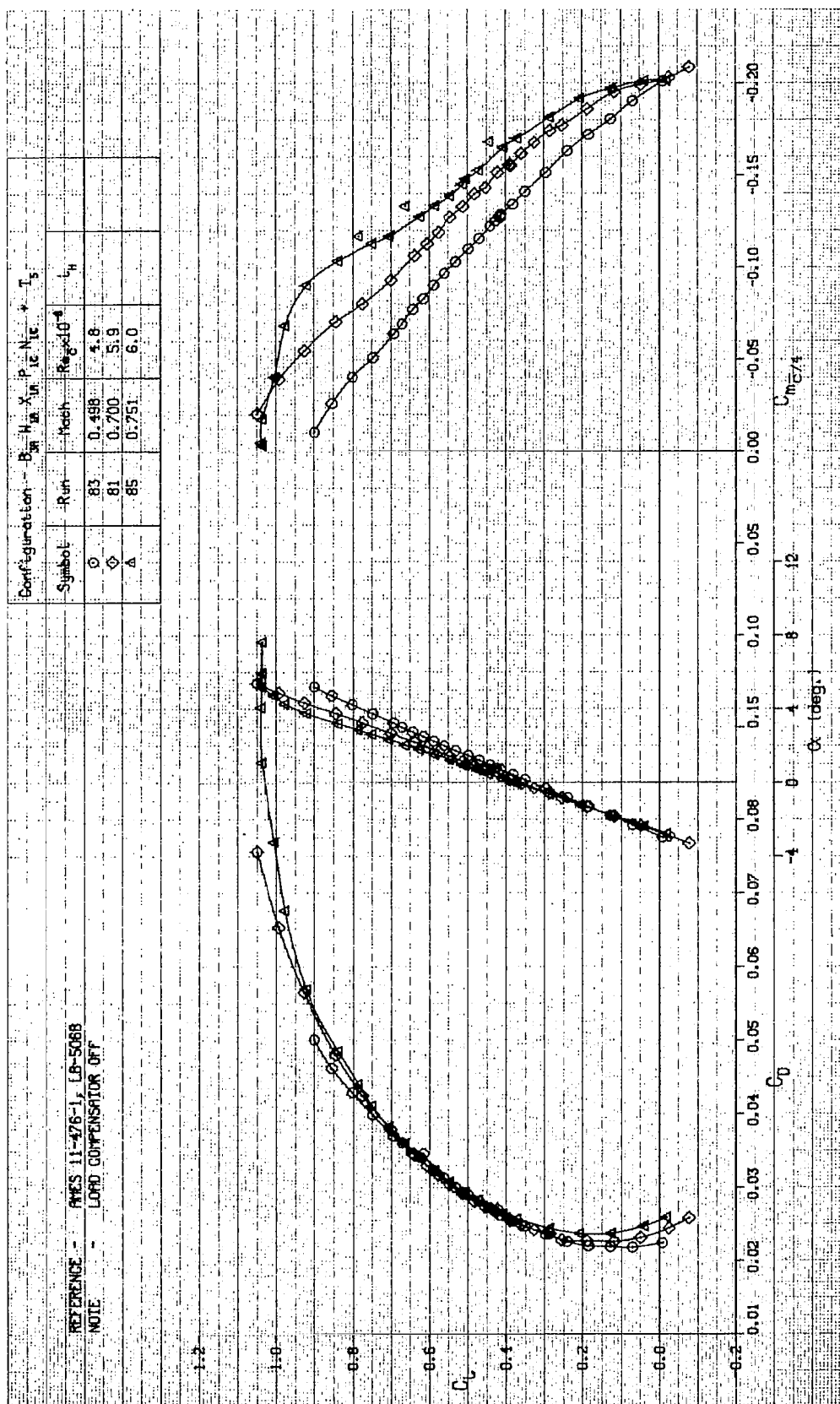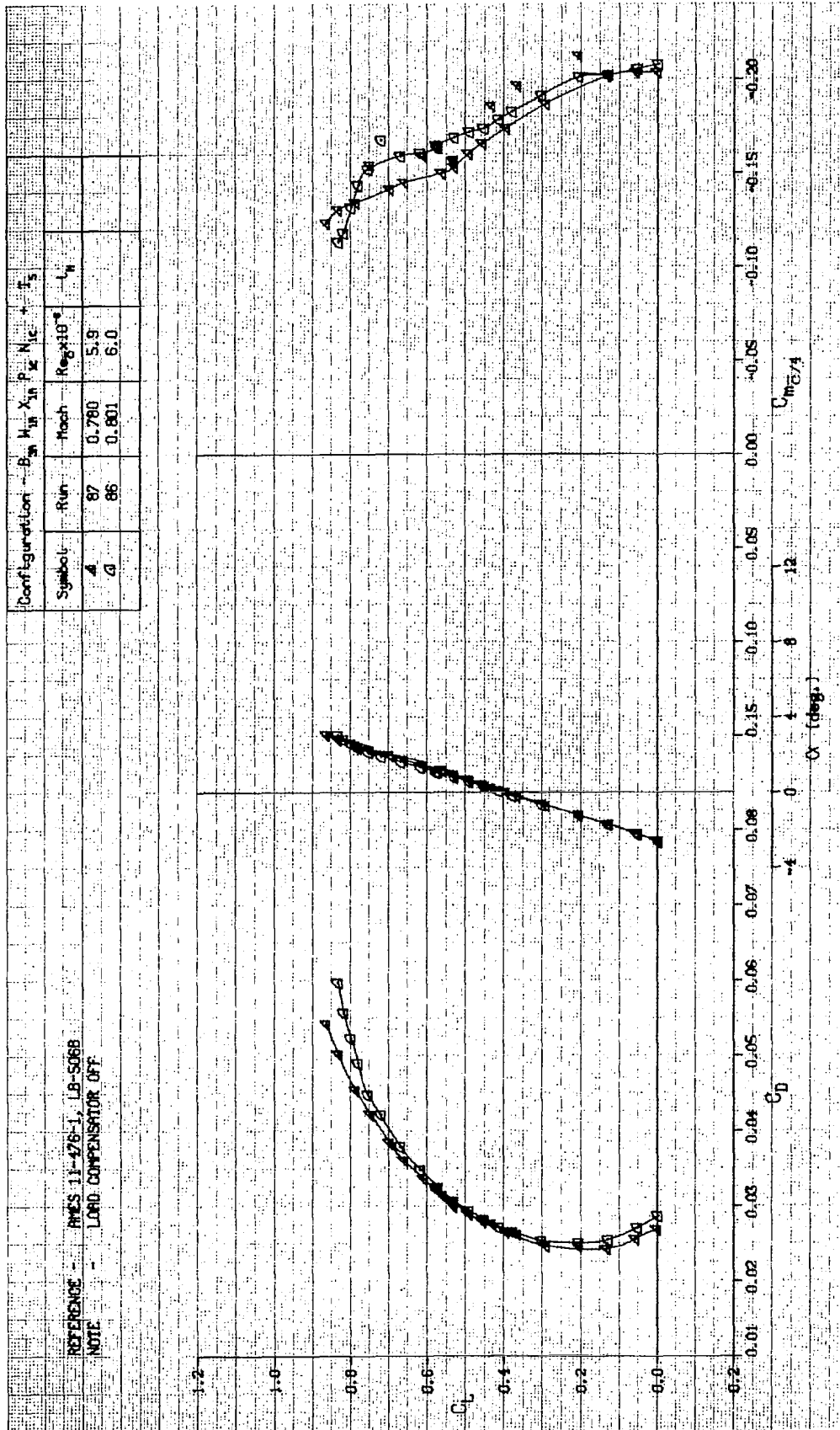FIGURE A-3. LIFT, DRAG, AND PITCHING MOMENT CHARACTERISTICS OF WING W_1, TRANSITION FREE.

A-3
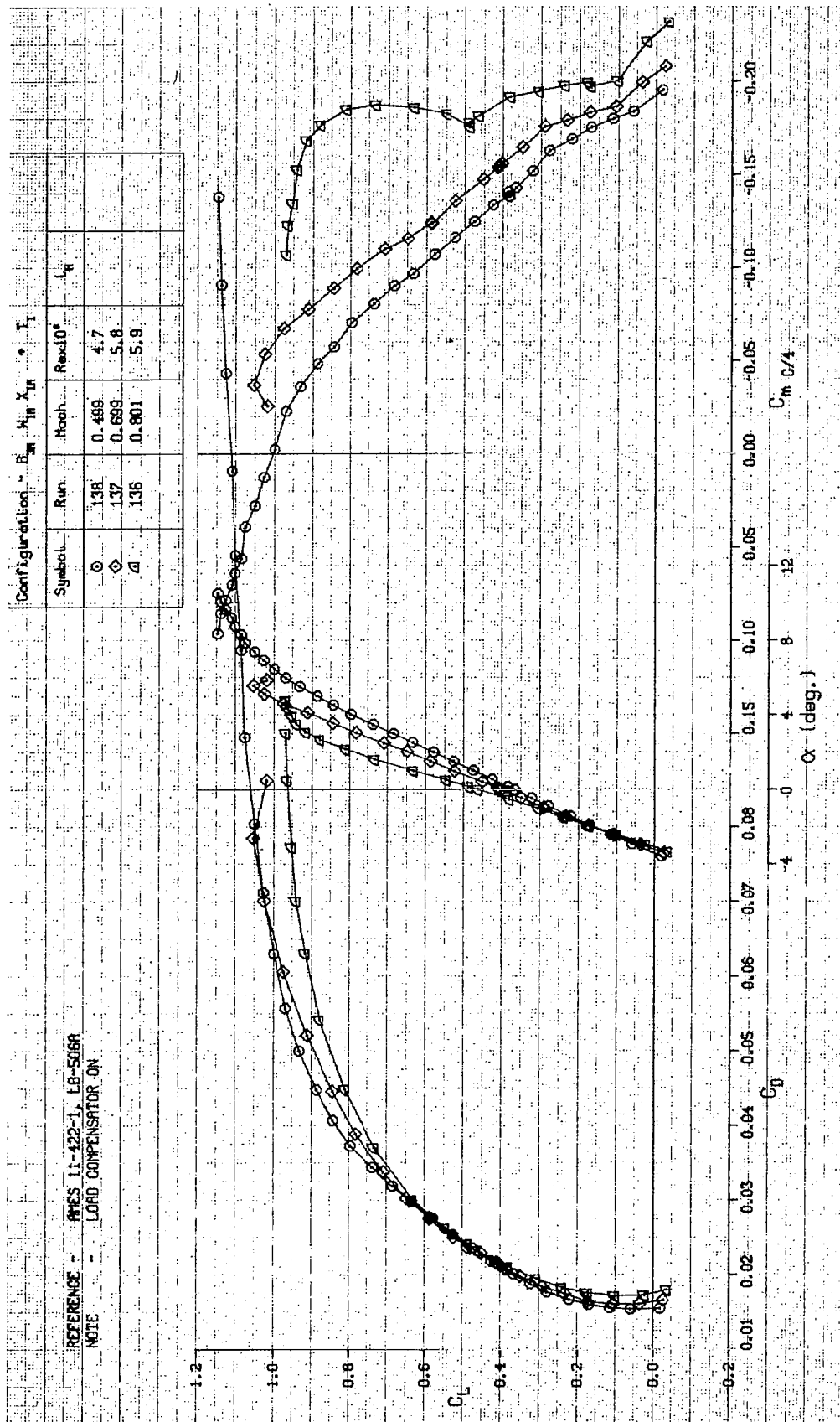
FIGURE A-4.   LIFT, DRAG, AND PITCHING MOMENT CHARACTERISTICS OF WING W₁, TRANSITION FREE

A-4
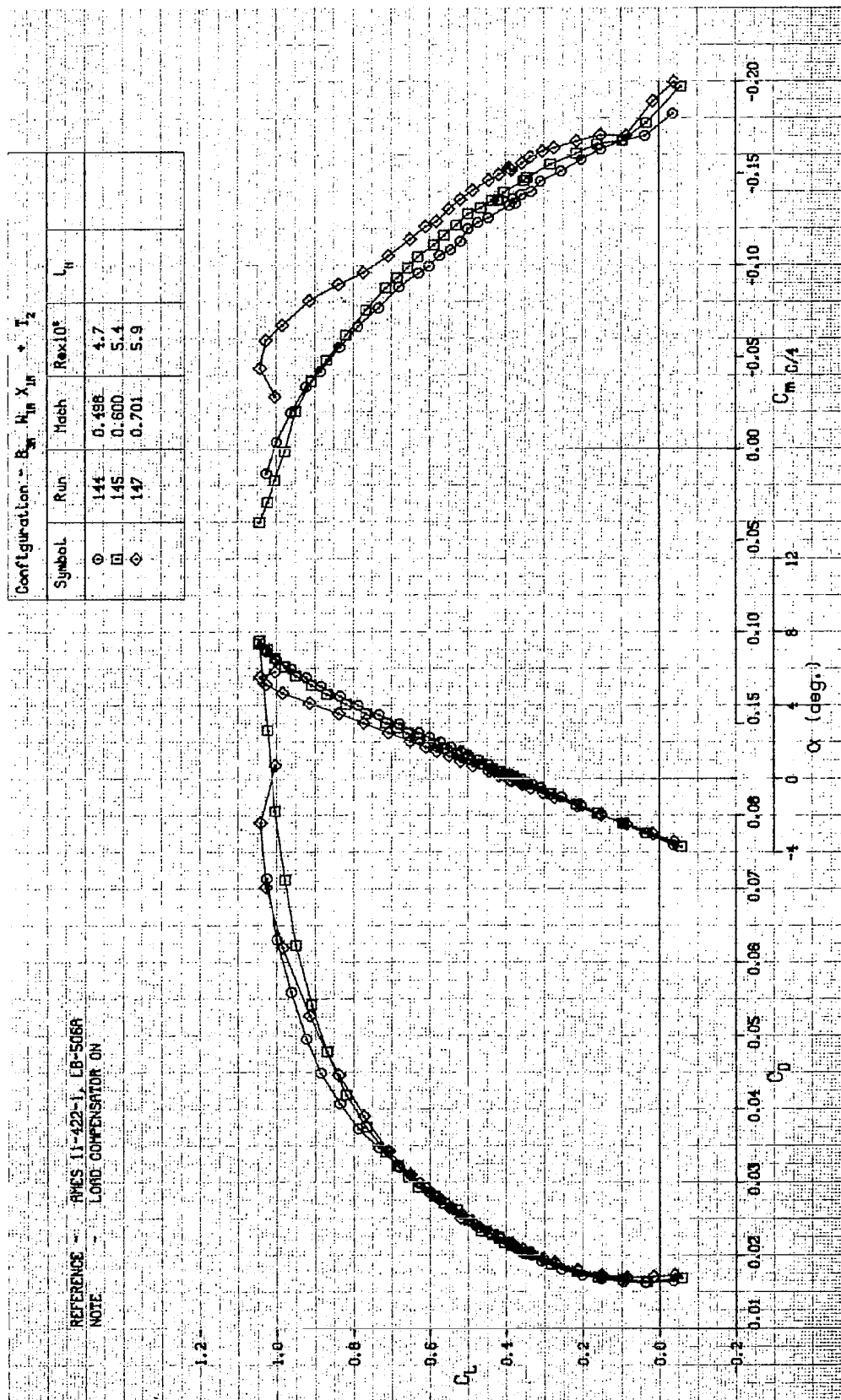
FIGURE A-5. LIFT, DRAG, AND PITCHING MOMENT CHARACTERISTICS OF WING W_1, TRANSITION FIXED

A-5
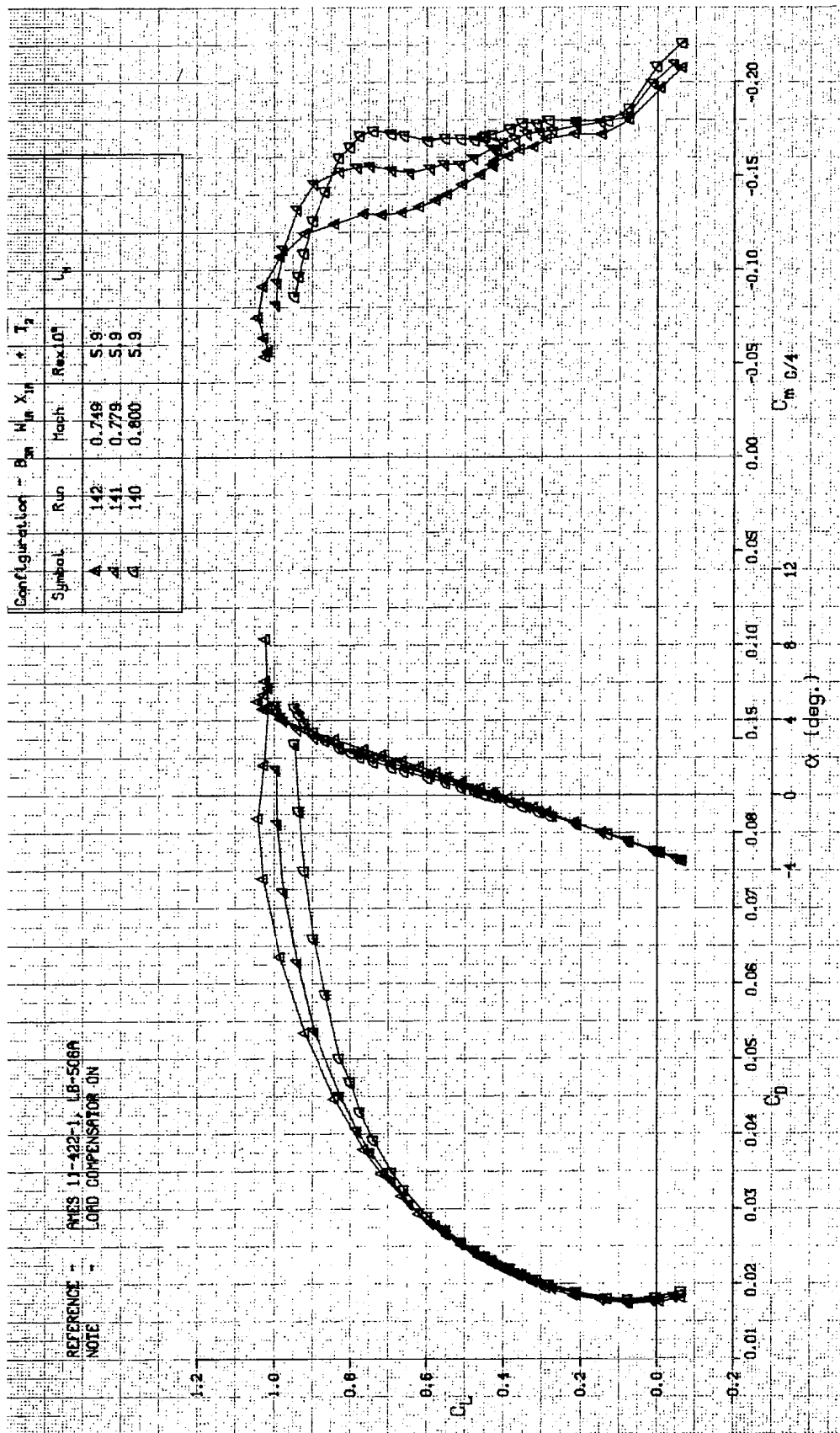
FIGURE A-6.   LIFT, DRAG, AND PITCHING MOMENT CHARACTERISTICS OF WING W_1, TRANSITION FIXED
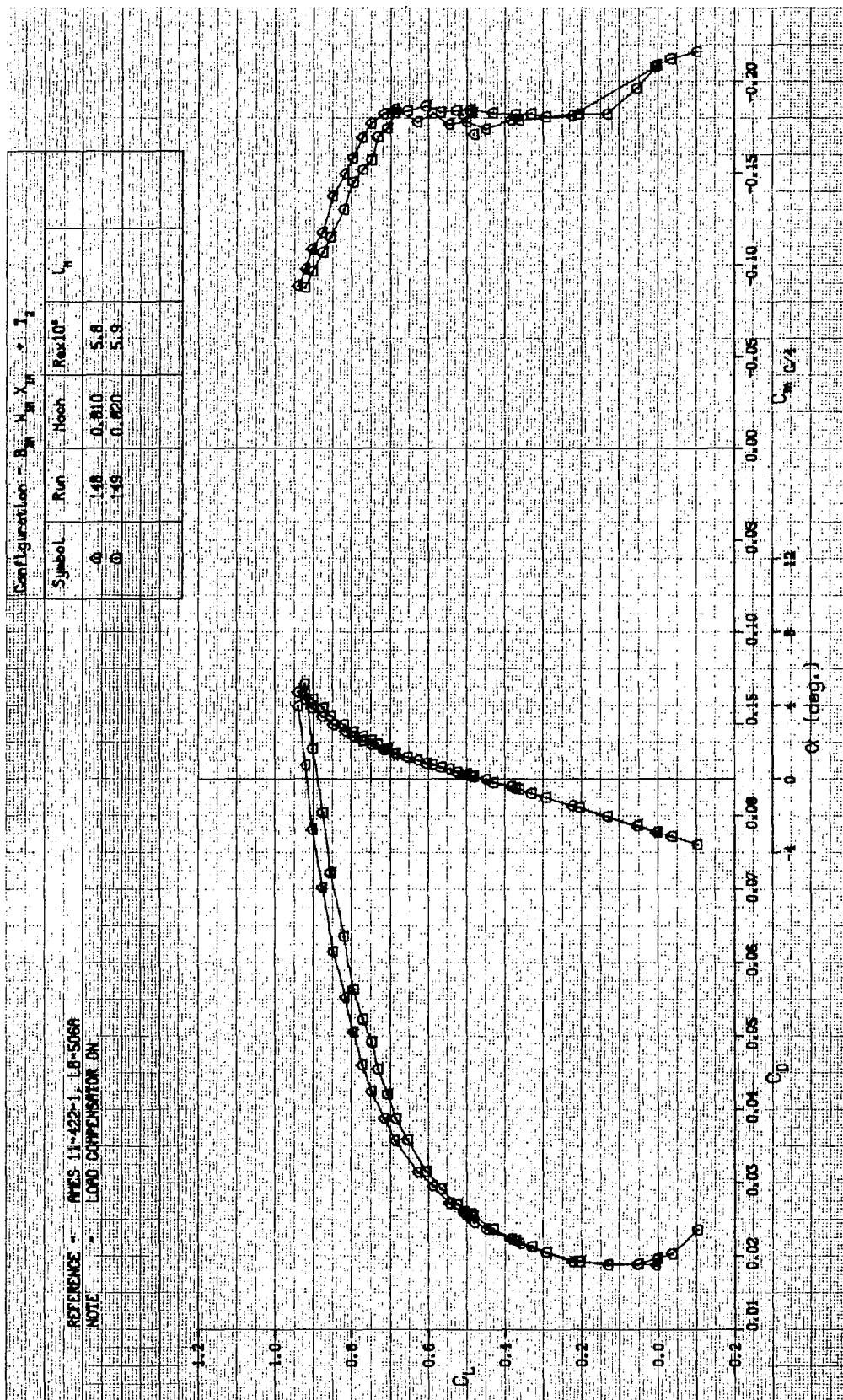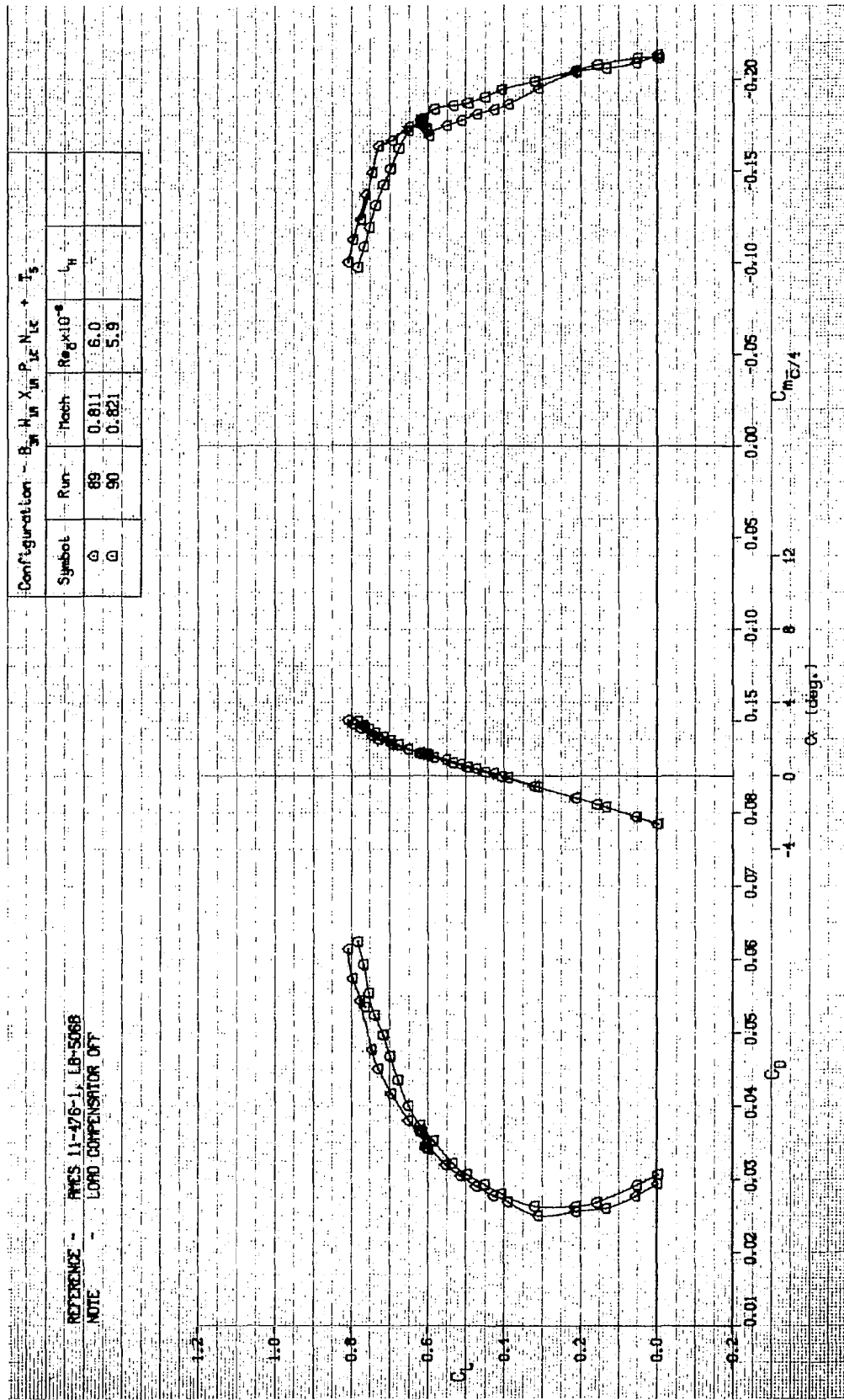
FIGURE A-7. LIFT, DRAG, AND PITCHING MOMENT CHARACTERISTICS OF WING W_1, TRANSITION FIXED
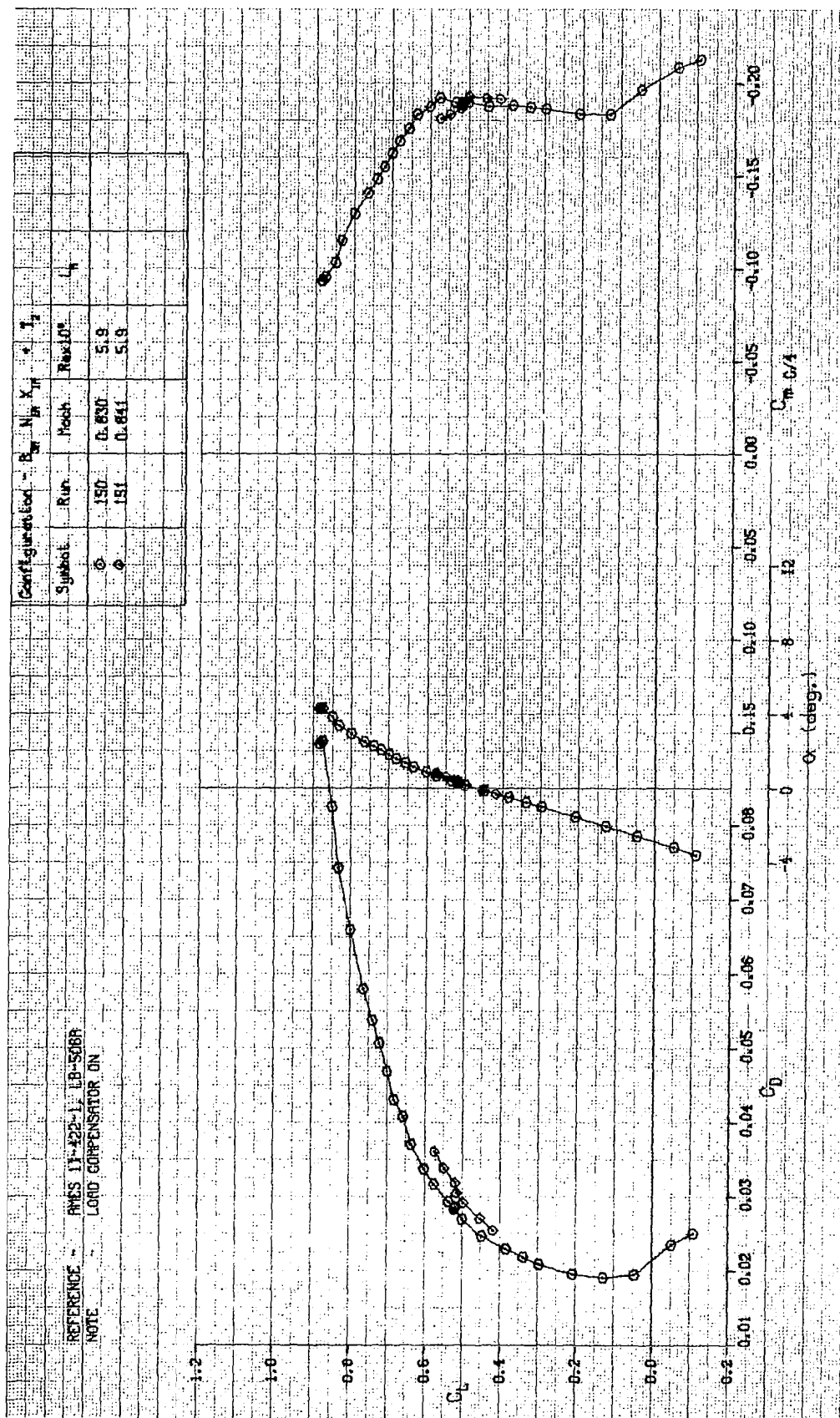
FIGURE A-8. LIFT, DRAG, AND PITCHING MOMENT CHARACTERISTICS OF WING W_1, TRANSITION FIXED
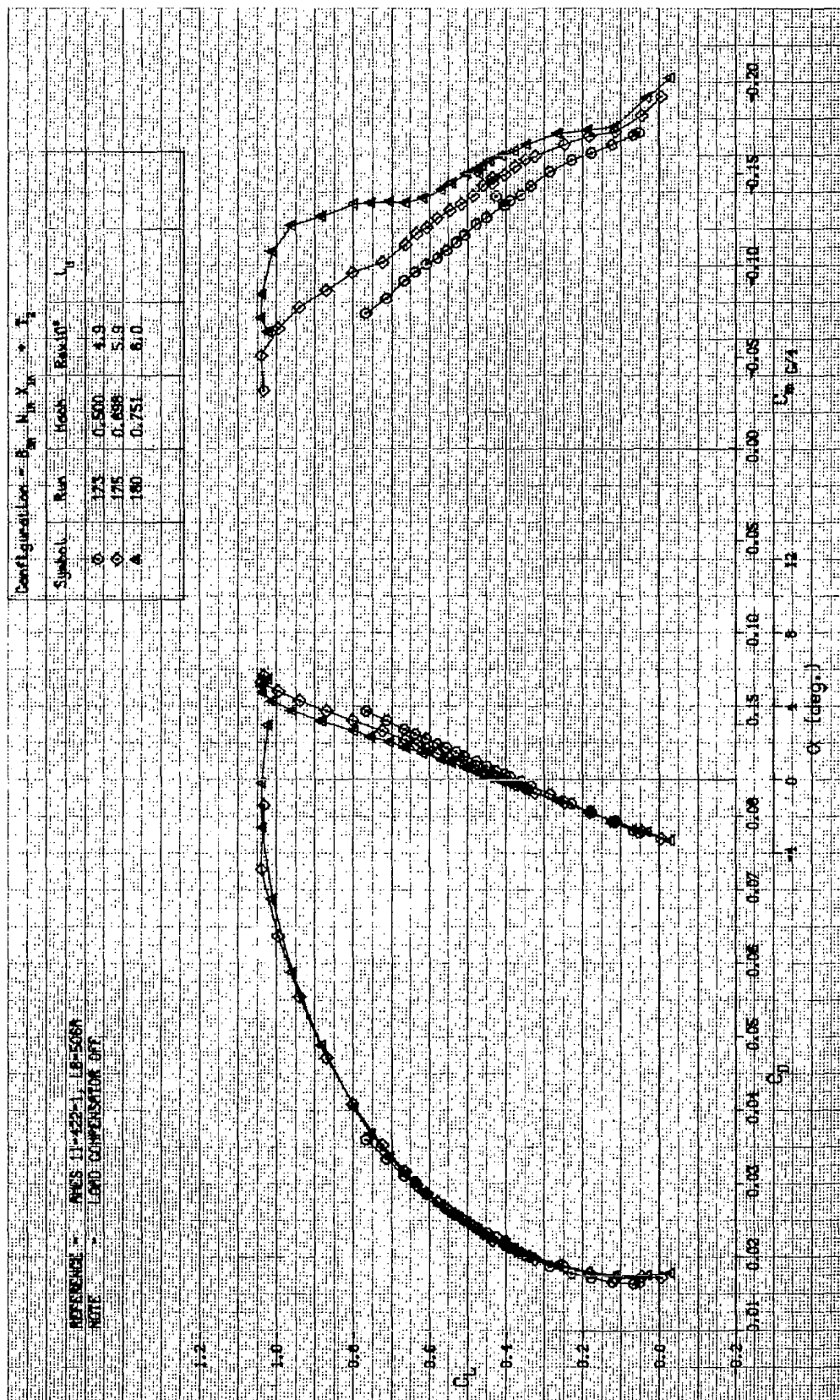
FIGURE A-9. LIFT, DRAG, AND PITCHING MOMENT CHARACTERISTICS OF WING W_1, TRANSITION FIXED

A-9
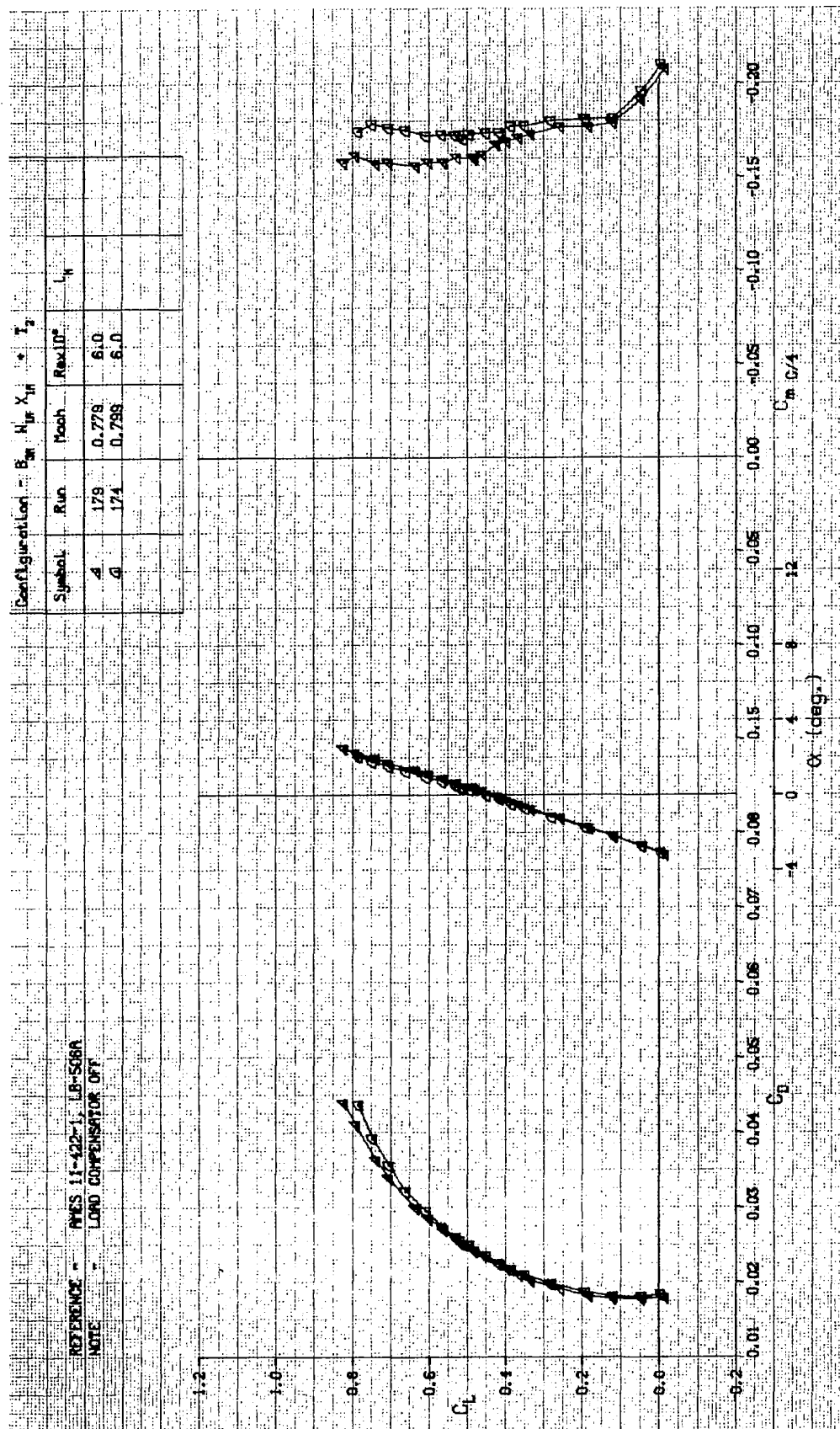
FIGURE A-10. LIFT, DRAG, AND PITCHING MOMENT CHARACTERISTICS OF WING W_1, TRANSITION FIXED
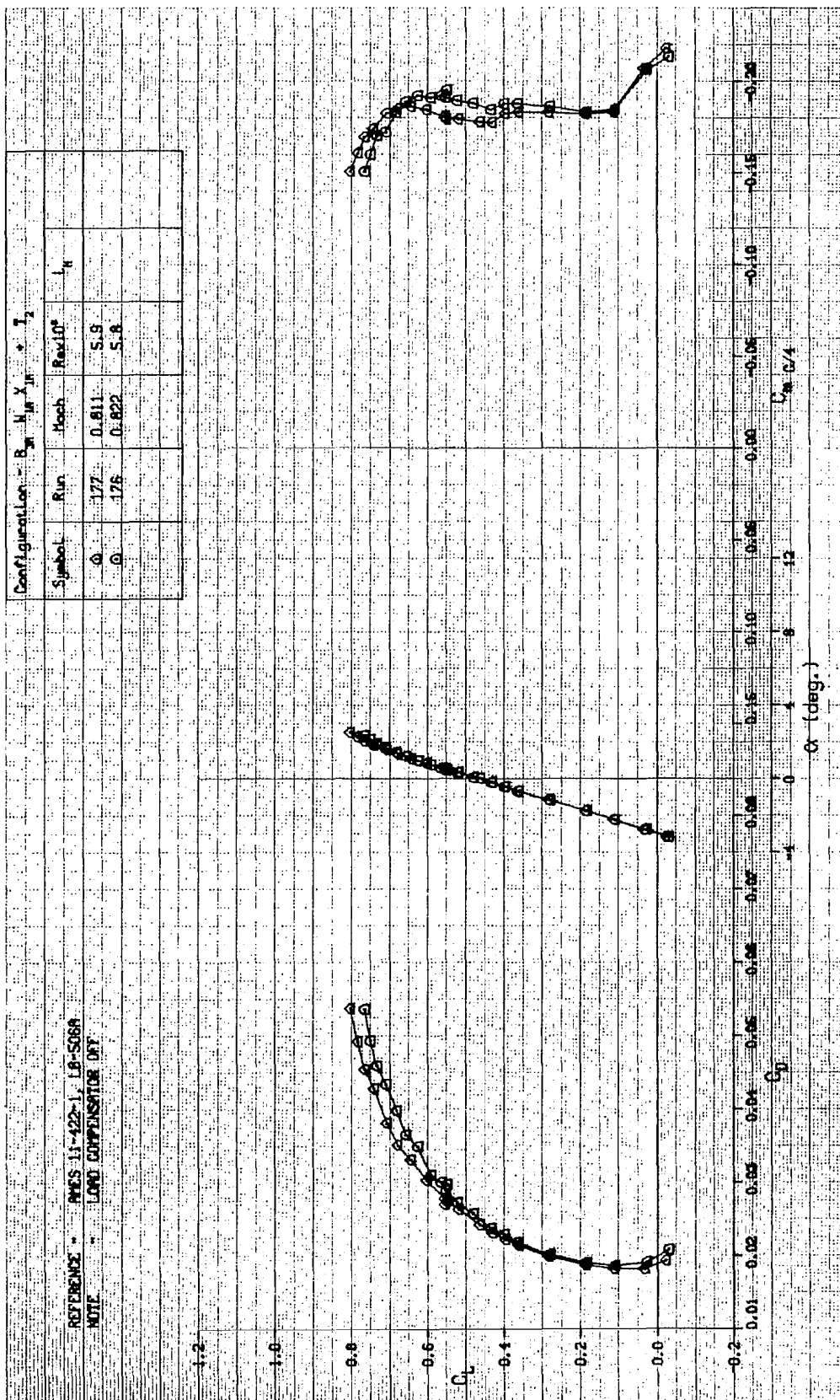
FIGURE A-11. LIFT, DRAG, AND PITCHING MOMENT CHARACTERISTICS OF WING W_1, TRANSITION FIXED
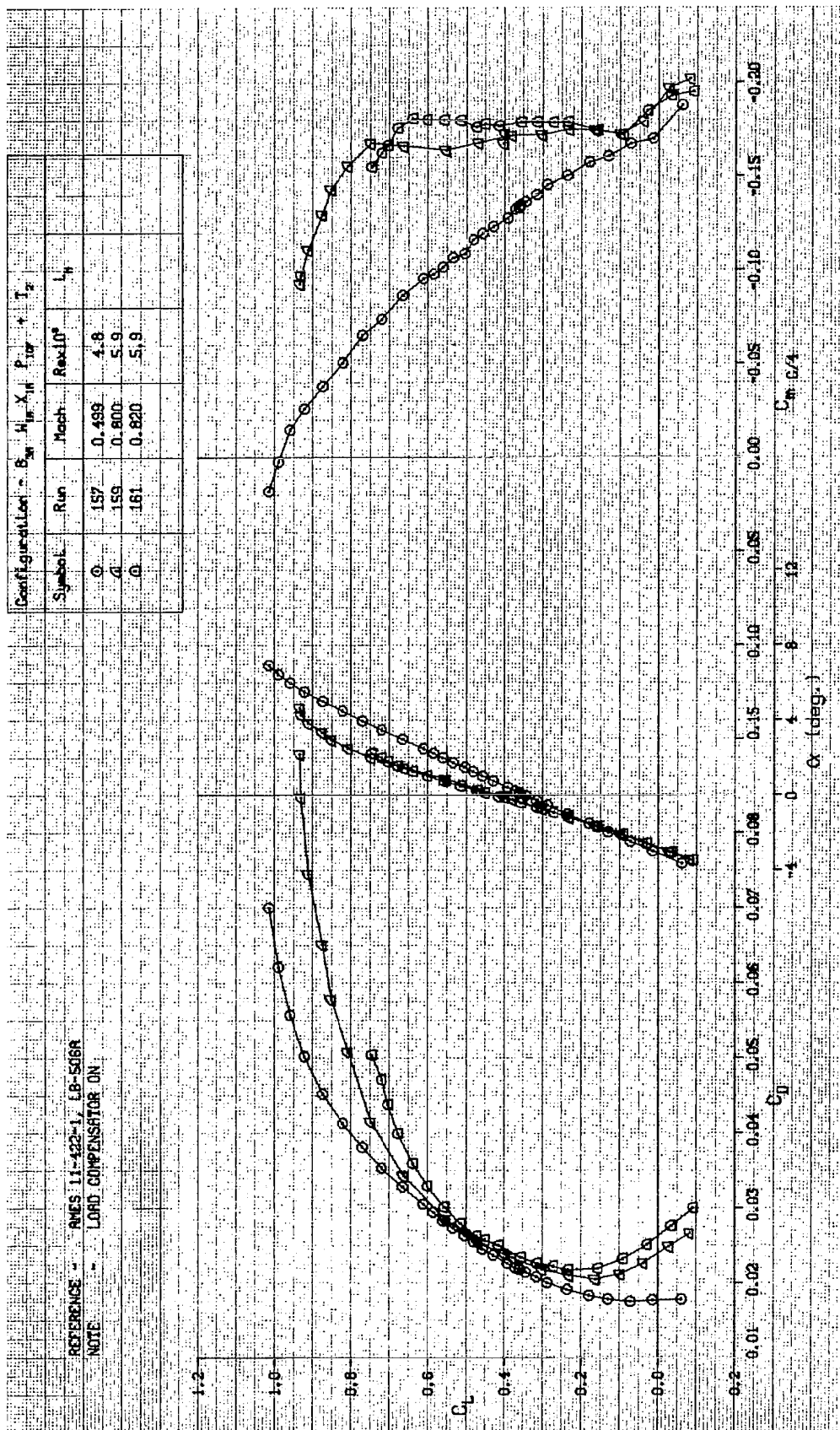
FIGURE A-12. LIFT, DRAG, AND PITCHING MOMENT CHARACTERISTICS OF WING W_1, WITH FAIRED PYLONS, TRANSITION FIXED
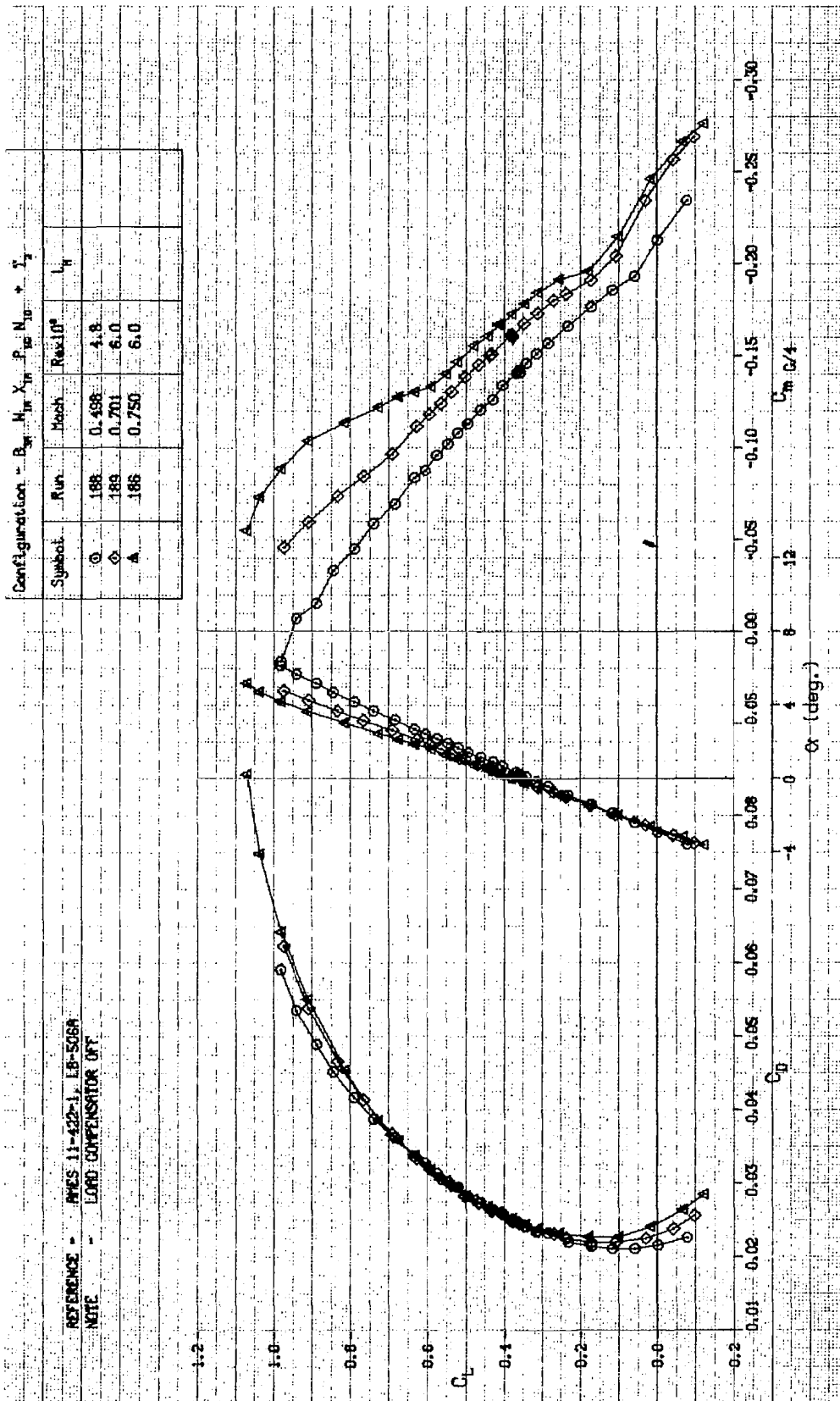
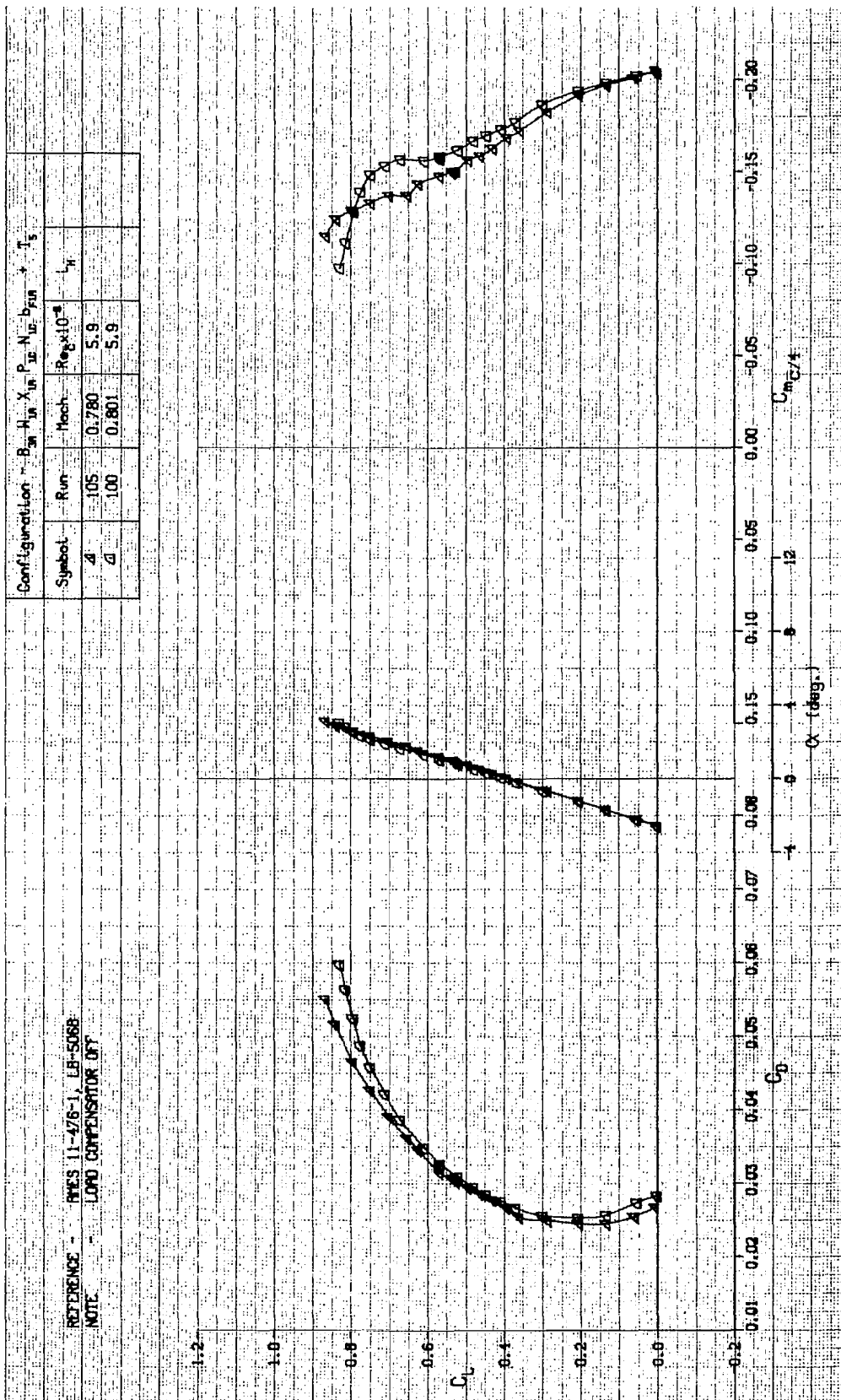FIGURE A-13. LIFT, DRAG, AND PITCHING MOMENT CHARACTERISTICS OF WING W_1, WITH NACELLES AND PYLONS, TRANSITION FIXED

A-13
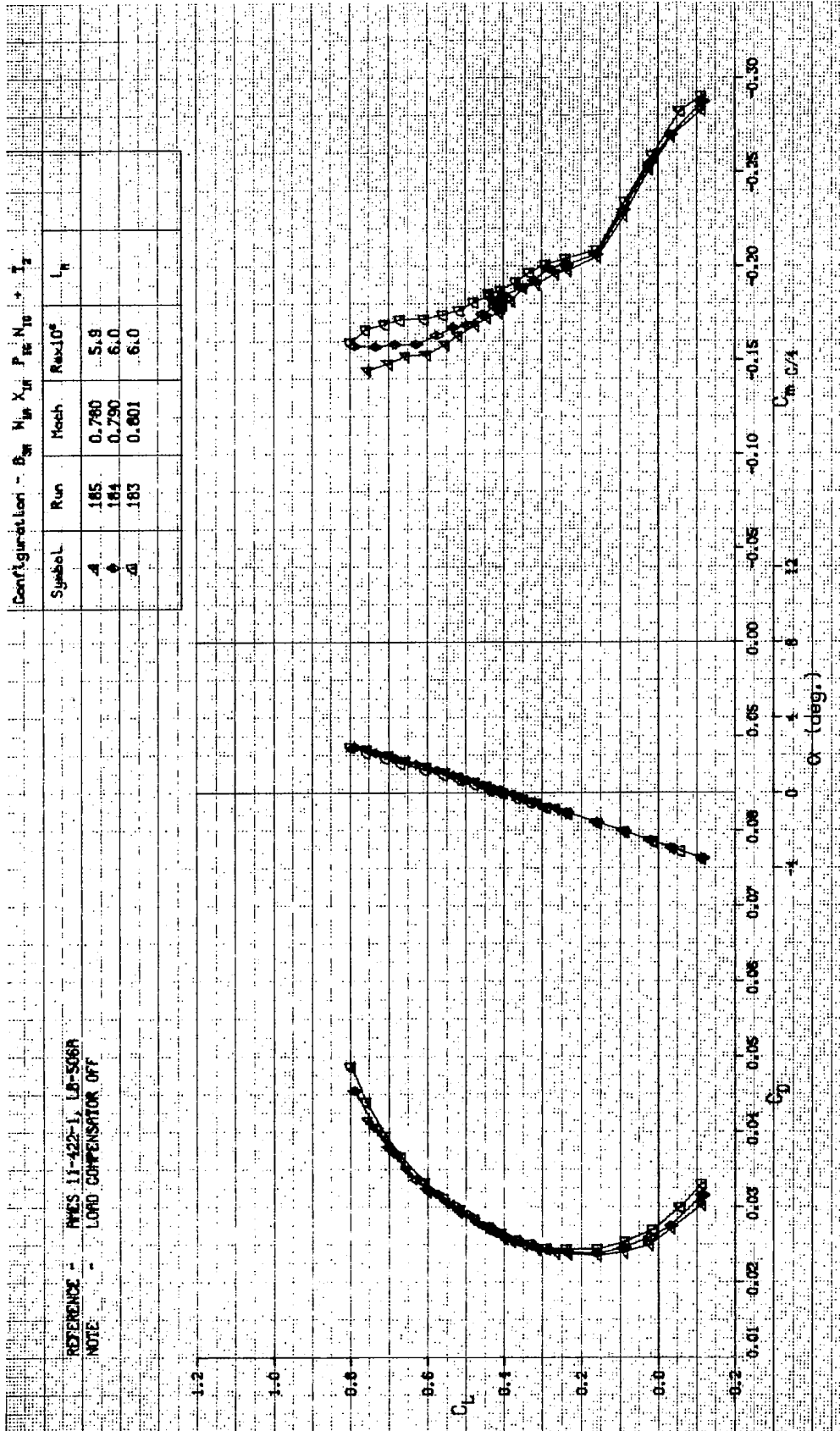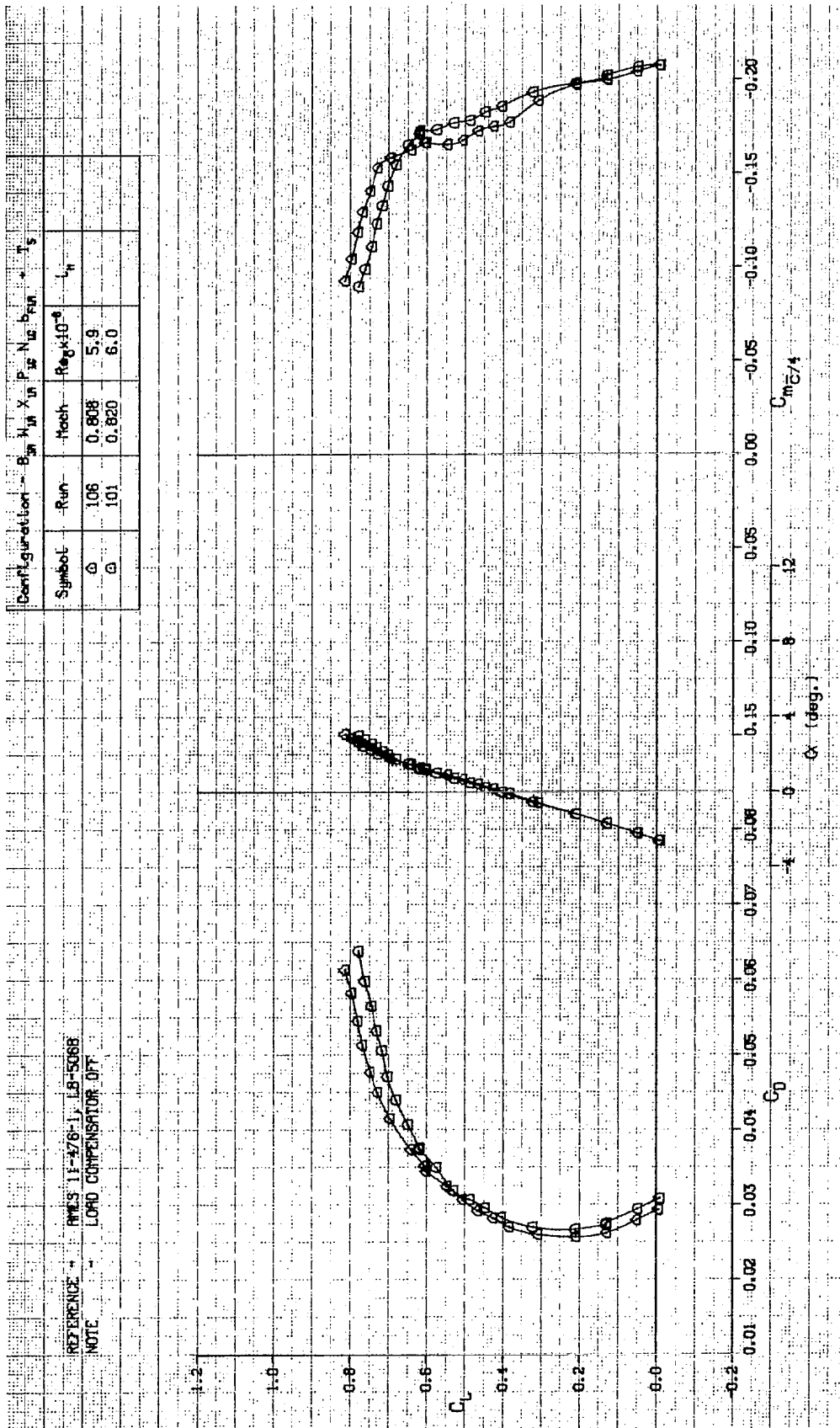
FIGURE A-14. LIFT, DRAG, AND PITCHING MOMENT CHARACTERISTICS OF WING W_1, WITH NACELLES AND PYLONS, TRANSITION FIXED
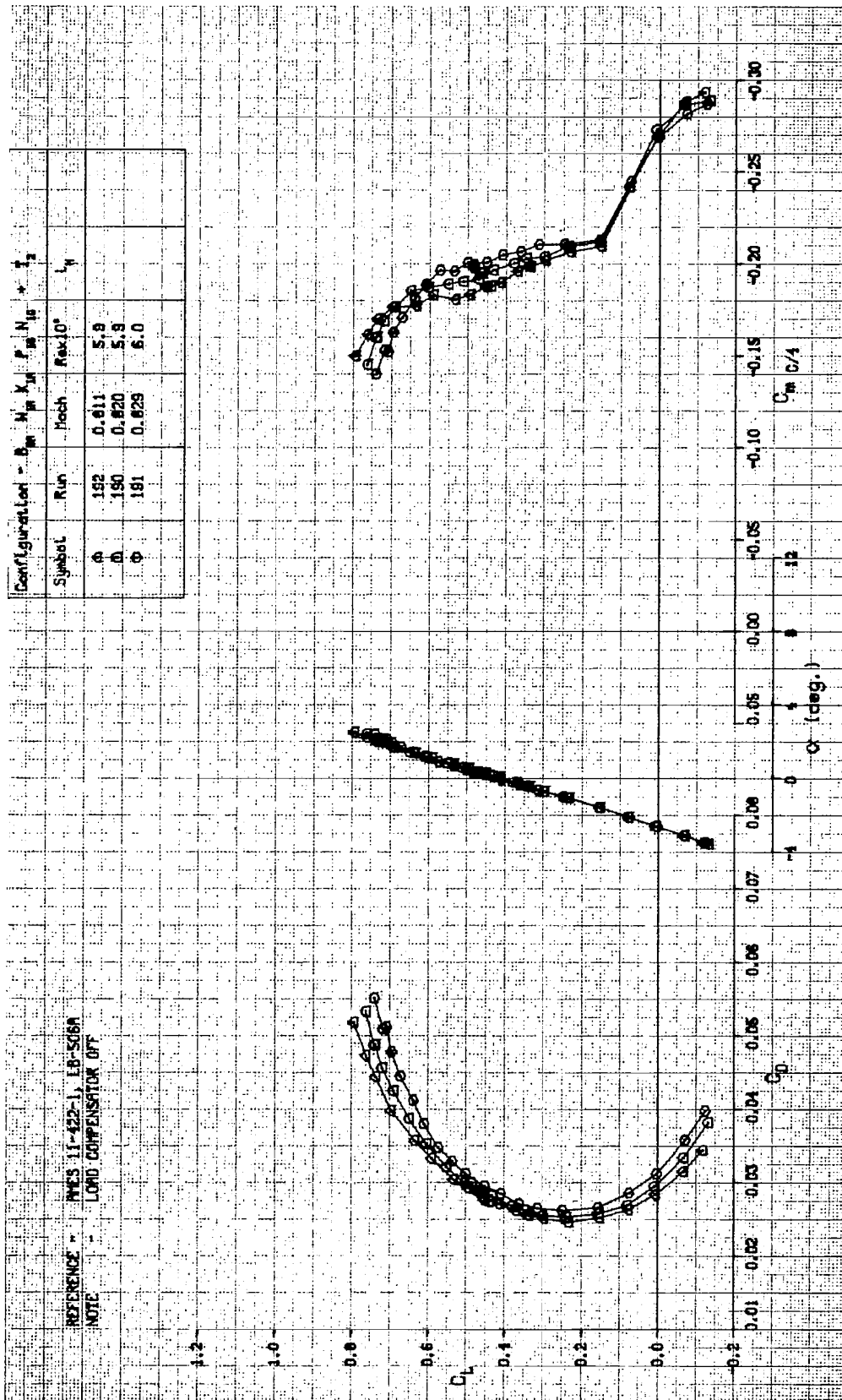
FIGURE A-15. LIFT, DRAG, AND PITCHING MOMENT CHARACTERISTICS OF WING W_1, WITH NACELLES AND PYLONS, TRANSITION FIXED

A-15
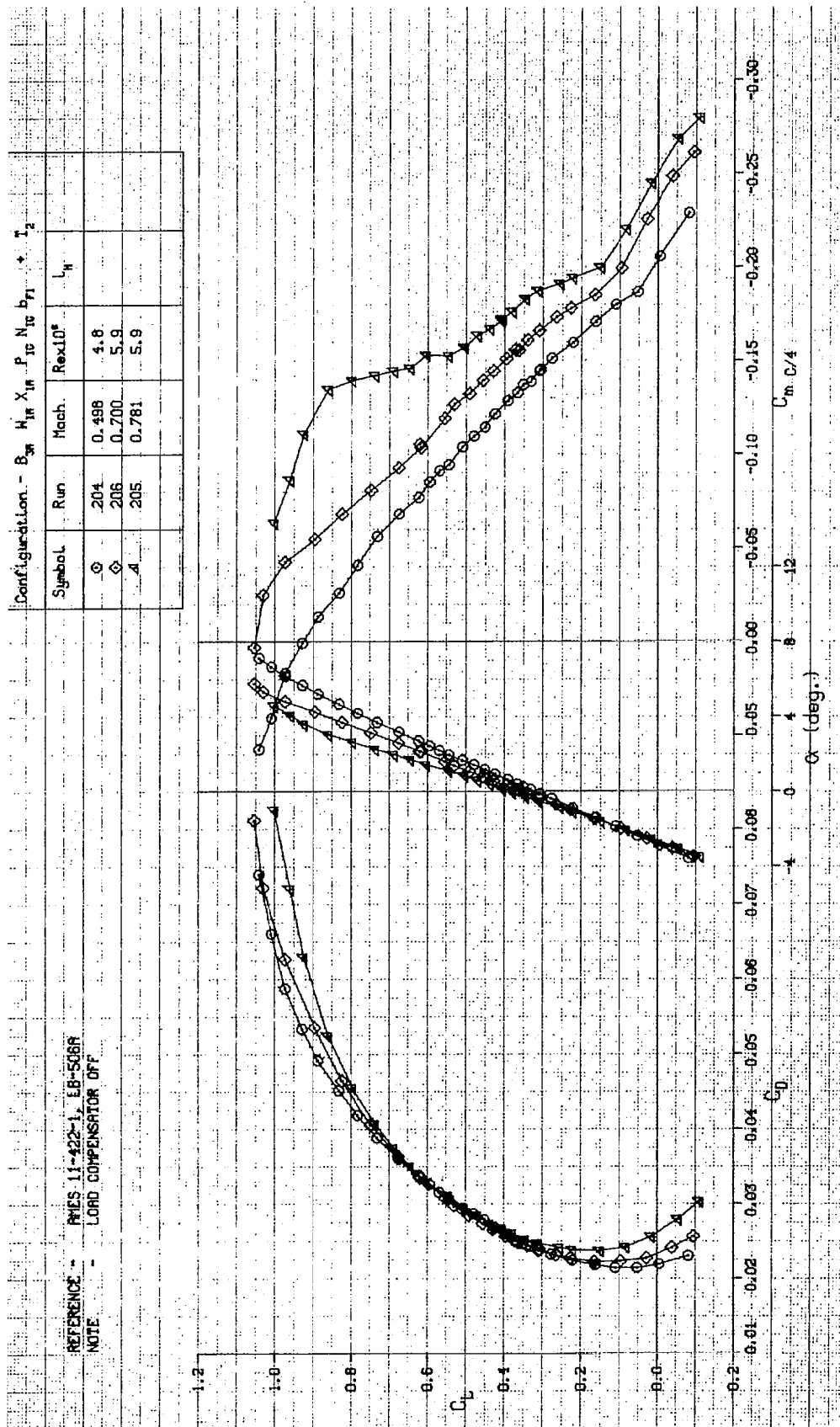
FIGURE A-16. LIFT, DRAG, AND PITCHING MOMENT CHARACTERISTICS OF WING W₁, WITH NACELLES, PYLONS, AND FLAP LINKAGE FAIRINGS, TRANSITION FIXED
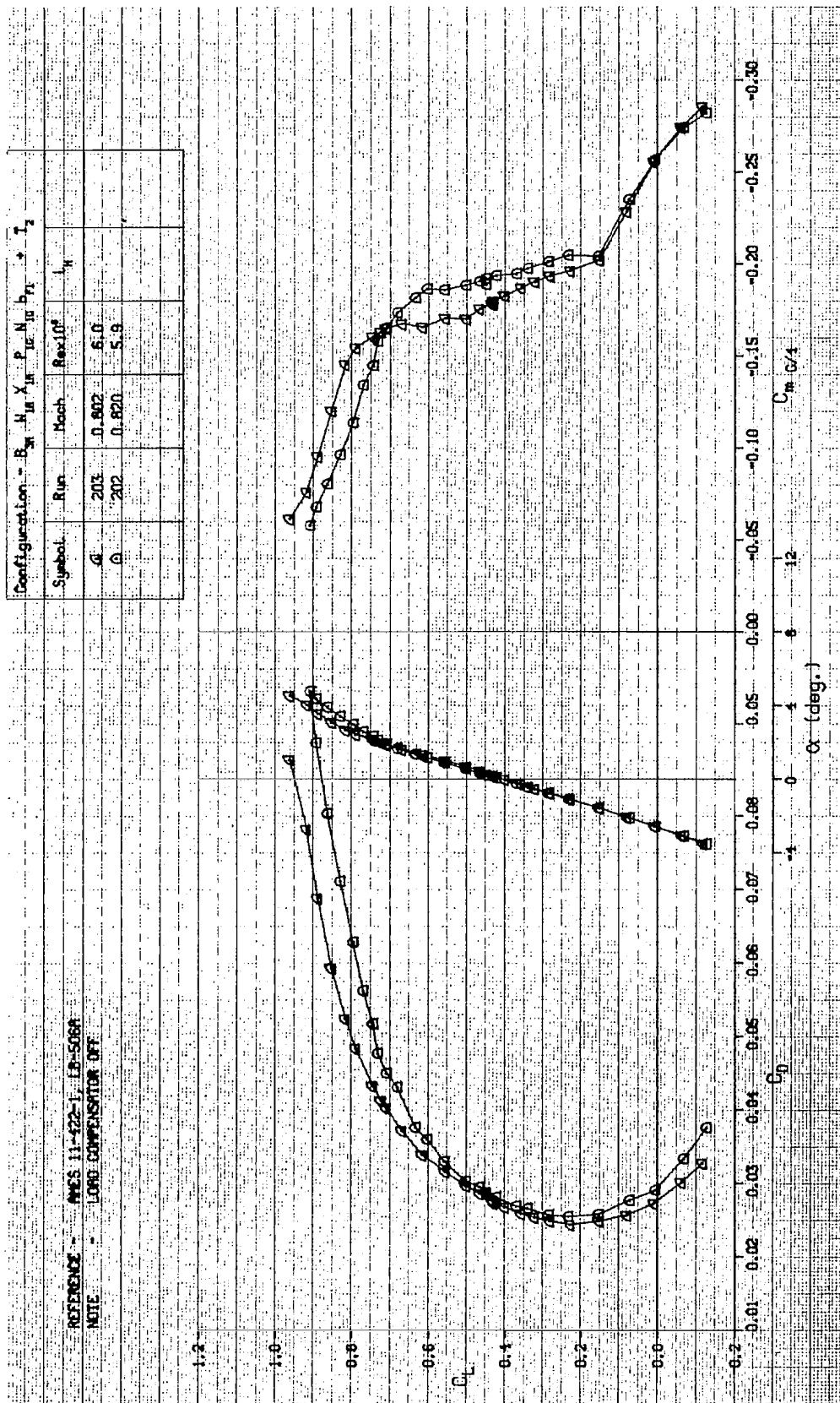
FIGURE A-17. LIFT, DRAG, AND PITCHING MOMENT CHARACTERISTICS OF WING W₁, WITH NACELLES, PYLONS, AND FLAP LINKAGE FAIRINGS, TRANSITION FIXED
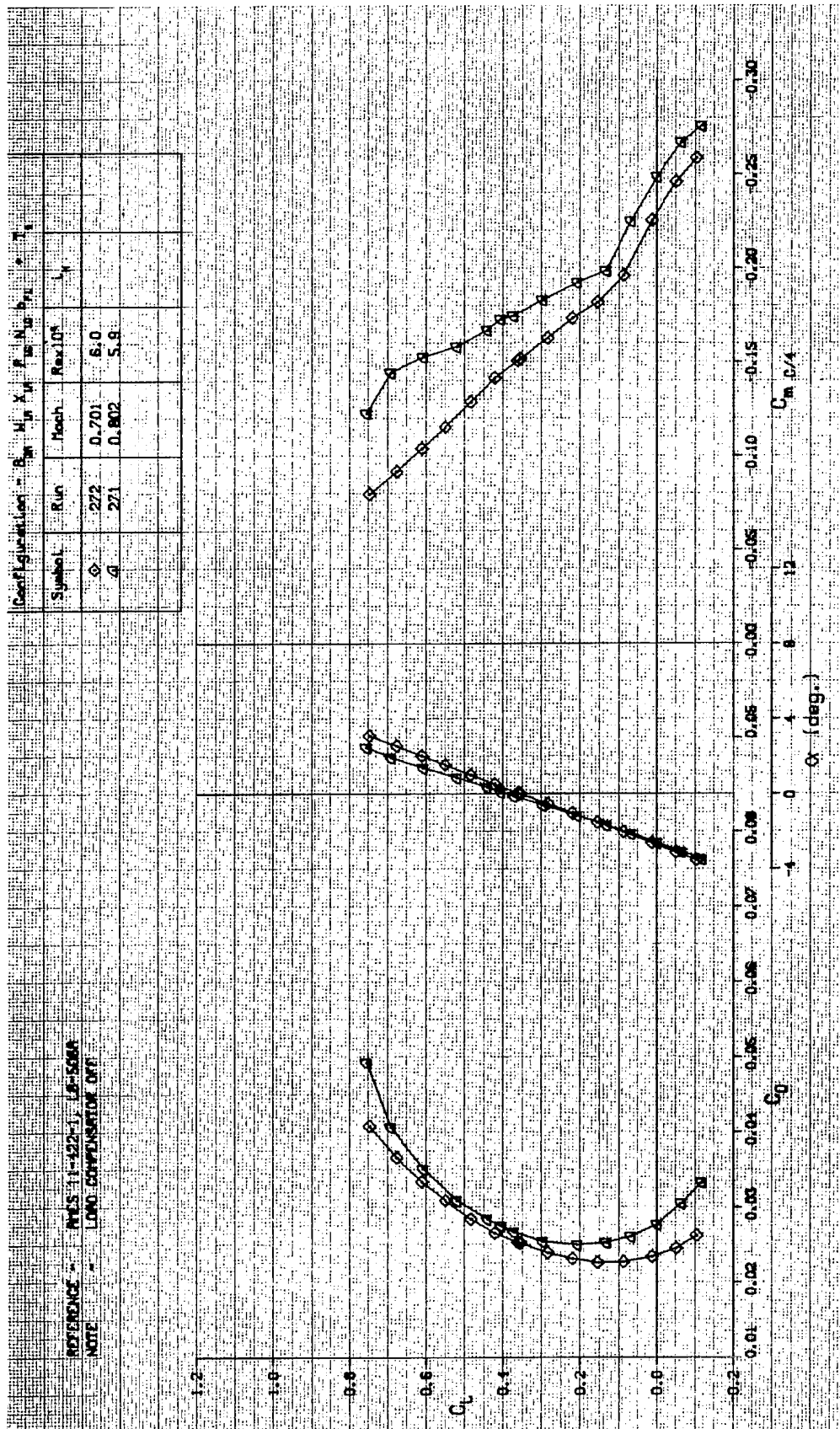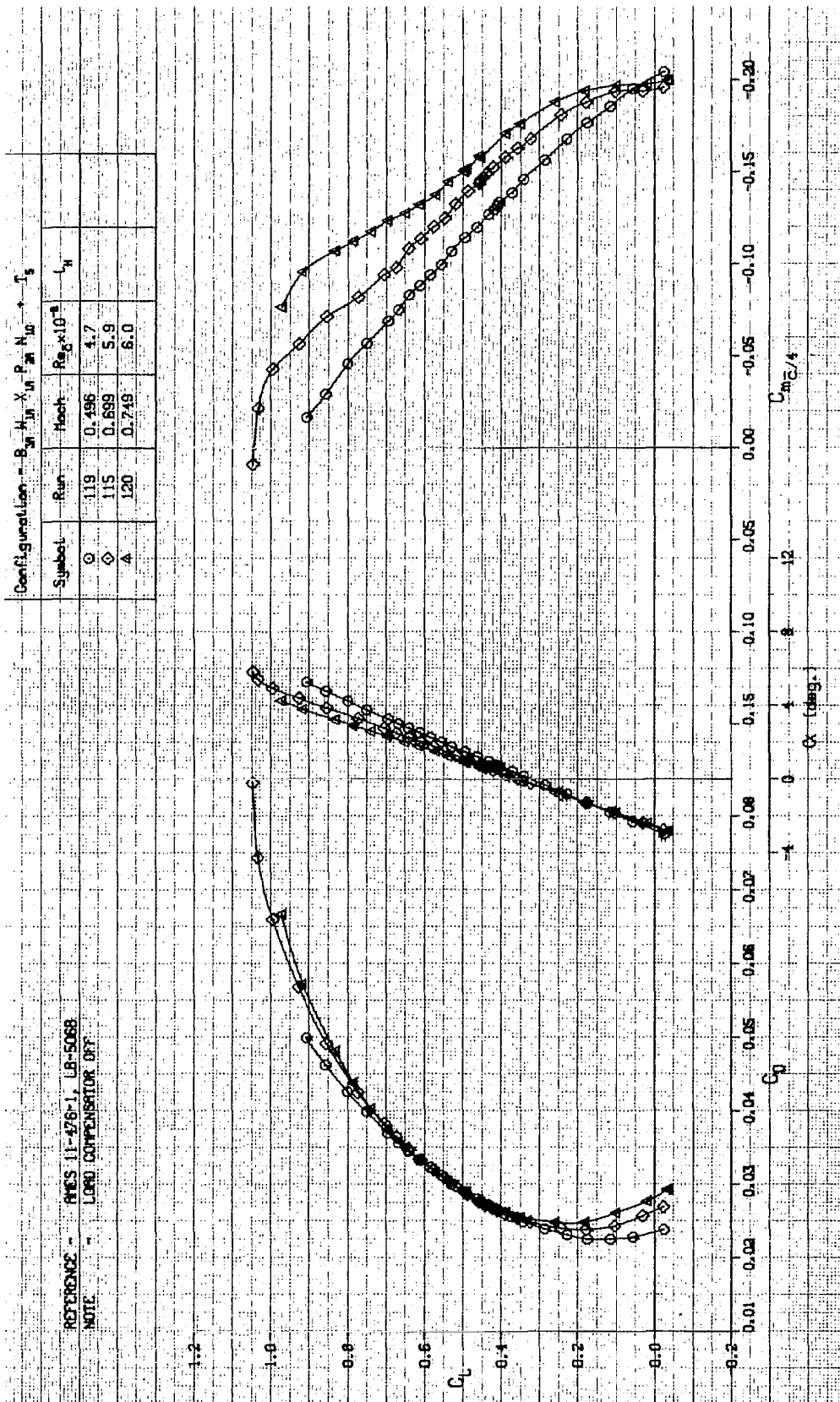
FIGURE A-18. LIFT, DRAG, AND PITCHING MOMENT CHARACTERISTICS OF WING W_1, WITH NACELLES, PYLONS, AND FLAP LINKAGE FAIRINGS, TRANSITION FIXED
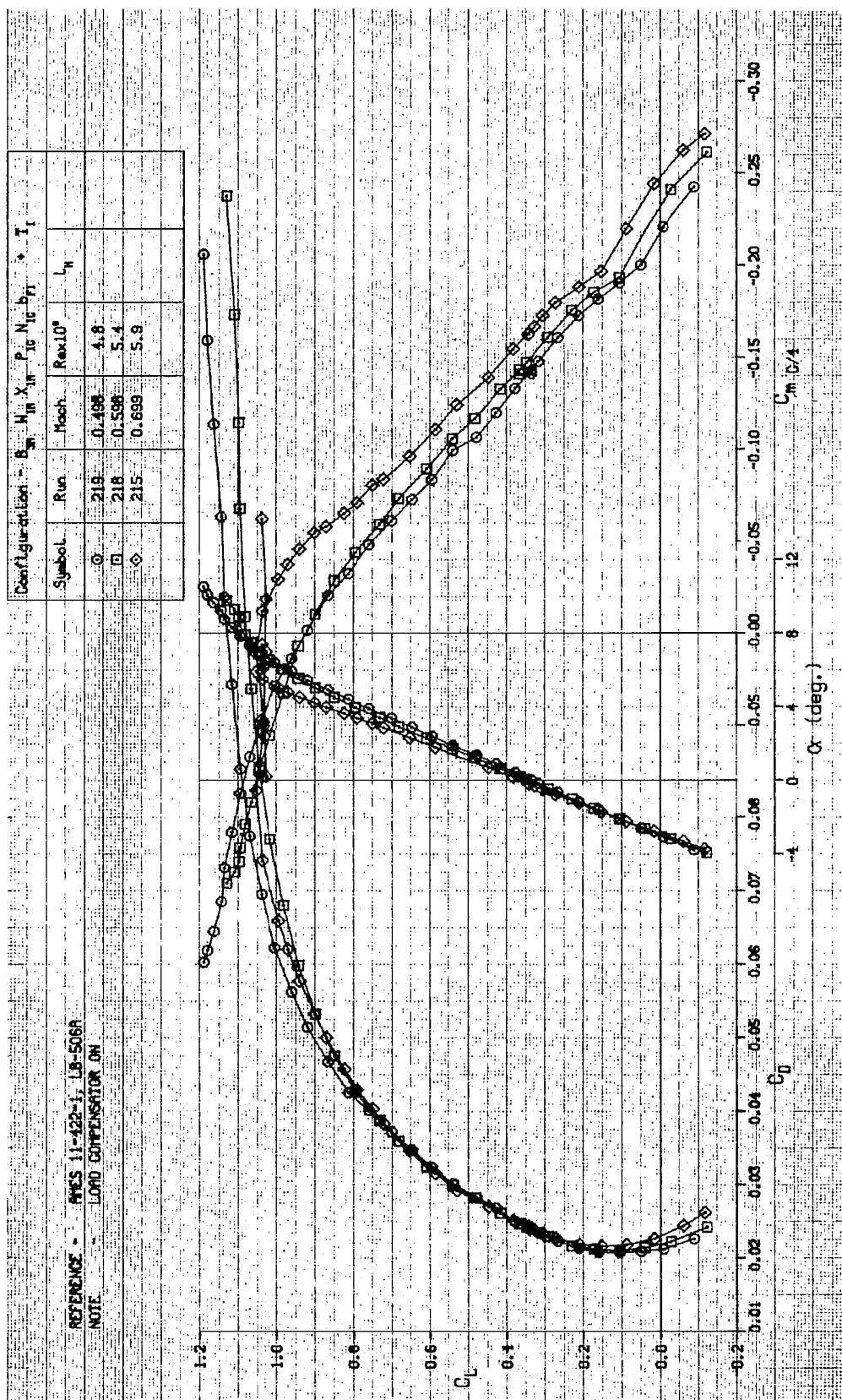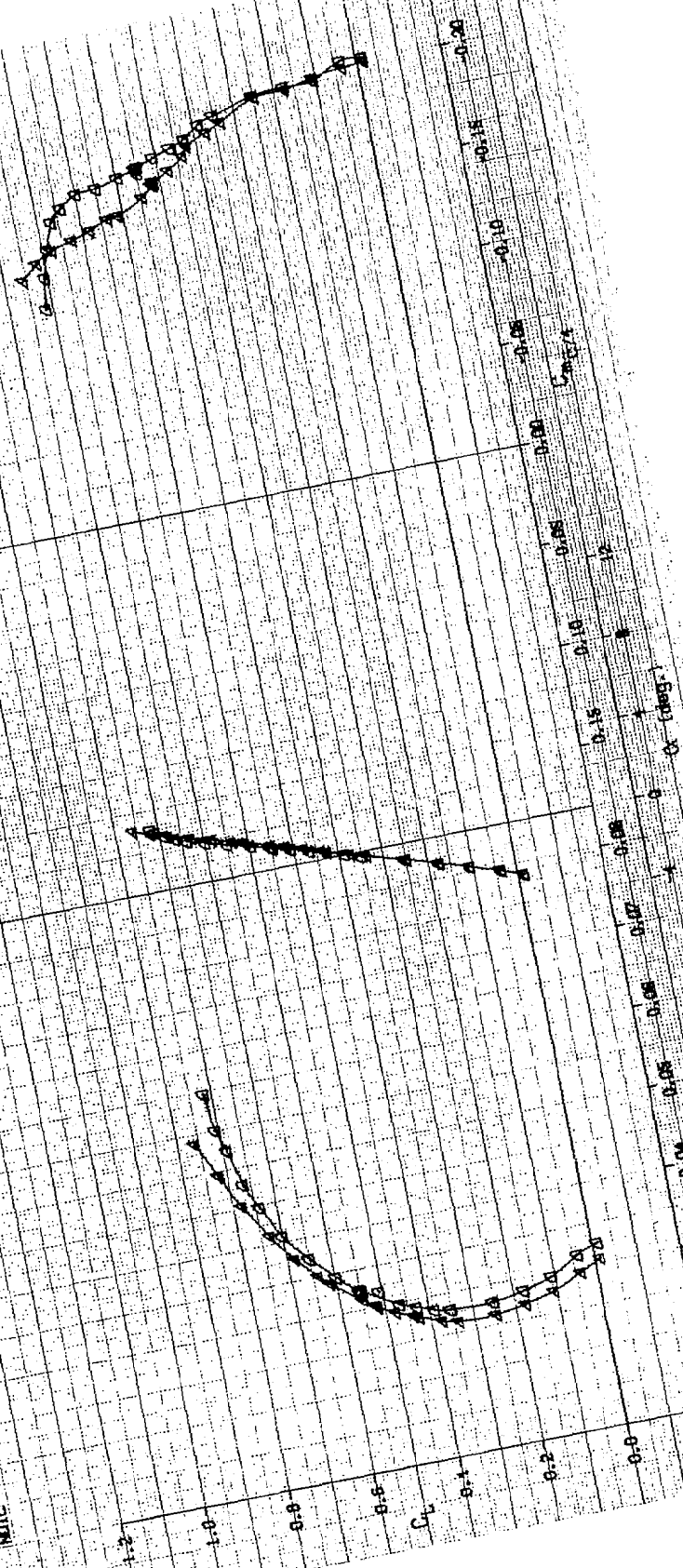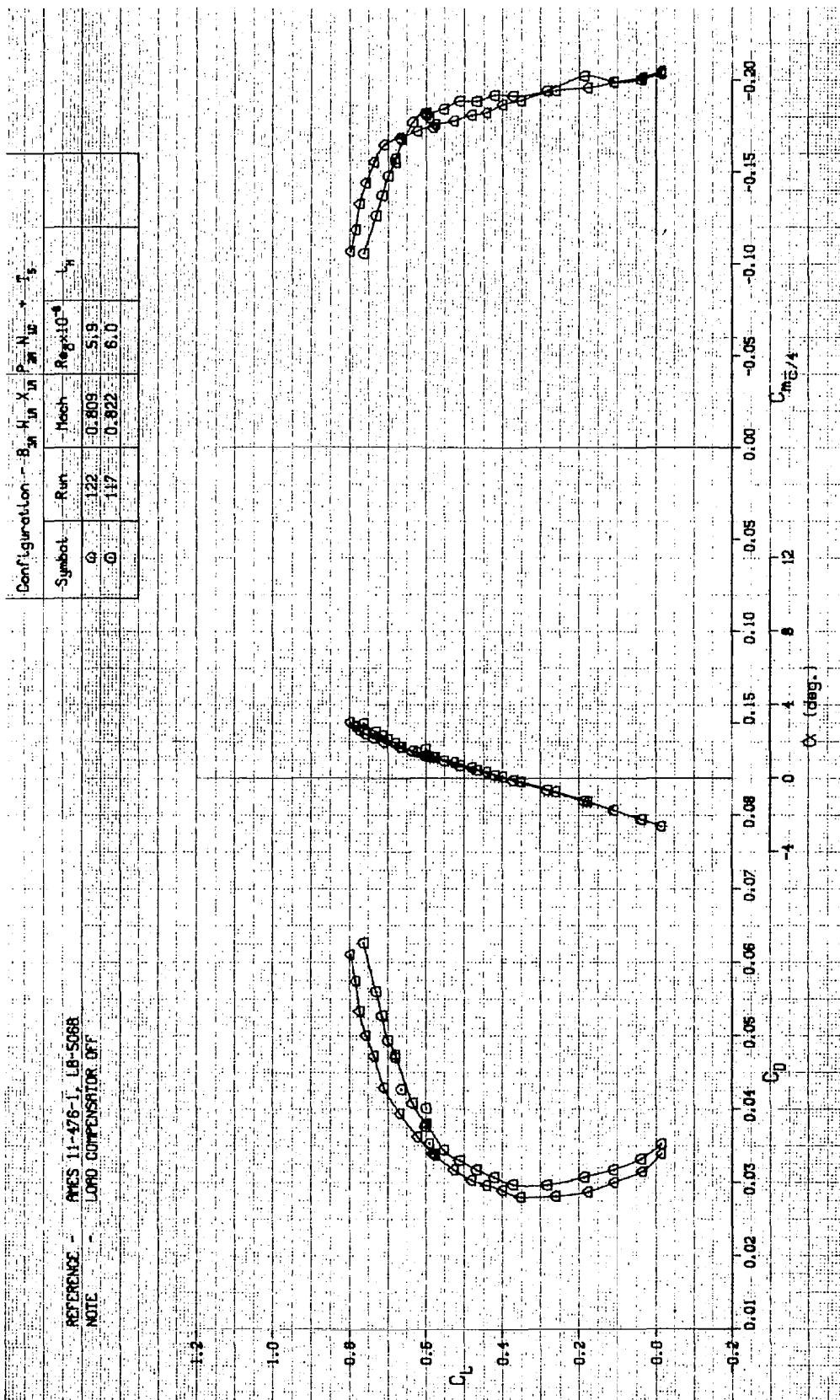
FIGURE A-19. LIFT, DRAG, AND PITCHING MOMENT CHARACTERISTICS OF WING W₁, WITH NACELLES, PYLONS, AND FLAP LINKAGE FAIRINGS, TRANSITION FREE

A-19
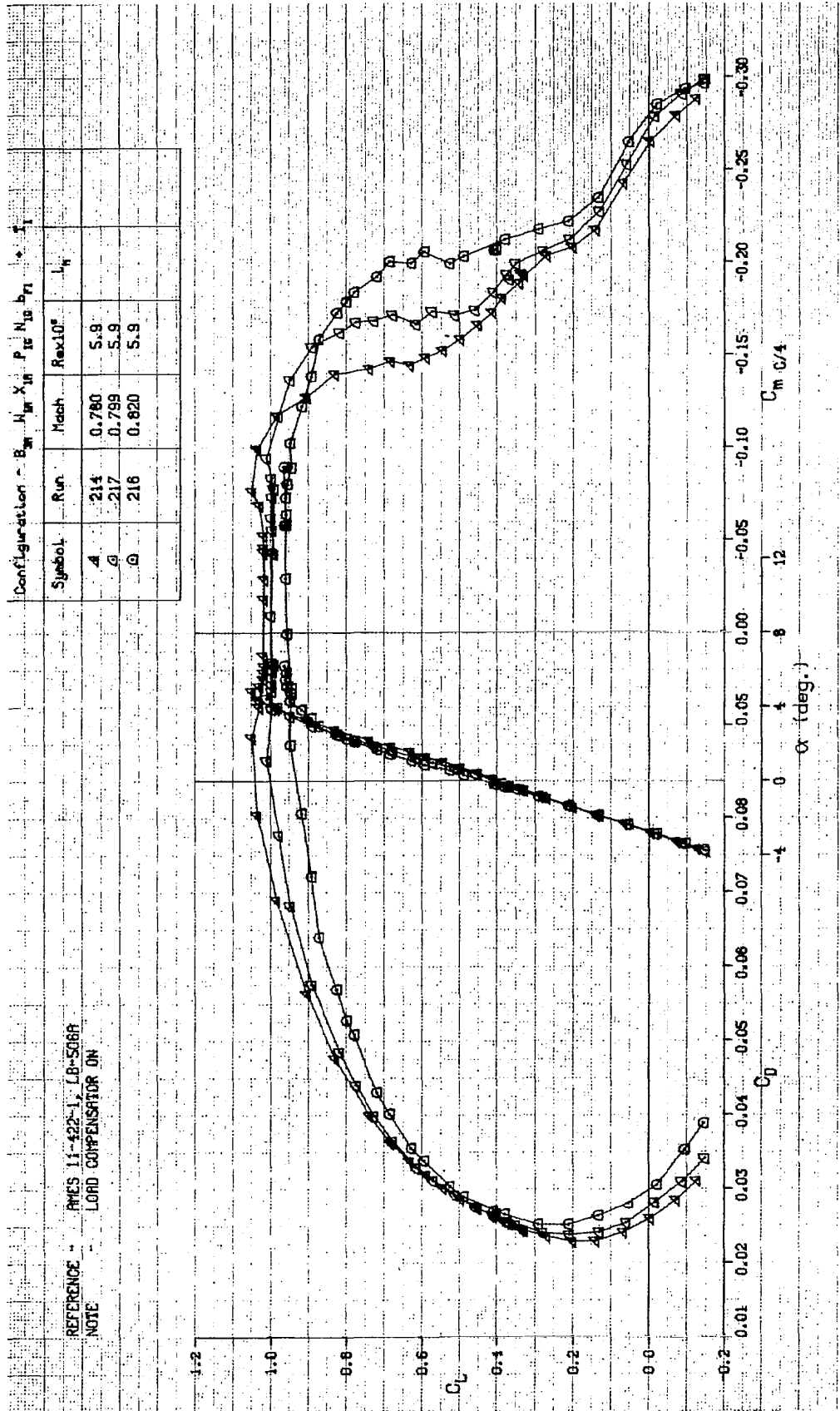
FIGURE A-20. LIFT, DRAG, AND PITCHING MOMENT CHARACTERISTICS OF WING W_1, WITH NACELLES, PYLONS, AND FLAP LINKAGE FAIRINGS, TRANSITION FREE
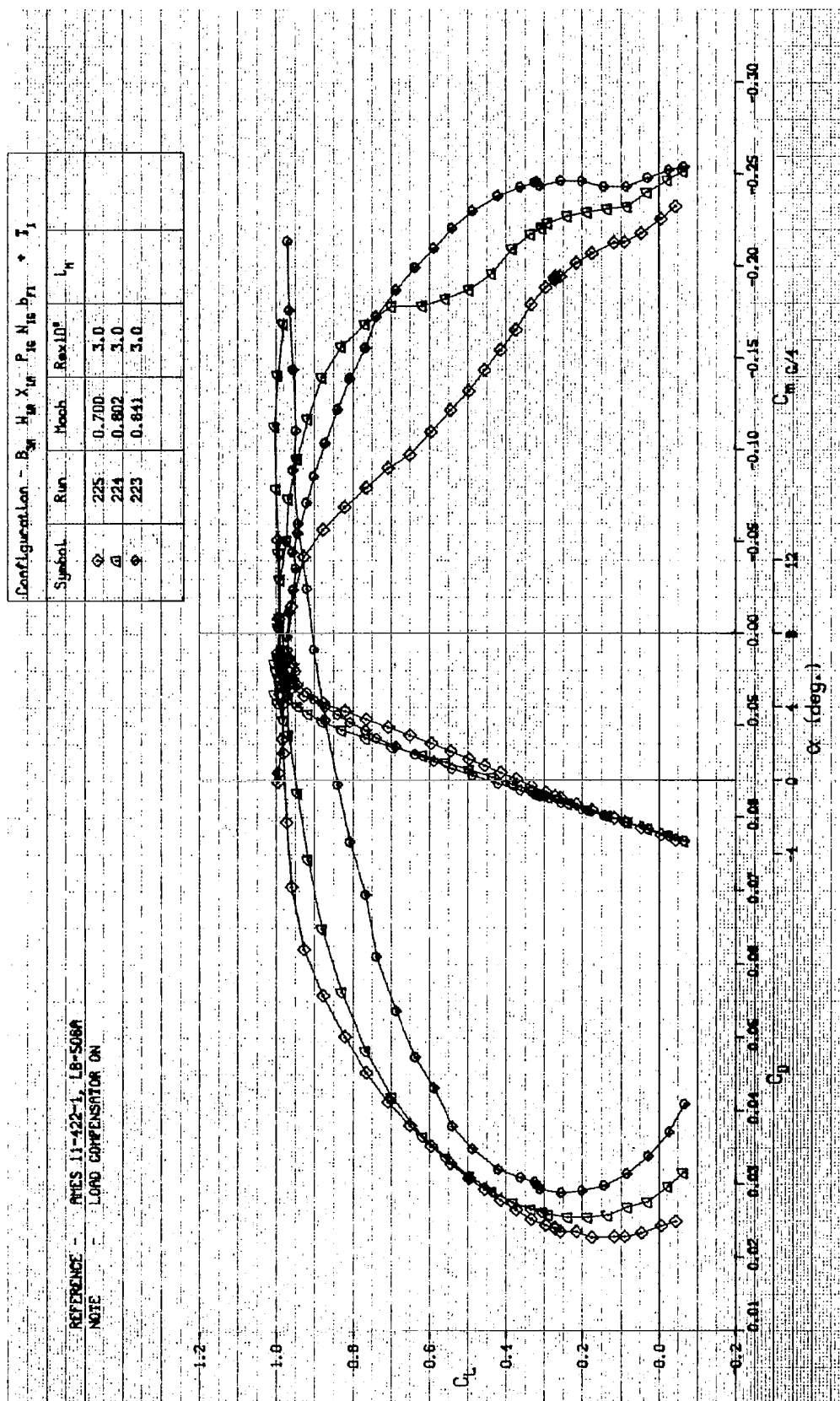
FIGURE A-21. LIFT, DRAG, AND PITCHING MOMENT CHARACTERISTICS OF WING W₁, WITH NACELLES, PYLONS, AND FLAP LINKAGE FAIRINGS, TRANSITION FREE
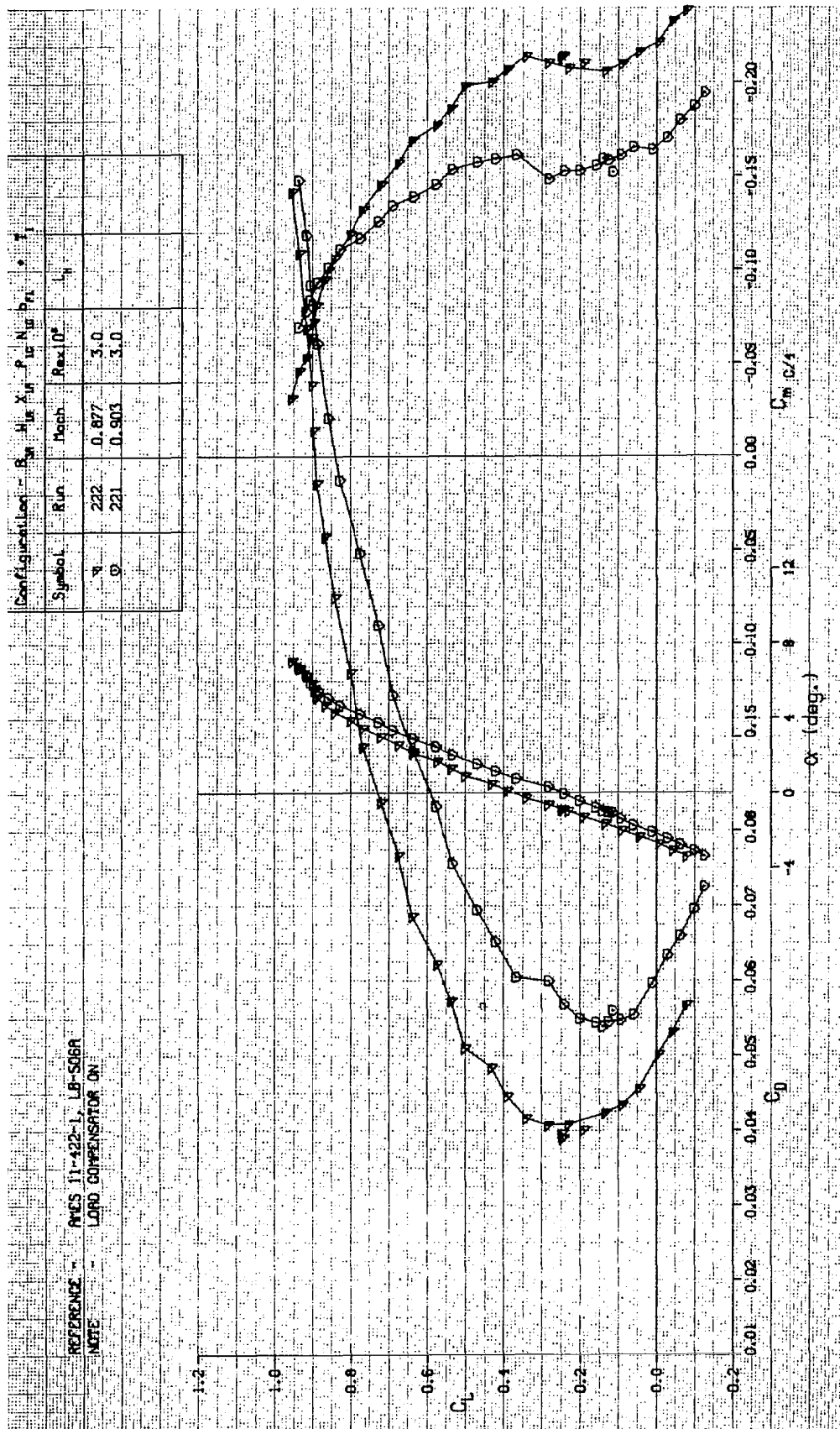
FIGURE A-22. LIFT, DRAG, AND PITCHING MOMENT CHARACTERISTICS OF WING W_1, WITH NACELLES, PYLONS, AND FLAP LINKAGE FAIRINGS, TRANSITION FREE
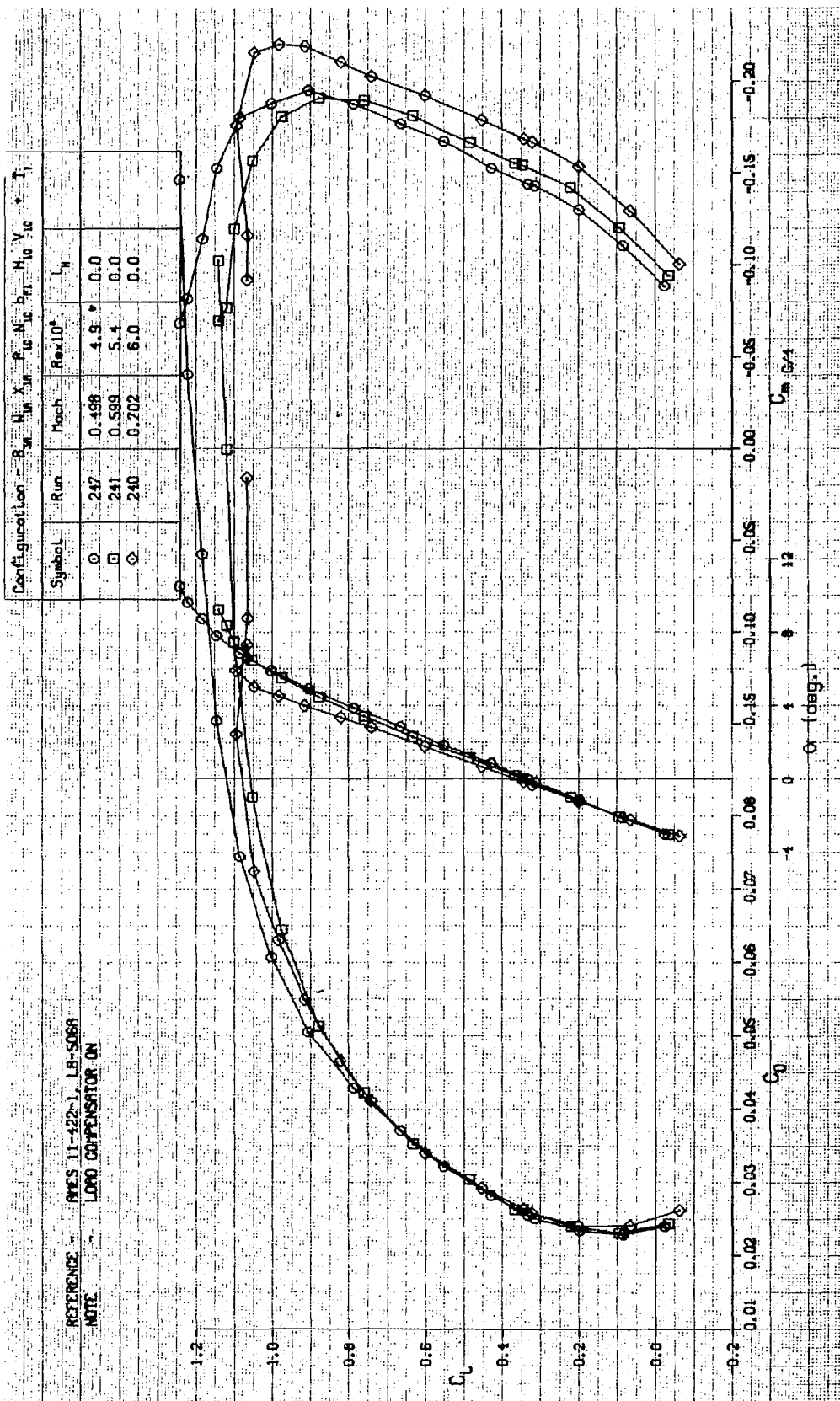
FIGURE A-23. LIFT, DRAG, AND PITCHING MOMENT CHARACTERISTICS OF WING W₁, WITH NACELLES, PYLONS, FLAP LINKAGE FAIRINGS, AND TAIL, TRANSITION FREE
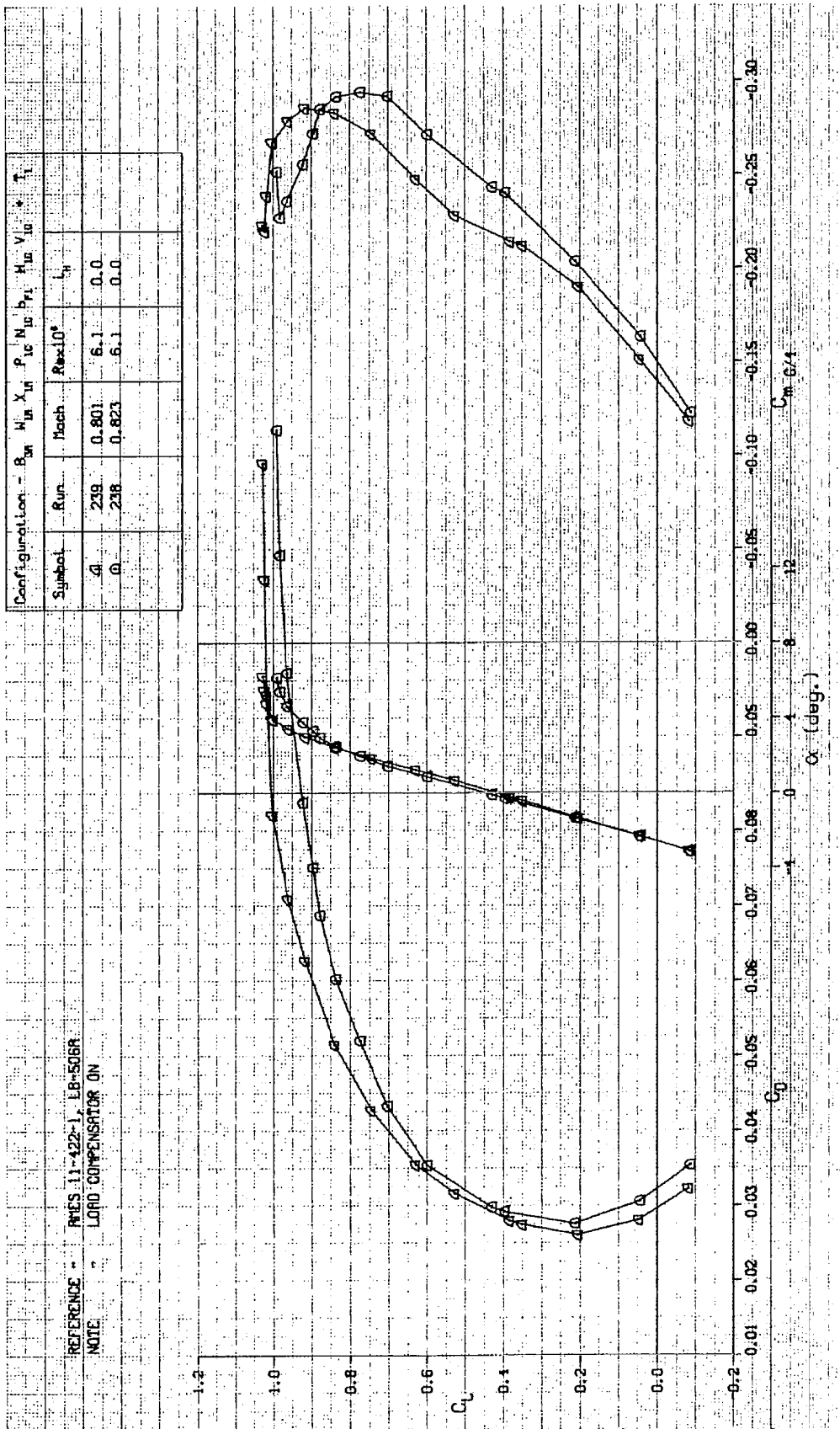
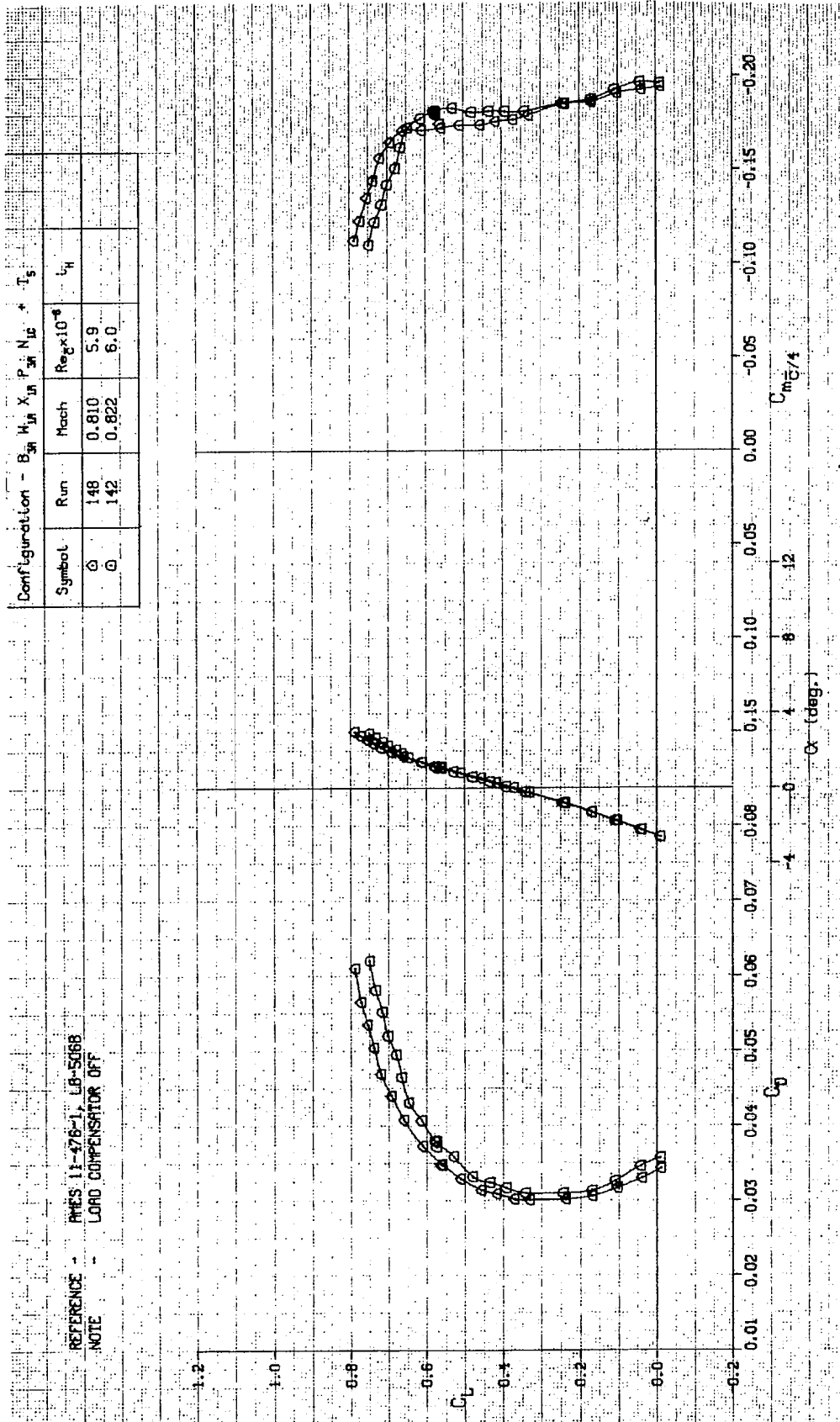FIGURE A-24. LIFT, DRAG, AND PITCHING MOMENT CHARACTERISTICS OF WING W_1, WITH NACELLES, PYLONS, FLAP LINKAGE FAIRINGS, AND TAIL, TRANSITION FREE

Configuration - B_{3R} H_{1R} X_{1R} P_{1C} N_{1C} b_{F1} N_{1C} H_{1C} V_{1C} $+_r$ T_r

Symbol	Run	Mach	$Rex10^6$	i_H
◁	246	0.799	3.0	0.0
⊘	245	0.839	3.0	0.0

FIGURE A-25. LIFT, DRAG, AND PITCHING MOMENT CHARACTERISTICS OF WING W_1, WITH NACELLES, PYLONS, FLAP LINKAGE FAIRINGS, AND TAIL, TRANSITION FREE
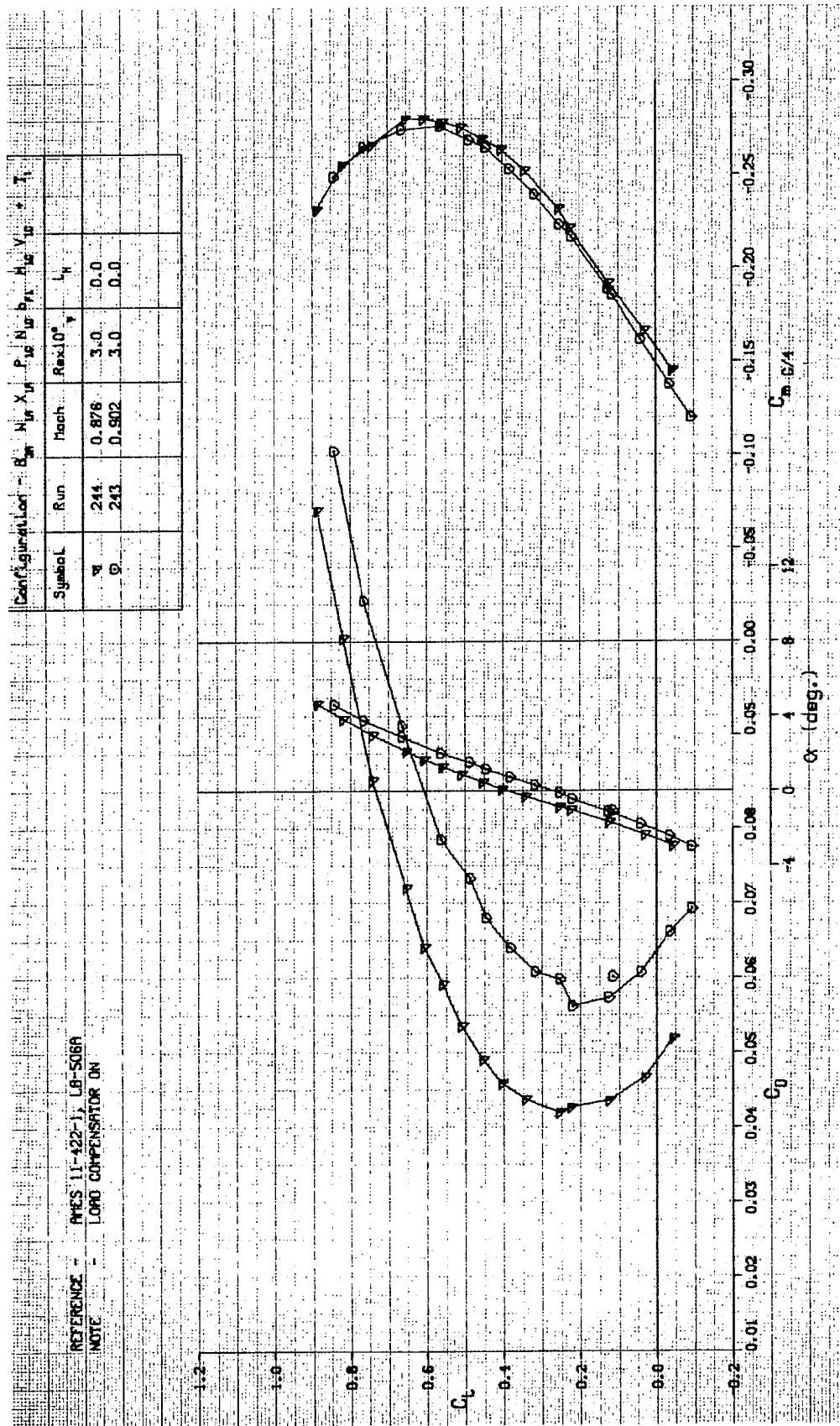
FIGURE A-26. LIFT, DRAG, AND PITCHING MOMENT CHARACTERISTICS OF WING W₁, WITH NACELLES, PYLONS, FLAP LINKAGE FAIRINGS, AND TAIL, TRANSITION FREE
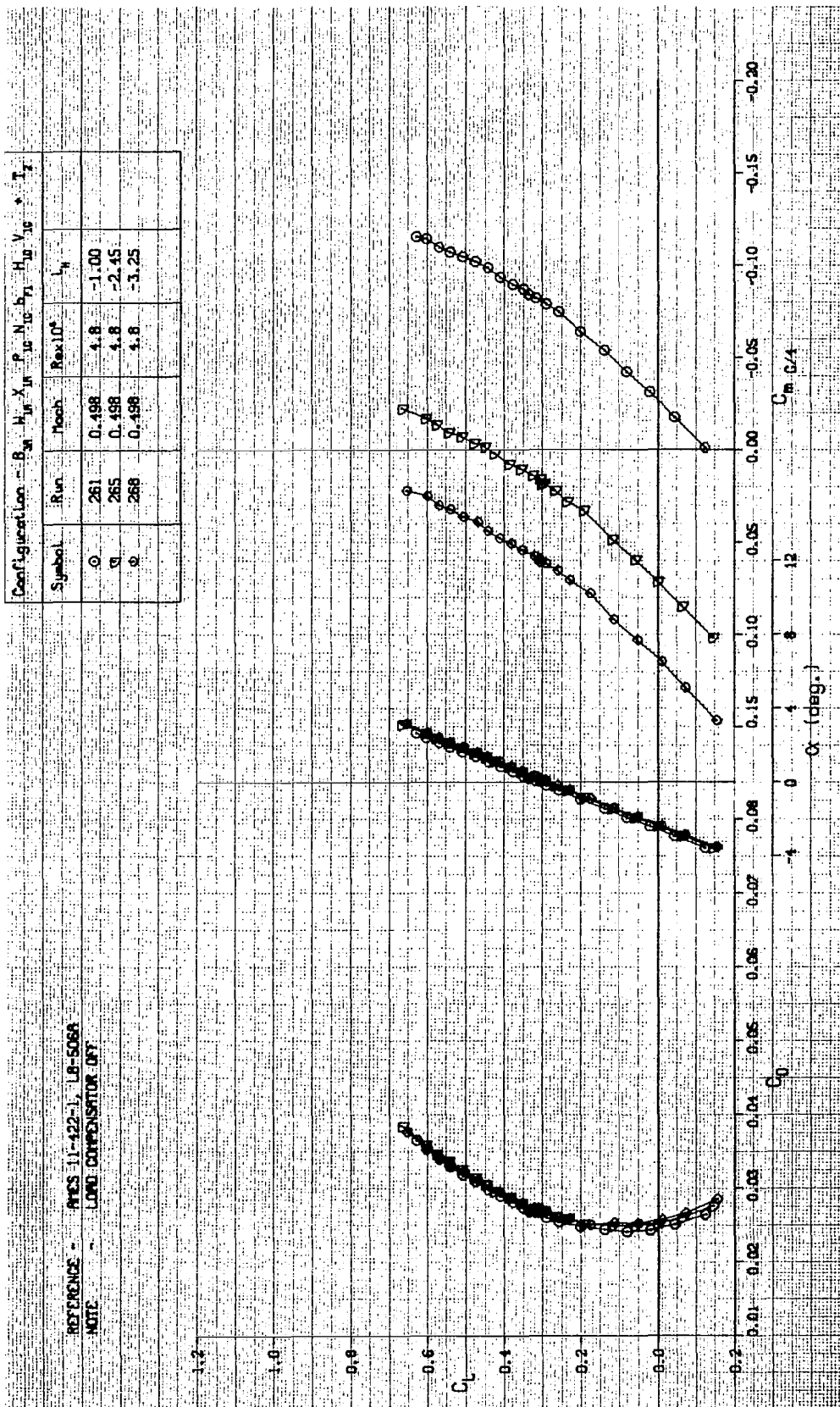
FIGURE A-27. LIFT, DRAG, AND PITCHING MOMENT CHARACTERISTICS OF WING W_1, WITH NACELLES, PYLONS, FLAP LINKAGE FAIRINGS, AND TAIL, TRANSITION FIXED
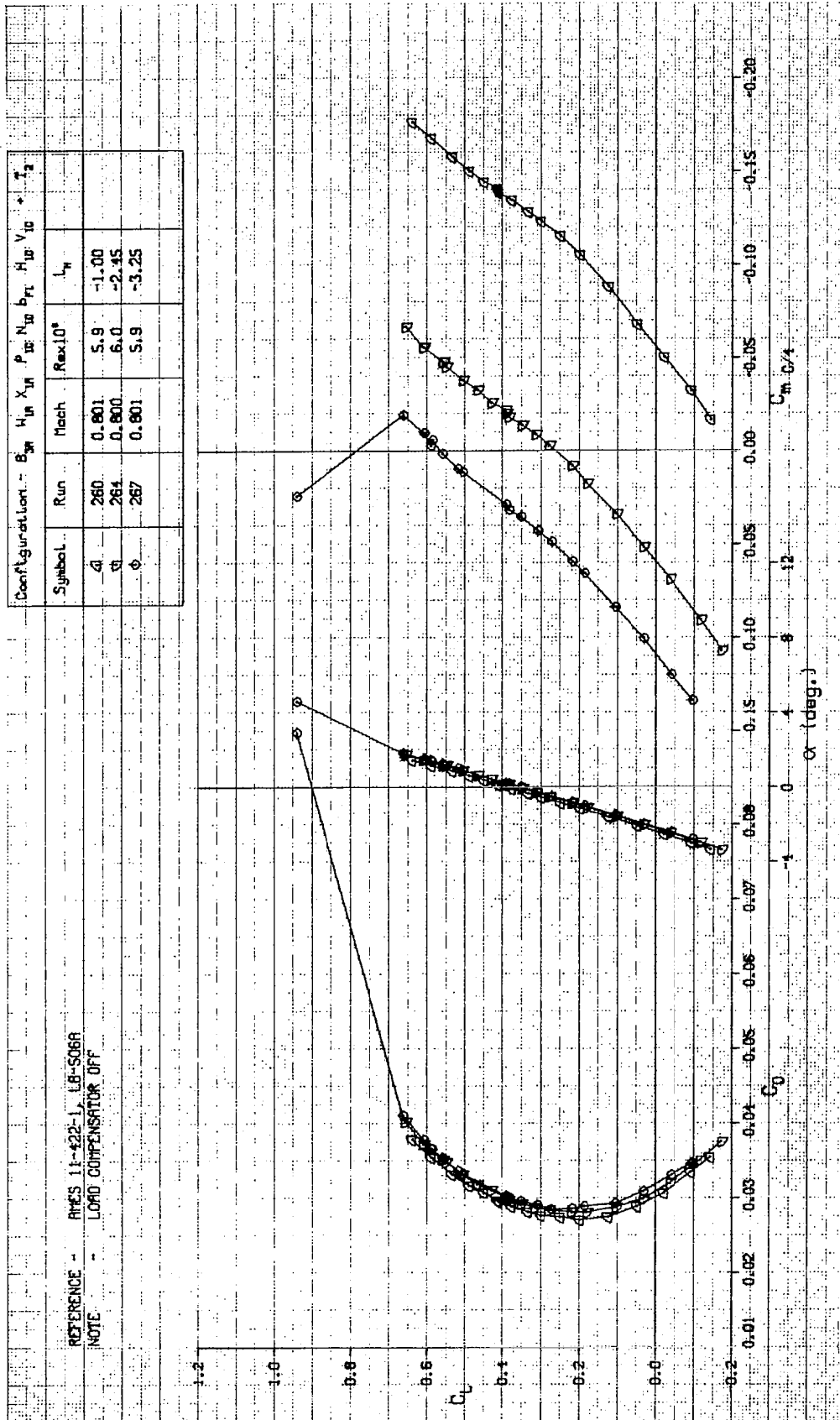
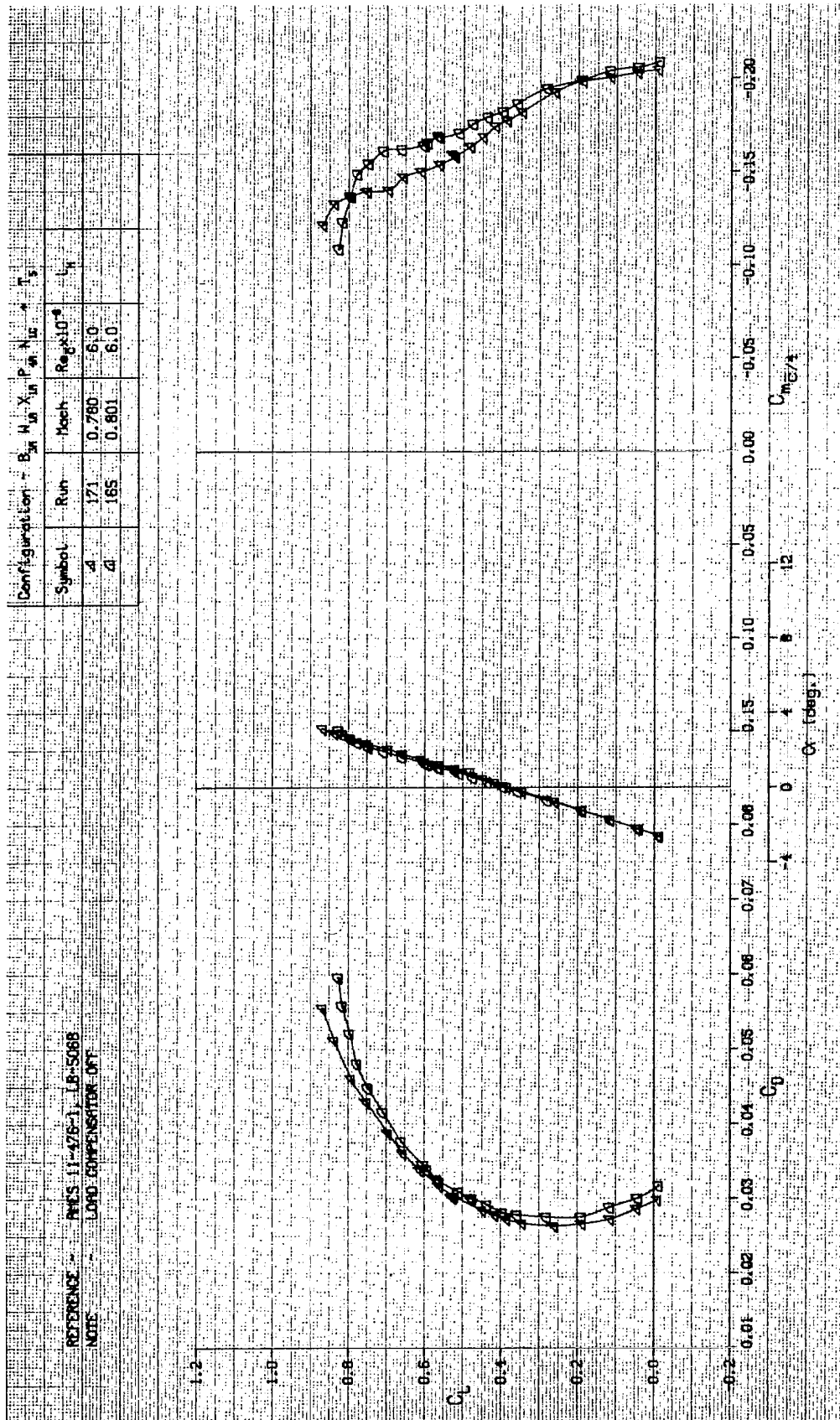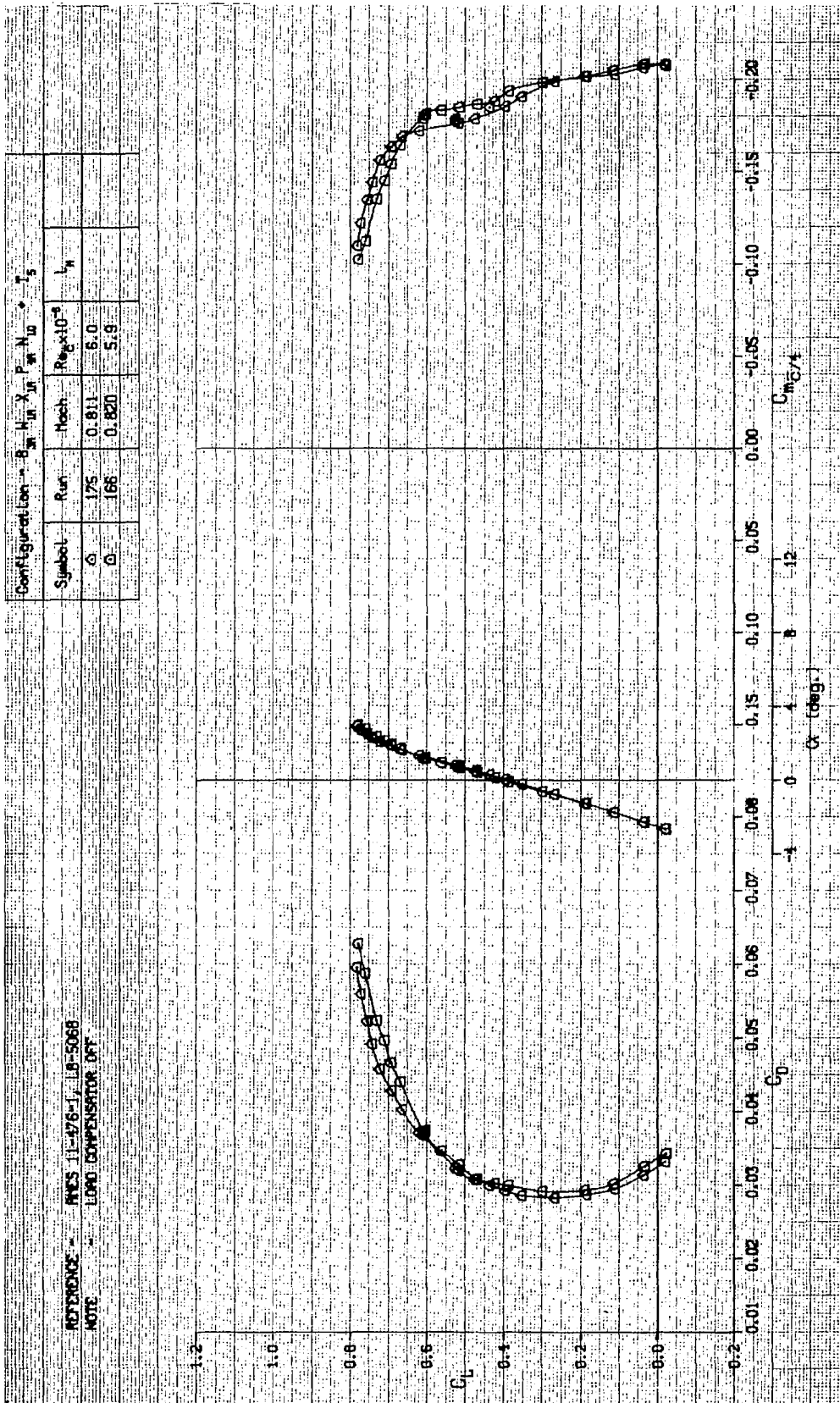FIGURE A-28. LIFT, DRAG, AND PITCHING MOMENT CHARACTERISTICS OF WING W_1, WITH NACELLES, PYLONS, FLAP LINKAGE FAIRINGS, AND TAIL, TRANSITION FIXED
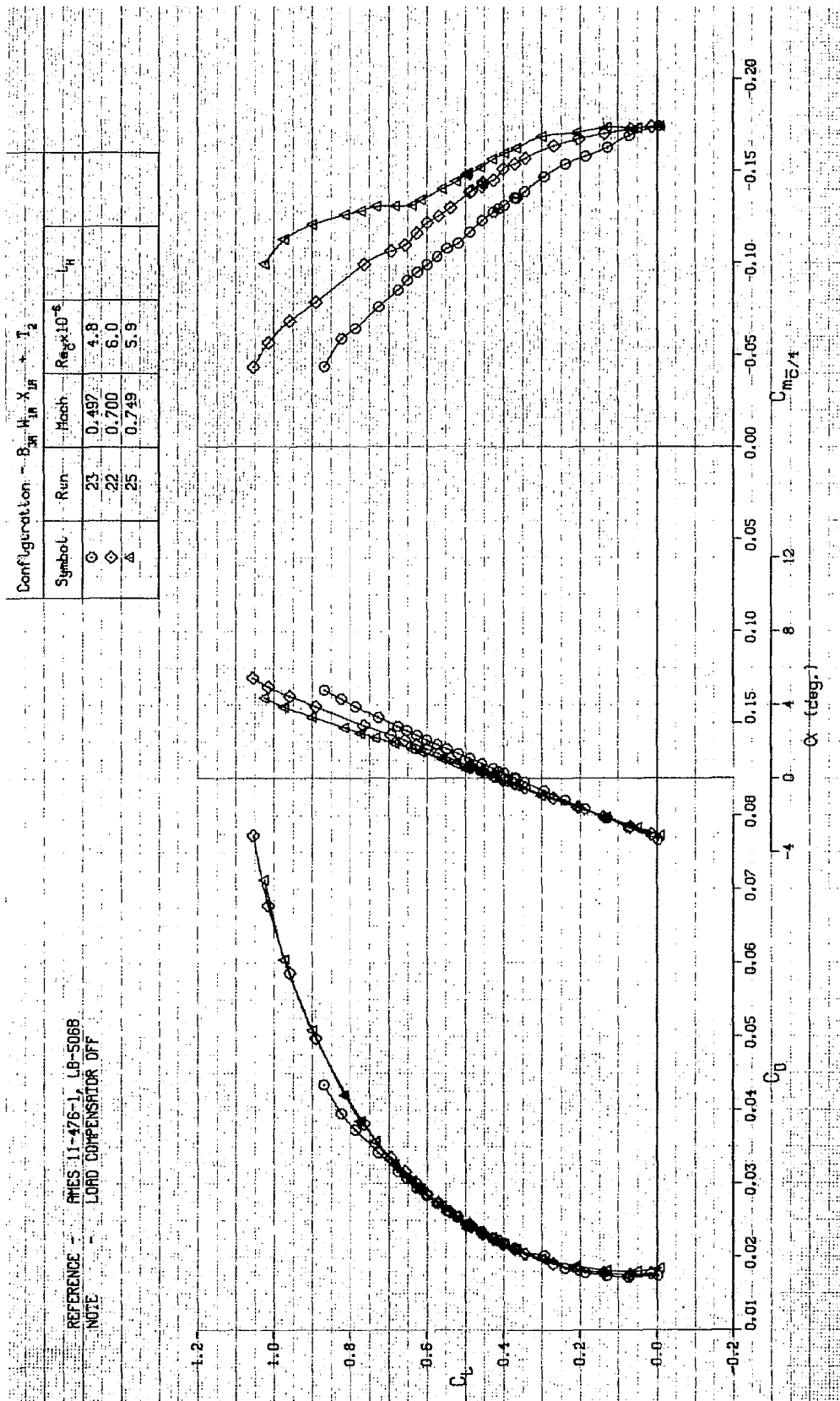
FIGURE A-29. LIFT, DRAG, AND PITCHING MOMENT CHARACTERISTICS OF WING W_1, TRANSITION FIXED
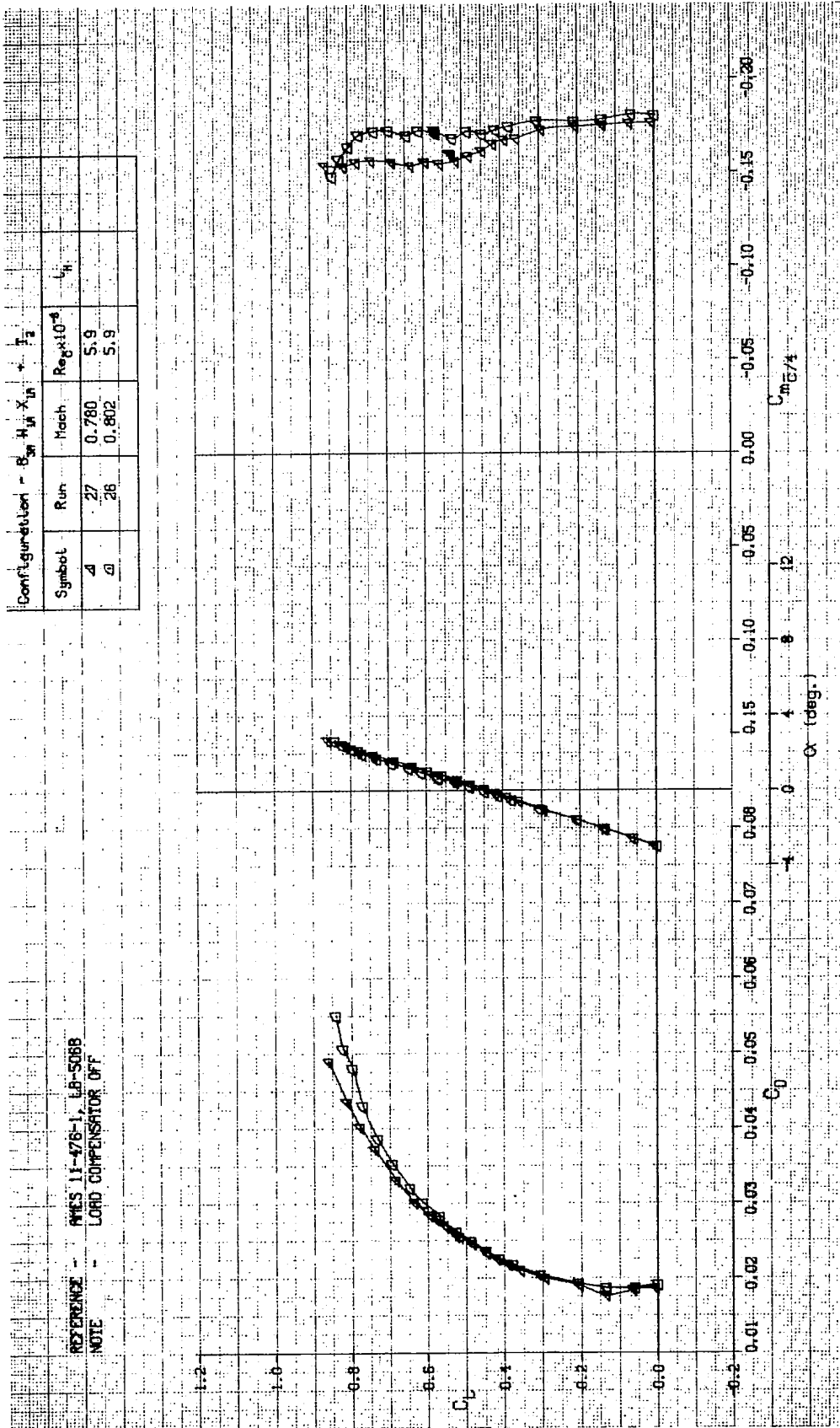
FIGURE A-30. LIFT, DRAG, AND PITCHING MOMENT CHARACTERISTICS OF WING W_1, TRANSITION FIXED
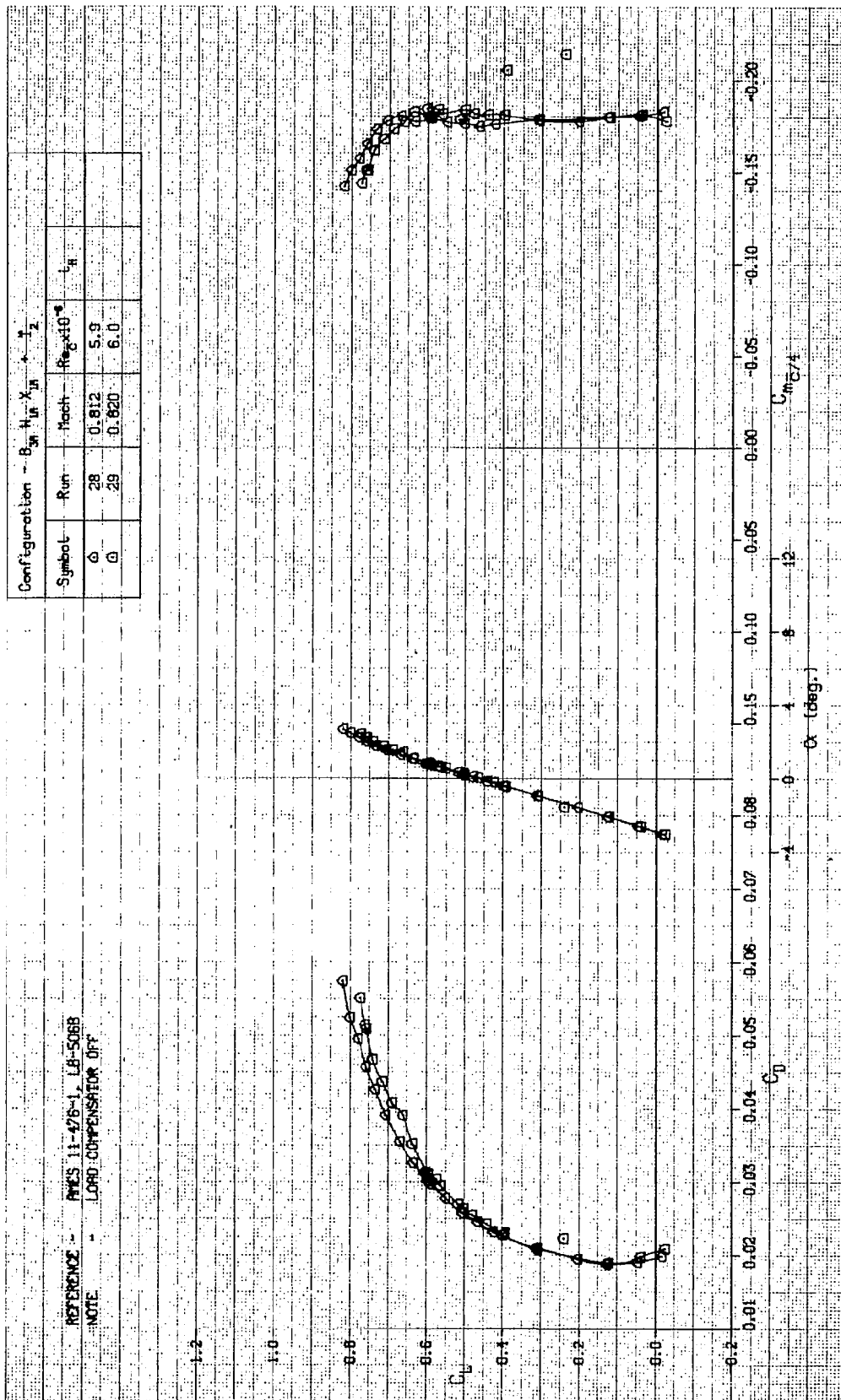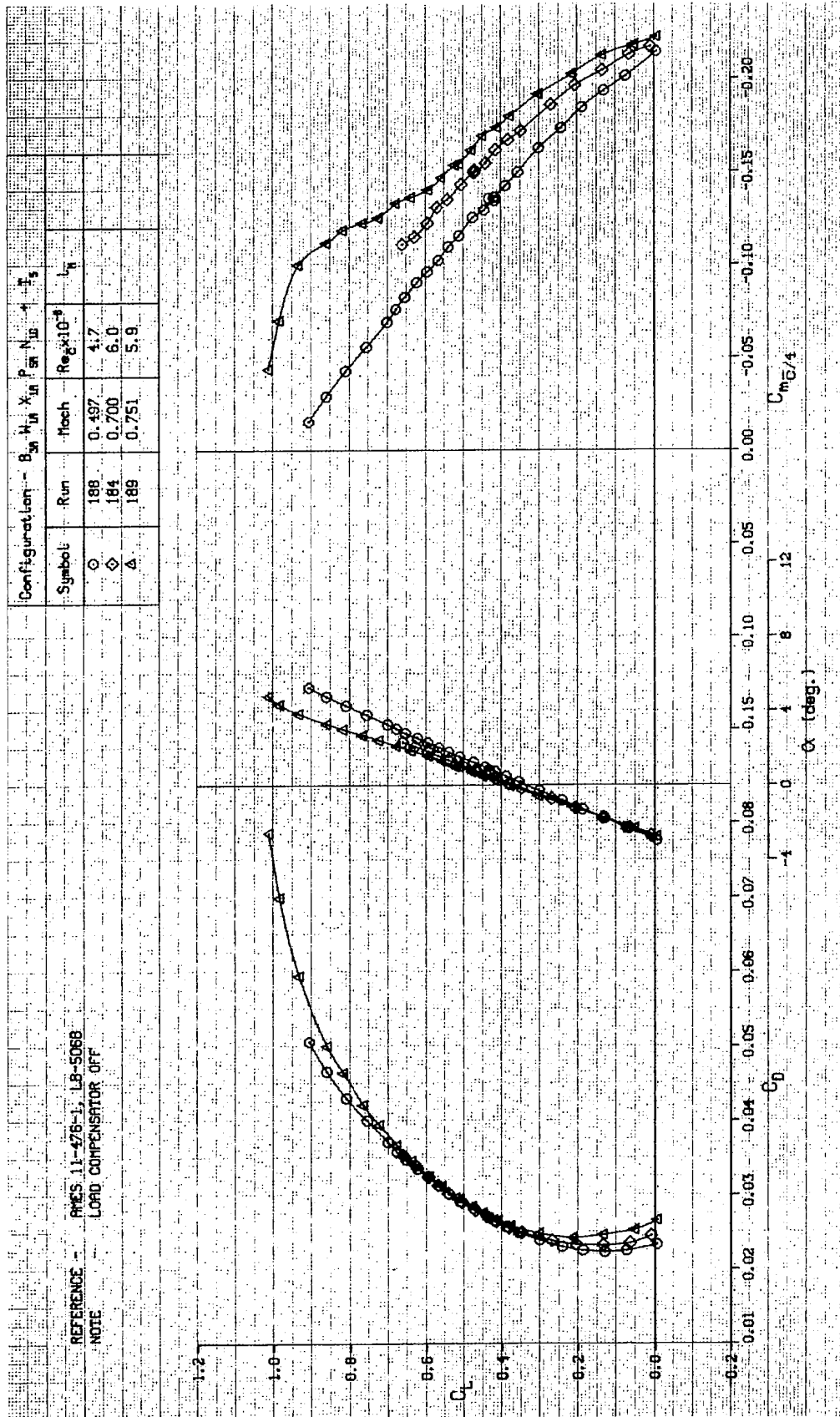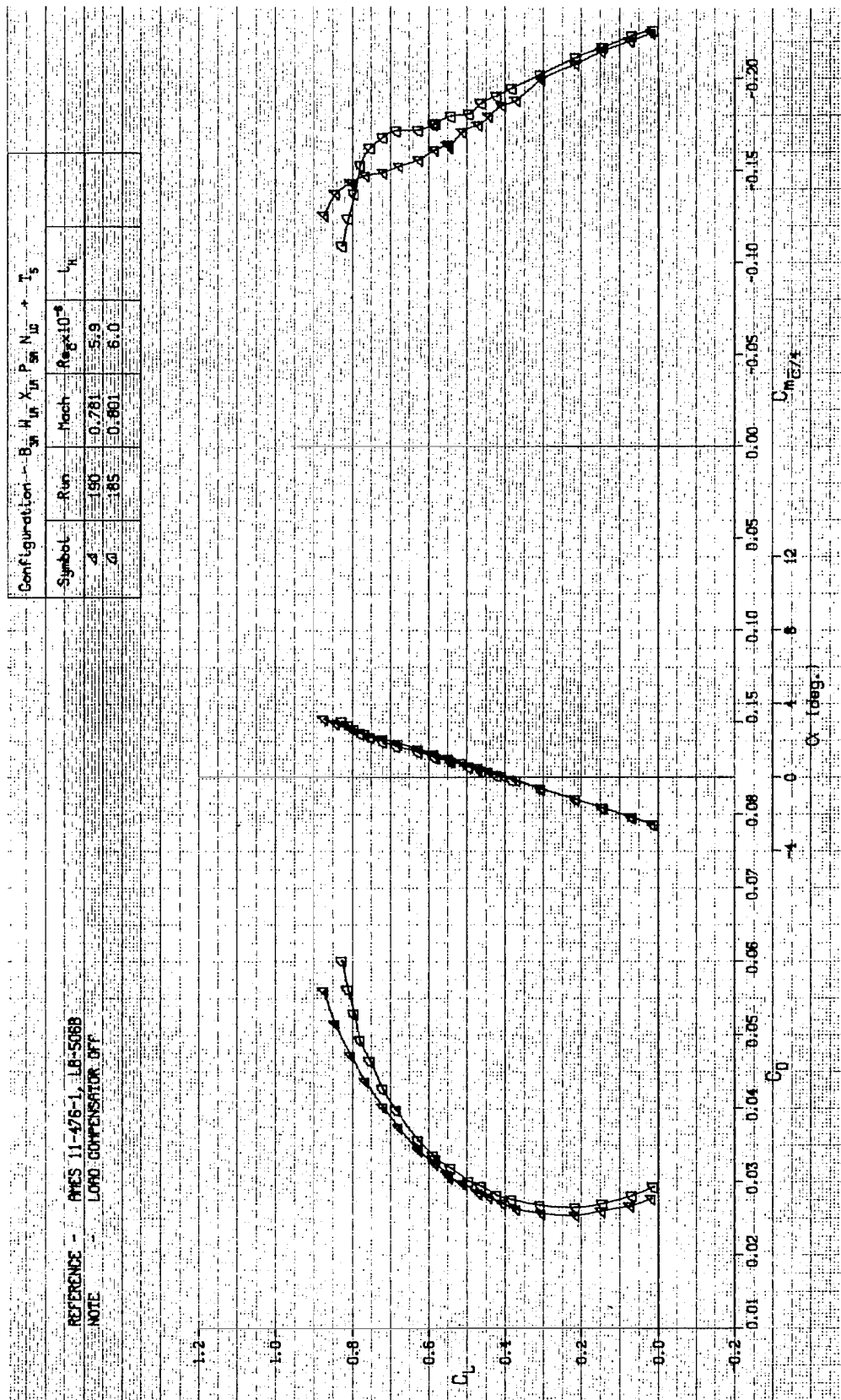
FIGURE A-31. LIFT, DRAG, AND PITCHING MOMENT CHARACTERISTICS OF WING W_1, TRANSITION FIXED

FIGURE A.32. LIFT, DRAG, AND PITCHING MOMENT CHARACTERISTICS OF WING W_1, TRANSITION FIXED

FIGURE A-33. LIFT, DRAG, AND PITCHING MOMENT CHARACTERISTICS OF WING W_1, TRANSITION FIXED

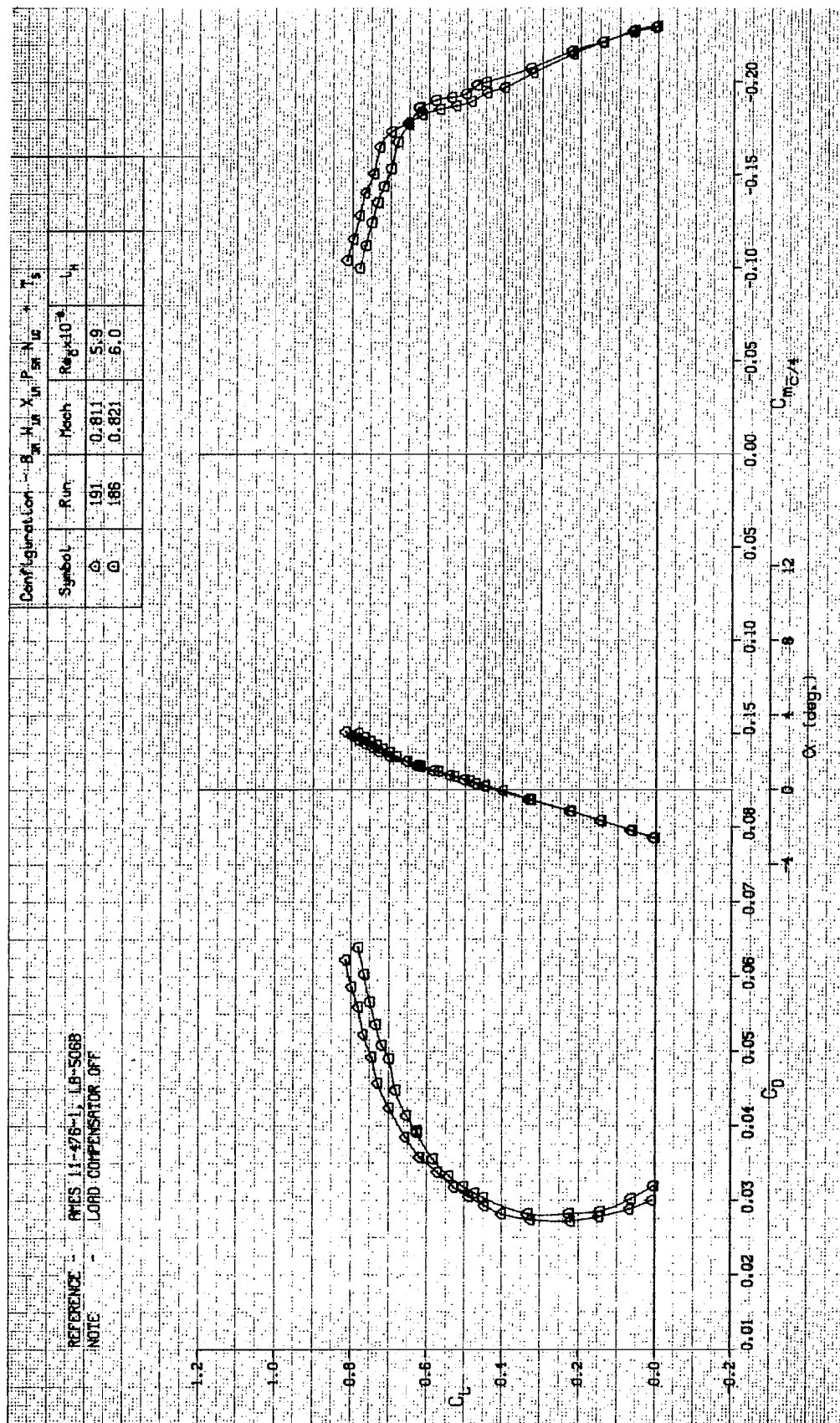FIGURE A-34. LIFT, DRAG, AND PITCHING MOMENT CHARACTERISTICS OF WING W_1, TRANSITION FIXED

A-34

FIGURE A-35. LIFT, DRAG, AND PITCHING MOMENT CHARACTERISTICS OF WING W_1, WITH NACELLES AND PYLONS, TRANSITION FIXED

FIGURE A-36. LIFT, DRAG, AND PITCHING MOMENT CHARACTERISTICS OF WING W_1, WITH NACELLES AND PYLONS, TRANSITION FIXED

REFERENCE - AMES 11-476-1, LB-506B
NOTE - LOAD COMPENSATOR OFF

Configuration - B_5, W_1, X_{1n}, P_{1c}, N_{1c}, T_5

Symbol	Run	Mach	$Re_8 \times 10^{-6}$	i_w
	87	0.780	5.9	
	86	0.801	6.0	

C_L

C_D

$C_{m_{\overline{c}/4}}$

α (deg.)

FIGURE A-37. LIFT, DRAG, AND PITCHING MOMENT CHARACTERISTICS OF WING W_1, WITH NACELLES AND PYLONS, TRANSITION FIXED

A-37
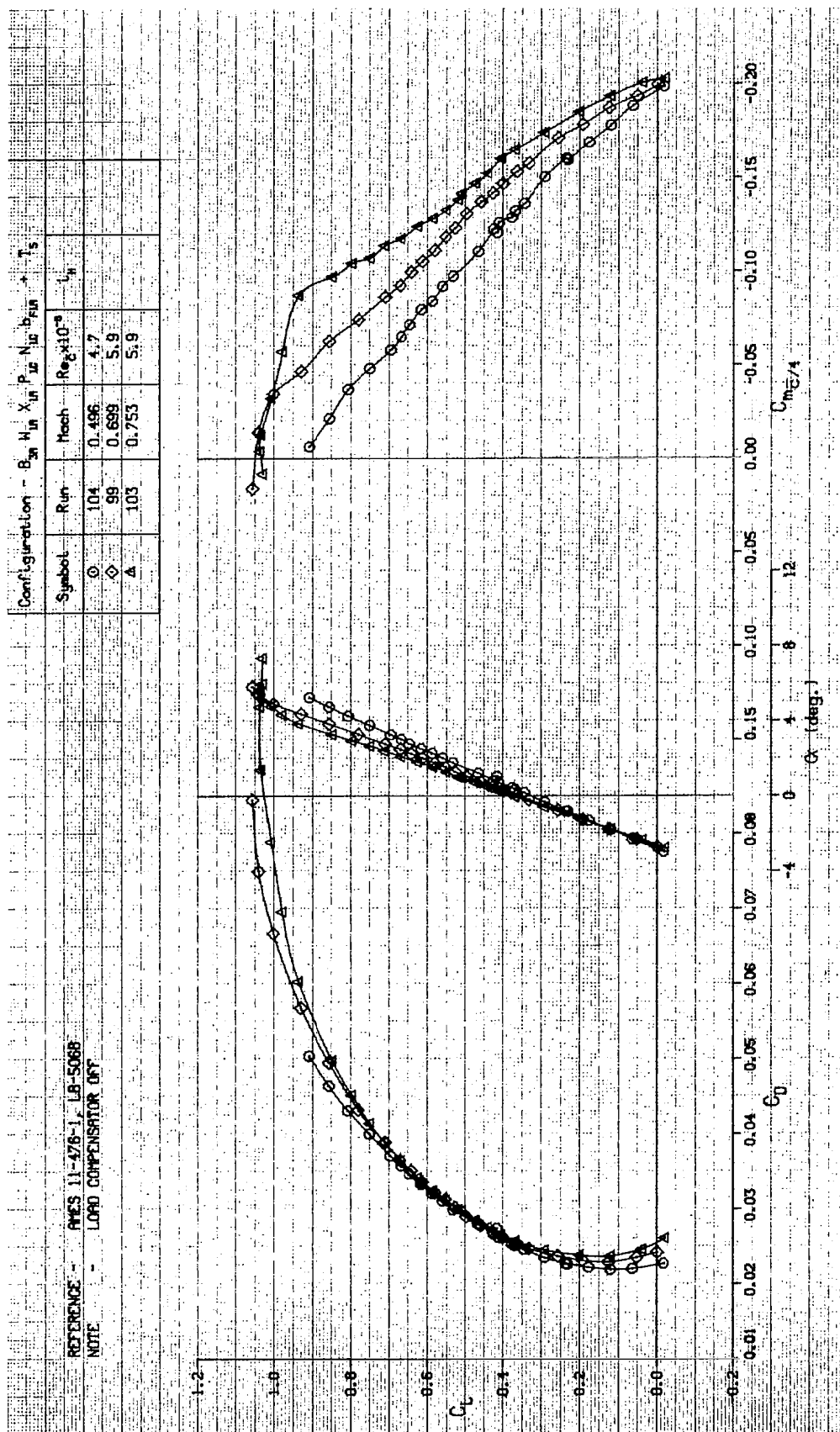
FIGURE A-38. LIFT, DRAG, AND PITCHING MOMENT CHARACTERISTICS OF WING W_1, WITH NACELLES, PYLONS, AND FLAP LINKAGE FAIRINGS, TRANSITION FIXED
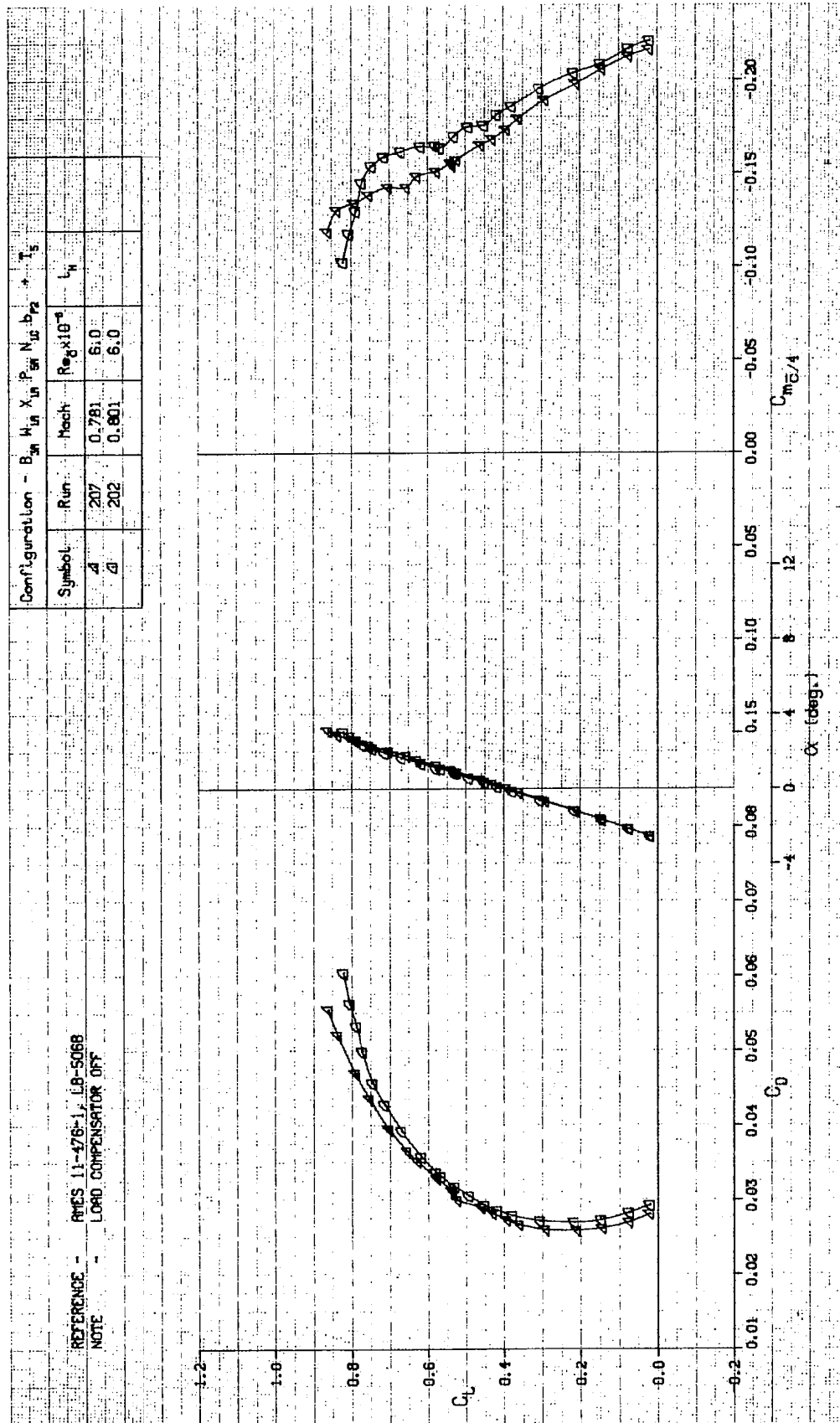
FIGURE A-39. LIFT, DRAG, AND PITCHING MOMENT CHARACTERISTICS OF WING W₁, WITH NACELLES, PYLONS, AND FLAP LINKAGE FAIRINGS, TRANSITION FIXED
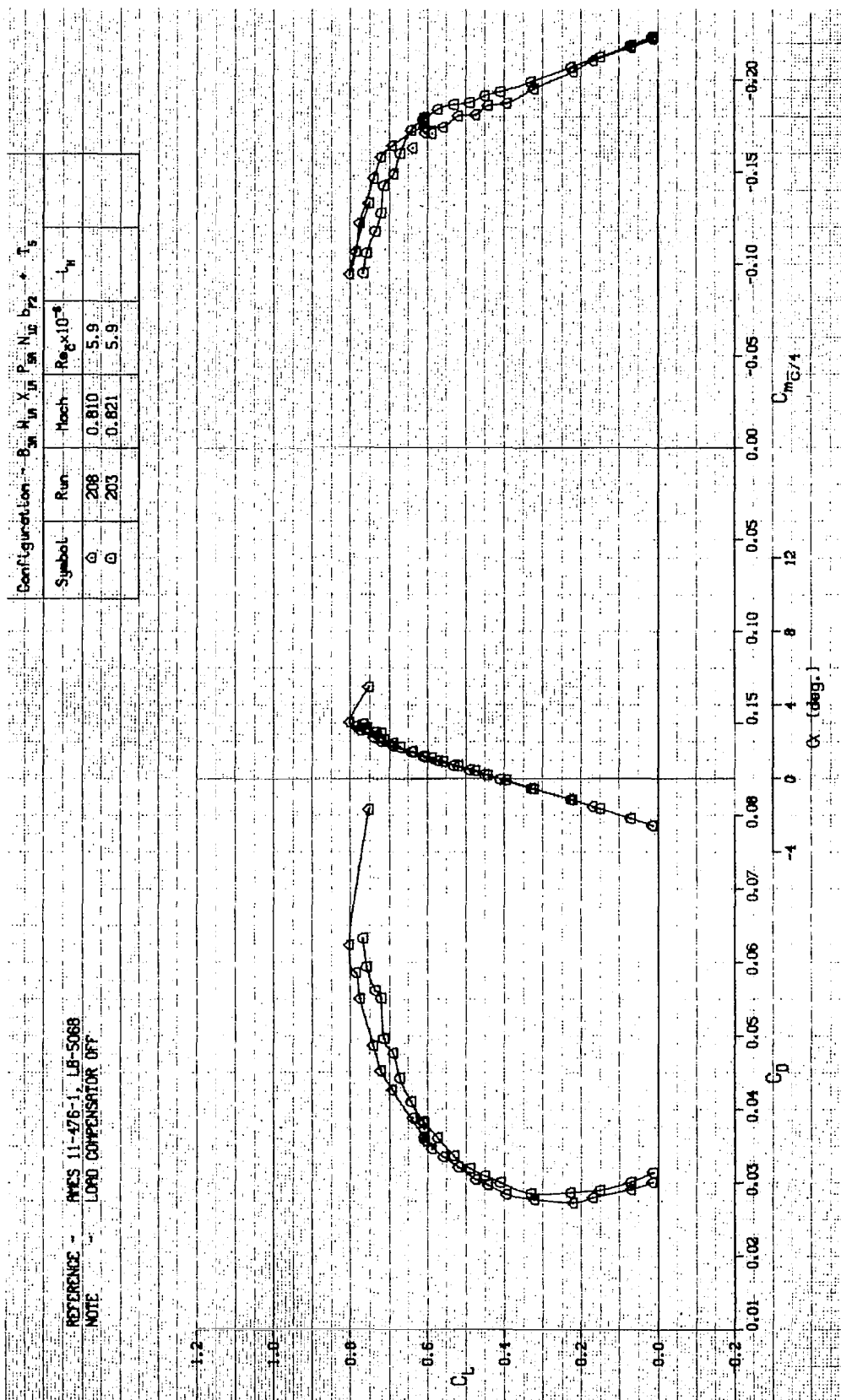
FIGURE A-40. LIFT, DRAG, AND PITCHING MOMENT CHARACTERISTICS OF WING W_1, WITH NACELLES, PYLONS, AND FLAP LINKAGE FAIRINGS, TRANSITION FIXED
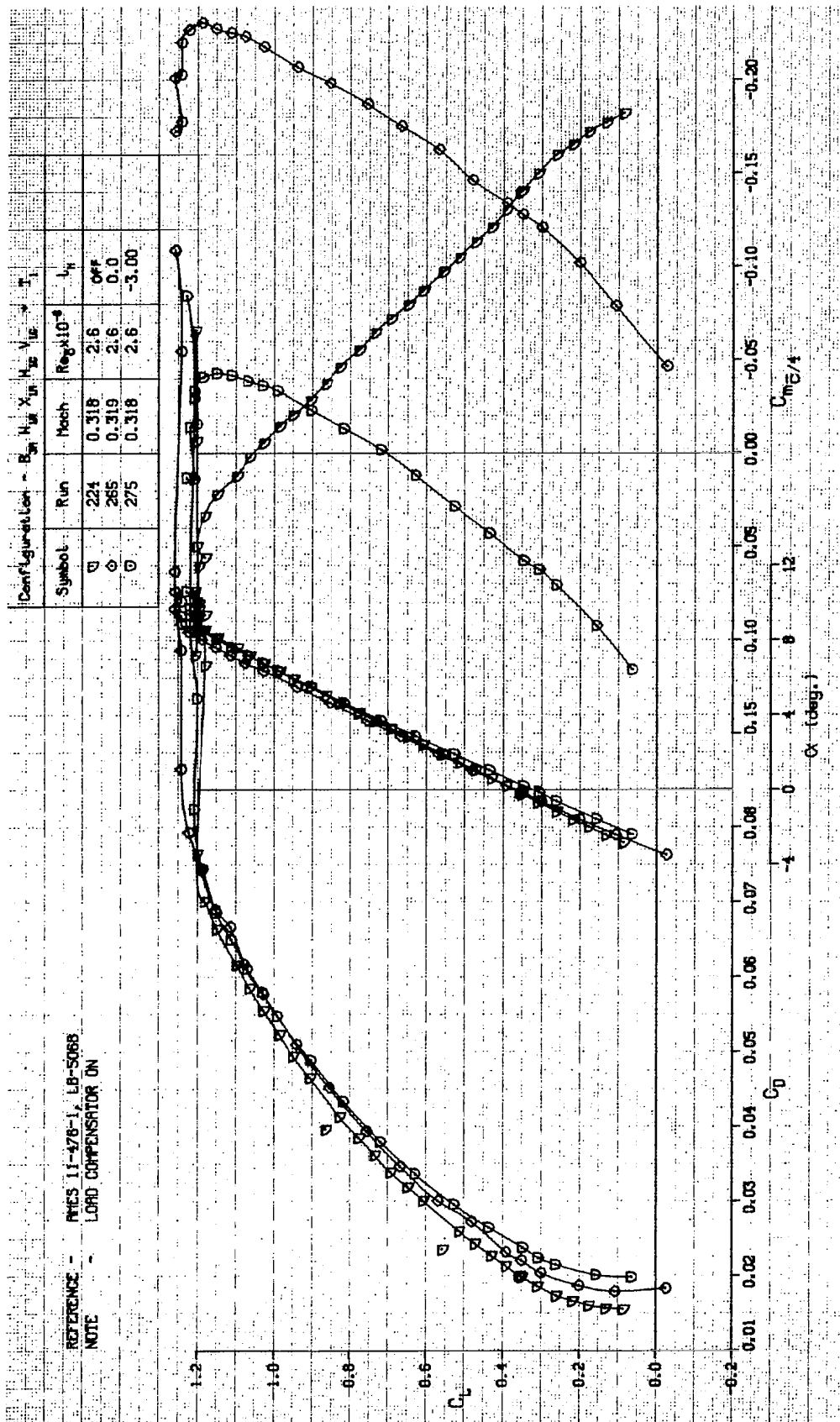
FIGURE A-41. LIFT, DRAG, AND PITCHING MOMENT CHARACTERISTICS OF WING W_1, WITH NACELLES AND PYLONS, TRANSITION FIXED
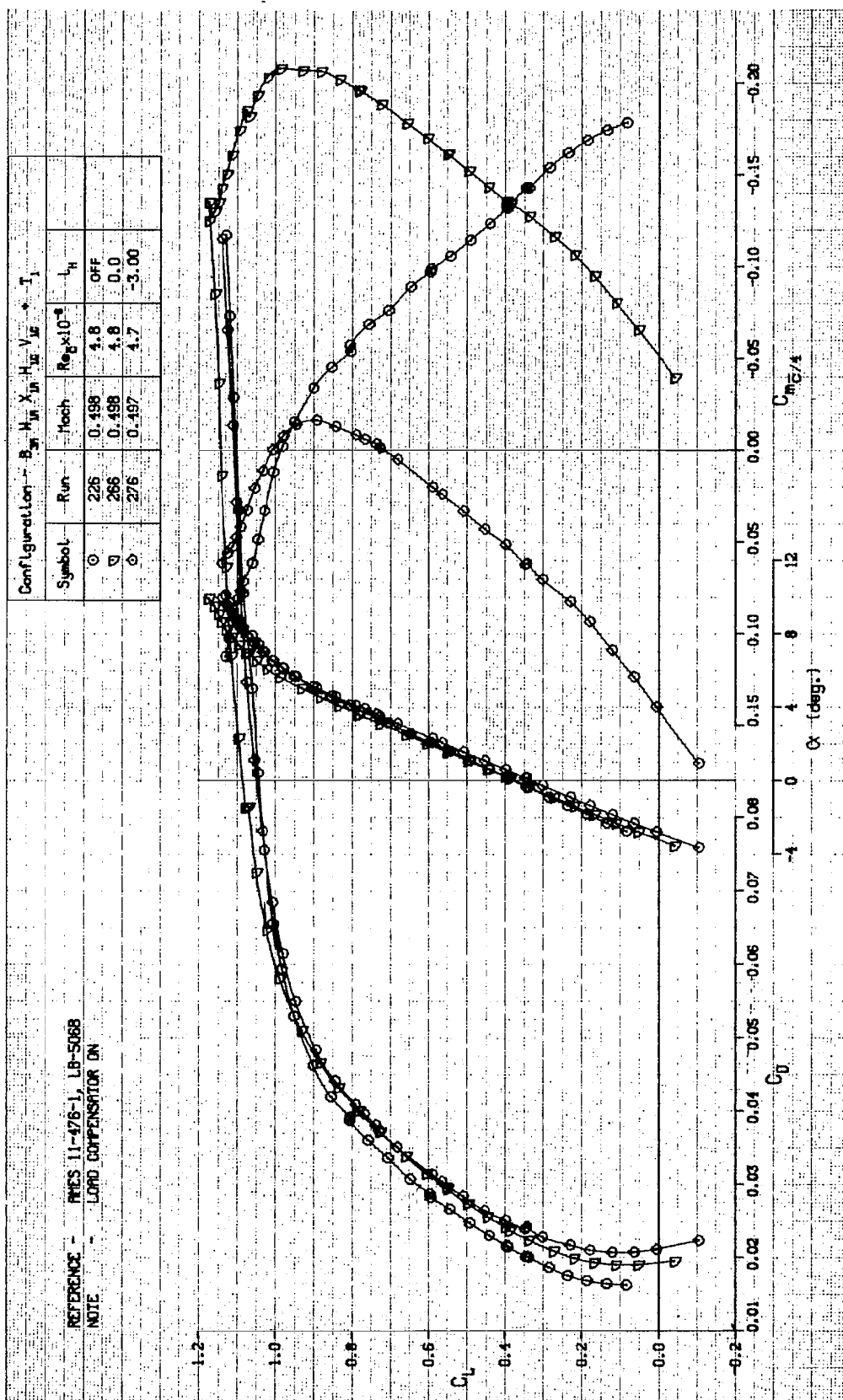
REFERENCE -- AVCS II-A76-1, LB-50888
NOTE -- LONG CONPENSATOR OFF

Symbol	Configuration	Run	Mach.	Rec×10⁻⁶
△		121	0.781	6.0
◁		116	0.800	5.9

PYLONS, TRANSITION FIXED

C_L

$C_{m_{0.25}}$

C_D

α (deg.)

A-42

FIGURE A-43. LIFT, DRAG, AND PITCHING MOMENT CHARACTERISTICS OF WING W_1, WITH NACELLES AND PYLONS, TRANSITION FIXED
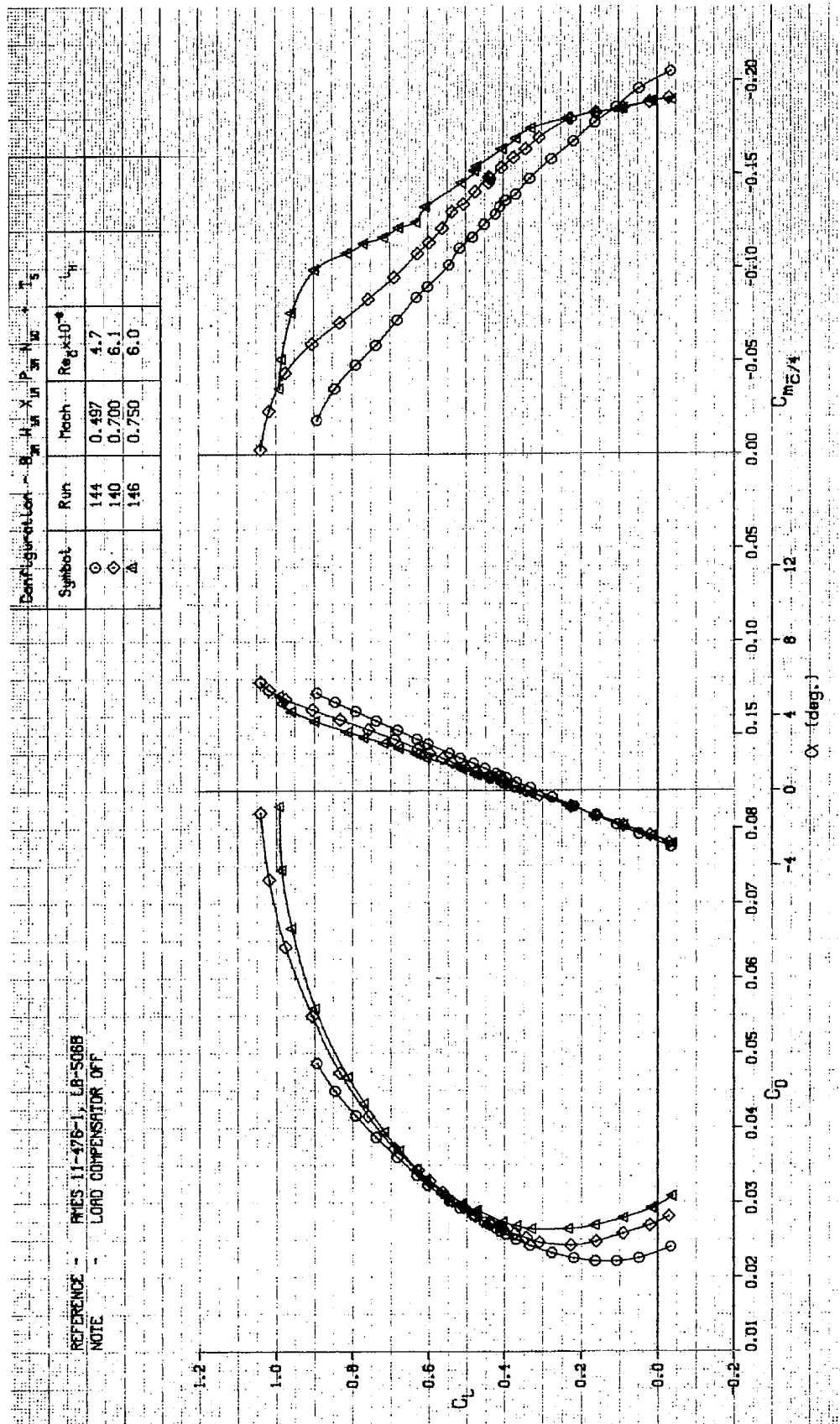
FIGURE A-44. LIFT, DRAG, AND PITCHING MOMENT CHARACTERISTICS OF WING W_1, WITH NACELLES AND PYLONS, TRANSITION FIXED

A-44

Configuration - B_3, H_1, X_1, P_3, N_{12} + T_5

Symbol	Run	Mach	$Re_{\bar{c}} \times 10^{-6}$	i_H
◁	147	0.780	5.9	
◻	141	0.801	5.9	

REFERENCE - AMCS 11-476-1, L8-506B
NOTE - LOAD COMPENSATOR OFF

C_L

C_D

$C_{m\bar{c}/4}$

α (deg.)
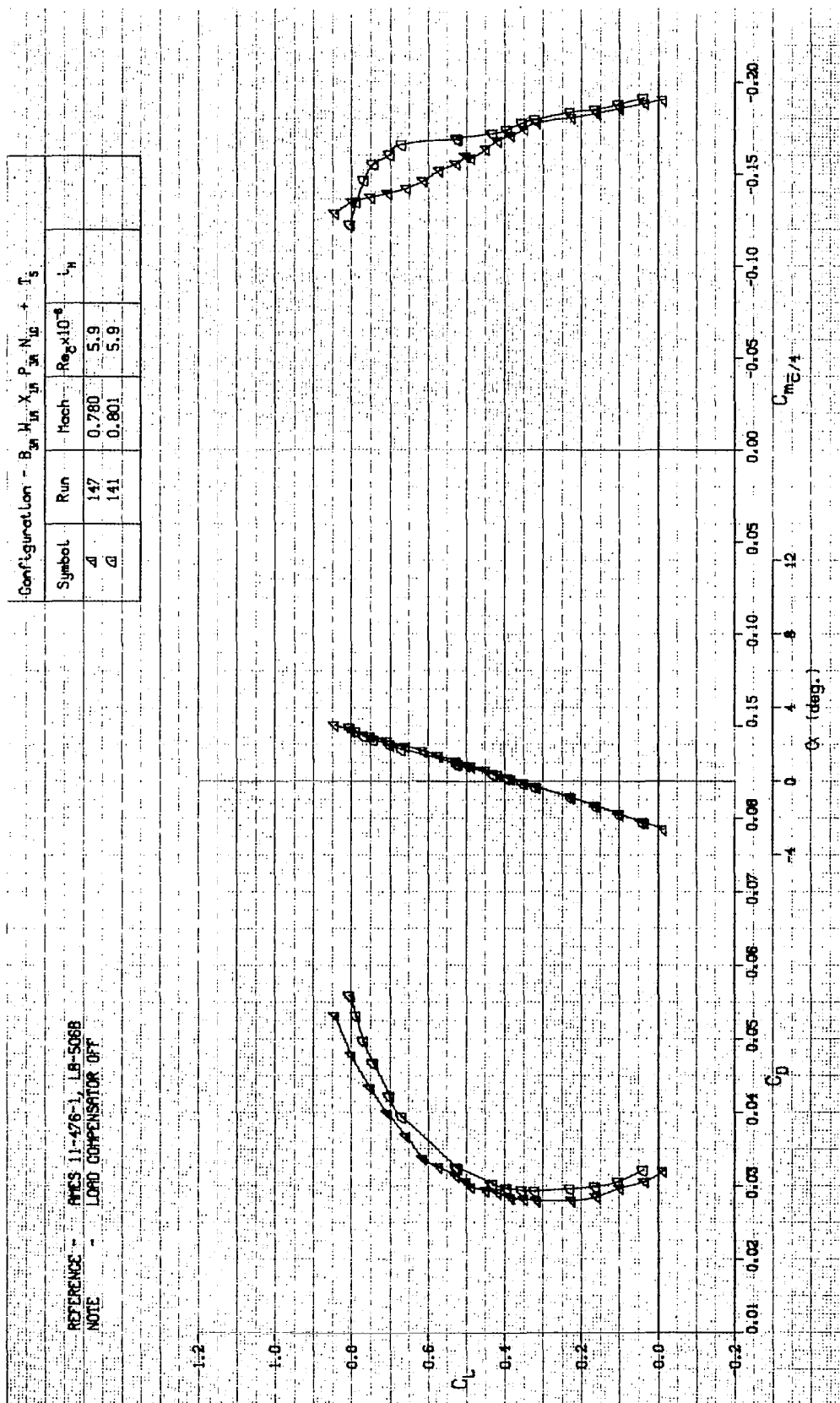
FIGURE A-45. LIFT, DRAG, AND PITCHING MOMENT CHARACTERISTICS OF WING W_1, WITH NACELLES AND PYLONS, TRANSITION FIXED

FIGURE A-46. LIFT, DRAG, AND PITCHING MOMENT CHARACTERISTICS OF WING W_1, WITH NACELLES AND PYLONS, TRANSITION FIXED

A-46
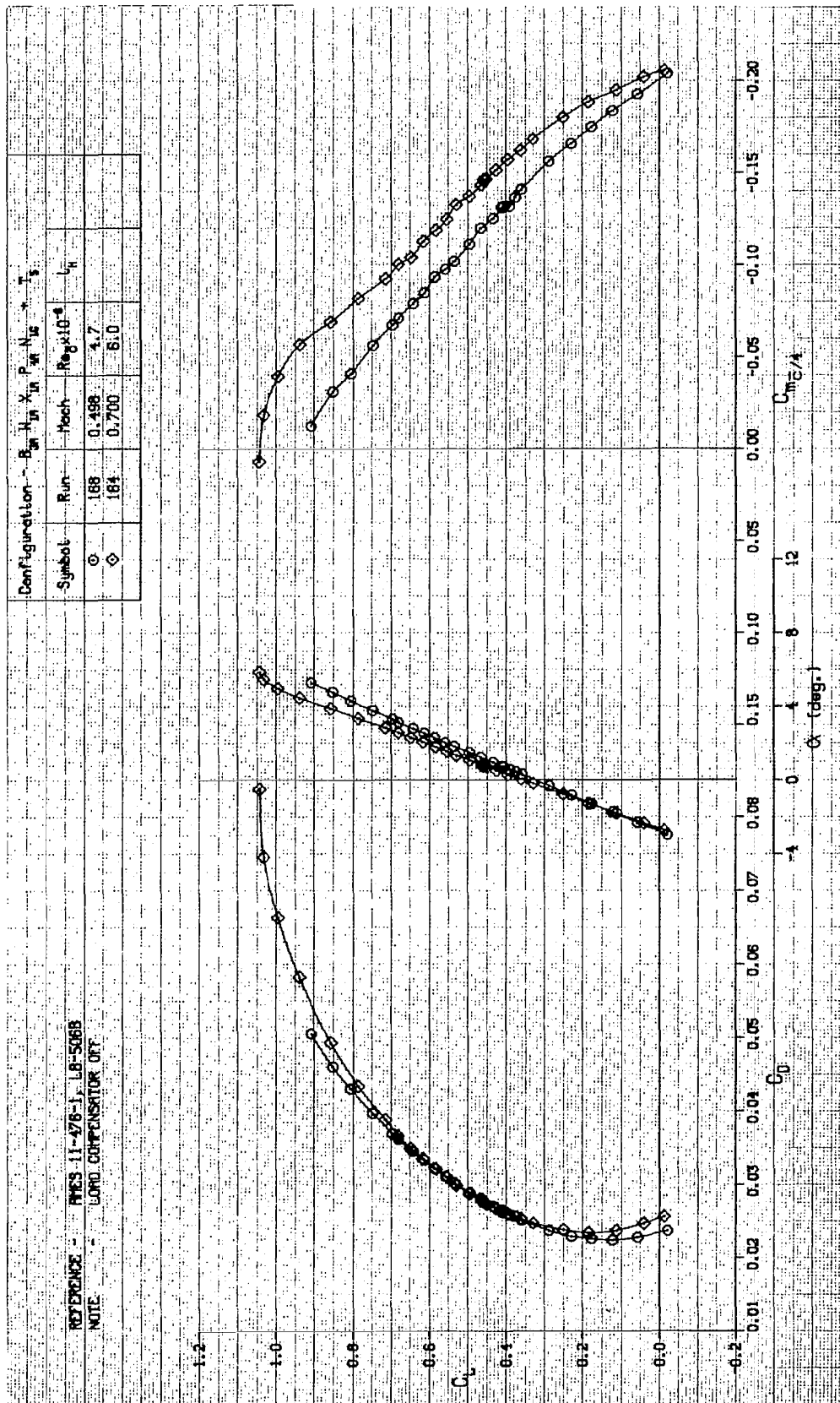
FIGURE A-47. LIFT, DRAG, AND PITCHING MOMENT CHARACTERISTICS OF WING W_1, WITH NACELLES AND PYLONS, TRANSITION FIXED

FIGURE A-48. LIFT, DRAG, AND PITCHING MOMENT CHARACTERISTICS OF WING W_1, WITH NACELLES AND PYLONS, TRANSITION FIXED

A-48

FIGURE A-49. LIFT, DRAG, AND PITCHING MOMENT CHARACTERISTICS OF WING W_1, WITH NACELLES AND PYLONS, TRANSITION FIXED

FIGURE A-50. LIFT, DRAG, AND PITCHING MOMENT CHARACTERISTICS OF WING W_1, WITH NACELLES AND PYLONS, TRANSITION FIXED

FIGURE A-51. LIFT, DRAG, AND PITCHING MOMENT CHARACTERISTICS OF WING W_1, WITH NACELLES AND PYLONS, TRANSITION FIXED

FIGURE A-52. LIFT, DRAG, AND PITCHING MOMENT CHARACTERISTICS OF WING W_1, WITH NACELLES AND PYLONS, TRANSITION FIXED
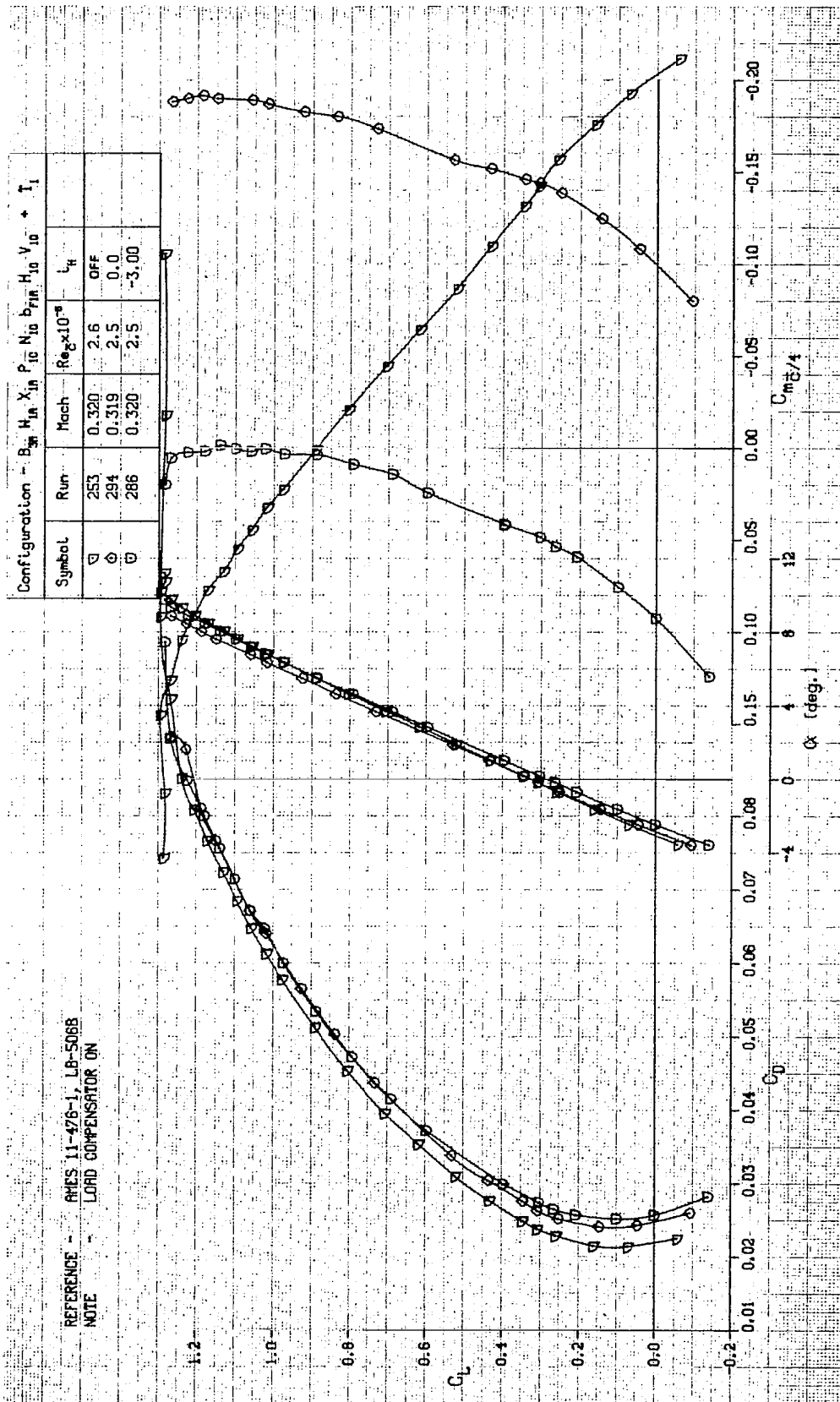
A-52
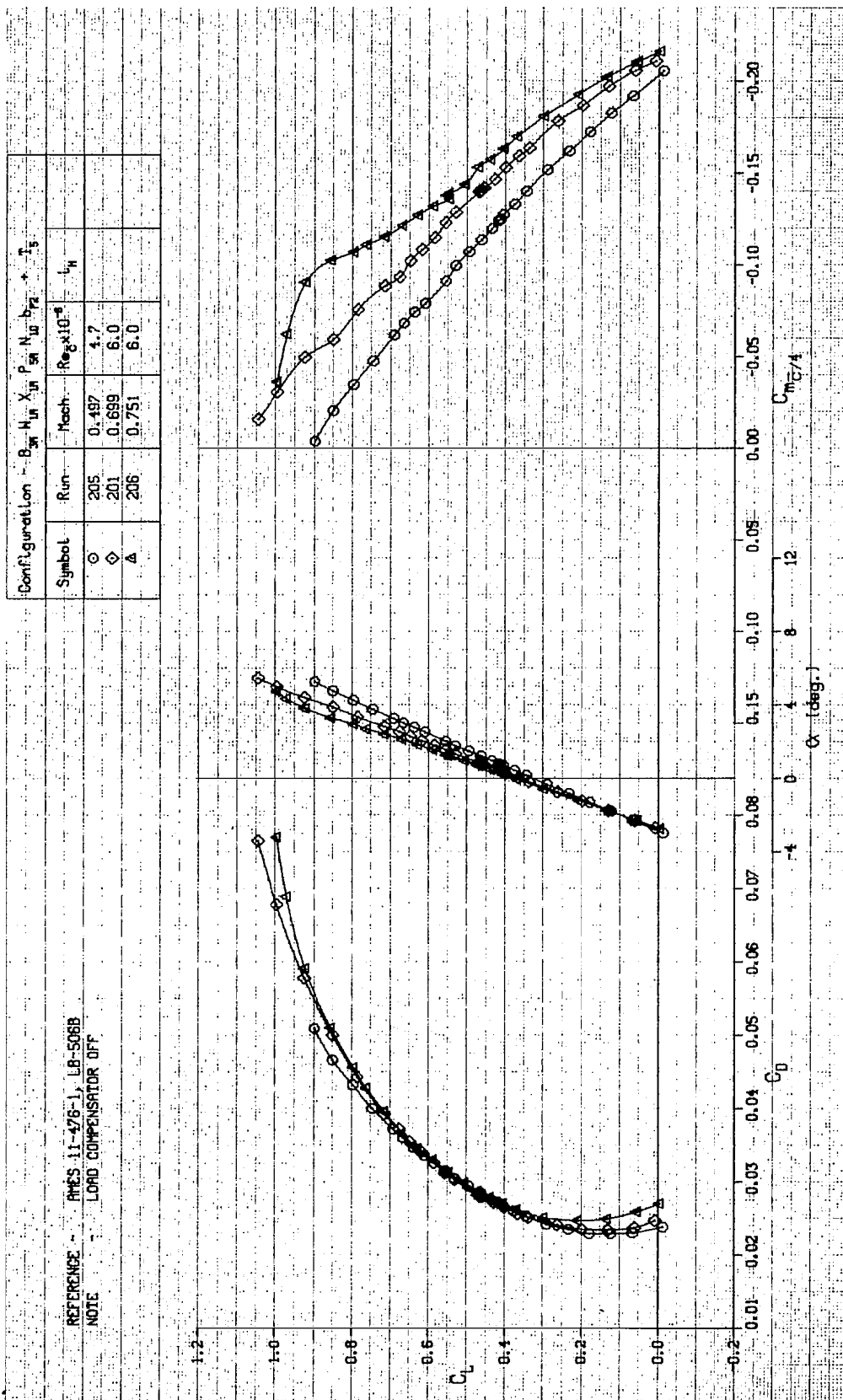
FIGURE A-53. LIFT, DRAG, AND PITCHING MOMENT CHARACTERISTICS OF WING W₁, WITH NACELLES, PYLONS, AND FLAP LINKAGE FAIRINGS, TRANSITION FIXED

FIGURE A-54. LIFT, DRAG, AND PITCHING MOMENT CHARACTERISTICS OF WING W_1, WITH NACELLES, PYLONS, AND FLAP LINKAGE FAIRINGS, TRANSITION FIXED
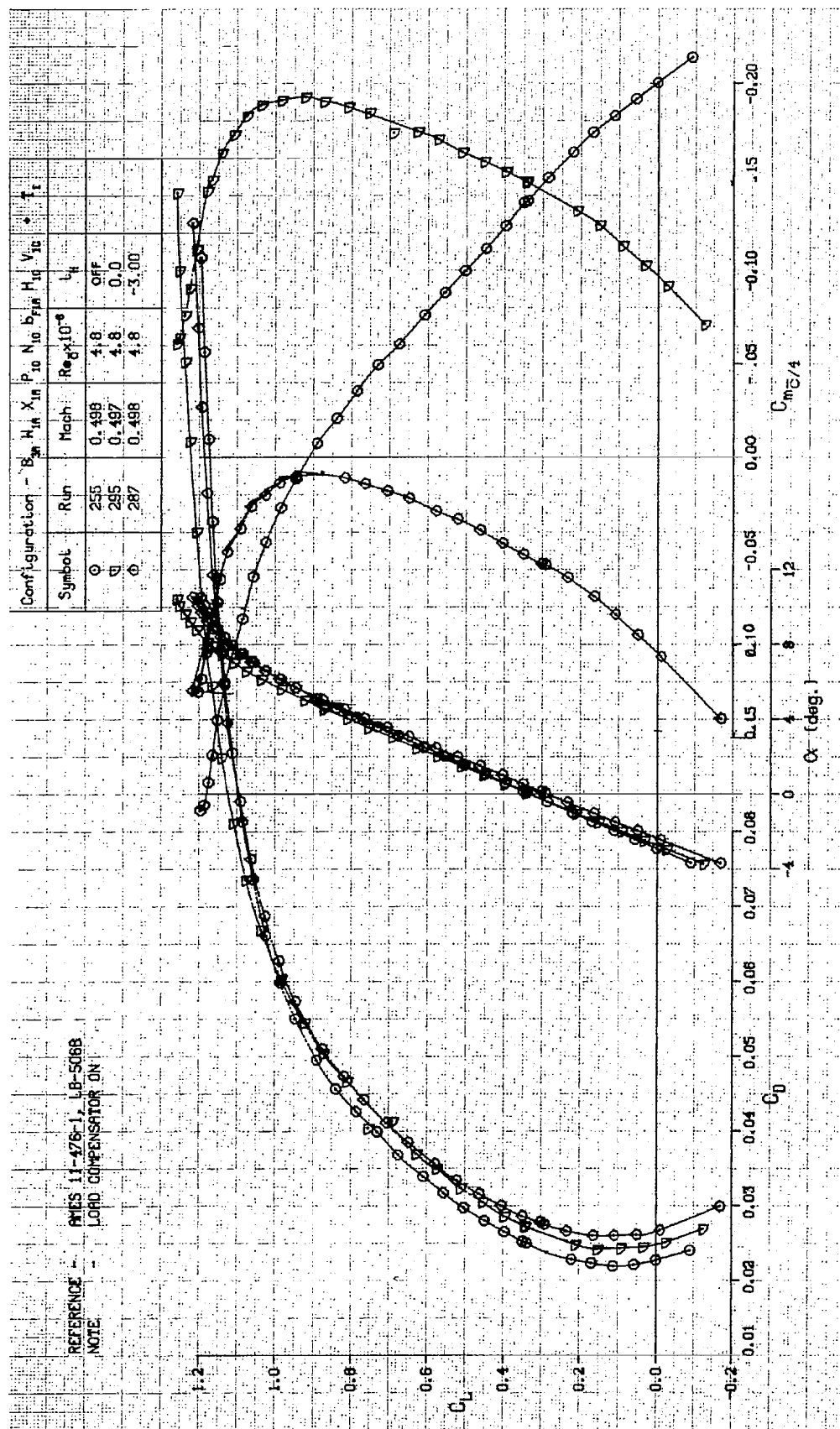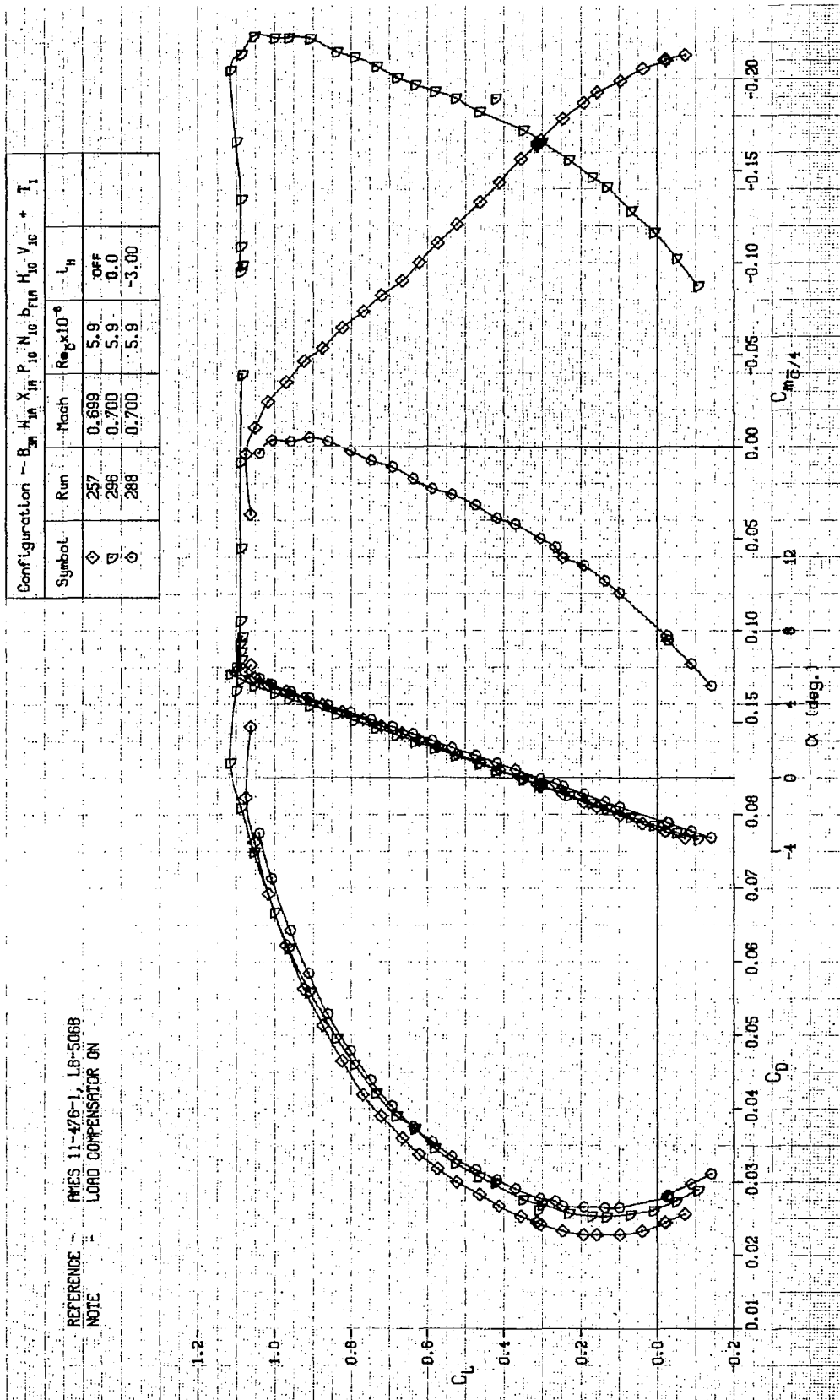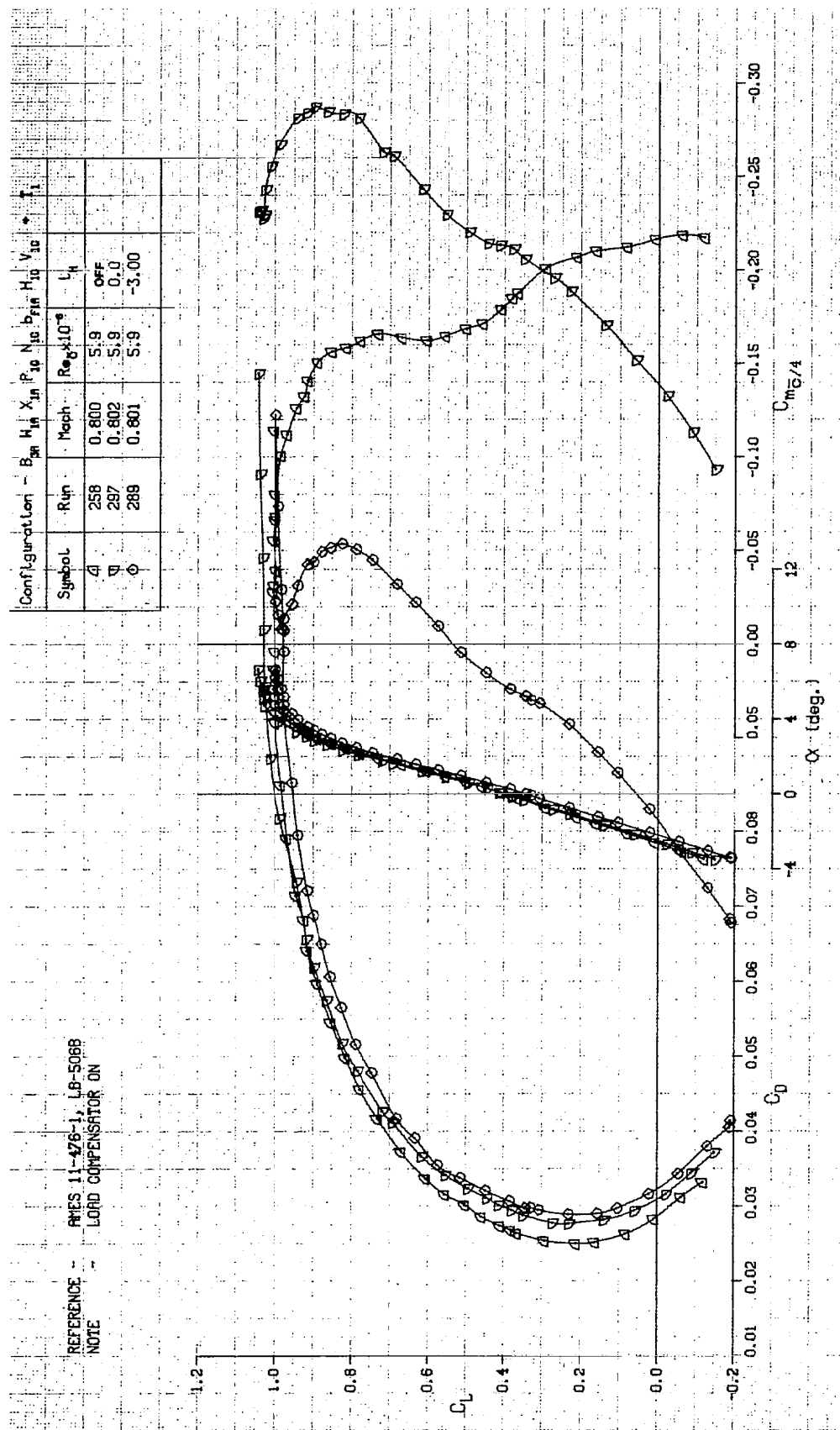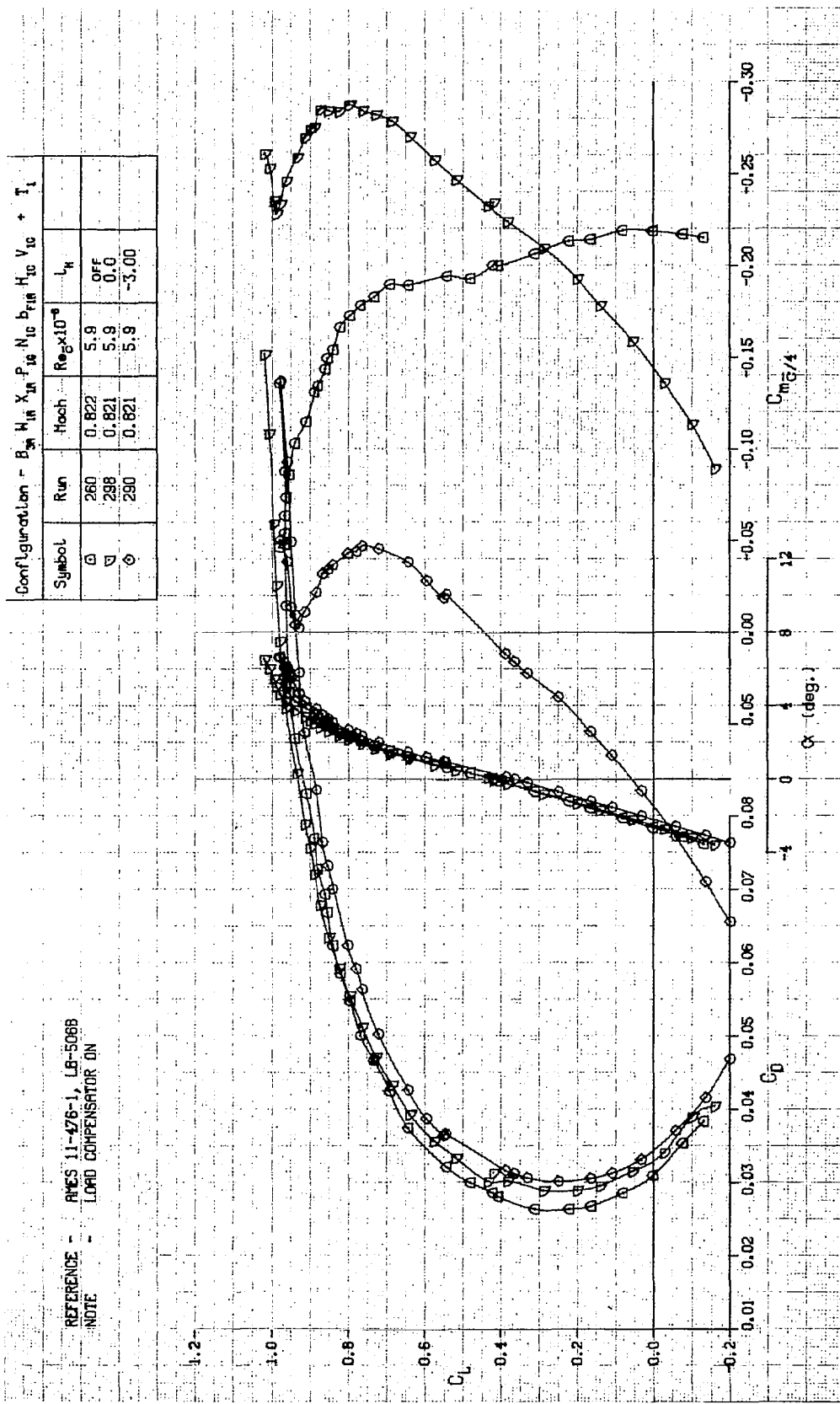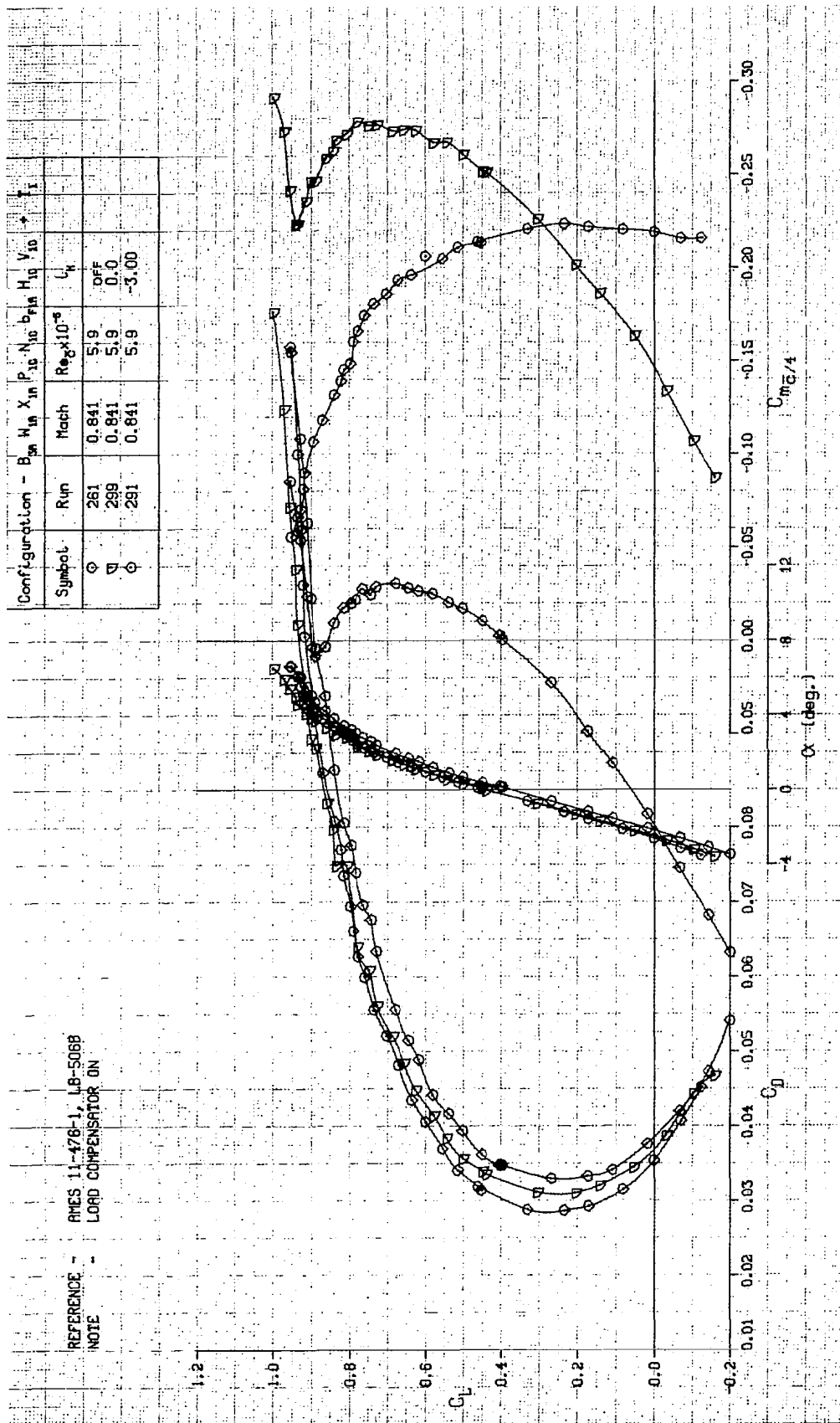
FIGURE A-55. LIFT, DRAG, AND PITCHING MOMENT CHARACTERISTICS OF WING W$_1$, WITH NACELLES, PYLONS, AND FLAP LINKAGE FAIRINGS, TRANSITION FIXED

FIGURE A-56. LIFT, DRAG, AND PITCHING MOMENT CHARACTERISTICS OF WING W_1, AND TAIL, TRANSITION FREE

Configuration -- B_{35} H_{JR} X_{JR} H_{JR} V_{JE} + T_1

Symbol	Run	Mach	$Re_{\bar{c}} \times 10^{-6}$	i_H
⊙	226	0.498	4.8	OFF
▽	266	0.498	4.8	0.0
◇	276	0.497	4.7	-3.00

C_L

$C_{m_{\bar{c}/4}}$

α (deg.)

C_D

FIGURE A-57. LIFT, DRAG, AND PITCHING MOMENT CHARACTERISTICS OF WING W_1, AND TAIL, TRANSITION FREE.
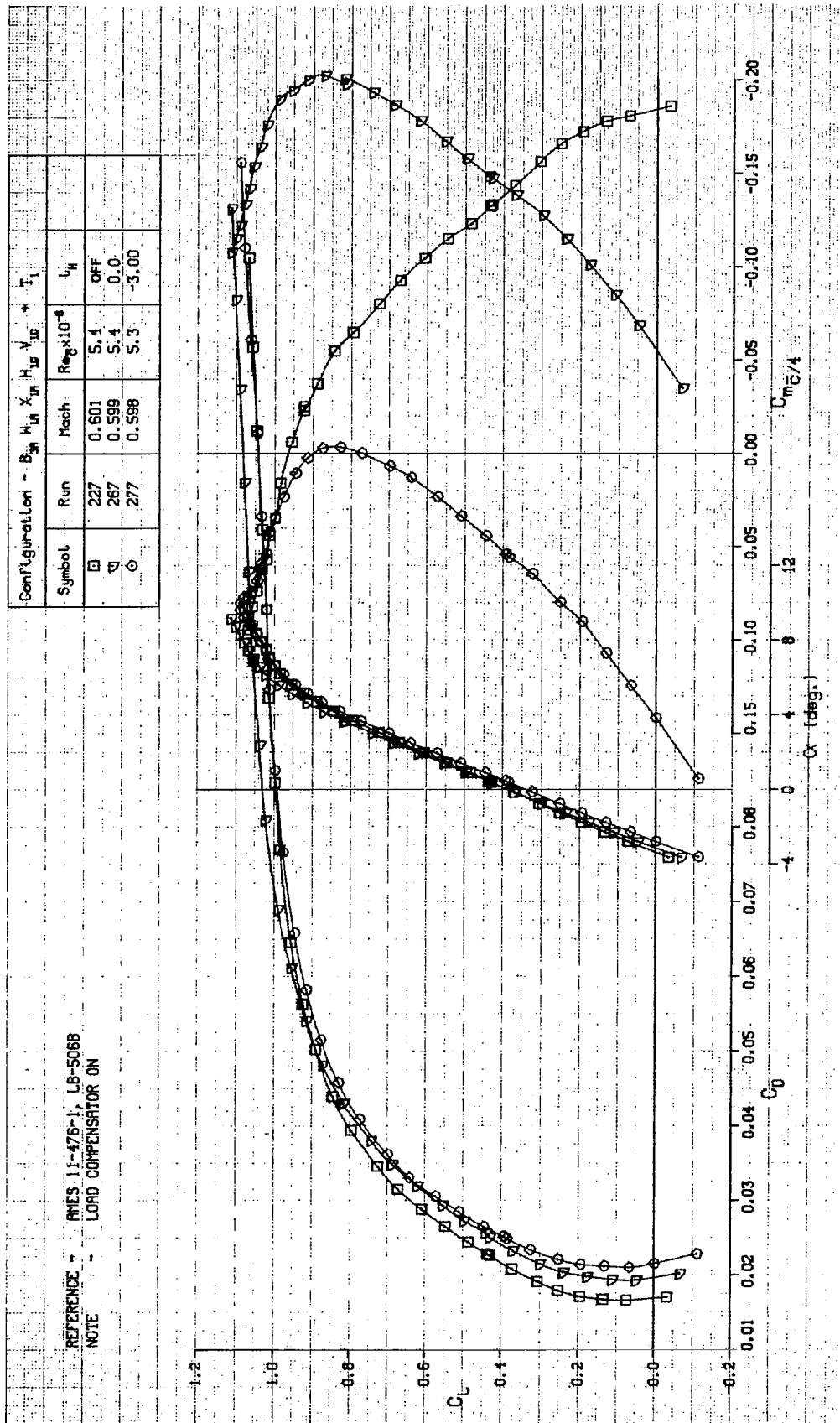
FIGURE A-58. LIFT, DRAG, AND PITCHING MOMENT CHARACTERISTICS OF WING W_1, AND TAIL, TRANSITION FREE
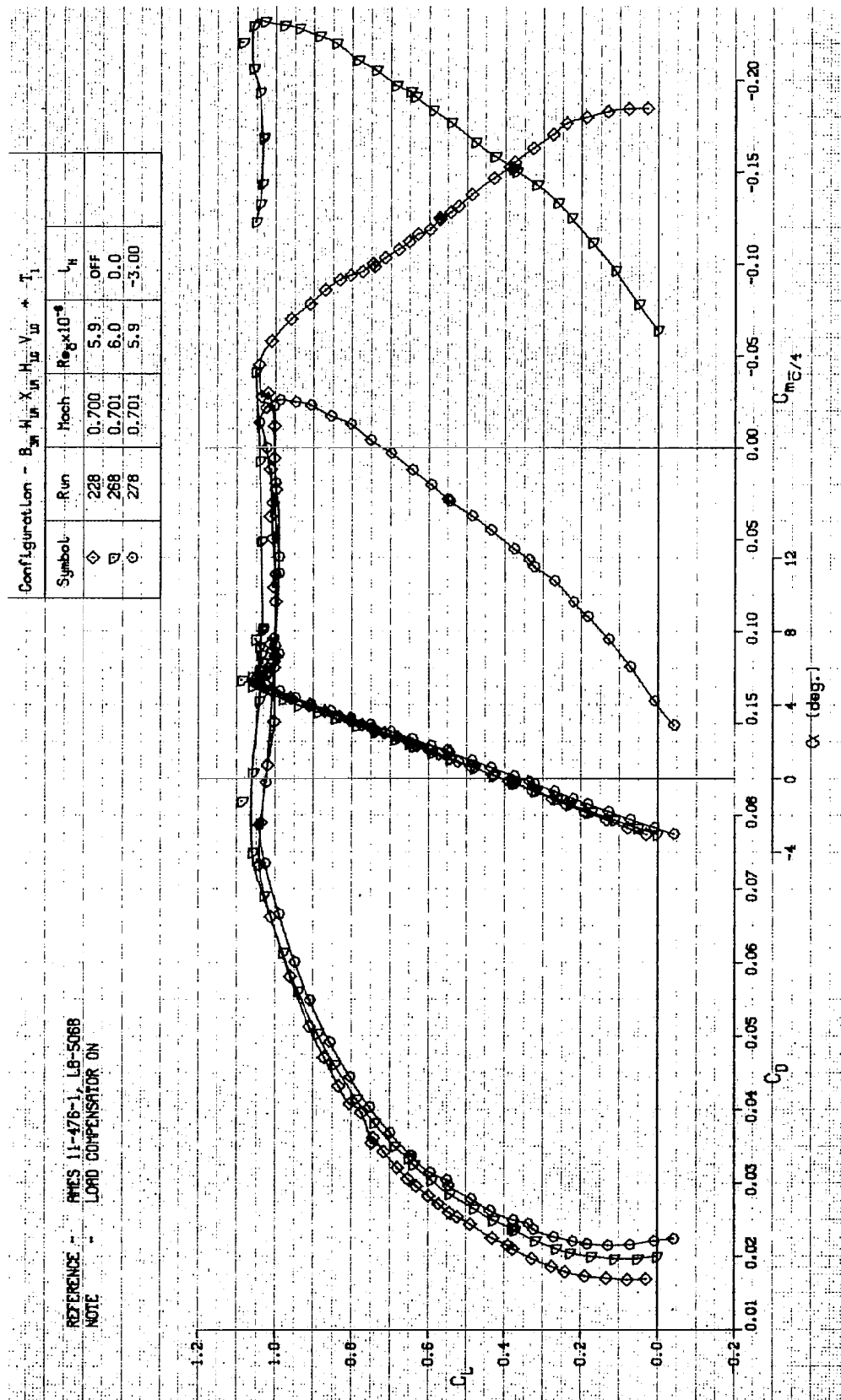
FIGURE A-59. LIFT, DRAG, AND PITCHING MOMENT CHARACTERISTICS OF WING W_1, AND TAIL, TRANSITION FREE

A-59
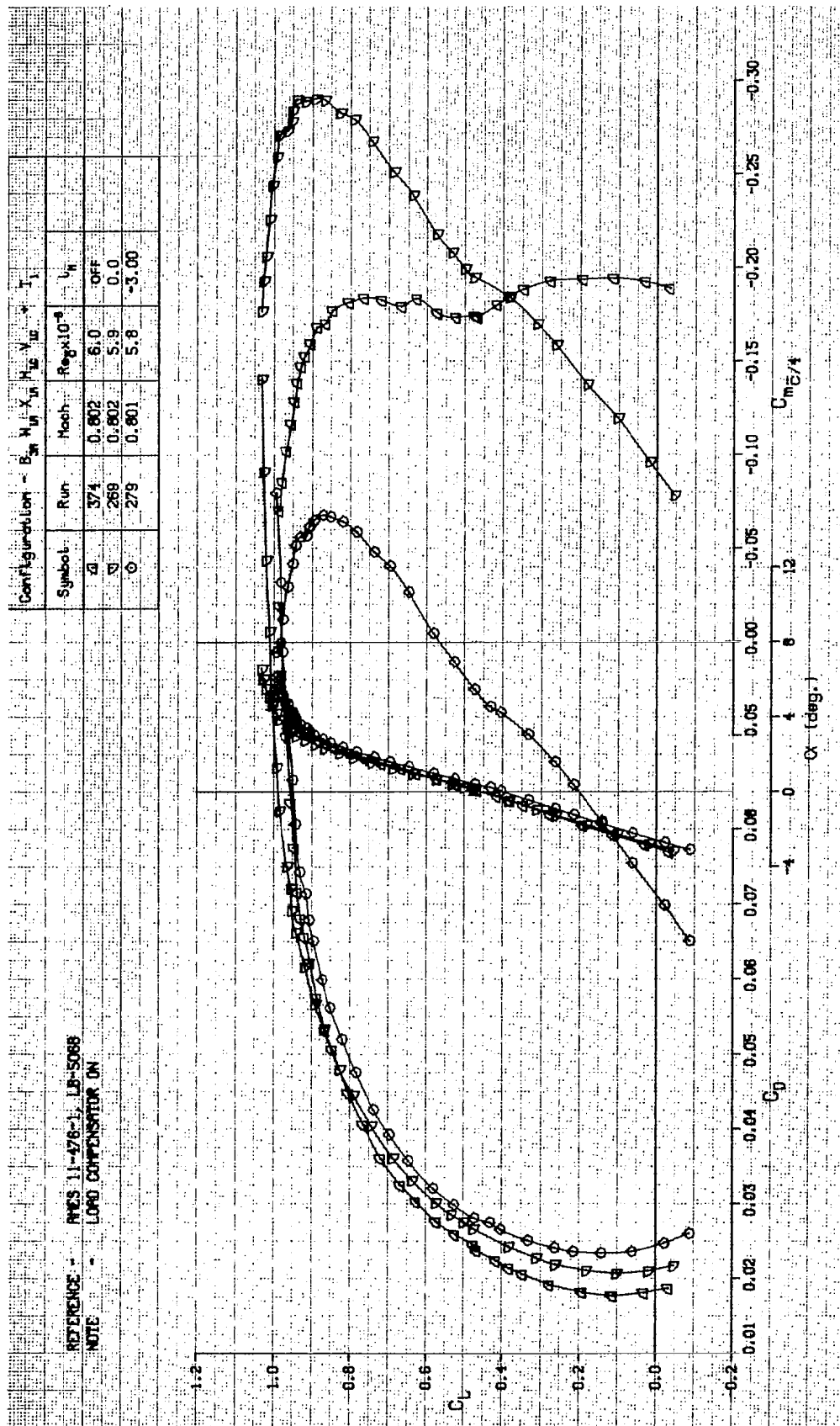
FIGURE A-60. LIFT, DRAG, AND PITCHING MOMENT CHARACTERISTICS OF WING W_1, AND TAIL, TRANSITION FREE
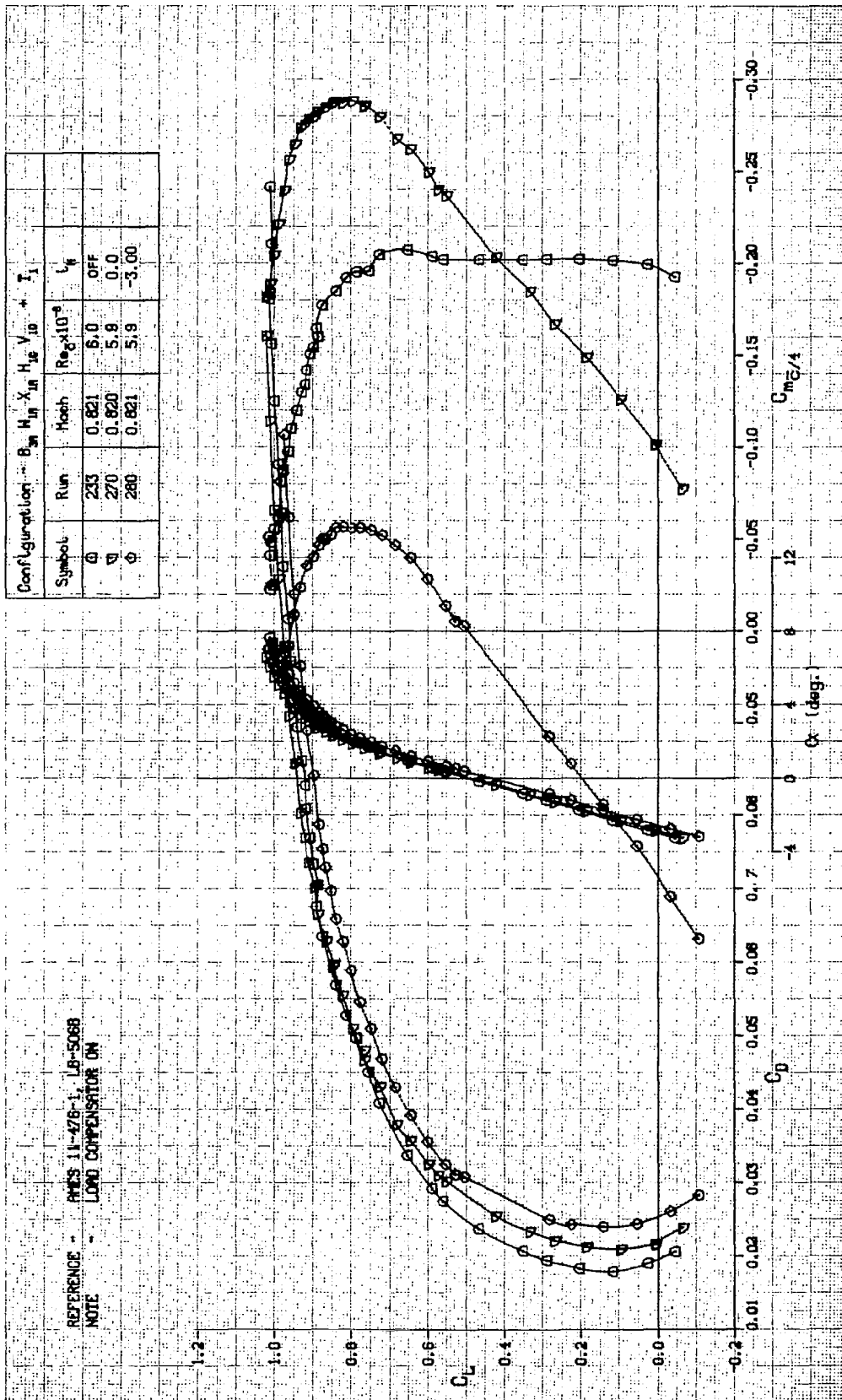
FIGURE A-61. LIFT, DRAG, AND PITCHING MOMENT CHARACTERISTICS OF WING W_1, AND TAIL, TRANSITION FREE
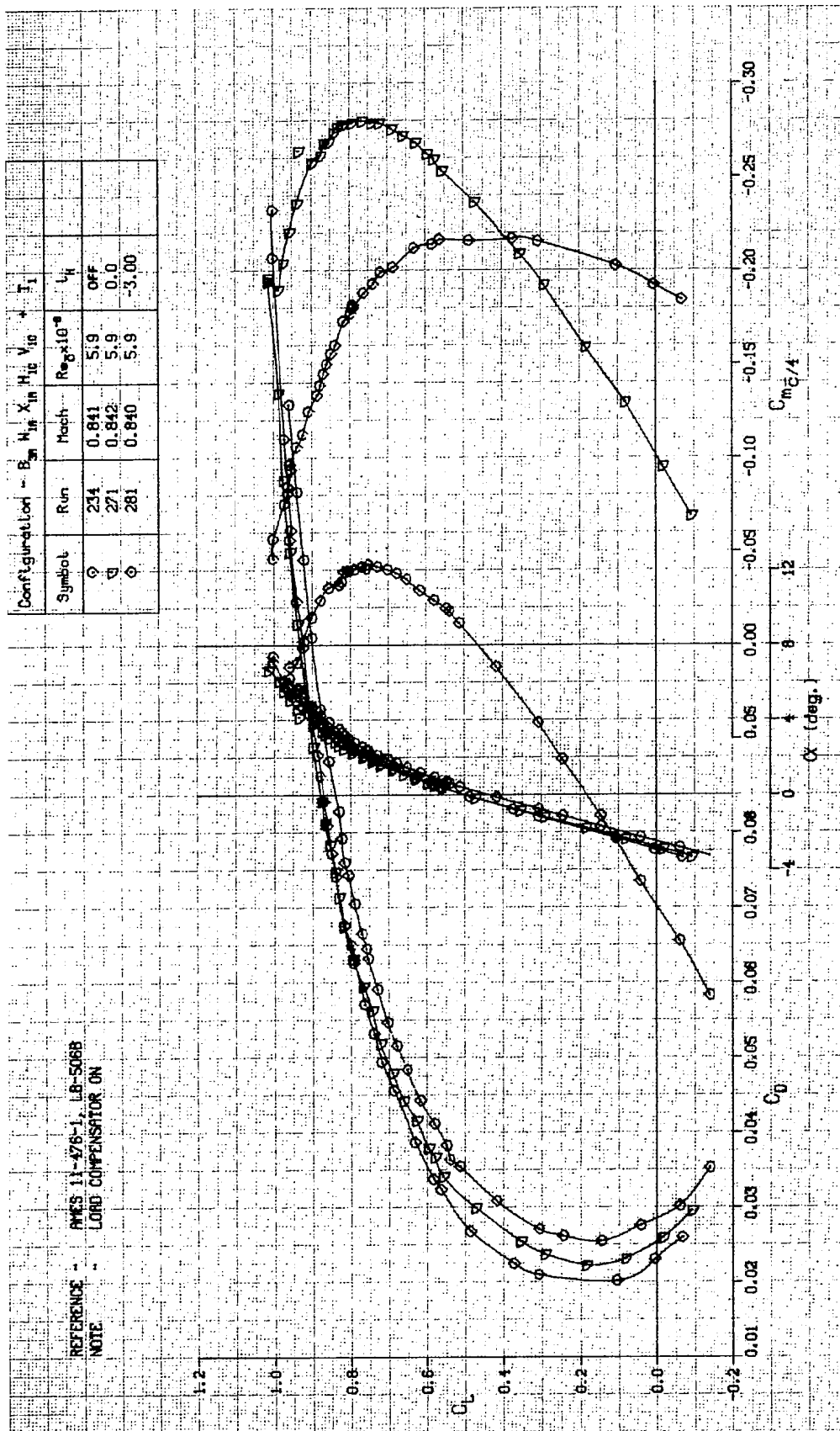
FIGURE A-62. LIFT, DRAG, AND PITCHING MOMENT CHARACTERISTICS OF WING W_1, AND TAIL, TRANSITION FREE
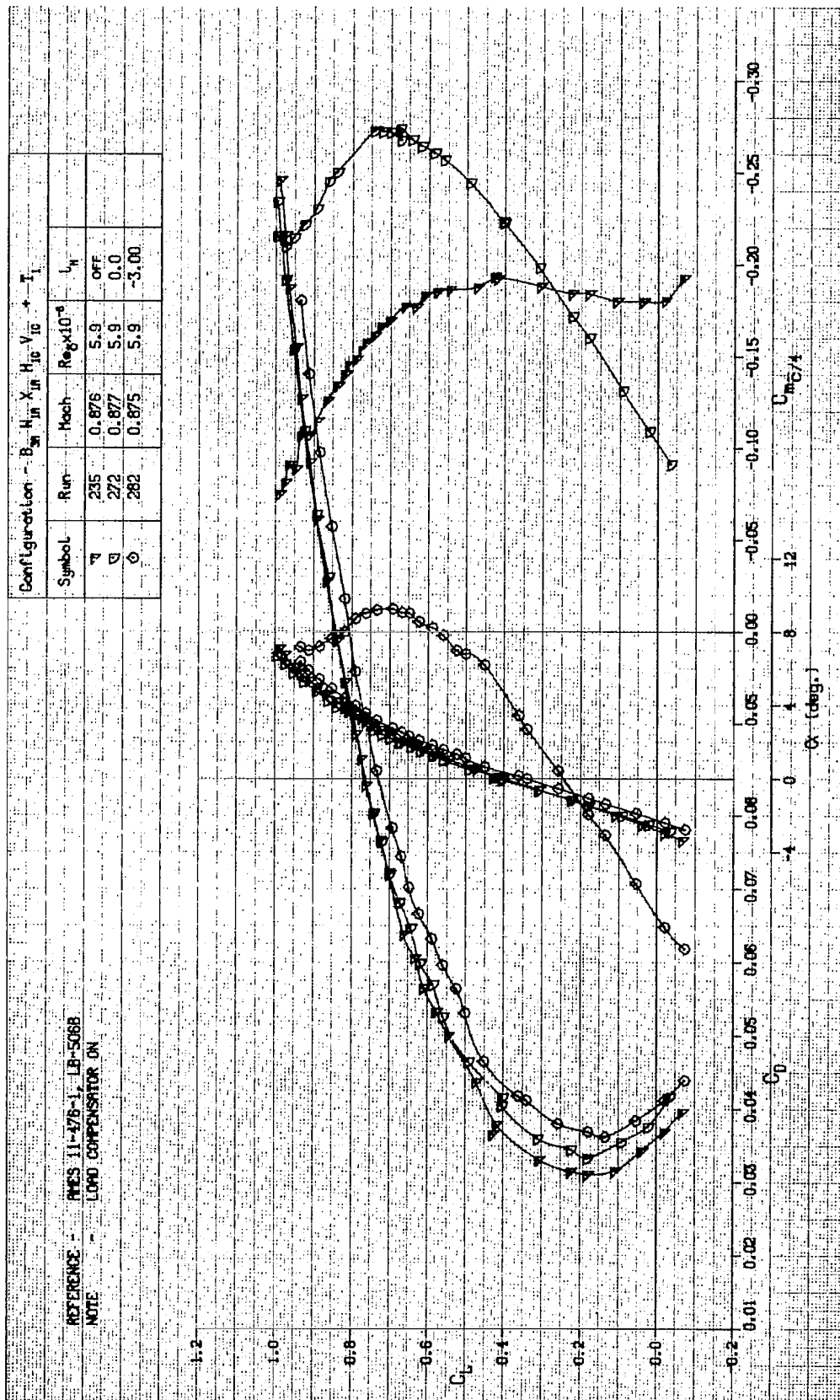
FIGURE A-63. LIFT, DRAG, AND PITCHING MOMENT CHARACTERISTICS OF WING W_1, AND TAIL, TRANSITION FREE
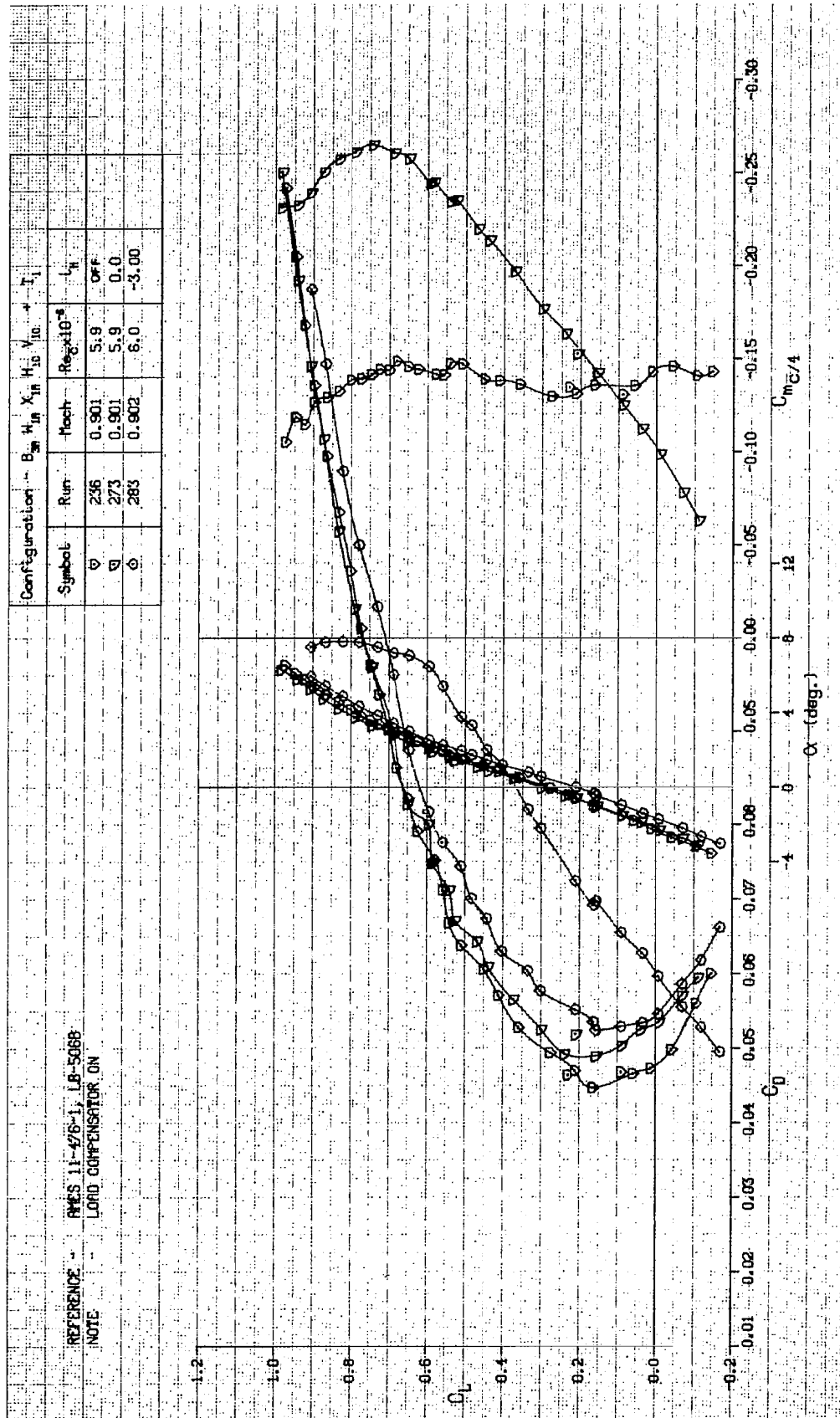
FIGURE A-64. LIFT, DRAG, AND PITCHING MOMENT CHARACTERISTICS OF WING W_1, AND TAIL, TRANSITION FREE

FIGURE A-65. LIFT, DRAG, AND PITCHING MOMENT CHARACTERISTICS OF WING W_1, WITH NACELLES, PYLONS, FLAP LINKAGE FAIRINGS, AND TAIL, TRANSITION FREE
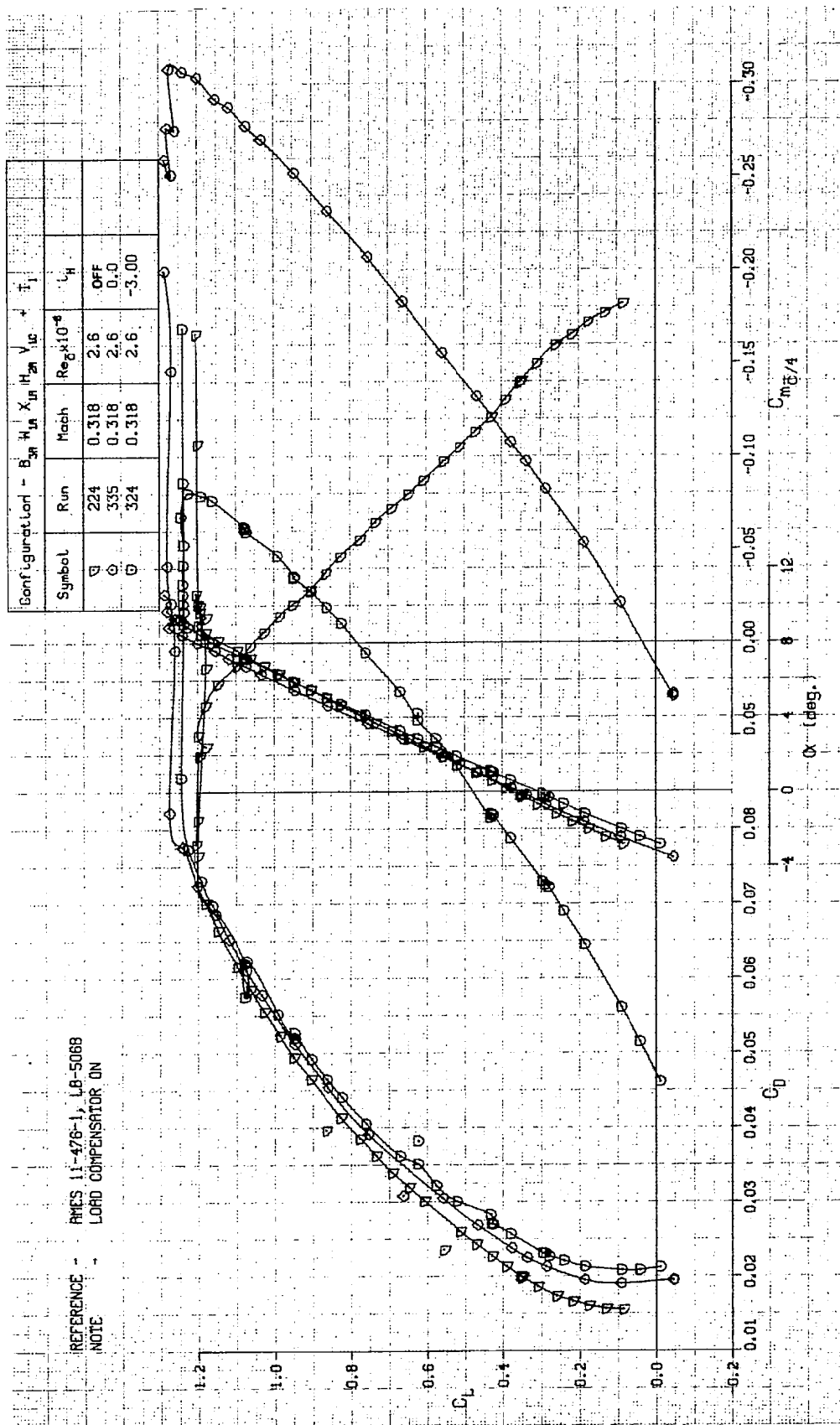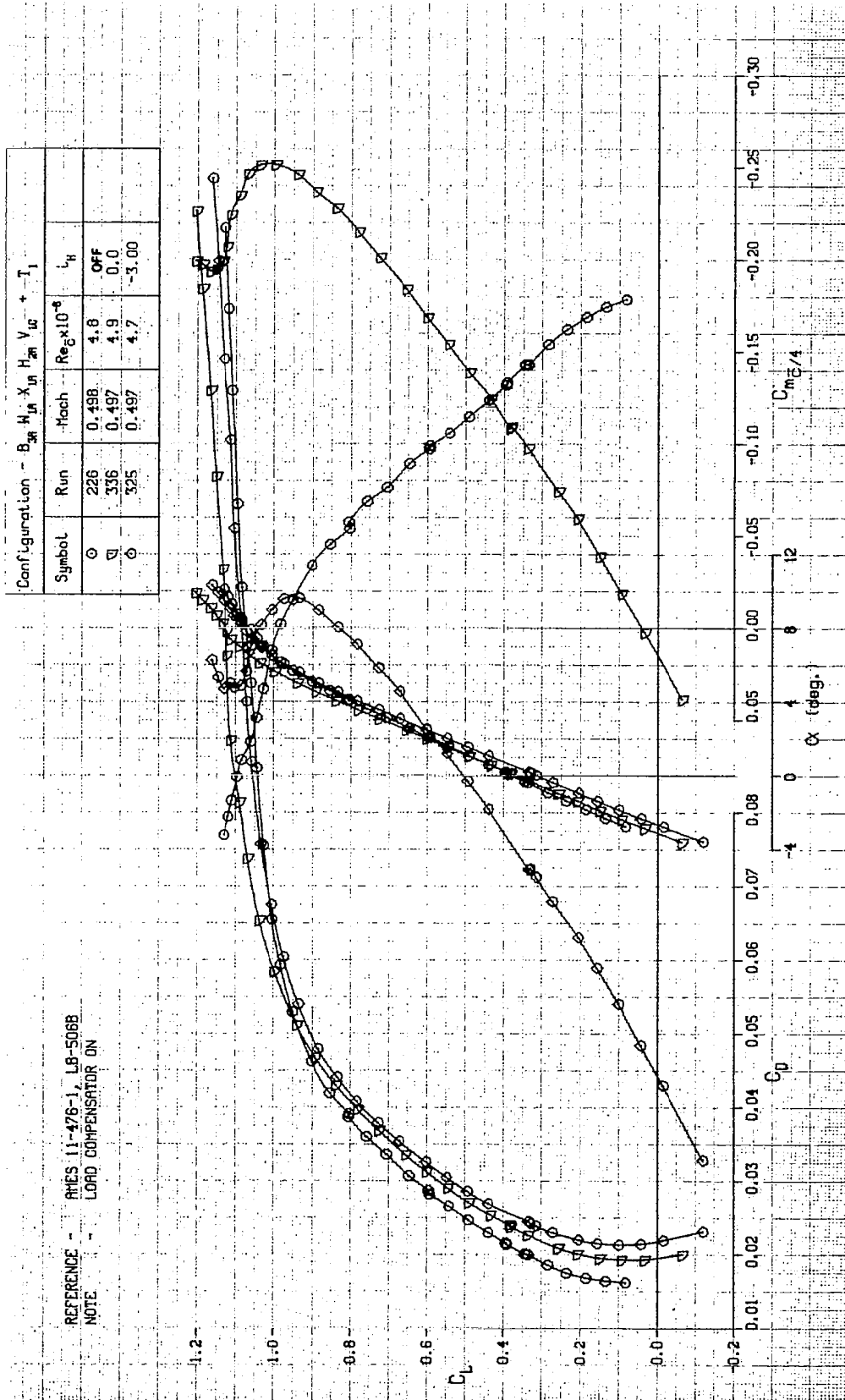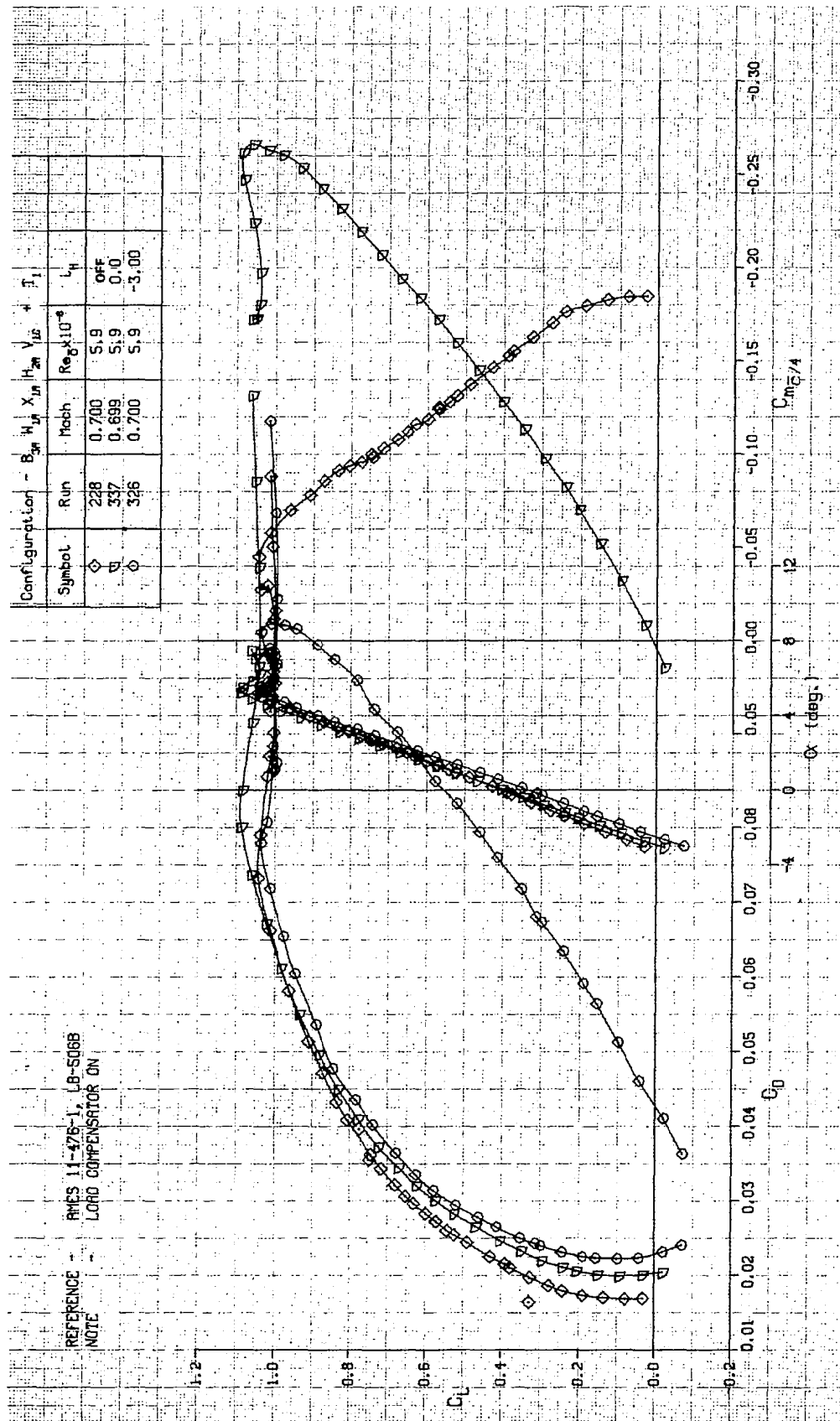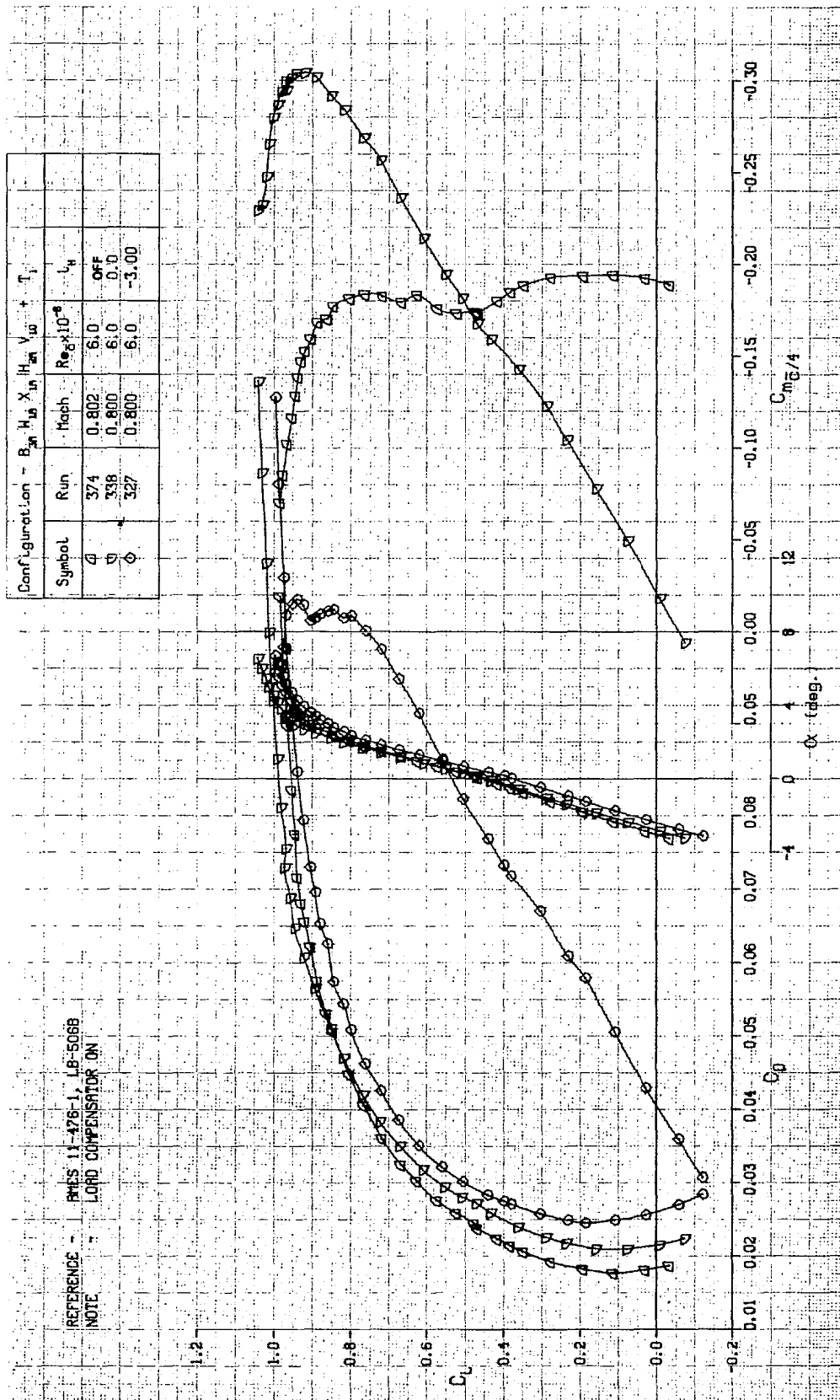
FIGURE A-66. LIFT, DRAG, AND PITCHING MOMENT CHARACTERISTICS OF WING W₁, WITH NACELLES, PYLONS, FLAP LINKAGE FAIRINGS, AND TAIL, TRANSITION FREE

FIGURE A-67. LIFT, DRAG, AND PITCHING MOMENT CHARACTERISTICS OF WING W_1, WITH NACELLES, PYLONS, FLAP LINKAGE FAIRINGS, AND TAIL, TRANSITION FREE

FIGURE A-68. LIFT, DRAG, AND PITCHING MOMENT CHARACTERISTICS OF WING W₁, WITH NACELLES, PYLONS, FLAP LINKAGE FAIRINGS, AND TAIL, TRANSITION FREE

FIGURE A-69. LIFT, DRAG, AND PITCHING MOMENT CHARACTERISTICS OF WING W₁, WITH NACELLES, PYLONS, FLAP LINKAGE FAIRINGS, AND TAIL, TRANSITION FREE

FIGURE A-70. LIFT, DRAG, AND PITCHING MOMENT CHARACTERISTICS OF WING W_1, WITH NACELLES, PYLONS, FLAP LINKAGE FAIRINGS, AND TAIL, TRANSITION FREE
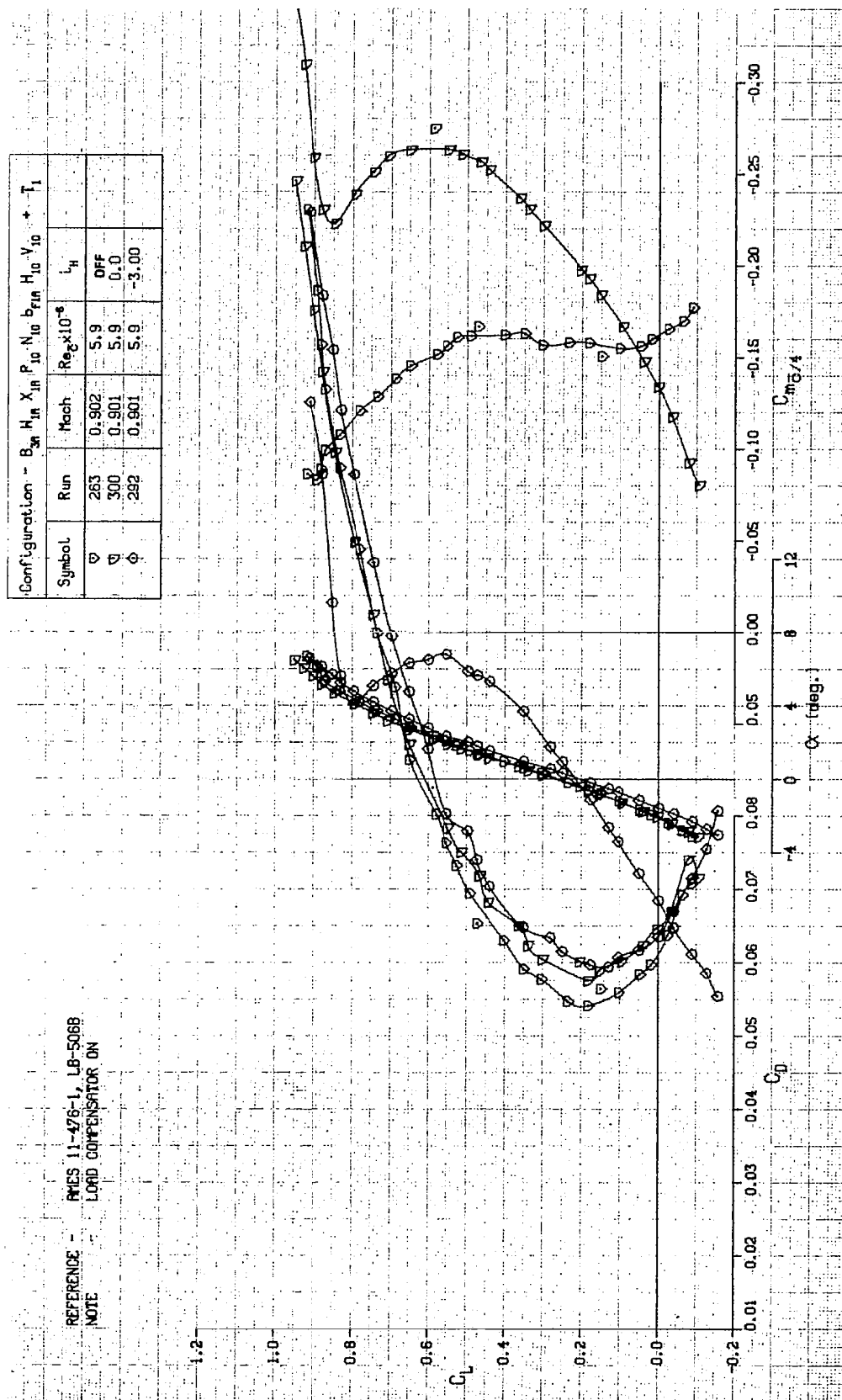
FIGURE A-71. LIFT, DRAG, AND PITCHING MOMENT CHARACTERISTICS OF WING W₁, WITH NACELLES, PYLONS, FLAP LINKAGE FAIRINGS, AND TAIL, TRANSITION FREE
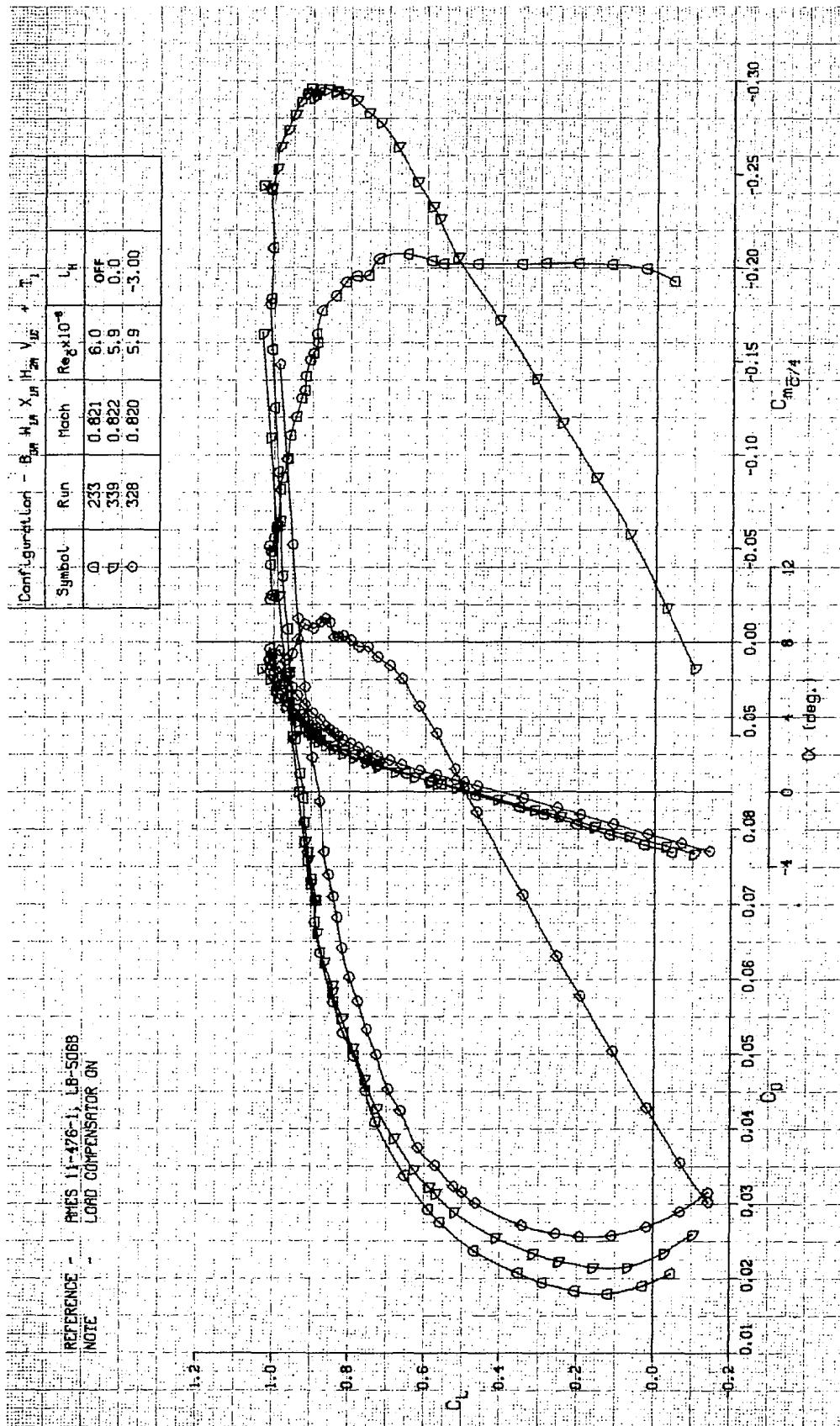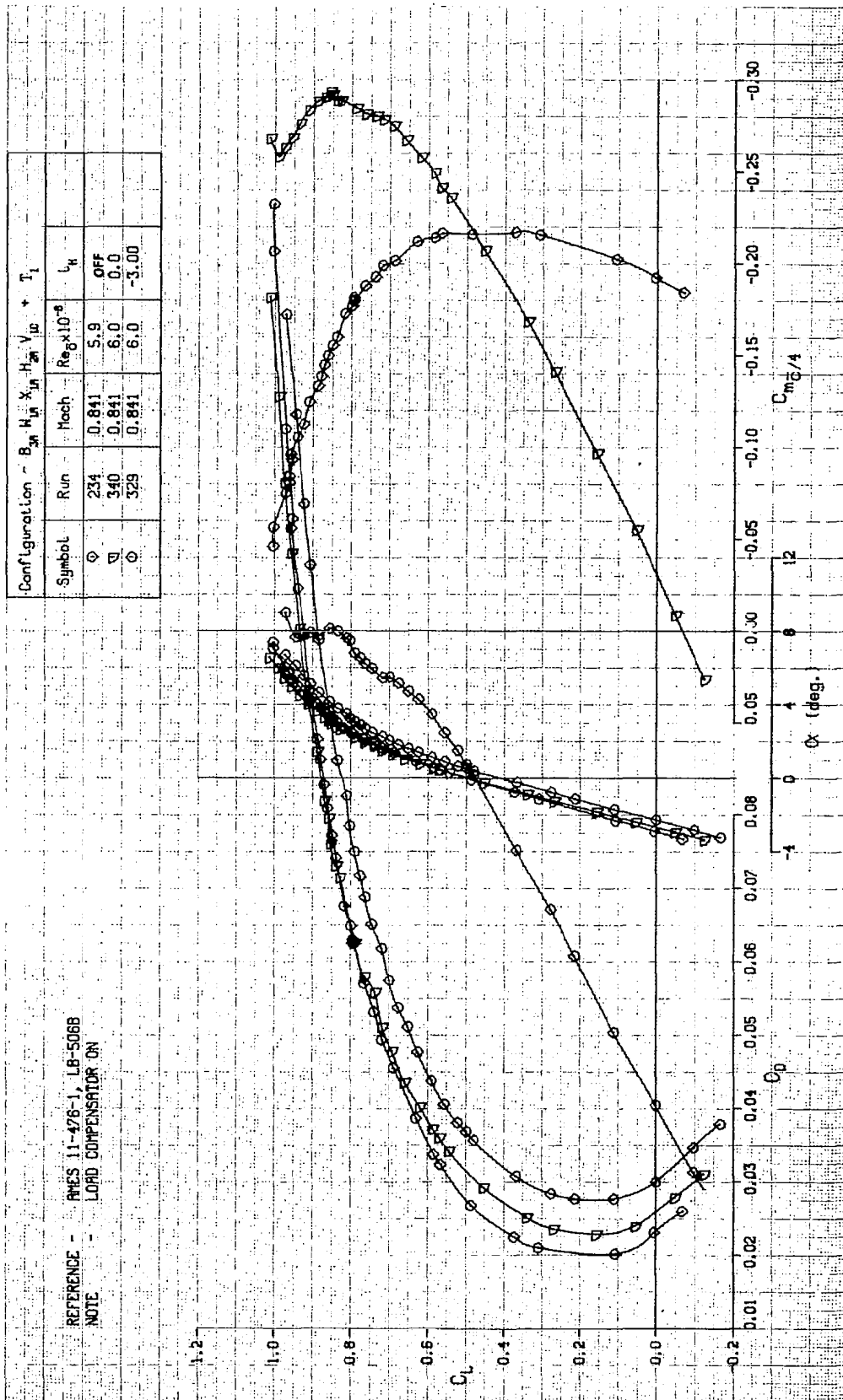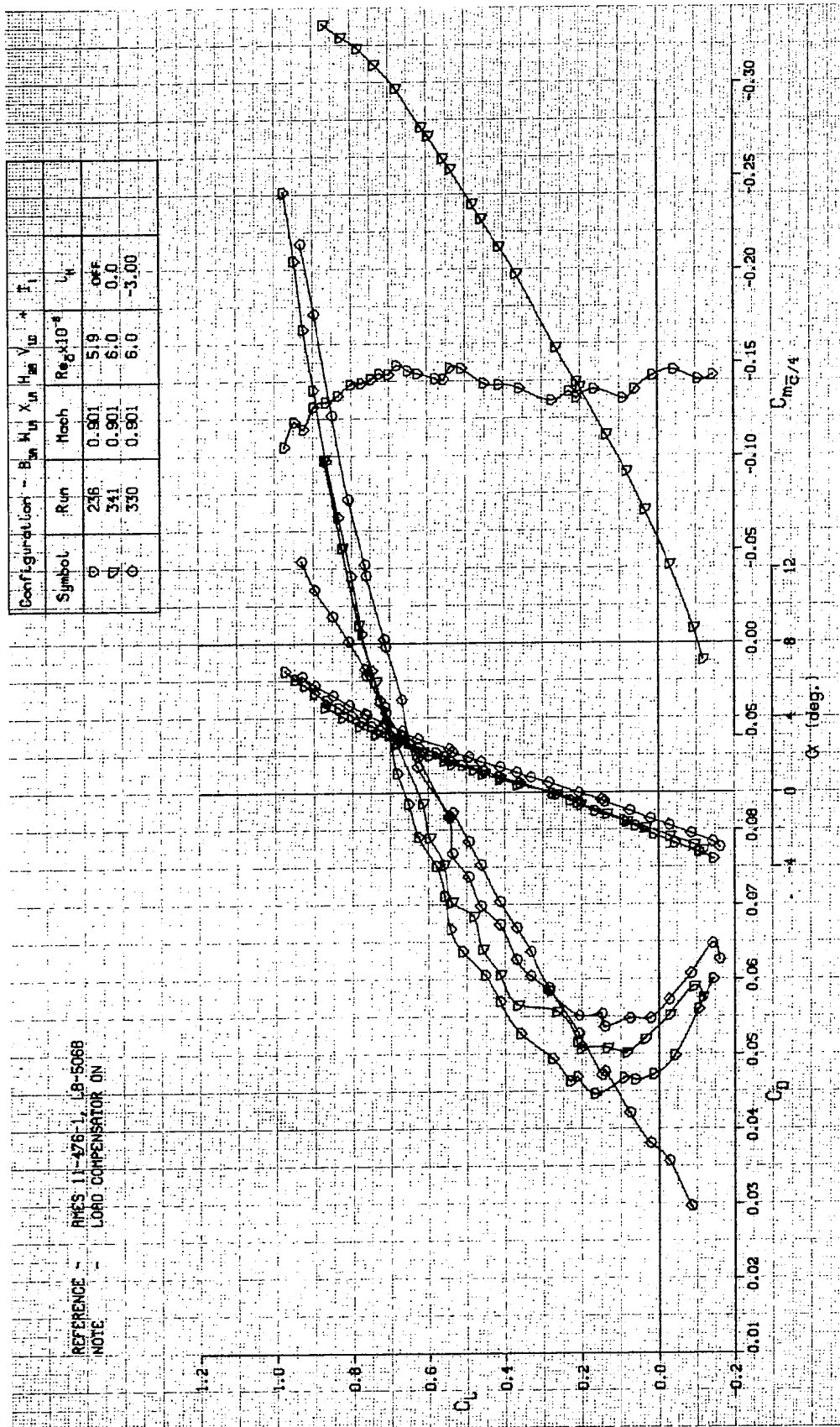
FIGURE A-72. LIFT, DRAG, AND PITCHING MOMENT CHARACTERISTICS OF WING W_1, AND TAIL, TRANSITION FREE

FIGURE A-73. LIFT, DRAG, AND PITCHING MOMENT CHARACTERISTICS OF WING W_1, AND TAIL, TRANSITION FREE
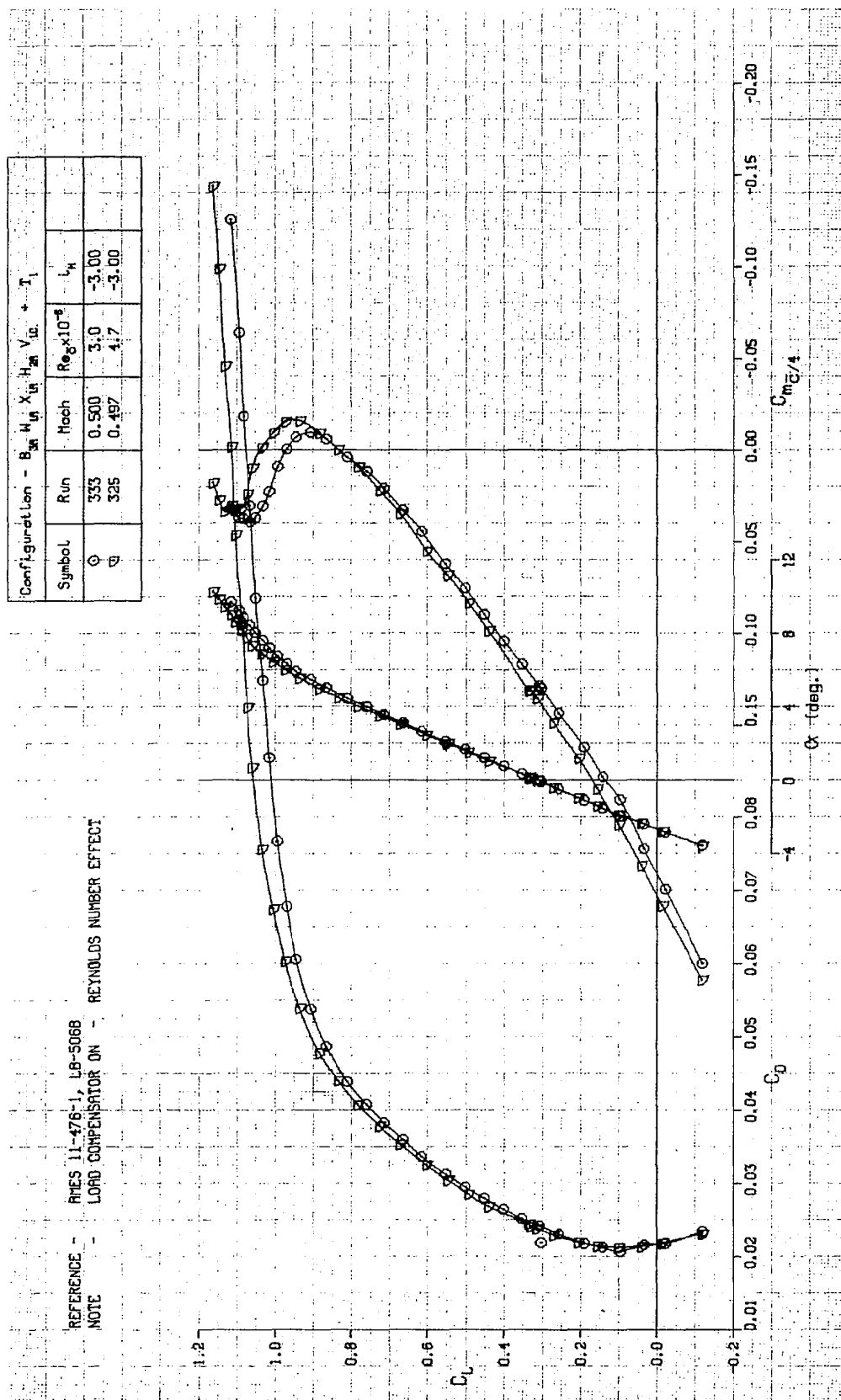
FIGURE A-74. LIFT, DRAG, AND PITCHING MOMENT CHARACTERISTICS OF WING W_1, AND TAIL, TRANSITION FREE

FIGURE A-75. LIFT, DRAG, AND PITCHING MOMENT CHARACTERISTICS OF WING W_1, AND TAIL, TRANSITION FREE

A-75

FIGURE A-76. LIFT, DRAG, AND PITCHING MOMENT CHARACTERISTICS OF WING W_1, AND TAIL, TRANSITION FREE
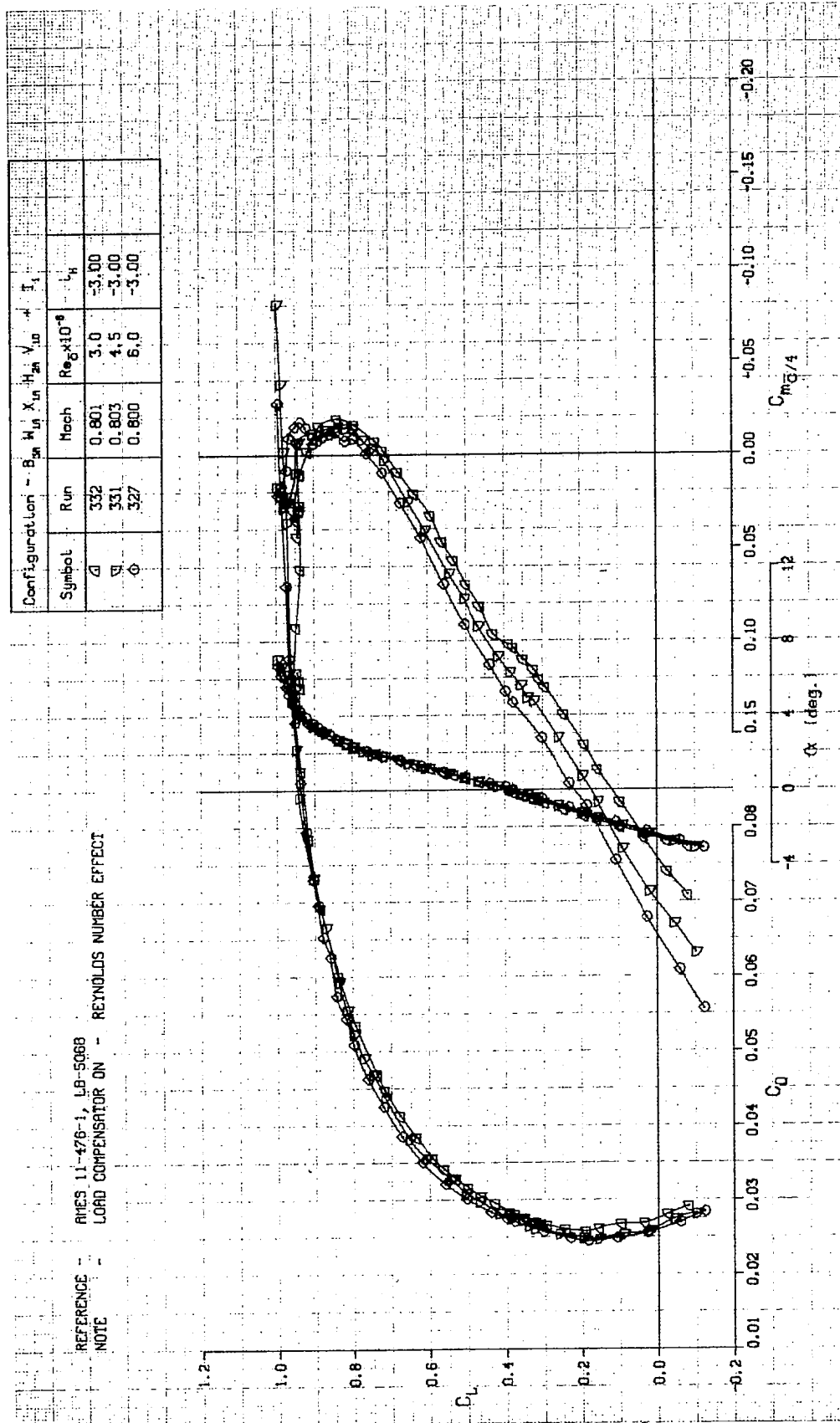
A-76

FIGURE A-77. LIFT, DRAG, AND PITCHING MOMENT CHARACTERISTICS OF WING W_1, AND TAIL, TRANSITION FREE

FIGURE A-78. LIFT, DRAG, AND PITCHING MOMENT CHARACTERISTICS OF WING W_1, AND TAIL, TRANSITION FREE

Configuration -- B_{1n} W_{1n} X_{1n} H_{3n} V_{1n} * i_1					
Symbol	Run	Mach	$Re_c \times 10^{-6}$	i_H
⬠	216	0.901	5.9	off.
▽	341	0.901	6.0	0.0
◇	350	0.901	6.0	-3.00

REFERENCE - AMES 11-476-1, LB-5068
NOTE - LOAD COMPENSATOR ON

$C_{m_{\bar{c}/4}}$

α (deg.)

C_D

C_L

FIGURE A-79. LIFT, DRAG, AND PITCHING MOMENT CHARACTERISTICS OF WING W_1, AND TAIL, TRANSITION FREE

FIGURE A-80. LIFT, DRAG, AND PITCHING MOMENT CHARACTERISTICS OF WING W_1, AND TAIL, TRANSITION FREE
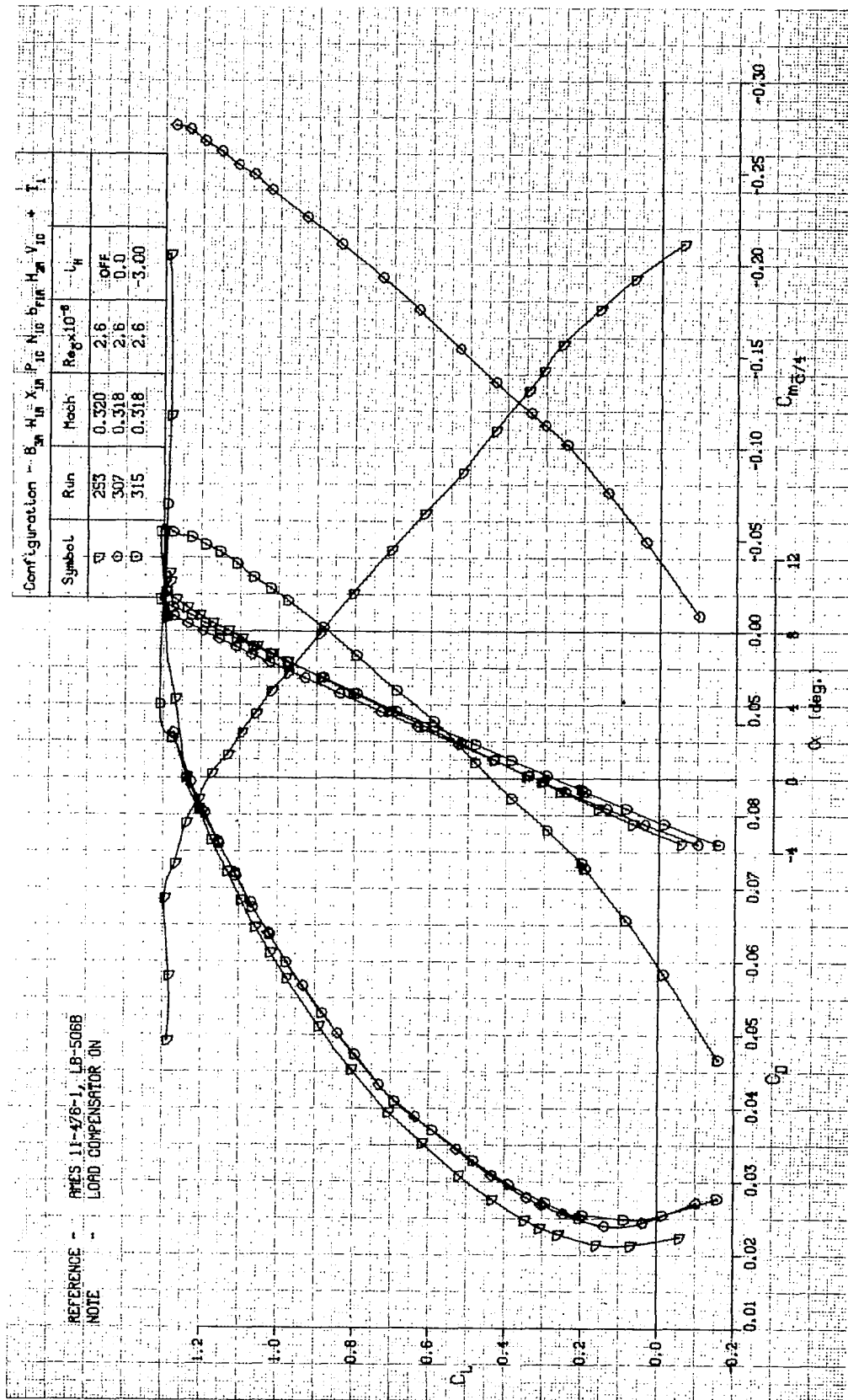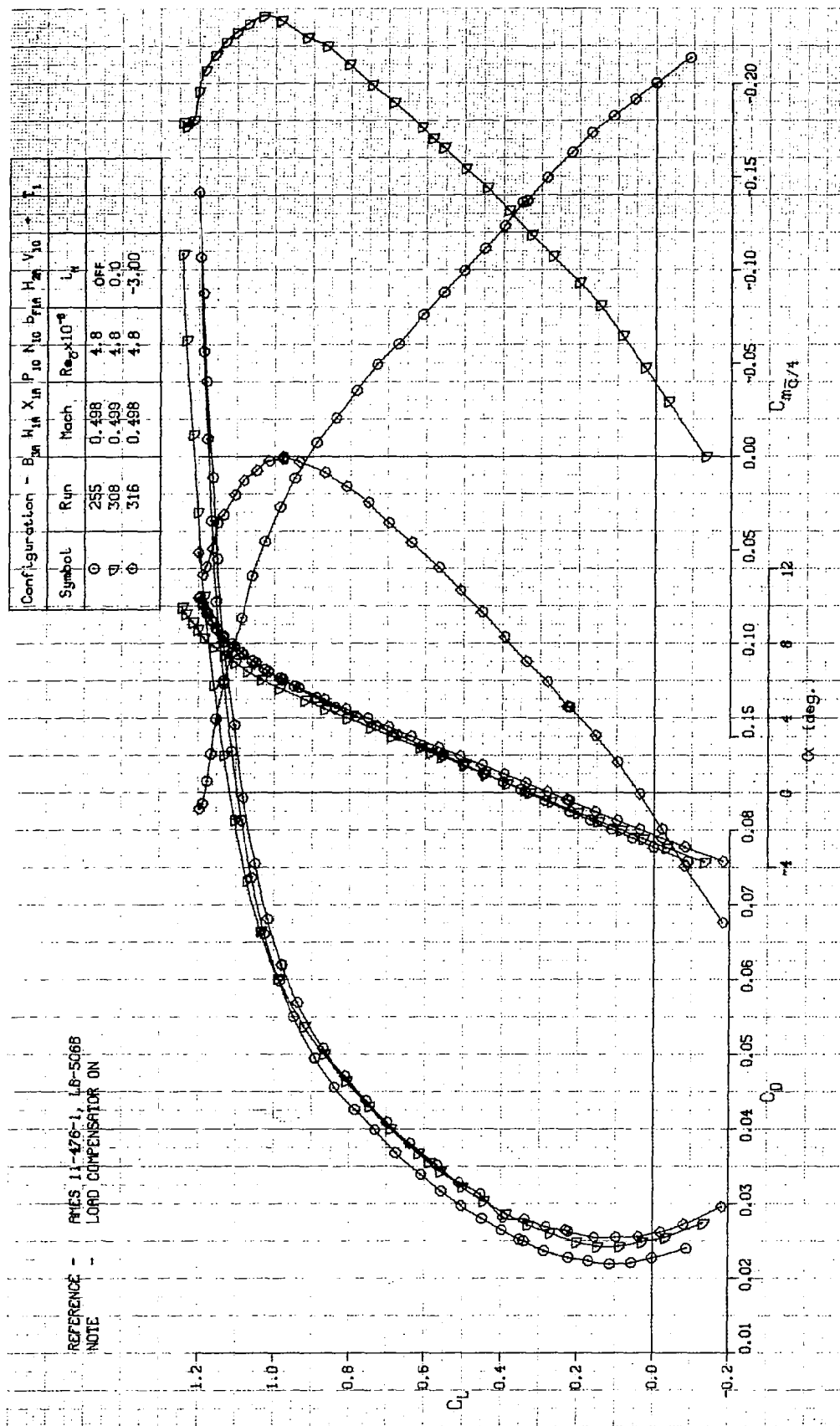
A-80

FIGURE A-81. LIFT, DRAG, AND PITCHING MOMENT CHARACTERISTICS OF WING W_1, WITH NACELLES, PYLONS, FLAP LINKAGE FAIRINGS, AND TAIL, TRANSITION FREE

FIGURE A-82. LIFT, DRAG, AND PITCHING MOMENT CHARACTERISTICS OF WING W$_1$, WITH NACELLES, PYLONS, FLAP LINKAGE FAIRINGS, AND TAIL, TRANSITION FREE
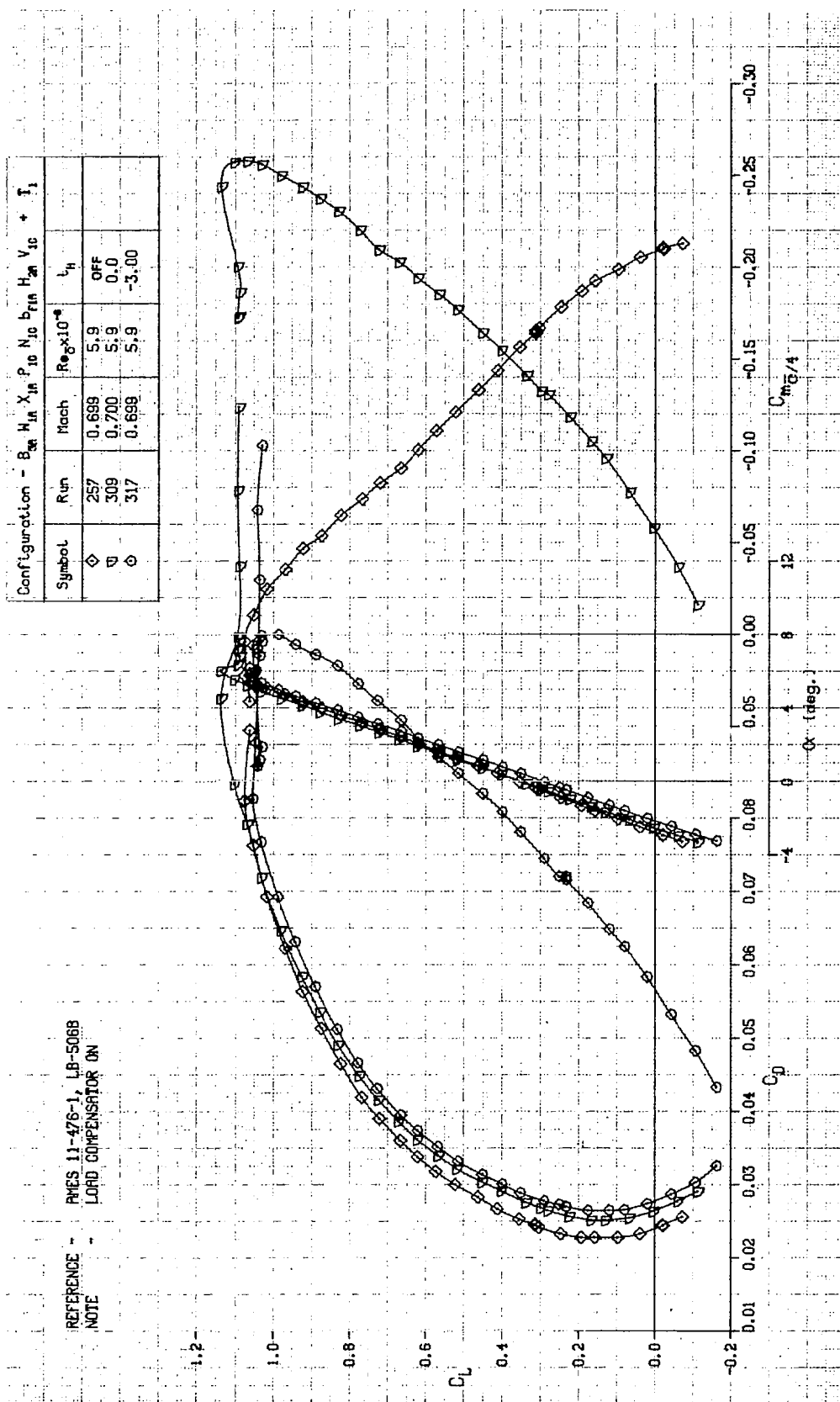
FIGURE A-83. LIFT, DRAG, AND PITCHING MOMENT CHARACTERISTICS OF WING W_1, WITH NACELLES, PYLONS, FLAP LINKAGE FAIRINGS, AND TAIL, TRANSITION FREE
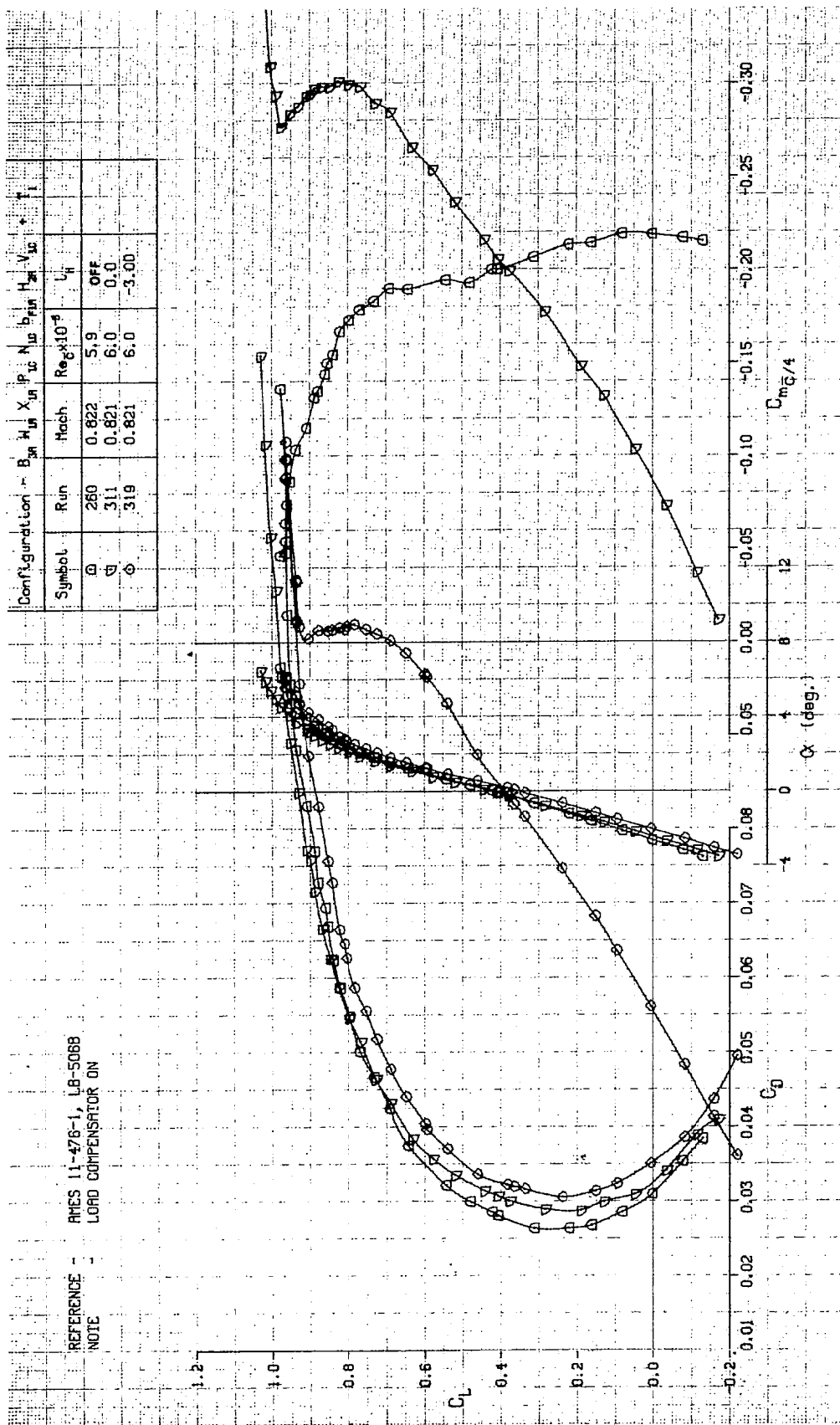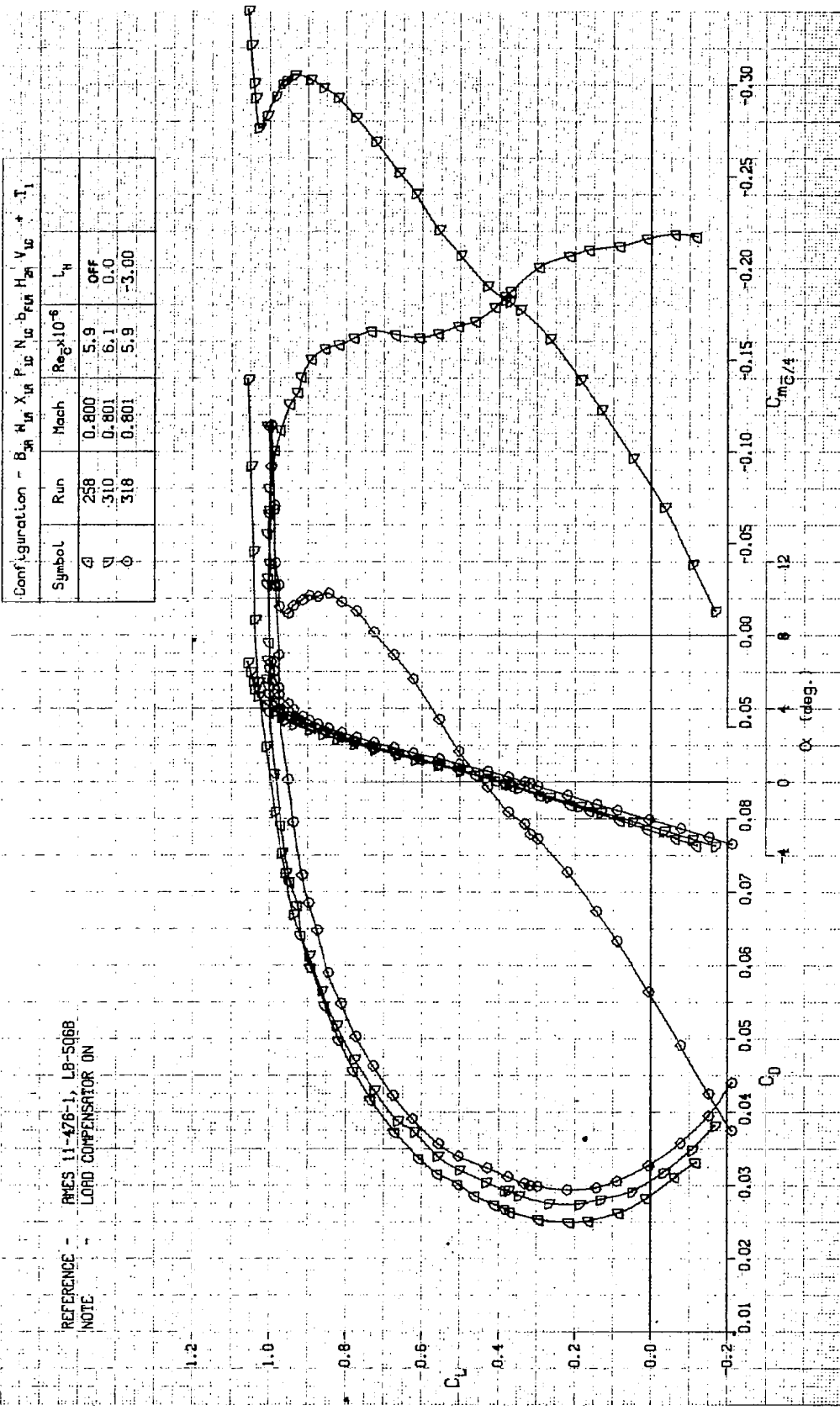
Configuration – B_{5A} W_{1B} X_{1B} iP_{1C} N_{1C} b_{P1N} H_{2N} V_{1C} $\cdot$ T_1					
Symbol	Run	Mach	$Re_{\bar{c}} \times 10^{-6}$	U_H
▫	260	0.822	5.9	OFF
◁	311	0.821	6.0	0.0
◇	319	0.821	6.0	-3.00

REFERENCE – AMES 11-476-1, LB-506B
NOTE – LOAD COMPENSATOR ON

C_L

C_D

α (deg.)

$C_{m\bar{c}/4}$

FIGURE A-84. LIFT, DRAG, AND PITCHING MOMENT CHARACTERISTICS OF WING W_1, WITH NACELLES, PYLONS, FLAP LINKAGE FAIRINGS, AND TAIL, TRANSITION FREE
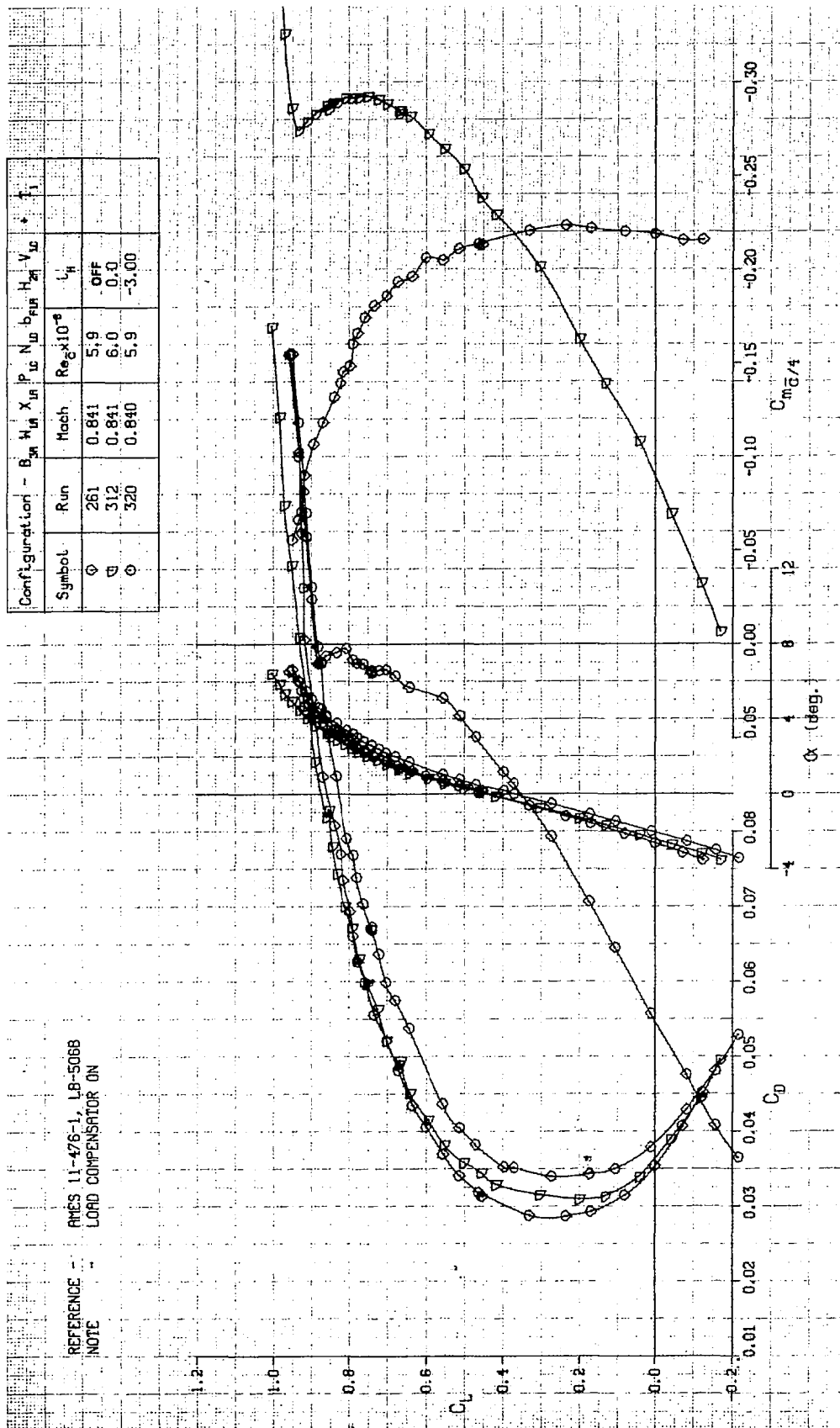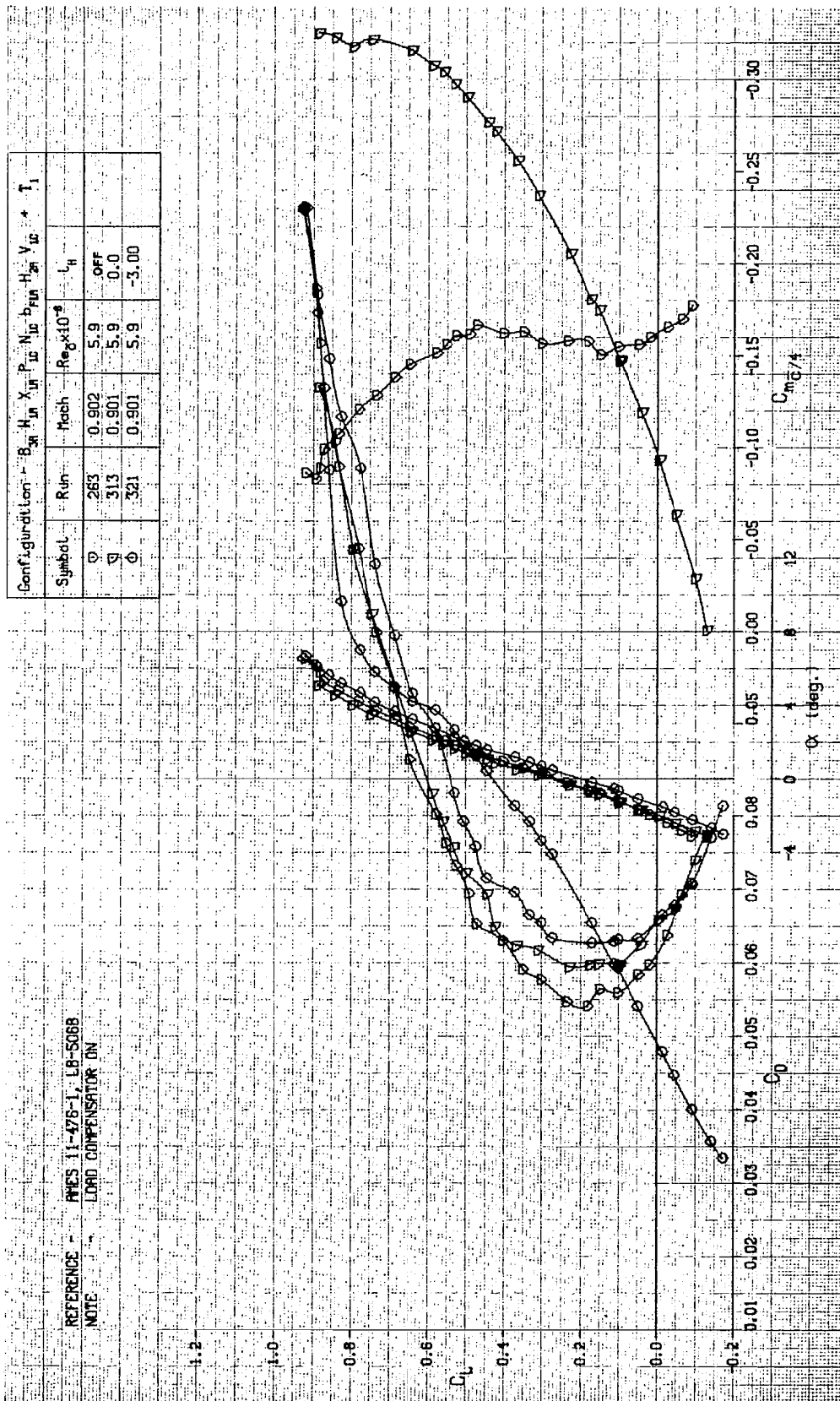
A-84

FIGURE A-85. LIFT, DRAG, AND PITCHING MOMENT CHARACTERISTICS OF WING W_1, WITH NACELLES, PYLONS, FLAP LINKAGE FAIRINGS, AND TAIL, TRANSITION FREE

FIGURE A-86. LIFT, DRAG, AND PITCHING MOMENT CHARACTERISTICS OF WING W_1, WITH NACELLES, PYLONS, FLAP LINKAGE FAIRINGS, AND TAIL, TRANSITION FREE
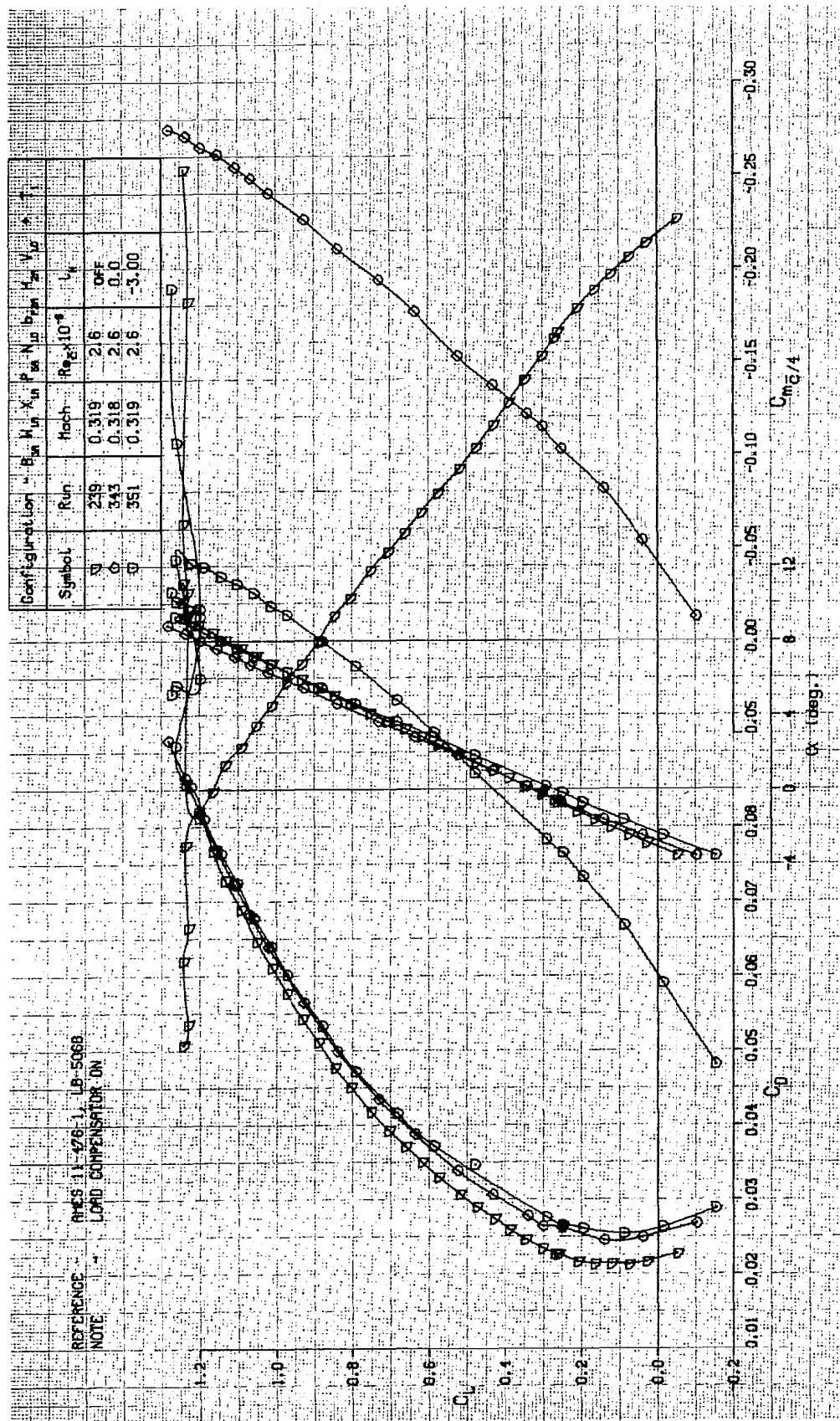
A-86

FIGURE A-87. LIFT, DRAG, AND PITCHING MOMENT CHARACTERISTICS OF WING W₁, WITH NACELLES, PYLONS, FLAP LINKAGE FAIRINGS, AND TAIL, TRANSITION FREE

FIGURE A-88. LIFT, DRAG, AND PITCHING MOMENT CHARACTERISTICS OF WING W_1, WITH NACELLES, PYLONS, FLAP LINKAGE FAIRINGS, AND TAIL, TRANSITION FREE
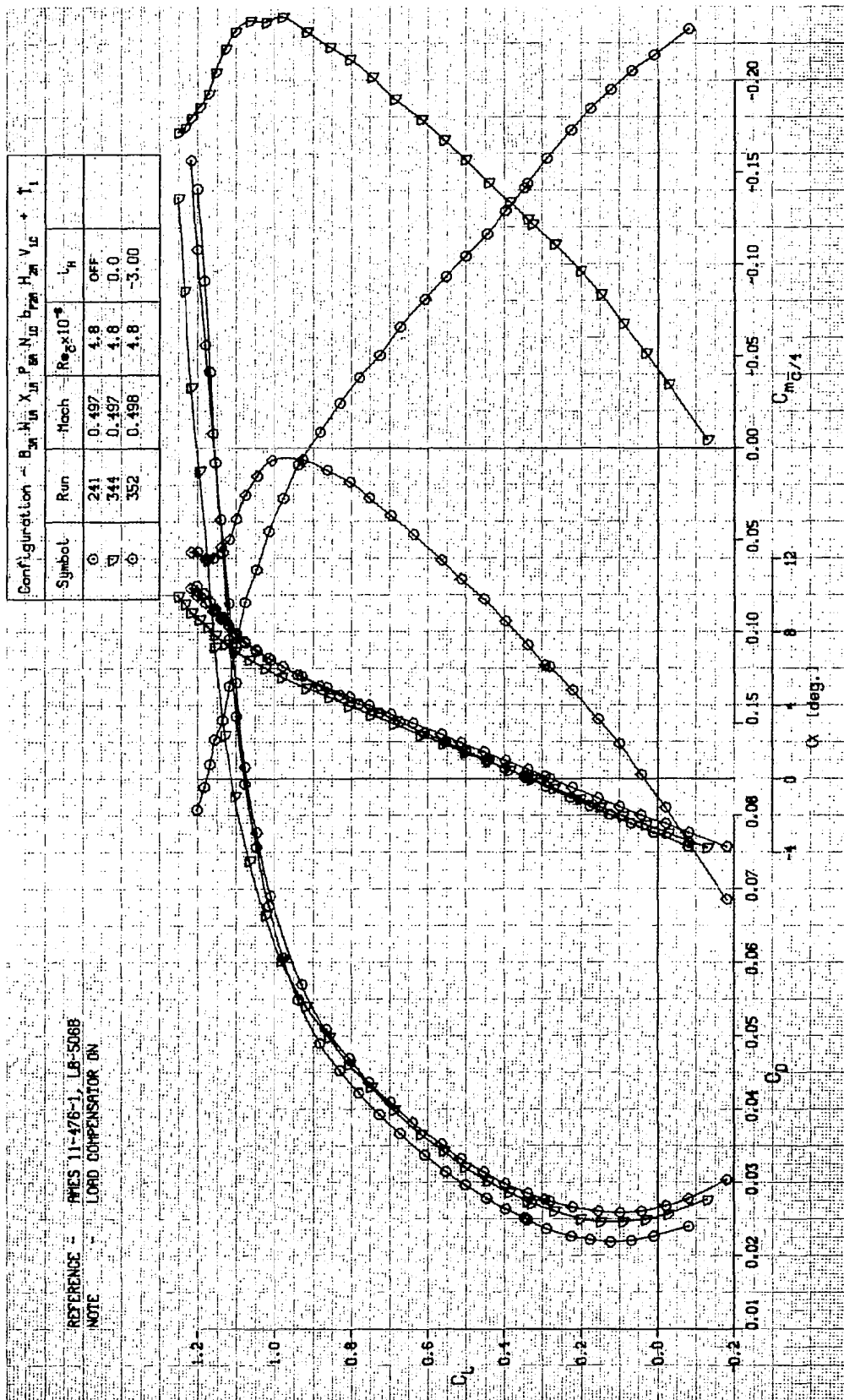
FIGURE A-89. LIFT, DRAG, AND PITCHING MOMENT CHARACTERISTICS OF WING W_1, WITH NACELLES, PYLONS, FLAP LINKAGE FAIRINGS, AND TAIL, TRANSITION FREE
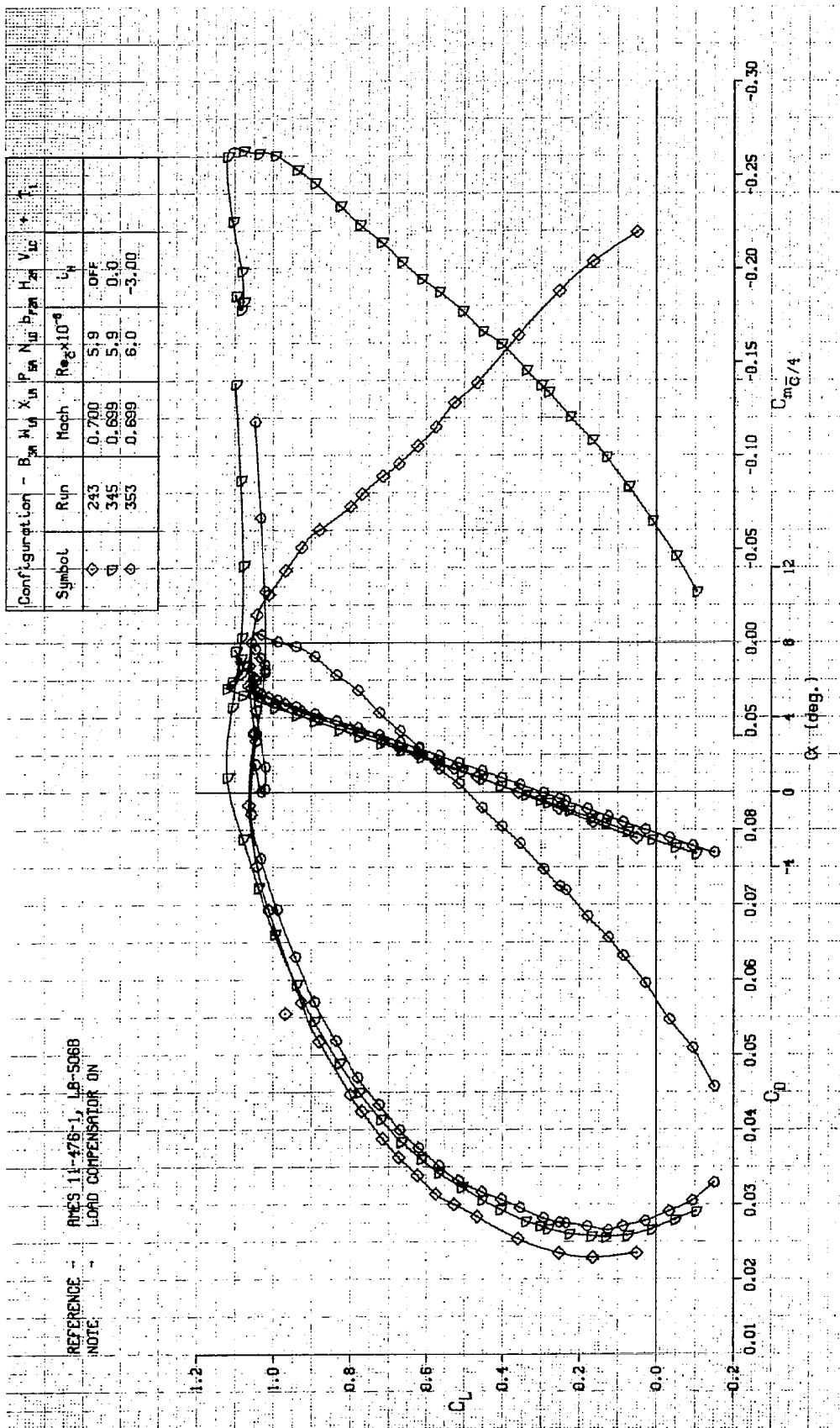
FIGURE A-90. LIFT, DRAG, AND PITCHING MOMENT CHARACTERISTICS OF WING W₁, WITH NACELLES, PYLONS, FLAP LINKAGE FAIRINGS, AND TAIL, TRANSITION FREE
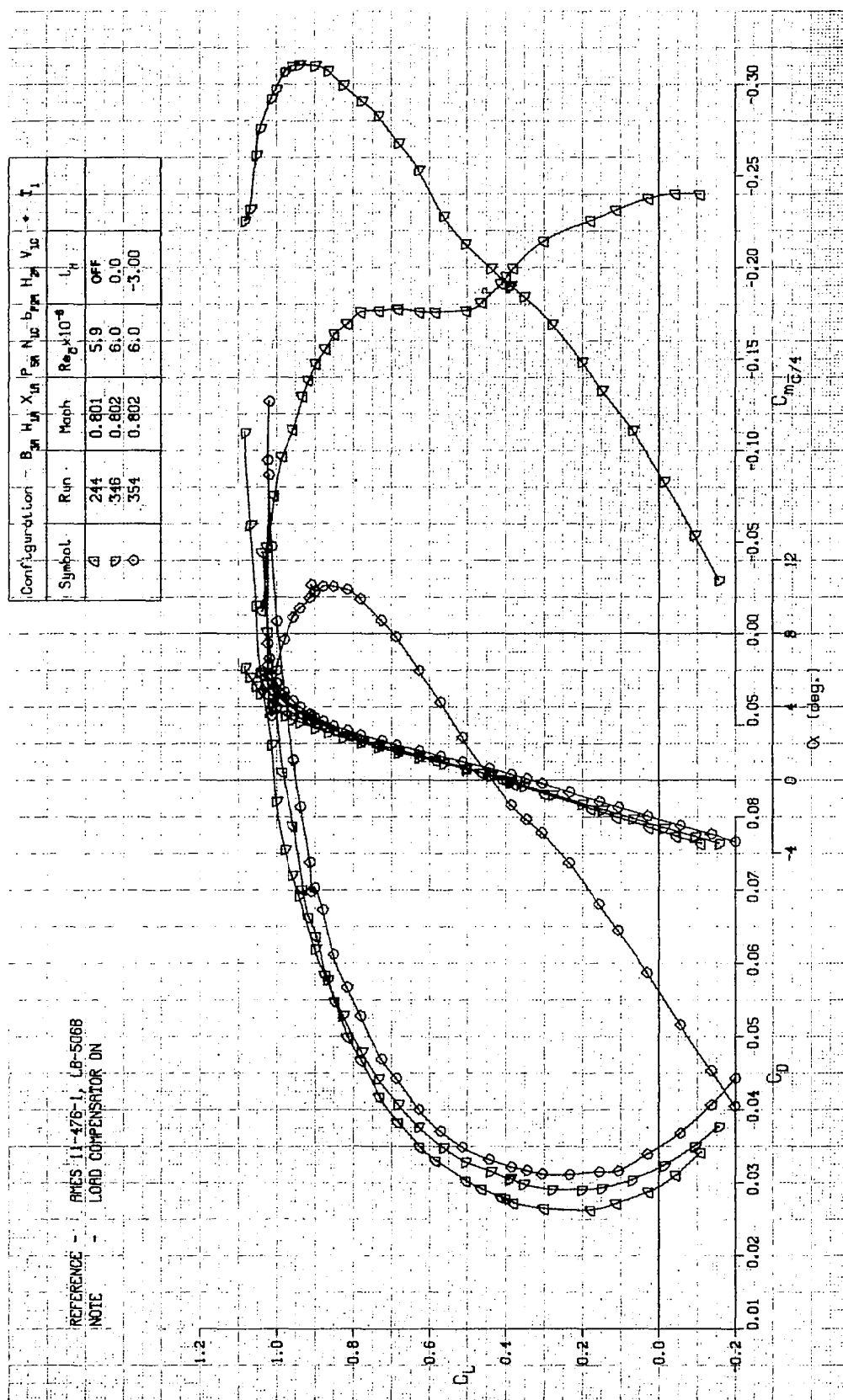
FIGURE A-91. LIFT, DRAG, AND PITCHING MOMENT CHARACTERISTICS OF WING W$_1$, WITH NACELLES, PYLONS, FLAP LINKAGE FAIRINGS, AND TAIL, TRANSITION FREE
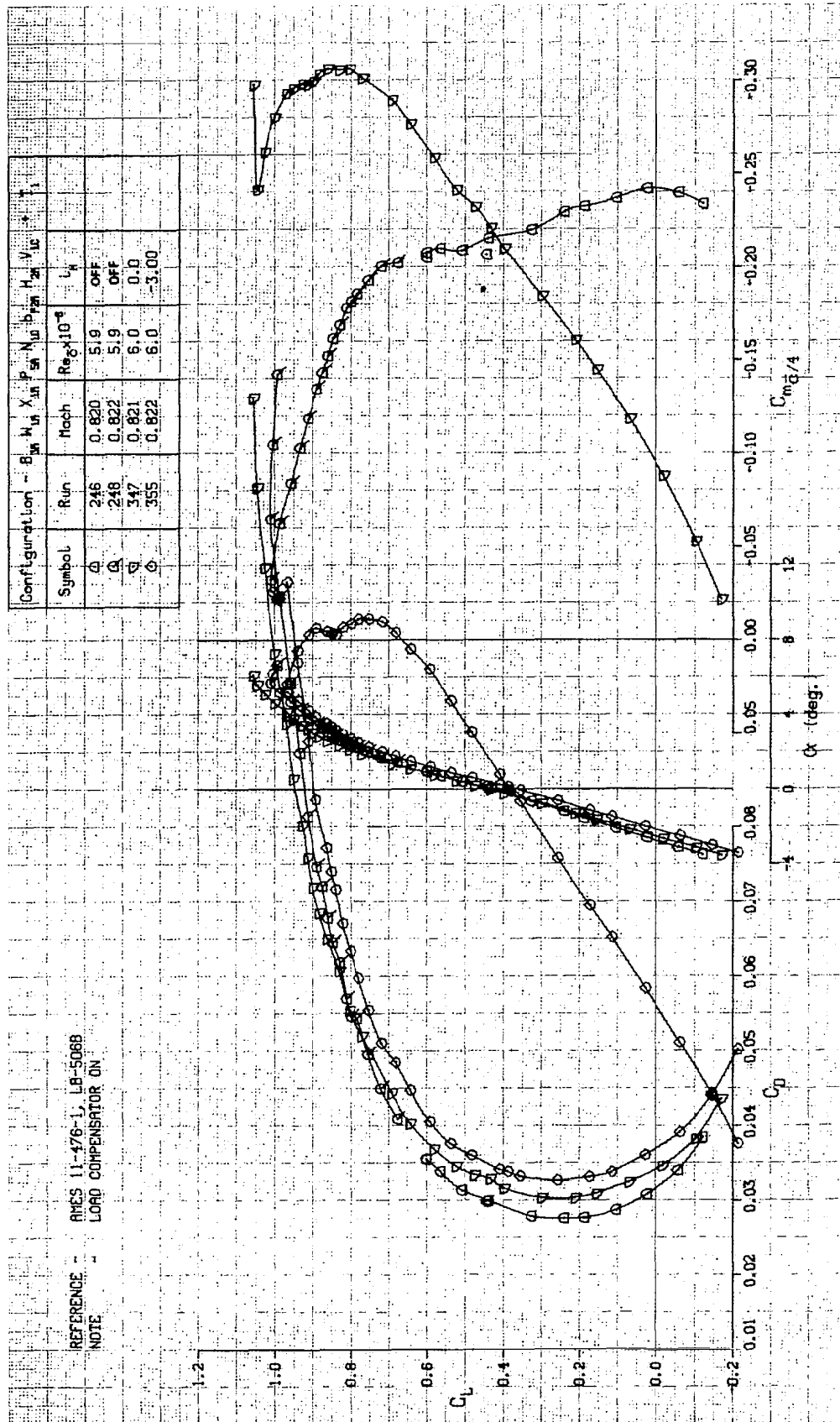
FIGURE A-92. LIFT, DRAG, AND PITCHING MOMENT CHARACTERISTICS OF WING W_1, WITH NACELLES, PYLONS, FLAP LINKAGE FAIRINGS, AND TAIL, TRANSITION FREE

FIGURE A-93. LIFT, DRAG, AND PITCHING MOMENT CHARACTERISTICS OF WING W₁, WITH NACELLES, PYLONS, FLAP LINKAGE FAIRINGS, AND TAIL, TRANSITION FREE
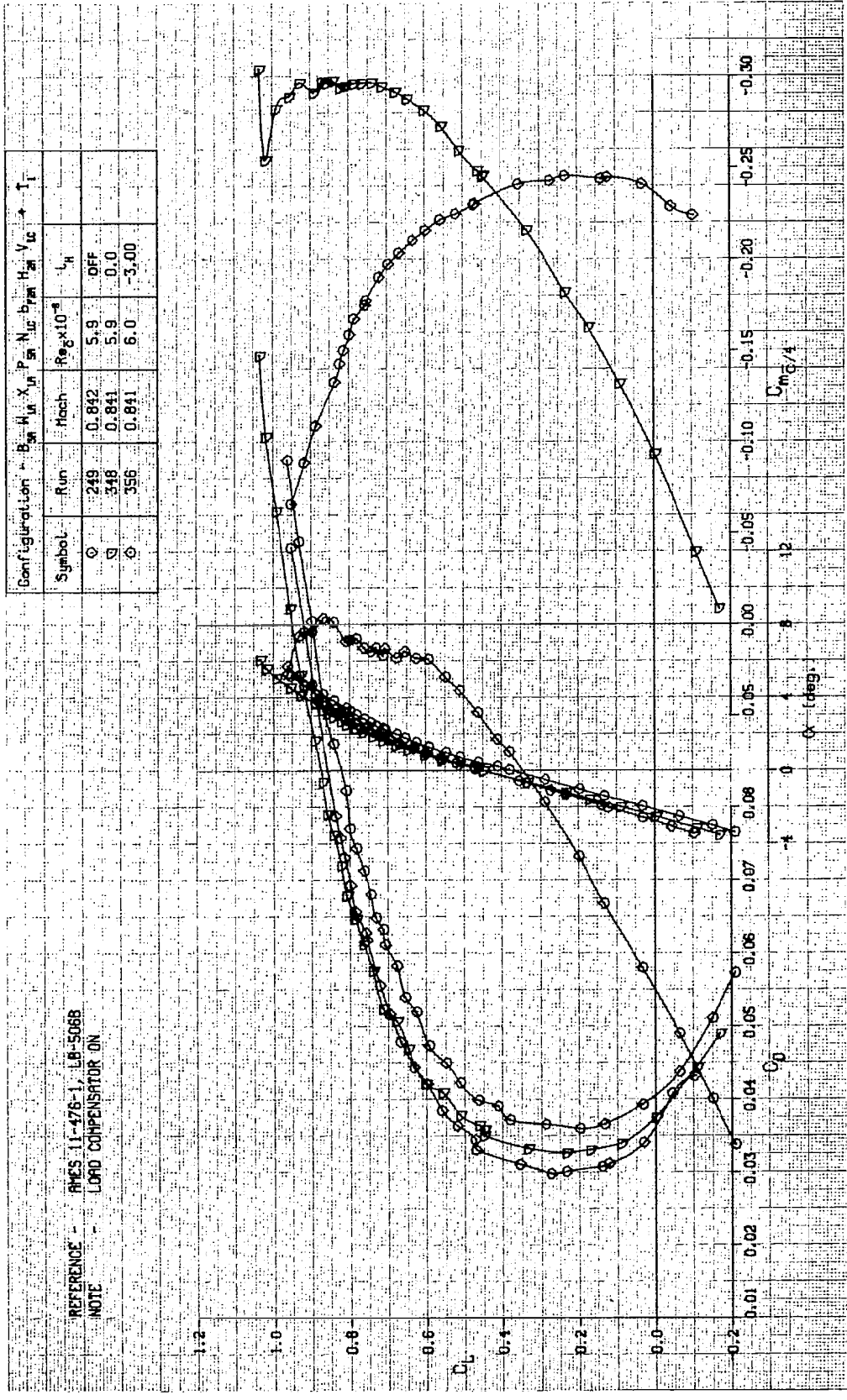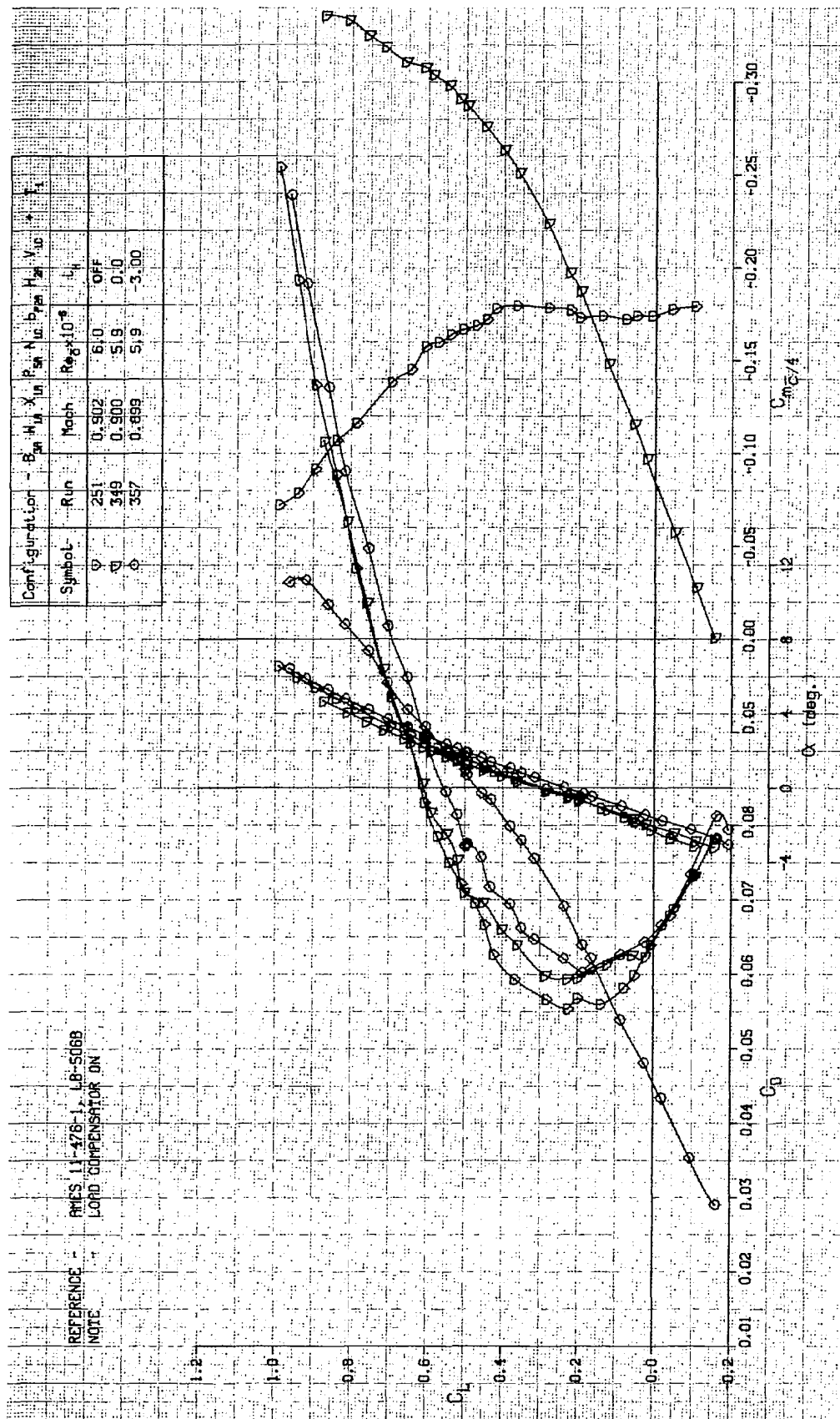
FIGURE A-94. LIFT, DRAG, AND PITCHING MOMENT CHARACTERISTICS OF WING W₁, WITH NACELLES, PYLONS, FLAP LINKAGE FAIRINGS, AND TAIL, TRANSITION FREE

FIGURE A-95. LIFT, DRAG, AND PITCHING MOMENT CHARACTERISTICS OF WING W₁, WITH NACELLES, PYLONS, FLAP LINKAGE FAIRINGS, AND TAIL, TRANSITION FREE

FIGURE A-96. LIFT, DRAG, AND PITCHING MOMENT CHARACTERISTICS OF WING W₁, WITH NACELLES, PYLONS, FLAP LINKAGE FAIRINGS, AND TAIL, TRANSITION FREE
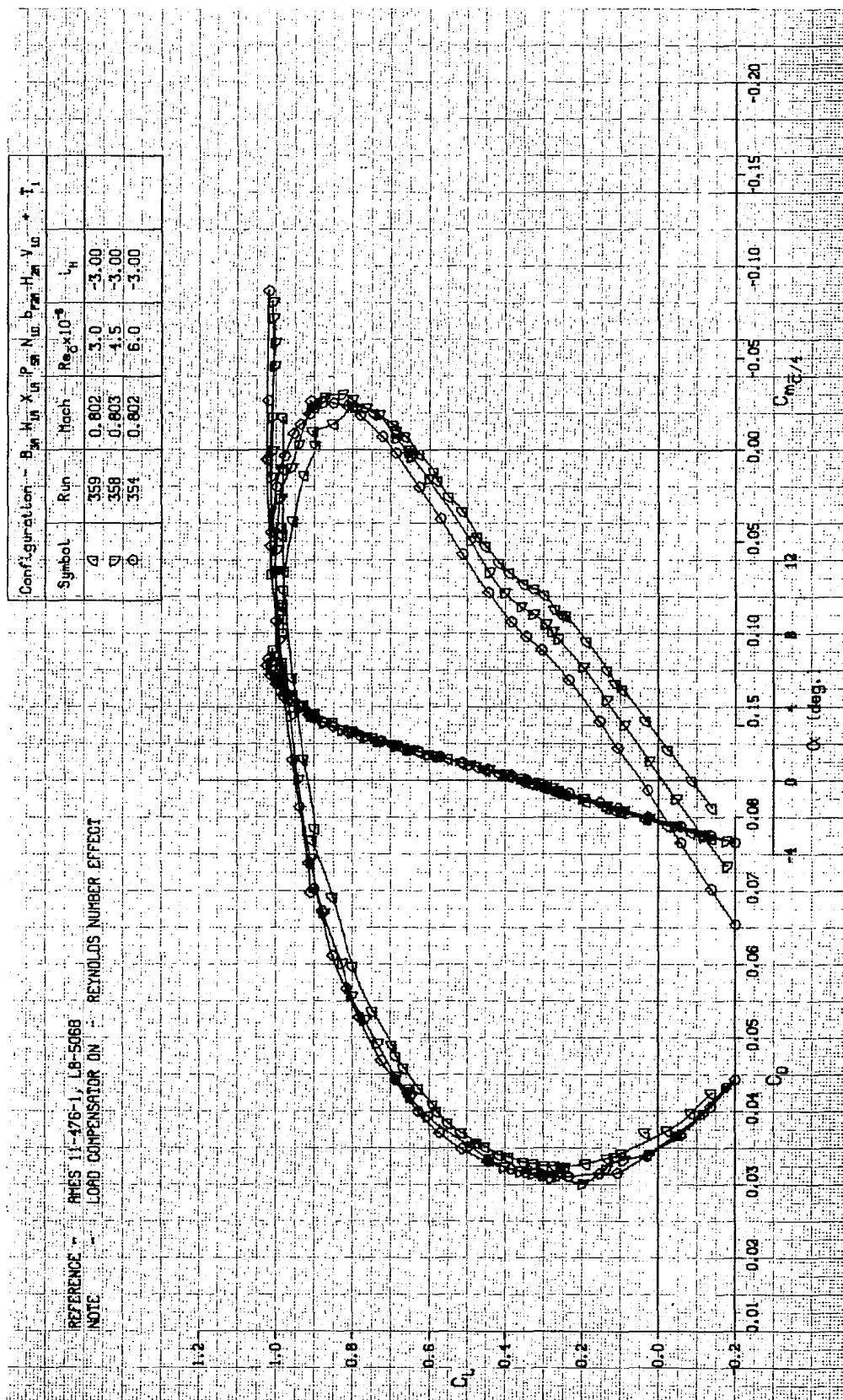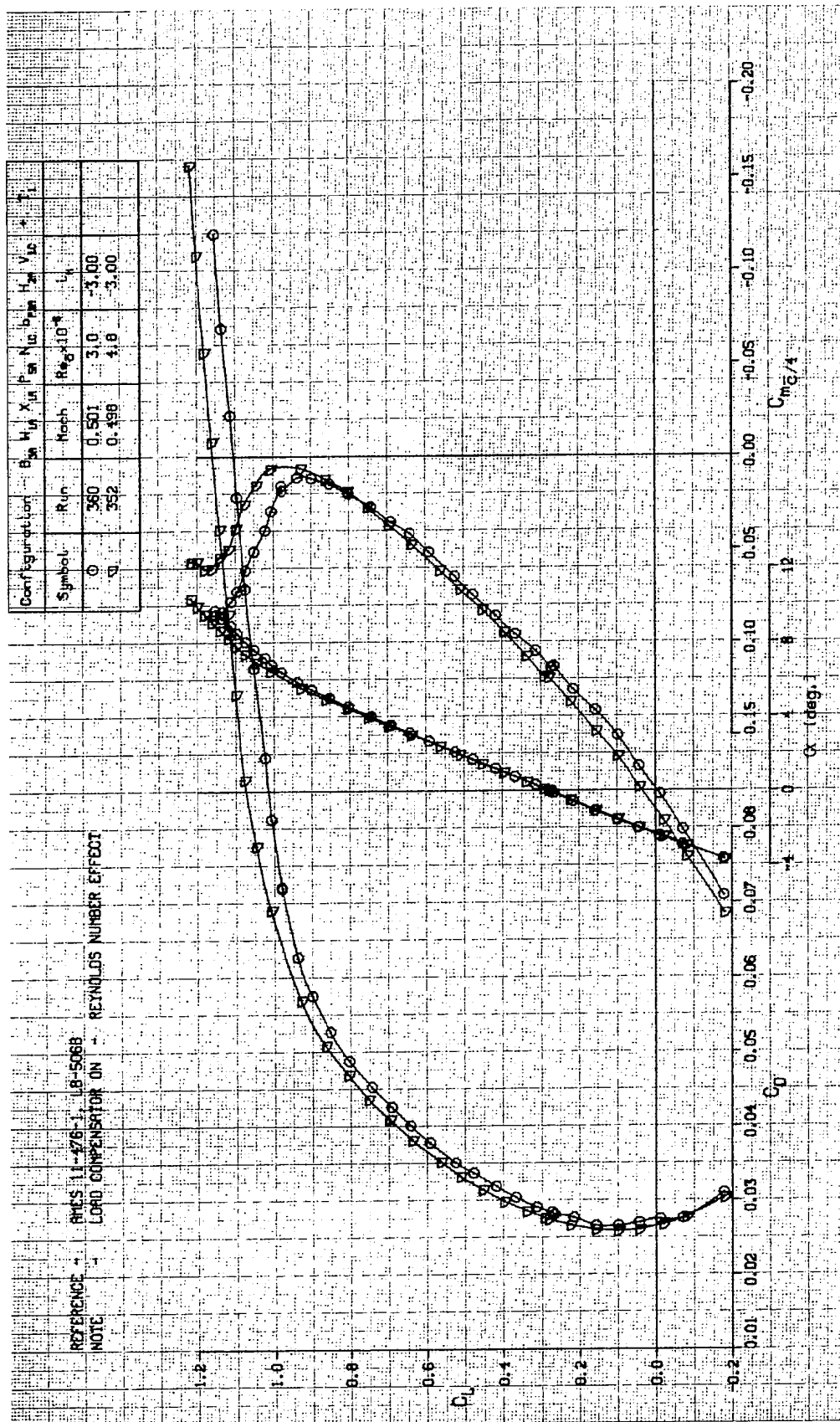
1. Report No. NASA CR-3524	2. Government Accession No.	3. Recipient's Catalog No.
4. Title and Subtitle CONFIGURATION DESIGN STUDIES AND WIND TUNNEL TESTS OF AN ENERGY EFFICIENT TRANSPORT WITH A HIGH-ASPECT-RATIO SUPERCRITICAL WING		5. Report Date May 1982
		6. Performing Organization Code
7. Author(s) Preston A. Henne, John A. Dahlin, Charles C. Peavey, and Donna S. Gerren		8. Performing Organization Report No. ACEE-17-FR-1644
9. Performing Organization Name and Address Douglas Aircraft Company McDonnell Douglas Corporation 3855 Lakewood Boulevard Long Beach, CA 90846		10. Work Unit No.
		11. Contract or Grant No. NAS1-15327
12. Sponsoring Agency Name and Address National Aeronautics and Space Administration Washington, DC 20546		13. Type of Report and Period Covered Contractor Report
		14. Sponsoring Agency Code

15. Supplementary Notes

Langley Technical Monitor: T. G. Gainer   Topical Report
Energy Efficient Transport Technology Project

16. Abstract

This report presents the results of design studies and wind tunnel tests of high-aspect-ratio supercritical wings suitable for a medium-range, narrow-body transport aircraft flying near M = 0.80. The basic characteristics of the wing design were derived from system studies of advanced transport aircraft where detailed structural and aerodynamic tradeoffs were used to determine the most optimum design from the standpoint of fuel usage and direct operating cost. These basic characteristics included wing area, aspect ratio, average thickness, and sweep. The detailed wing design was accomplished through application of previous test results and advanced computational transonic flow procedures. In addition to the basic wing/body development, considerable attention was directed to nacelle/pylon location effects, horizontal tail effects, and boundary layer transition effects. Results of these tests showed that the basic cruise performance objectives were met or exceeded, and that the high-aspect-ratio supercritical wing can be designed to realize a sizeable advantage over conventional aircraft wings in terms of fuel usage.

17. Key Words (Suggested by Author(s)) Wings Drag rise High Aspect Ratio Pitching moment Supercritical Aircraft design Buffet Transonic testing Transonic design	18. Distribution Statement FEDD Distribution Subject Category 01

19. Security Classif. (of this report) Unclassified	20. Security Classif. (of this page) Unclassified	21. No. of Pages 196	22. Price